1:50 Scale Testing of Three Floating Wind Turbines at MARIN and Numerical Model Validation Against Test Data

DeepCwind Consortium National Research Program Final Project Report Vol. I

Department of Energy Award Number: DE-EE0003278.001

UMaine Report: 16-30-DOE3278

Principle Investigator: Dr. Habib Dagher, PE

Co-Principle Investigators: Dr. Anthony Viselli, PE**,** Dr. Andrew Goupee**,** Dr. Richard Kimball, and Mr. Christopher Allen, M.Sc.

Advanced Structures and Composites Center
35 Flagstaff Rd
University of Maine
Orono, ME 04469

Telephone: 207-581-2123
FAX: 207-581-2074
composites@umit.maine.edu
www.composites.umaine.edu

***Acknowledgment*:**
This material is based upon work supported by the Department of Energy under Award Number DE-EE0003278.

Prepared by:

Andrew J. Goupee
University of Maine

Habib J. Dagher
University of Maine

James Browning
University of Colorado

Alexander J. Coulling
University of Maine

Matthew J. Fowler
University of Maine

Anant Jain
Intertek

Jason M. Jonkman
National Renewable Energy Laboratory

Richard W. Kimball
Maine Maritime Academy

Bonjun Koo
Technip

Matthew Lackner
University of Massachusetts

Kostas Lambrakos
Technip

Ho-Joon Lim
Technip

Heather R. Martin

University of Maine

Marco Masciola

National Renewable Energy Laboratory

Paul Molta

National Renewable Energy Laboratory

Ian Prowell

MMI Engineering

Amy N. Robertson

National Renewable Energy Laboratory

Gordon Stewart

University of Massachusetts

Andrew H. P. Swift

Texas Tech University

Dale A. Thomas III

Maine Maritime Academy

Anthony M. Viselli

University of Maine

Contents

Table of Figures

1 Introduction

The United States has a great opportunity to harness an indigenous abundant renewable energy resource: offshore wind. In 2010, the National Renewable Energy Laboratory (NREL) estimated there to be over 4,000 GW of potential offshore wind energy found within 50 nautical miles of the US coastlines (Musial and Ram, 2010). The US Energy Information Administration reported the total annual US electric energy generation in 2010 was 4,120 billion kilowatt-hours (equivalent to 470 GW) (US EIA, 2011), slightly more than 10% of the potential offshore wind resource. In addition, deep water offshore wind is the dominant US ocean energy resource available comprising 75% of the total assessed ocean energy resource as compared to wave and tidal resources (Musial, 2008). Through these assessments it is clear offshore wind can be a major contributor to US energy supplies.

The caveat to capturing offshore wind along many parts of the US coast is deep water. Nearly 60%, or 2,450 GW, of the estimated US offshore wind resource is located in water depths of 60 m or more (Musial and Ram, 2010). At water depths over 60 m building fixed offshore wind turbine foundations, such as those found in Europe, is likely economically infeasible (Musial *et al.*, 2006). Therefore floating wind turbine technology is seen as the best option for extracting a majority of the US offshore wind energy resource.

1.1 Motivation

In order to pursue commercial development of floating wind turbine technology a validated aero-hydro-servo-elastic numerical model is needed to accurately predict the dynamic system behavior during the design and optimization process. Currently, there are very few publicly available coupled numerical models for simulating the performance of floating wind turbines. These codes, such as the NREL's FAST (Jonkman and Buhl, 2005; Jonkman, 2007), have yet to be fully validated against real data as little published information of this type currently exists.

As of the writing of this report, there exists only two commercial scale floating wind turbines in the world: the Hywind by Statoil (Neville, 2009) and the WindFloat by Principle Power (Aubault *et al.*, 2009; Cermelli *et al.*, 2009; Roddier *et al.*, 2009) . The Hywind spar-buoy design supports a 2.3 MW horizontal axis wind turbine and is instrumented to capture key performance data. The WindFloat concept supports a 2 MW horizontal axis wind turbine mounted to a three column semi-submersible and is also instrumented to capture coupled aero-hydro-servo-elastic data. For both of these prototypes, however, the collected information is confidential and is not available to the public. Therefore, this information is inaccessible for many of the parties interested in calibrating and validating numerical analysis codes for offshore floating wind turbines.

Other limited sources of data do exist from the scale model testing of floating wind turbine concepts in a wave basin. Froude scale basin model testing is a refined science and is commonly used to test designs of large scale offshore vessels and structures by the oil and gas industry, military, and marine industries (*e.g.* see Chakrabarti, 1994). A basin model test requires less time, resources and risk than a full scale test while providing real and accurate data for model validation. Protocol for properly modeling the coupled wind and wave loads on a floating wind turbine in a wave basin test environment, however, have not been established. The diverse loads experienced by a floating wind turbine are characterized by dynamic wind spectra, irregular wave loads and many other complex factors. These varied environmental loads combined with challenging fluid-structure interaction, turbine performance and flexible member structural dynamics phenomena make the prospect of performing an accurate scale model test a challenging one. Despite the aforementioned difficulty, a select few floating wind turbine model tests have been performed in wave basins. These include efforts by Principle Power Inc. (Roddier *et al.*, 2010), Hydro Oil & Energy (Skaare *et al.*, 2007) and WindSea AS (Windsea, 2012). However, these tests only cover select floating wind

turbine concepts and report only limited to modest information regarding the scaling methodologies and testing techniques employed. In addition, the differing methods utilized in the aforementioned model tests make it difficult to directly compare the relative performance of the various floating wind turbine concepts considered. Therefore, it is clear that a comprehensive, high-quality data set of several floating wind turbine concepts is needed for the continued development and validation of coupled floating wind turbine simulators.

1.2 Objectives

The primary goal of the basin model test program discussed herein is to properly scale and accurately capture physical data of the rigid body motions, accelerations and loads for different floating wind turbine platform technologies. The intended use for this data is for performing comparisons with predictions from various aero-hydro-servo-elastic floating wind turbine simulators for calibration and validation. Of particular interest is validating the floating offshore wind turbine simulation capabilities of NREL's FAST open-source simulation tool. Once the validation process is complete, coupled simulators such as FAST can be used with a much greater degree of confidence in design processes for commercial development of floating offshore wind turbines.

The test program subsequently described in this report was performed at MARIN (Maritime Research Institute Netherlands) in Wageningen, the Netherlands. The models considered consisted of the horizontal axis, NREL 5 MW Reference Wind Turbine (Jonkman *et al.*, 2009) with a flexible tower affixed atop three distinct platforms: a tension leg platform (TLP), a spar-buoy modeled after the OC3 Hywind (Jonkman, 2010) and a semi-submersible. The three generic platform designs were intended to cover the spectrum of currently investigated concepts, each based on proven floating offshore structure technology. The models were tested under Froude scale wind and wave loads. The high-quality wind environments, unique to these tests, were realized in the offshore basin via a novel wind machine which exhibits negligible swirl and low turbulence intensity in the flow field. Recorded data from the floating wind turbine models included rotor torque and position, tower top and base forces and moments, mooring line tensions, six-axis platform motions and accelerations at key locations on the nacelle, tower, and platform. A large number of tests were performed ranging from simple free-decay tests to complex operating conditions with irregular sea states and dynamic winds.

With the data in hand, analysis of the floating wind turbine responses revealed several of the unique dynamic behaviors of the various floating wind turbine concepts. In particular, the tests highlighted the interplay of the combined wind and wave forcing on floating wind turbine motions and structural load behavior. After analyzing the response of the floating wind turbine concepts, the data was used to validate the floating wind turbine simulator FAST through correlation of the numerical simulation output and test data for the three floating wind turbine types. In addition, validation of coupled simulators other than FAST was also undertaken. A much greater understanding of the strengths and weaknesses of the FAST tool was established through these efforts. In addition to the validation of FAST, several other simulators were investigated many of which utilized more sophisticated hydrodynamics and mooring modules than the standard FAST tools. These efforts were quite helpful in providing suggested improvements for addressing the shortcomings of FAST's fluid-structure interaction calculations. An additional benefit of the validation exercises was the identification of several possibilities for improving model testing procedures for future floating wind turbine wind/wave basin model tests. Some of these improvements, in particular those focused on properly scaling wind turbine performance, were put into practice via a retesting of the semi-submersible configuration at MARIN's offshore basin. The data gathered from this retesting campaign verified the findings of the initial testing campaign as

well as shed light on the possibilities of using an improved wind turbine in a floating wind turbine model test campaign.

1.3 Report Layout

The remainder of this report is organized as follows. In Section 2, an overview of the floating wind turbine model test scaling methods developed for this program are presented. In addition, Section 2 also covers a verification of the scaling laws using FAST simulations in addition to a discussion of Reynolds number effects and their impact on obtaining the correct wind turbine performance in a Froude-scaled experiment. In Section 3, the technical specifications for three floating wind turbines, in addition to the model instrumentation and test matrix, are presented. For Section 4, select test data is analyzed and the unique dynamic behaviors of each of the three systems is discussed. In Section 5, the model test data is used to calibrate and subsequently validate FAST models of each of the three floating wind turbine systems considered in this report. In addition, Section 5 also investigates the predicative capabilities of improved versions of FAST using the model test data. Afterward, Section 6 presents improved model wind turbine design methodologies and accompanying test data for use in future floating wind turbine wind/wave basin model tests. Section 7 discusses the findings of a floating wind turbine retesting campaign using an improved wind turbine with a focus on verifying the validity of the data in Section 4. This is followed by Section 8, which summarizes the conclusions of this report and suggests options for future work.

2 Scaling Methods

Basin model testing is a refined science and is commonly used to test designs of large scale offshore vessels and structures by the oil and gas industry, military, and marine industries (e.g. see (Chakrabarti, 1994)). A basin model test is ideal as it requires less time, resources and risk than a full scale test while providing real and accurate data for system global response. However, even though wave basin testing is well refined for many types of offshore configurations, protocol for properly modeling coupled wind and wave loads on a floating wind turbine in a wave basin test environment has not been established.

Floating wind turbines are complex structures with numerous variables contributing to their complicated dynamic behavior. Simultaneous wind and wave loading, turbine aerodynamics and flexible towers make execution of an accurate scale model test a significant challenge. Despite the aforementioned difficulties, a few select floating wind turbine basin model tests have been performed. Principle Power Inc. tested a 1/67th scale semi-submersible wind turbine platform, WindFloat (Roddier *et al.*, 2010). In 2006, Hydro Oil & Energy conducted a 1/47th scale model test of a 5 MW spar-buoy floating wind turbine at Marintek's Ocean Basin Laboratory in Trondheim, Norway (Skaare *et al.*, 2007). Another basin test by WindSea of Norway was performed under wind and wave environments at Force Technology on a 1/64th scale tri-wind turbine semi-submersible platform (Windsea, 2012). These model tests provided valuable information to respective stake holders and advanced knowledge of floating wind turbine dynamics. However, the methodologies and techniques used during these model tests differed significantly and not all details of the tests have been thoroughly presented in the public domain. Therefore, there is a clear need for a comprehensive, unified model testing methodology for Froude scale testing of floating wind turbines.

In light of this need, this section presents a method for performing combined wind/wave model testing of floating wind turbines under Froude scale conditions. Topics covered include scaling relationships, wind generation techniques and issues concerning the strong dependence of wind turbine aerodynamic behavior on Reynolds number. The method verified using FAST simulations and is demonstrated using results of combined wind/wave 1/50th scale model testing performed at MARIN on three floating horizontal axis wind turbine concepts each supporting a model of the 5 MW, 126 m rotor diameter horizontal axis NREL Reference Wind Turbine (Jonkman *et al.*, 2009). The results and corresponding analysis demonstrate that the issues resulting from aerodynamic Reynolds number dissimilitude do not hamper the ability to capture quality global response data for floating wind turbines.

2.1 Overview of Scaling Methods for Floating Wind Turbines

In order to establish a scaling methodology, a particular set of rules and constraints must be selected. The suggested scaling relationships employed for modeling of floating offshore wind turbines are as follows:

1. *Froude number similitude is employed from prototype to scale model*. Offshore platform wave basin tests are typically scaled using Froude number and geometric similarity. Although a Froude model does not scale all parameters properly the dominant factors in the hydrodynamic problem, gravity and inertia, are properly scaled (Chakrabarti, 1994). For a floating wind turbine, this covers most properties of interest which influence the global dynamic response of the system, excepting the aerodynamic wind forces. Employing a Reynolds number scaling scheme, common for model aerodynamic experiments, is impractical for a floating body subjected to wave forcing. Therefore, Froude scaling is best suited for model testing of floating wind turbines. The Froude number for a free surface wave is

$$Fr_{wave} = C/\sqrt{gL},$$

where C is the wave celerity, or propagation speed, g is the local acceleration due to gravity and L is a characteristic length. The scaling relationship maintained from model scale to the full scale prototype is expressed as

$$Fr_p = Fr_m,$$

where p and m stand for prototype and model, respectively.

2. *Froude scaled wind is employed during basin model testing.* If aerodynamic turbine features are insensitive to Reynolds number, then the wind force to wave force ratio from prototype to model scale is maintained by utilizing Froude scaled wind, defined as

$$Fr_{wind} = U/\sqrt{gL},$$

where U is the wind inflow velocity. Note that the characteristic length L is the same for both the wind and wave Froude numbers. An alternative, yet consistent, way to represent Froude scaled wind is by maintaining the ratio of wind speed to wave celerity from model to full scale. This ratio is identified by the variable Q and represented as

$$Q = U/C.$$

3. *The wind turbine tip speed ratio, TSR, is to be maintained from prototype to scale model. TSR* is computed as

$$TSR = \Omega r/U,$$

where Ω is the rotor rotational speed and r is the blade tip radius. Maintaining *TSR* between the prototype and model is performed by satisfying the relationship

$$TSR_p = TSR_m.$$

Maintaining *TSR* ensures that the turbine rotational speed as well as any system excitation frequencies resulting from rotor imbalance or aerodynamic interaction with the tower will possess the correct frequency. In addition, maintaining *TSR* will yield properly scaled turbine thrust forces and rotor torque in conjunction with a Froude scaled wind environment, assuming a low dependence on Reynolds number for the wind turbine airfoil section lift and drag coefficients. The impact of Reynolds dependent wind blade lift and drag coefficients is discussed in a later section.

While not discussed at length here, it is also important to note that scaling of current loads requires additional measures to accommodate for the mismatch in model and prototype Reynolds numbers (e.g. see (Chakrabarti, 1994) for suggested methods). That stated, the preceding scaling relationships are utilized to obtain the scale factors shown in Table 1 for characterizing a scaled floating wind turbine.

Table 1: Scaling factors for floating wind turbine model testing.

Parameter	Scale Factor
Length (e.g. displacement, wave height)	λ
Area	λ^2
Volume	λ^3
Angle	1
Density	1
Mass	λ^3
Time (e.g. wave period)	$\lambda^{0.5}$
Frequency (e.g. rotor rotational speed)	$\lambda^{-0.5}$
Velocity (e.g. wind speed, wave celerity)	$\lambda^{0.5}$
Acceleration	1
Force (e.g. wind, wave, structural)	λ^3
Moment (e.g. structural, rotor torque)	λ^4
Power	$\lambda^{3.5}$
Young's Modulus	λ
Stress	λ
Mass Moment of Inertia	λ^5
Area Moment of Inertia	λ^4

The scale factors are a function of the scale parameter λ which is defined as the ratio of length scales between the prototype and model. With the scale parameter defined, the model value of a desired parameter is obtained by dividing the prototype quantity by the appropriate scale factor in Table 1. For example, if the scale parameter is $\lambda = 50$ and the prototype rotor speed is 10 rpm, then the model rotor speed is equal to $10/50^{-0.5}$, or 70.7 rpm.

To demonstrate some of the practical challenges with constructing a scale model wind turbine, the scale factors in Table 1 are employed to create model specifications for the NREL 5 MW Reference Wind Turbine and OC3 Hywind tower (Jonkman 2010) used for model testing with $\lambda = 50$. The specifications for the various wind turbine and tower components are listed in Table 2. As can be seen in the table, the rated power of the machine is quite low, nearly one millionth the prototype value. In addition, the rotor speed is significantly higher and the wind speed environment, much lower. From a practical standpoint, these quantities do not provide major challenges when constructing a physical model or its accompanying environment. The mass of the components, such as the blade and nacelle, however, are a different matter.

Table 2: Prototype and model specifications for the NREL 5 MW Reference Wind Turbine and OC3 Hywind Tower with scaling parameter $\lambda = 50$.

Property	**Prototype**	**Model**
Rated Power	5 MW	5.7 W
Rated Rotor Speed	12.1 rpm	85.6 rpm
Rated Wind Speed	11.4 m/s	1.6 m/s
Blade Mass	17,740 kg	0.14 kg
Blade Length	61.5 m	1.23 m
Hub Mass	56,780 kg	0.45 kg
Nacelle Mass	240,000 kg	1.92 kg
Tower Mass	249,718 kg	1.998 kg
Tower Length	77.6 m	1.55 m
Tower Base Stiffness	6.04×10^{11} N·m^2	1.93×10^{3} N·m^2

This fact is illustrated by the model blade which must be over a meter in length and possess a mass of only 0.14 kg. These blade parameters are necessary in order to correctly model the wind turbine gyroscopic moments. Simultaneously creating an accurate representation of the prototype blade geometry and achieving the mass target is not a simple endeavor. To accomplish this task for the model testing considered here, model wind turbine blades are manufactured from two thin layers of woven carbon fiber epoxy composite material in a bladder molding process. An image of a completed blade is shown in Figure 1.

Figure 1: Lightweight 1/50th scale carbon fiber epoxy composite model wind turbine blade.

Meeting the mass targets for other tower top components which together impact the tower bending natural frequency, such as the hub and nacelle, also requires careful engineering and design, especially in order to accommodate instrumentation for measuring rotor position, rotor torque, nacelle accelerations, etc. Other creative measures are necessary to meet additional model requirements. For example, to achieve the correct tower bending stiffness to properly emulate the fundamental tower bending frequency, perfectly scaling the material stiffness and tower geometry may be difficult, or even unrealistic as no suitable material may exist. Therefore, it is suggested that the material choice and geometry be tuned together to obtain the desired stiffness, even if neither quantity in and of itself represents the desired model value based on the prototype specifications. For example, the model turbine employed in this study utilizes a tower crafted from two common size hollow aluminum rod sections tailored in length, inner and outer diameter such that the tower mass target and overall tower bending stiffness is achieved. The tower, while not strictly Froude-scaled, yields the correct fundamental tower bending frequencies. An image of the model wind turbine mounted to a semi-submersible platform (a spar-buoy and a TLP were also tested) is shown in Figure 2.

An additional practical challenge outside of creating a functional model wind turbine at such a small scale is the issue of manufacturing a quality Froude scale wind environment for the wind turbine to operate in. The wind environment should be of a high quality with little evidence of fan generated swirl and low turbulence intensity. This requires a dedicated wind generator consisting of a series of fans, screens, as well as a contracting nozzle.

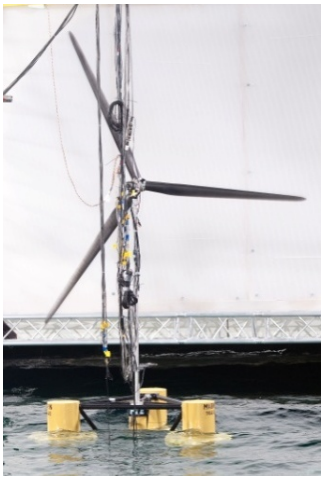

Figure 2: 1/50th scale model NREL 5 MW Reference Wind Turbine mounted to a semi-submersible platform.

In addition, the output area of the nozzle should cover the entire wind turbine rotor in quality wind even as the floating system moves through its expected range of motion. Therefore, a large wind generation system is ideal. However, too large a system is impractical as it will be very costly to build, maintain and operate. Therefore, a balance must be struck in choosing a model wind turbine size, and hence λ. Ideally the size will be small enough to reduce wind generator requirements, but large enough to yield achievable weight targets for the wind turbine components. Development efforts from the multi-platform floating wind turbine model test program and accompanying wind machine, a schematic of which is shown in Figure 3, suggest a scale parameter λ of approximately 50 is well suited for floating wind turbine experiments of commercial machines.

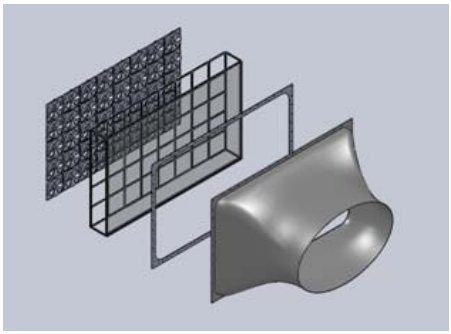

Figure 3: Exploded view of wind generation machine for floating wind turbine wind/wave basin experiments showing, from left to right, a fan bank, screens and a contracting nozzle.

By employing the scaling factors in Table 1 as well as the various recommendations in this section, an adequate floating wind turbine model can be constructed for wind/wave basin testing. However the aerodynamic properties of a typical commercial scale wind turbine rotor are sensitive to Reynolds number, unlike the hydrodynamic properties of the floating platform which possess a weaker dependence on Reynolds number. This scenario creates difficulties in achieving the correct wind forcing from a Froude scale wind turbine and corresponding wind environment. A discussion of the implications of testing a prototype rotor that possesses a strong dependence on Reynolds number will be presented in a later section.

2.2 Verification of Scaling Laws Using FAST

To examine the scaling laws used by DeepCwind, we have conducted a research study to verify them using FAST (Jonkman et. al, 2005). The process, as described in this section, examines if there are any differences between the system responses obtained from full-scale and model-scale simulations in FAST. This assessment is important because all of the results of the tests at MARIN were converted to full scale for reporting purposes. Our verification strategy in this report section is based only on the scaling laws from the previous section and does not include any comparison of actual results from the DeepCwind wind/wave basin experiments. The scaling laws are investigated using two floating offshore wind turbine models, a modified version of the OC3 Hywind and the MIT/NREL TLP. These models are not the exact ones tested in the wave basin, but are sufficient for examining the validity of the scaling approach used for the DeepCwind model tests. The remainder of this section describes the verification procedure, system configurations studied, assumptions and results.

2.2.1 Scaling Law Verification Procedure

This section gives an overview of the FAST code verification and testing process for scaling laws that interlink the full scale and model scale parameters. The process used for verification is described as follows (and depicted in Figure 4):

1. Full-scale FAST models of the two floating offshore wind systems to be examined are modeled.

2. Using the scaling laws, the FAST models are converted to model scale.
3. Simulations are performed at model scale for a variety of load cases.
4. The outputs obtained from the model-scale simulations (forces, displacements) are scaled back up to full scale using the same scaling laws.
5. Simulations are performed using the full-scale model for a variety of load cases.
6. The simulations results from the up-scaled model are then compared to the simulation results from the full-scale model. If the scaling laws are consistent, these results should be the same.

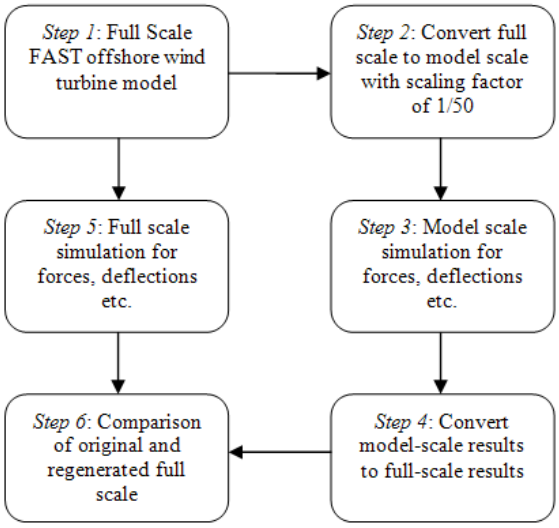

Figure 4: Flowchart for scaling simulation procedure.

2.2.2 System Configurations: Turbine, Platforms, Wind and Wave Specifications

To examine the similarity in system performance between full scale and model scale, simulations are conducted with a variety of loading conditions. Verification of the scaling law accuracy is accomplished through the analysis of two different platform configurations: a modified version of the OC3-Hywind spar buoy and the MIT/NREL TLP. These systems are chosen due to the diversity in design and mooring configuration, and therefore response characteristics.

The turbine used for this research is a 5-MW reference wind turbine (onshore and offshore) from NREL, which is a three-bladed, upwind turbine with rated power of 5 MW. The design of this turbine is a reinvention inspired from the technical specifications of Multibrid M5000, REpower 5M, WindPACT, RECOFF and DOWEC wind turbines (Jonkman et. al., 2009). Some of the properties of the turbine are stated below:

Table 3: Structural and aerodynamic properties of 5-MW wind turbine.

Structural and Aerodynamic Properties	Numerical Value
Tip radius	63 m
Hub radius	1.5 m
Tower Height	87.6 m
Rotor Pre-cone angle	2.5 deg
Nacelle Mass	240000 kg
Hub Mass	56780 kg
Air Density	1.225 kg/m^3
Kinematic Viscosity	0.00001464 m^2/sec

The two platform configurations incorporated and compared in this research for various wind and wave loading tests include: the OC3-Hywind spar buoy (Jonkman, 2010) and the NREL/MIT tension leg platform (TLP) (Matha, 2010) configuration. Details on design specifications for these platforms are given below in Table 4 and Figure 5:

Table 4: Structural and hydrodynamic properties of platform configurations.

Properties	TLP	Spar-buoy
Tower Draft from MSL	0	-10 m
Center of Moment (Platform) from MSL	40.612 m	89.9155 m
Platform Mass	8600410 kg	7466330 kg
Water displaced in a still water condition	12179.60 m^3	8029.21 m^3
Platform Diameter	18 m	6.5 m
Coefficient of Drag	0.6	0.6

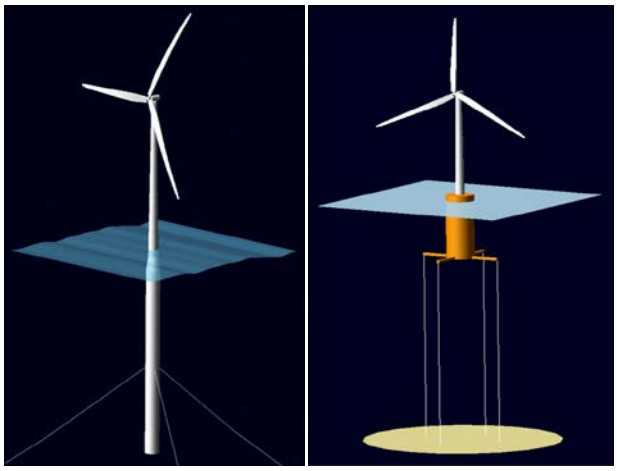

Figure 5: Sketches of OC3-Hywind spar buoy (left) and NREL/MIT TLP (right).

Simulated wind files are generated by using NREL's TurbSim code (B.J. Jonkman, 2009), which generates turbulent wind files to evaluate turbine response in various wind conditions. Wave effects are simulated using HydroDyn (Jonkman, 2007) which generates the hydrodynamic forces and loads using WAMIT (WAMIT Inc., 1998) as a pre-processor for defining the hydrodynamic coefficients of the platform. HydroDyn simulates loads and forces for periodic (consistent amplitude and frequency) and irregular waves. Periodic waves are simulated by using Airy wave theory and non-periodic waves are generated according to JONSWAP/Pierson-Moskowitz spectra (Jonkman, 2007). Predetermined wave conditions for these functions are defined in input files in terms of water density, water depth, significant wave height, peak spectral period and wave direction.

When these scaling laws are applied to the existing wind turbine and offshore floating platform designs, new input files are created for FAST using MATLAB scripts for maintaining accuracy and consistency. FAST v7.00.01a-bjj is applied in all simulations (Jonkman et. al., 2005).

2.2.3 Assumptions

For standardization of scaling laws simulations, we have created and followed few assumptions which are applied to all test procedures demonstrated in this report. These conditions are described below:

1. Fluid properties such as kinematic viscosity for full scale and model scale are constant.
2. Blade airfoil schedule and corresponding coefficients of lift and drag are not scaled for model tests.
3. The generator is prescribed to rotate at a constant speed.
4. Blade and tower vibration modes are constant for full scale and model scale.
5. Control module is inactive in the simulations. Therefore, control algorithm bound parameters such as pitch and yaw angle are either zero or maintained at a constant value for different wind and wave loading conditions.
6. Standard simulation time is assumed to be 630 seconds.
7. The wind and waves are aligned.

2.2.4 Results

The simulations (conducted for both platform configurations) are divided into six categories, as described below:

1. *Static analysis:* The first simulation that was performed is a static analysis to ensure that the mass, buoyancy and mooring pretension of the system are balanced, and therefore are scaled appropriately.
2. *Free-decay tests with initial offsets*: In these tests, the decay pattern is examined to compare structural frequencies and damping characteristics of the systems. Wind and waves are not used in these simulations.
3. *Steady wind and still water:* These tests are conducted to characterize structural response of the system from wind loads only. Wave conditions are ignored in this category. A steady wind at 8 m/s and 1.13 m/s for full scale and model scale, respectively is used with zero vertical and horizontal wind shear. In addition to wind speed, rotor speed is set at 9 rpm and 63.63 rpm for full scale and model scale respectively, according to specifications given for 5-MW wind turbine design.
4. *Still air and periodic waves:* These tests are conducted for assessment of system response from wave-induced loads only. Wind conditions are ignored in this category. Periodic wave conditions such as significant wave height, is 6 m and 0.12 m for full scale and model scale, respectively.
5. *Steady wind and periodic waves*: In these tests, both aerodynamic and hydrodynamic excitations are included in the simulations. The significant wave height is 6 m and 0.12 m for full scale and model scale, respectively. Rotor angular speed is maintained at a constant 9 rpm and 63.63 rpm for full scale and model scale respectively.
6. *Turbulent wind and irregular wave*s: This category of tests is very significant to analyze system response as it represents an extreme stochastic wind/wave loading schedule. The turbulent wind is averaged at 8 m/s at full scale and 1.13 m/s at model scale; with a turbulence intensity of 40%. The waves are irregular with a mean significant wave height of 6 m and 0.12 m for full scale and model scale respectively. As stated earlier, the rotor rpm is kept consistent at 9 rpm and 63.63 rpm for full scale and model scale respectively, with stochastic wind and wave loads.

These tests are conducted independently on both full scale and scale models. The output parameters calculated by FAST are very extensive and therefore only a limited number of parameters are analyzed to ensure the results are similar. The output parameters analyzed include:

1. *Blades*: loads at the base and in-plane and out-of-plane deflections at the tip;
2. *Tower*: tower-top shear, axial force and bending moments
3. *Platf*orm: 6-DOF motion of the platform and loads at the connection point between the platform and tower (tower base)
4. *Mooring Lines*: fairlead and anchor tensions

The scaling laws applied to the above mentioned output parameters that are used to analyze the full scale and model scale compliance are given in Table 5. These laws are also based on Froude scaling regime.

Table 5: Scaling laws for relevant output parameters in FAST code.

Output Parameter	Scaling Law
Blade tip deflections	λ
Tower Shear Forces	λ^3
Tower Bending Moments	λ^4
Platform Translational Displacements	λ
Mooring Line Tensions	λ

The output parameters from simulation at both scales and for both platform configurations are shown in Figure 6, Figure 8, Figure 10 and Figure 12 for the spar-buoy platform and Figure 7, Figure 9, Figure 11 and Figure 13 for the TLP. In all these tests, the full-scale and model-scale results are in excellent compliance. But for this report, we have selected only certain test conditions that represent a higher intensity of stochastic wind and wave loads i.e. turbulent wind and non-periodic wave load tests; and different output parameters pertaining to major wind turbine structural components. The following set of figures describe blade tip deflections, tower-top shear forces and bending moments, platform rotational and translational motions, and mooring line fairlead and anchor tensions for spar-buoy and tension-leg platforms. Full-scale and model-scale results are plotted together by blue and red lines and vice-versa for spar buoy and TLP, respectively. In Figure 6 and Figure 7, it is shown that the out of plane and in plane blade tip deflections perfectly coincide with each other. Because Reynolds number is maintained, we have assumed that the airfoil definitions and coefficients of lift and drag of full-scale and model-scale blades are exactly similar, we can conclude that the Froude scaling is capable of scaling the boundary layer flow around an airfoil, under controlled and consistent aerodynamic conditions. Since the aerodynamic conditions for the rotor on both the platform configurations are similar, the simulated tip deflections graphs show good alignment for both cases. On the other hand, the shear and axial forces and bending moment trends for tower top/yaw bearing are quite different among the selected platform configurations.

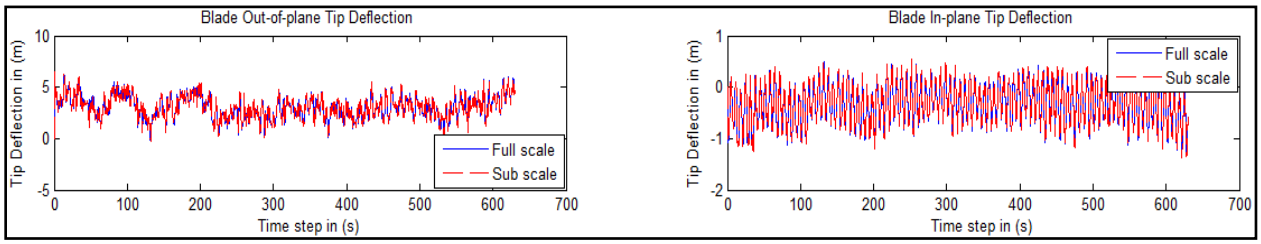

Figure 6: Time history of blade tip out of plane and in plane deflection for a turbine supported by OC3 Hywind spar-buoy platform.

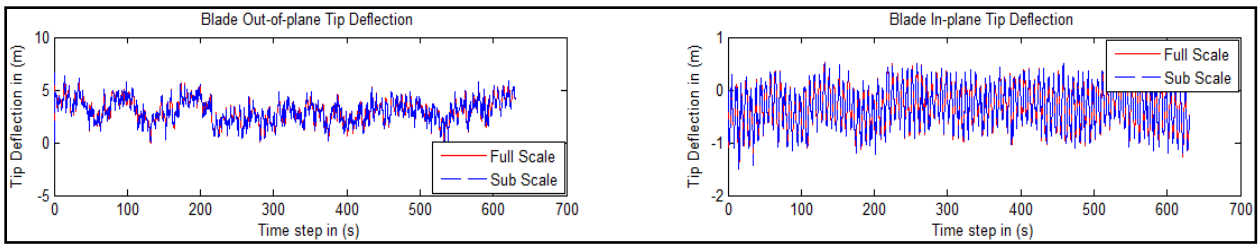

Figure 7: Time history of blade tip out of plane and in plane deflection for a turbine supported by MIT/NREL TLP system.

In Figure 8 (spar-buoy configuration), it is observed that tower top fore-aft shear force reaches to a maximum of approximately 1600N while the same shear force regime is limited to 1200N roughly for a TLP configuration (Figure 9). Similar differences have been observed for side-to-side and vertical force between spar-buoy and TLP systems, where TLP systems have more constrained displacements and rotations as compared to spar-buoy platform. It is important to note here that although the system properties (Table 3 and Table 4) are completely different for both configurations; their structural response is very much consistent when compared between a full-scale and a model-scale system. Moreover, the wind and wave loading regime is required to be similar to obtain such results.

The platform translational and rotational motions are further analyzed to ensure hydrodynamic similitude between the full scale and model scale system. In Figure 10 and Figure 11, it can be observed that surge, sway and heave displacements for spar-buoy platform are much higher in magnitude when compared to a TLP system. A similar pattern is documented for differences between the rotational displacements of the two platform configurations. The explanation for this restricted displacement characteristics is the added pretension in the mooring lines of a TLP system which is not present in the slack mooring lines of a spar-buoy system. This reasoning is further endorsed by the elevated mooring line tensions up to 6000N for a TLP system shown in Figure 13 with higher frequency of perturbations as compared to spar-buoy system (Figure 12). Moreover, the underlying fact that can be summarized from these results is that the hydrodynamic similitude requirements of different platform systems have been met by the scaling laws applied in this research.

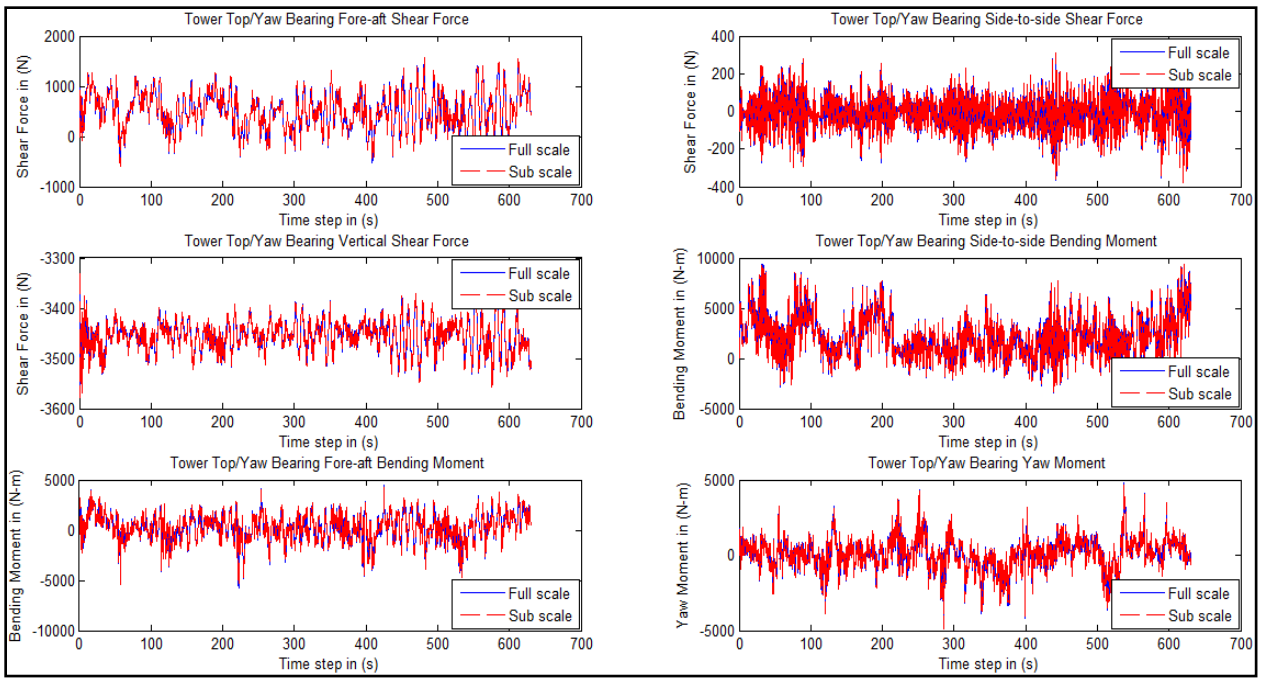

Figure 8: Time history of tower top/yaw bearing shear and axial forces; and bending moments for OC3 Hywind spar-buoy platform.

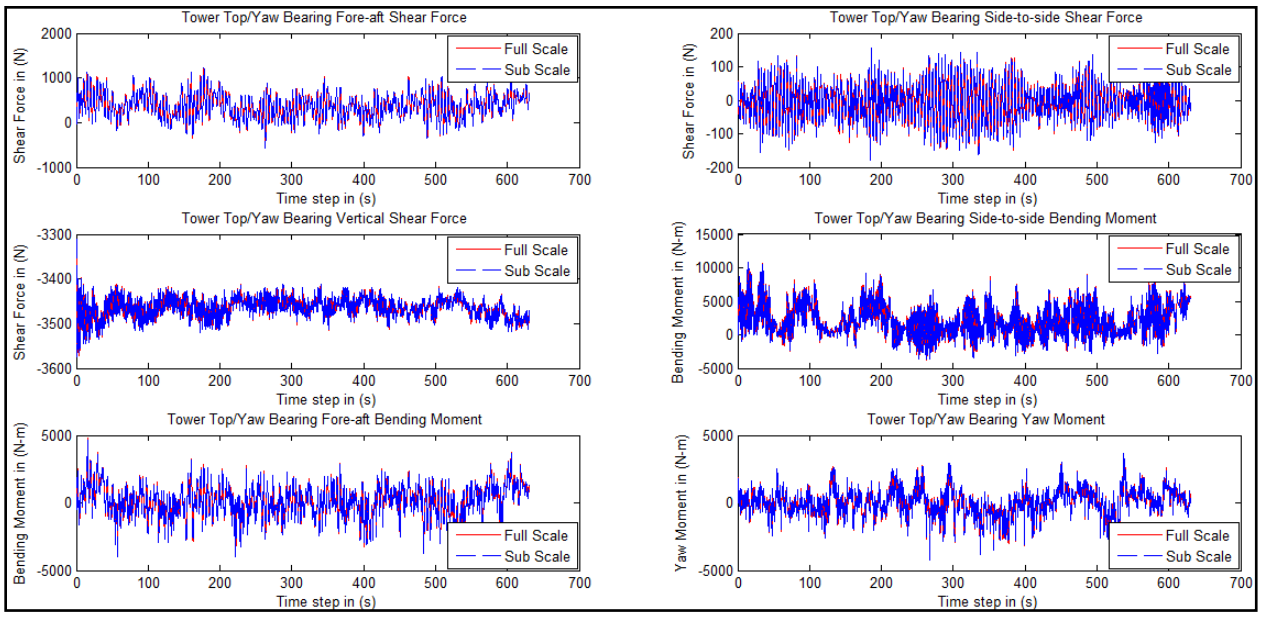

Figure 9: Time history of tower top/yaw bearing shear and axial forces; and bending moments for MIT/NREL TLP system.

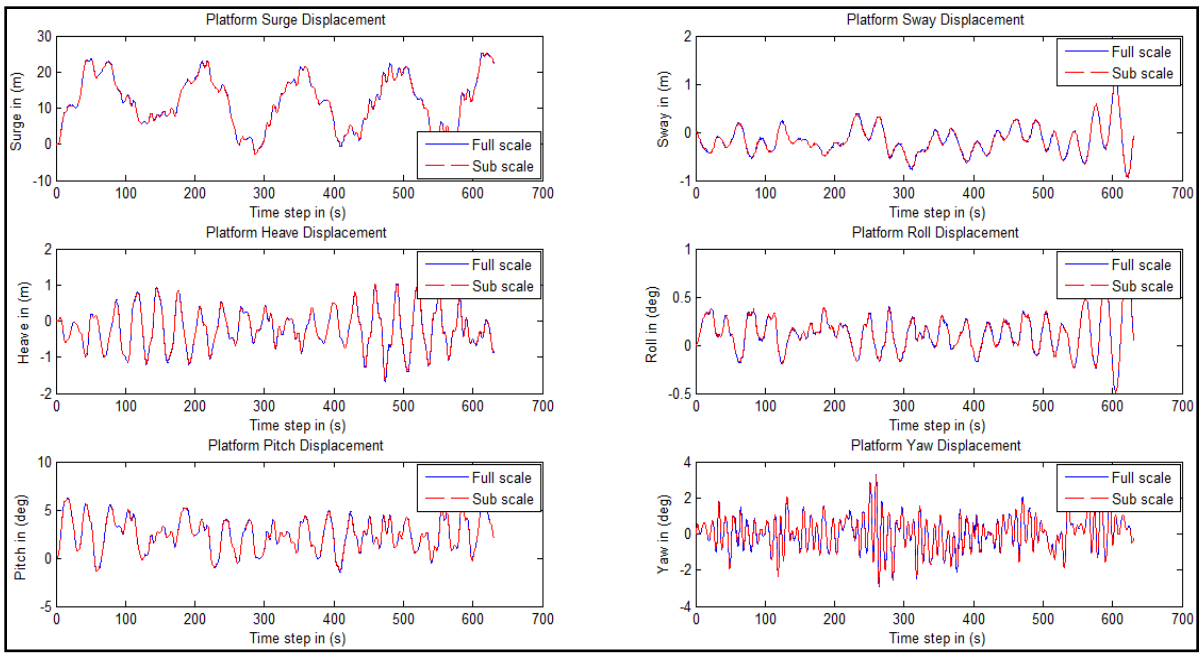

Figure 10: Time history of platform translational and rotational motions for OC3 Hywind spar-buoy platform.

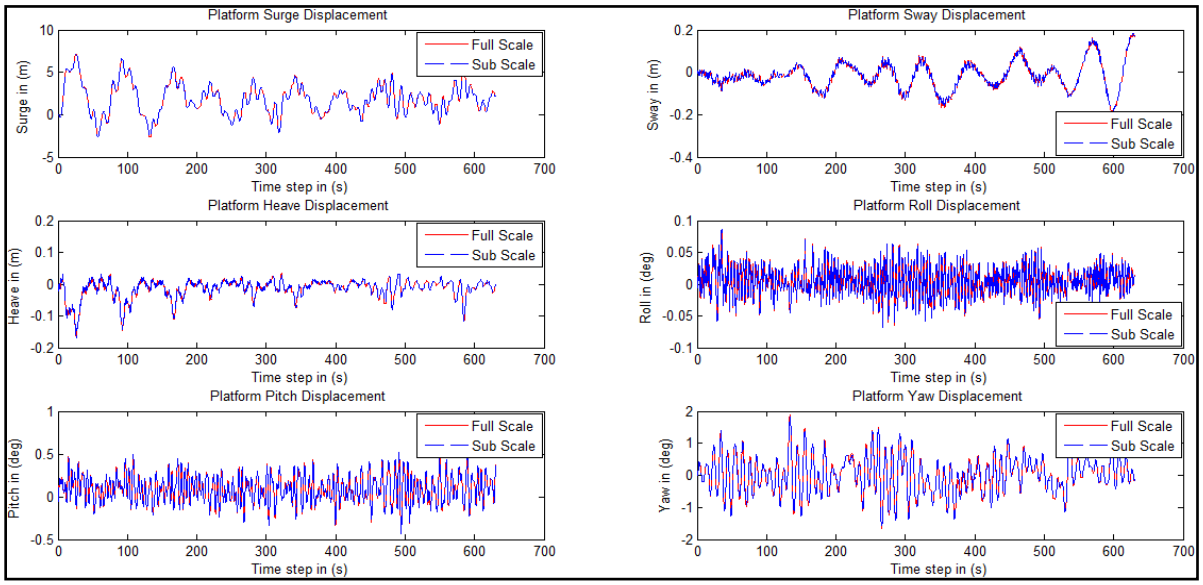

Figure 11: Time history of platform translational and rotational motions for MIT/NREL TLP system.

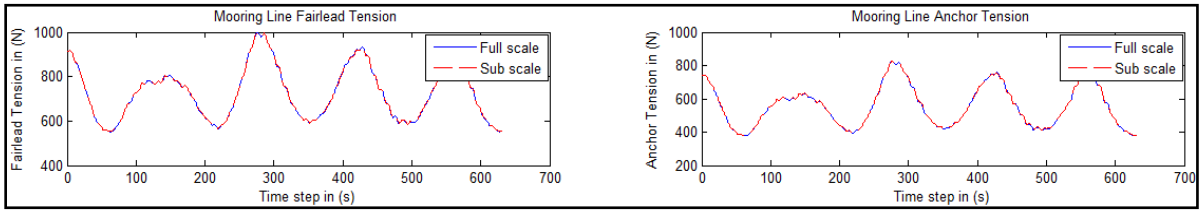

Figure 12: Time history of mooring line fairlead and anchor tension for OC3-Hywind spar-buoy platform.

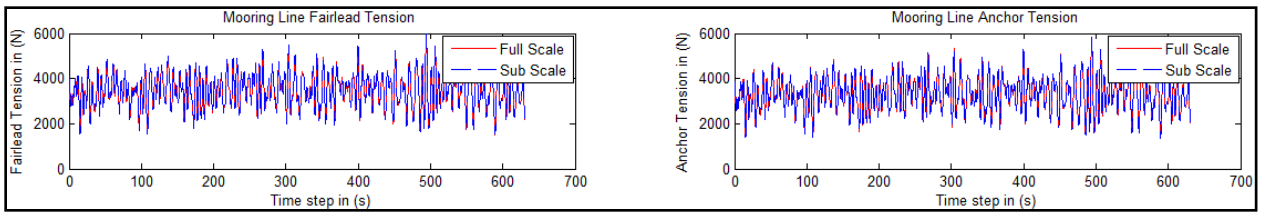

Figure 13: Time history of mooring line fairlead and anchor tension for MIT/NREL TLP system.

In Figure 14, we have shown time histories of wind speed and wave elevation. These parameters are helpful to understand the perturbations related to forces, moments, and motions of different structural components shown in the results of this section. The wind speed reaches to a highest value of 17 m/s for full scale and 2.4 m/s for model scale, respectively. The wave elevation which is measured from a platform reference point attained a maximum value of 5 m above and below the platform. These conditions are quite turbulent and represent a rigorous wind wave loading schedule which is very appropriate for scaling laws verification.

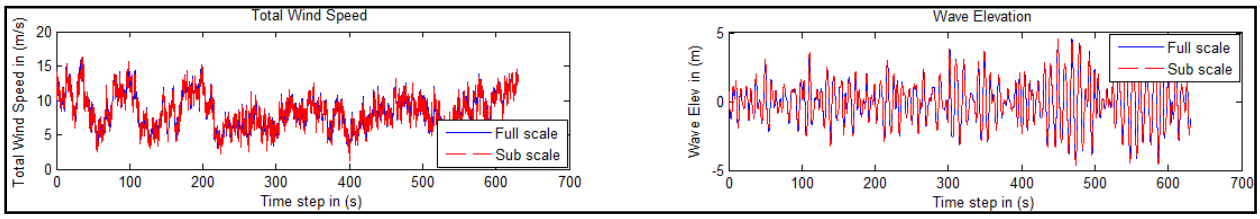

Figure 14: Time History of wind speed and significant wave height for both OC3 Hywind and MIT/NREL TLP system.

For the analyses in this section, the time histories of all the displacements, forces and deflections are not damped with increasing time, which is happening due to the continuous excitation by turbulent wind at a mean value of 8 m/s (full scale) and 1.13m/s (model scale); and irregular wave with a peak spectral period of 10 s and 1.41 s and a significant wave height of 6 m and 0.12 m at full scale and model scale, respectively.

When the output parameters for both platform configurations are compared, it is found that all the full-scale and model-scale quantities are in excellent agreement with the scaling laws. The reason behind the excellent agreement between full-scale and model-scale results is the parallel existence of Froude and Reynolds similitude. Such similarities are impossible to achieve in practical tests and a larger scaling factor between full scale and model scale further adds to the challenges because Reynolds number distortion increases with increasing fundamental scaling factor, by an exponential factor. These Reynolds-number associated difficulties form the basis of the discussion in the following section.

2.3 Reynolds Number Effects on Model Wind Turbine Performance

In this section, the impact of Reynolds number on properly scaling wind turbine thrust and torque are discussed. To illustrate this point, a combination of analysis and model wind turbine test data is employed.

As a fundamental step in the floating wind turbine model testing program, fixed base testing of the scale model wind turbine is performed in order to characterize the aerodynamic behavior of the model NREL 5MW Reference Wind Turbine in a Froude scale environment. The blades, shown in Figure 1 and documented in (Martin, 2011) accurately represent the NREL turbine geometry. The Froude scale environment the rotor is subjected to exhibits no swirl, a turbulence intensity of 4% at

the hub location and possesses a mean wind speed of 20.8 m/s. The performance of the turbine is characterized by two parameters: the power coefficient, C_P, and thrust coefficient, C_T. These non-dimensional quantities are computed as

$$C_P = \frac{P}{\frac{1}{2}\rho U^3 A}, \quad C_T = \frac{T}{\frac{1}{2}\rho U^2 A},$$

where P is the rotor power, T is the rotor torque, ρ is the density of the air and A is swept area of the rotor. To obtain the C_P and C_T test data, the rotor power and torque are measured from the model at various rotor speeds, and hence, TSRs. The results of the testing, in addition to the theoretical full scale performance as computed from NREL's coupled aero-hydro-servo-elastic wind turbine simulator, FAST (e.g. see (Jonkman and Buhl, 2005), is given in Figure 15. As is evident from the figure, the model rotor aerodynamic performance is markedly lower than the theoretical prototype performance, particularly for the performance coefficient.

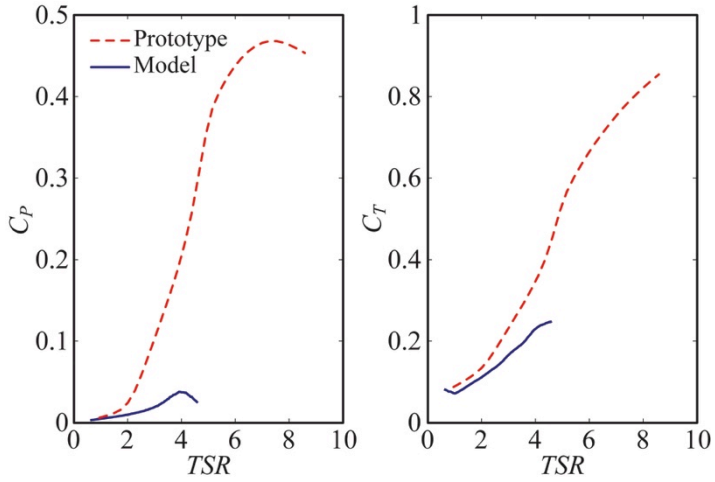

Figure 15: Comparison of ideal prototype rotor aerodynamic performance and realized model rotor aerodynamic performance.

For the model rotor, the peak performance coefficient of 0.04 is achieved at a *TSR* of 3.91 using a collective rotor pitch angle of 6.4°. For comparison's sake, the maximum C_P for the prototype rotor is 0.47 at a *TSR* of 7.5 while employing a collective blade pitch angle of 0.0°. The performance of the λ = 50 NREL rotor is an order of magnitude less than the prototype, with peak performance occurring at approximately half of the expected optimum *TSR*. Generally speaking, the lack of expected model performance is attributable to Reynolds number dissimilitude between the prototype and model scales. The specific impacts of the Reynolds number mismatch are discussed next.

To begin, it is noted that the Reynolds number quantifies the relationship between viscous and inertial qualities of a fluid flow. The Reynolds number, *Re*, is computed as

$$Re = \rho V L / \mu ,$$

where L is a characteristic length, V is a characteristic velocity and μ is the dynamic viscosity of the fluid. In the process of maintaining the Froude number for the floating wind turbine system and its accompanying environment, the Reynolds number for the hydrodynamic and aerodynamic flows are greatly diminished for the model. For floating body fluid-structure interaction flows, this is not a major concern as evidenced by the common practice of employing Froude scaling to conduct accurate floating body model tests that carefully emulate the full scale behavior. For wind turbines,

the drastic reduction in Reynolds number yields a major impact on wind turbine performance. This influence is realized in major alterations to the lift coefficient C_L and drag coefficient C_D of the airfoil sections comprising the wind turbine blade. These coefficients are a key component of the distributed lift force F_L and distributed drag force F_D of the airfoil section. These distributed forces are determined from the relationships

$$F_L = \frac{1}{2}\rho V^2 c C_L, \quad F_D = \frac{1}{2}\rho V^2 c C_D,$$

where V is the actual wind inflow magnitude experienced by the airfoil and c is the chord length of the airfoil. Note that C_L and C_D are functions of the angle of attack α which is determined by the direction of the velocity vector V relative to the chord length axis. To illustrate the factors which influence the magnitude and direction of V, the relationship between the direction of the incoming velocity and the lift and drag forces, and finally, the contributions from the lift and drag forces to the overall rotor thrust and torque, a generic wind turbine airfoil force diagram is shown in Figure 16.

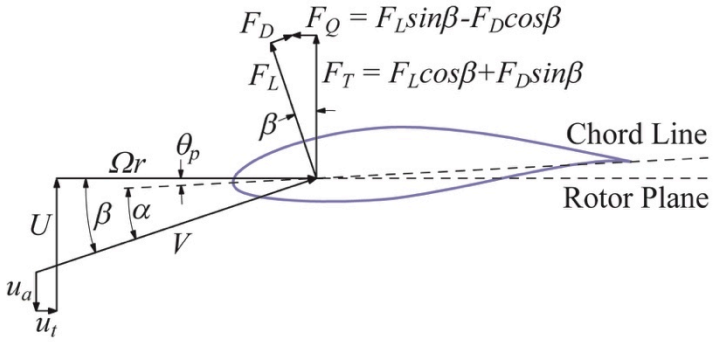

Figure 16: Generic wind turbine airfoil force diagram.

First, the velocity vector V is influenced by many factors. Contributions to the quantity include the incoming wind inflow U, the blade section tangential velocity Ωr, and the axial and tangential induced velocities u_a and u_t. The induced velocities result from the wind turbine rotor's wake of shed vorticity. The sum effect of all the vorticity in the wake modifies the flow field in the rotor plane and must be accounted for in order to properly compute the magnitude and direction of V. In numerical aerodynamic simulations of wind turbines, the induced velocities are often calculated using the blade element momentum theory (e.g. see (Leishman, 2000)), however, other possibilities do exist (e.g. see (Peters and He, 1991; Glauert, 1926)). Once V is established, the angle of attack α is determined from the angle between V and the rotor plane, β, and the blade pitch angle θ_p, as shown in Figure 16. With α established, the coefficients C_L and C_D can be determined and the distributed forces F_L and F_D computed. Note that the lift force is perpendicular to V, whereas the drag force is parallel to V. As shown in Figure 16, the components of F_L and F_D perpendicular to the rotor plane are both positive and contribute to the total rotor thrust, with F_L being the largest contributor. The thrust contribution from airfoil section is denoted F_T. The force component contributing to rotor torque is labeled F_Q in Figure 16. The positive contribution to F_Q arises from the component of F_L in the direction of the foil tangential motion, which is not very large relative to the magnitude of the lift force. The largest component of the drag force F_D lies in the rotor plane and opposes the motion of the airfoil section, therefore detracting from the net force available for producing torque, F_Q. With these observations in mind, it is evident that the rotor torque, and hence power, is severely impacted by modest increases in drag force. In addition, any reductions in the lift force will only diminish the already small positive contributions to torque production. For

the thick airfoil sections typically found on commercial scale wind turbines, reductions in Reynolds number typically diminish C_L and increase C_D, resulting in reduced rotor thrust and torque.

To better understand the reductions in rotor performance due to Reynolds number dissimilitude, the coefficients C_L and C_D are computed as a function of angle of attack α for the NACA 64-618 airfoil section located at 70% of the blade radius for both the prototype and model Reynolds numbers. For this particular section on the model blade, a 20.8 m/s inflow wind speed, 12.7 rpm rotor speed and airfoil chord length of 3.04 m (2.94 m/s, 90.0 rpm and 0.061 m at model scale) yields a Reynolds number of 35.7×10^3. For the prototype at a wind speed of 11.4 m/s and a slightly lower rotor speed of 12.1 rpm, the Reynolds number is orders of magnitude larger at 11.5×10^6. The reason for the differing operational conditions will become apparent in the subsequent section, but it will suffice to state that these two conditions yield similar thrust performance for the model and the prototype. This stated, the coefficients are computed using XFOIL (Drela, 1989), a higher-order panel code incorporating a fully-coupled viscous/inviscid interaction method designed specifically for airfoil analysis. The XFOIL analyses employ the aforementioned Reynolds numbers and a standard laminar to transition effect log factor, N_{crit}, of 9 (Drela and Giles, 1987). The results of the analyses are shown in Figure 17.

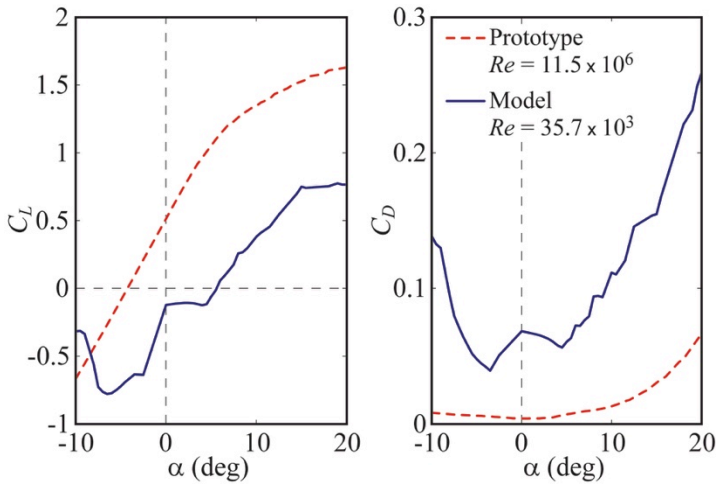

Figure 17: Lift and drag curve coefficients for the NACA 64-618 airfoil at prototype and model Reynolds numbers of 11.5×10^6 and 35.7×10^3, respectively.

The trends in Figure 17 clearly demonstrate that the lower Reynolds number of the model severely affect the performance of the airfoil, drastically reducing the lift coefficient and severely increasing the drag coefficient for the angles of attack shown, these angles covering the typical range of operational α for an airfoil. Further analysis with XFOIL indicates that the NACA 64-618 airfoil at the model Reynolds number undergoes laminar separation resulting in the altered coefficients of Figure 6. This stated, it must be noted that XFOIL analysis results in separated flows should be considered more qualitative than quantitative here as the predicted coefficients are likely not accurate. Nonetheless, thick foils, such as the NACA 64-618, are prone to laminar separation at low Reynolds numbers degrading airfoil performance. The NACA 64-618 foil possesses a thickness equal to 18% of its chord length, this being the thinnest airfoil in the NREL 5 MW Reference Wind Turbine blade shown in Figure 1. Sections near the root of this particular blade are even more prone to laminar separation as these airfoils approach a 1 to 1 ratio of thickness to chord length. These sections are necessary to achieve adequate structural bending stiffness for commercial wind blades which are large, heavy, slender structures. This is not a concern at prototype Reynolds numbers, however, as these thick airfoils possess small boundary layers and an organized flow around the foils resulting in high lift and low drag coefficients.

With lower lift coefficients and higher drag coefficients for the airfoils at lower Reynolds numbers, the result, understandably, is diminished airfoil lift forces and drastically increased airfoil drag forces for the various blade sections. This combination, as supported by Figure 16, results in a lower rotor C_T and lower rotor C_P. The extremely low rotor performance in Figure 15 is not surprising given the approximately tenfold increase in drag coefficient estimated for the model airfoil shown in Figure 17. This large increase in drag force for the outer foil sections, which generate most of the power, detracts greatly from the marginal lift force component in the rotor plane, yielding a very low net torque. The larger model drag force quickly overwhelms the positive lift force contribution to torque as *TSR* increases. This is due to the reduction in angle of attack, and hence lift force component in the rotor plane, as the rotor speed increases for a constant wind speed. This is the cause for the peak C_P occurring at much lower *TSR* for the model as compared to the prototype. The smaller model airfoil lift coefficient resulting from the lower Reynolds number is the main contributor to the lower observed C_T. However, the C_T disparity between the model and prototype is not as bad due to the larger positive contribution to thrust loading from the bigger model airfoil drag force.

While the present analysis may explain the poor turbine performance in Figure 15, the severe reduction in wind turbine performance is not ideal for a Froude scale experiment. The results of Figure 15 clearly indicate that a strictly Froude scaled model wind turbine of commercial design will produce too little thrust, and not nearly enough power, when subjected to Froude scale winds. Therefore, to conduct a proper Froude scale floating wind turbine experiment, alterations to the wind turbine and/or environment are required to achieve the appropriate aerodynamic forces that strongly influence the coupled response of a floating wind turbine system. Suggested corrective measures and the shortcomings of these measures are presented in the next section.

2.4 Analysis of Model Testing Wind Turbine Thrust Correction Methods

Previous analysis demonstrates that a model wind turbine with thick commercial airfoil sections and an accompanying wind environment which adheres strictly to the scaling protocol listed in Table 1 will not perform adequately for a proper experiment. Therefore, adjustments must be made to achieve the desired model turbine forces. The key forces the turbine transmits to the floating system include gyroscopic moments, rotor torque and rotor thrust. The first, the gyroscopic moment, is properly maintained by creating a model turbine with the correct Froude scale mass properties and operating the turbine at the correct Froude scale rotor speed. The second two forces, torque and thrust, are not maintained as previously mentioned. It is unlikely that any alterations will give rise to a scenario in which both forces are maintained exactly as one would desire. Therefore, a prioritization of the two forces is required. Setting this priority is rather straightforward since the overturning moment created by the thrust force and opposing mooring reaction is typically an order of magnitude greater than the overturning moment due to the aerodynamic rotor torque from which power is extracted. For the semi-submersible system of Figure 2, the overturning moment due to torque is less than 5% of the overturning moment due to thrust for a typical operating condition. With the priority established, possible methods for achieving the correct model thrust force include the following:

1. Increase the model wind speed to compensate for the low model C_T and achieve the correct prototype thrust forces. *TSR* between the prototype and model will not be maintained.
2. Roughen the leading edge of the model blade to trip the boundary layer transition from laminar to turbulent flow around the airfoil, reattaching the flow and improving the airfoil's lift and drag coefficients at model scale.

3. Design a low-Reynolds number specific model wind turbine blade geometry that, while may not resemble the prototype blade with regard to surface geometry, will yield appropriate thrust performance when subjected to an unmodified Froude scale environment.

In addition to these suggestions, one may implement combinations of the above methods to achieve the desired thrust forcing for the model.

With the suggested corrective measures outlined, the focus will now turn to the implementation of these measures and their associated shortcomings. The first suggestion, increasing the wind speed, is relatively straightforward to implement. For the model testing of the system in Figure 2, the wind speed is raised from 11.4 m/s to 20.8 m/s to achieve the desired thrust forces. For the various tests performed under steady winds, the increase in wind speed to 20.8 m/s yields mean thrust values ranging from 91-105% of the desired prototype value at the rated wind speed of 11.4 m/s during testing, this being 827 kN. The fact that these two conditions yield similar performance was alluded to in the previous section, and thus, is the reason for using these two distinct wind speeds in the Reynolds number dissimilitude analysis. That stated, adjusting the wind speed only maintains the mean thrust force for the model and does not necessarily capture all the sensitivities of the thrust force due to changes in various field variables. For example, this method does not inherently imply proper simulation of the variations in thrust force due to changes in inflow wind speed, changes in relative wind speed resulting from structure motion and changes in blade pitch angle, this last being critical for studies which aim to investigate the impact of active blade pitch damping on the global motions of the system. While no active blade pitch testing is performed during the model test program, tests are conducted which can help assess the impact of matching thrust via an increase in mean wind speed on the aerodynamic damping provided by the turbine, and hence, the measured global response of the floating system.

To begin this assessment, the global motion response of floating system most affected by aerodynamic wind turbine damping is first identified. This region of altered response will be identified using Figure 18 which compares two model tests of the floating semi-submersible floating wind turbine system, one with an operating wind turbine subjected to wind loading and the other without.

The figure, which shows the frequency domain pitch motion response, displays cases that both experience a sea state consisting of an H_s = 7.1 m significant wave height with a peak spectral period of 12.1 s. The distinction between the two cases is that the first possesses a parked turbine with no wind, while the second has an operating wind turbine at 12.7 rpm under steady, 20.8 m/s winds. As can be seen in the figure, the response for the two conditions is nearly identical in the wave energy frequency range, this being greater than 0.05 Hz.

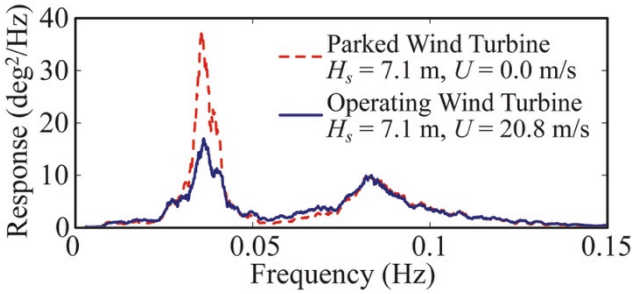

Figure 18: Comparison of floating semi-submersible wind turbine pitch motion response for the same sea state with and without an operating wind turbine.

The second-order difference frequency response, which is greatest near the floating turbine natural rigid body pitch frequency of 0.037 Hz, is significantly damped by the operating wind turbine.

While this is only a single example, the trend of damping the low frequency second-order response of the system illustrated in Figure 18 is consistent with observations in similar tests. Therefore, assuming that this trend would still hold if the turbine performance properly emulated the prototype, further investigation will focus solely on the wind turbine aerodynamic motion damping of the natural rigid body pitching motion of a floating wind turbine system.

To assess the shortcomings of the increased wind speed method on global response, the focus will now turn to pitch motion free decay tests and simulations for the semi-submersible floating system, these tests being characterized by floating system motion at the natural rigid body pitch motion frequency. The results of the model tests, as well as simulations from FAST, are given in Figure 19.

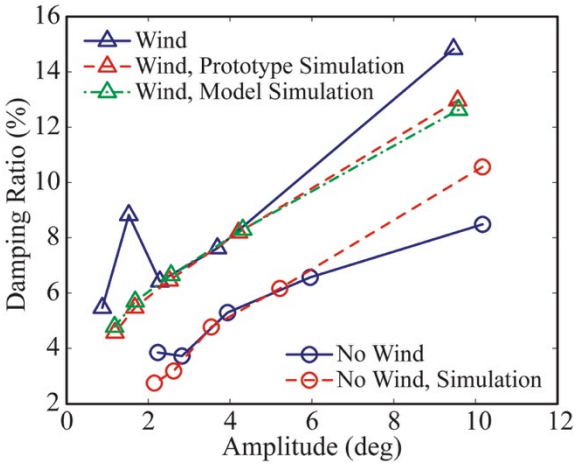

Figure 19: Damping ratio as a function amplitude for the floating semi-submersible wind turbine from model tests and simulations.

The figure displays the damping ratio as a function of amplitude for all of the cases analyzed. The figure displays five scenarios; two without wind and three with wind. The two without wind include model test data and a FAST simulation, each denoted with circular markers. As can be seen in the figure, the curves are very similar indicating that the FAST simulation hydrodynamic damping accurately represents physical reality, especially for modest motion amplitudes. It should be noted that the FAST simulator employed included modifications to allow for the inclusion of custom drag elements. This stated, the remaining three curves in Figure 19 each correspond to a free decay test with an operating wind turbine, which as observed from the figure, results in a considerable increase in pitch motion damping at the natural pitch frequency. For the model test, the wind turbine operates at 7.8 rpm and is subjected to steady 10.7 m/s winds. The same case is simulated with FAST using a numerical model of the physical model wind turbine. A comparison of the numerical model wind turbine and the measured model performance data is shown in Figure 20.

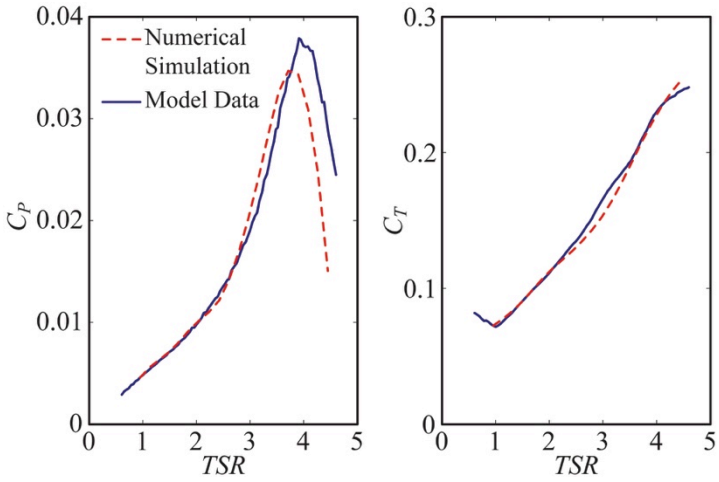

Figure 20: Comparison of numerical model and measured test performance data for the model wind turbine.

The numerical model, which is obtained by parameterizing XFOIL derived lift and drag coefficients and then optimizing the parameters via a genetic algorithm to minimize the error between the numerical model prediction and data for C_P and C_T, is a fair representation of the actual model wind turbine performance. That aside, the comparison between the free decay test results with an operating turbine and the corresponding simulations results shown in Figure 19 agree fairly well. To assess if the poorly performing model wind turbine subjected to increased wind speeds accurately portrays the full scale response, an additional simulation is performed using a numerical model of the prototype 5 MW turbine, the performance and thrust curves of which are shown in Figure 15. The operating and environmental conditions for this simulation were set such that the mean thrust on the wind turbine for the prototype simulation is similar to the model simulation, and hence, the test data. Due to the prototype's larger thrust coefficient, the prototype requires a lower steady wind speed of 5.9 m/s and a rotor speed of 7.9 rpm to obtain the same thrust force as the model. After running the simulation, Figure 20 clearly indicates that the additional aerodynamic damping provided by the model and prototype wind turbines is nearly identical despite the large discrepancies in C_T and mean wind speed. Both systems appear to increase the damping ratio by an additional 2-3%, regardless of amplitude, with the prototype simulation exhibiting a slightly stronger increase in damping force with rising amplitude. Nonetheless, these results indicate that matching of the mean thrust through increased wind speed for a poorly performing model wind turbine does not necessarily compromise the wind turbine aerodynamic damping effect.

To better understand why this is so, a Taylor series expansion of the wind turbine thrust force T for a fixed speed, fixed blade pitch wind turbine is taken about the mean wind speed U_M, yielding

$$T(U) \approx \frac{1}{2}\rho A[C_T(U_M)U_M^2 + \left\{2C_T(U_M)U_M + \frac{\partial C_T(U_M)}{\partial U}U_M^2\right\}\Delta U] + O(\Delta U^2),$$

where $\Delta U = U\text{-}U_m$ is the change in the relative wind velocity, either due to motion of the rotor or a change in wind inflow speed. In most realistic operating cases, the change in velocity is small relative to the mean wind speed, and hence, the terms associated with ΔU^2 are considered negligible here. In addition, the constant term involving the $C_T(U_M)U_M^2$ product is the same for both the model and prototype as a result of matching the mean thrust through increasing the inflow wind speed for the model relative to the prototype. The end result is that the second term characterizes the wind turbine damping, this term being proportional to ΔU. For the

aforementioned free decay tests under steady wind, ΔU is controlled by the natural pitch period of the floating wind turbine structure, this being the same for both the model and the prototype. The lone discrepancy between the two scales is the term pre-multiplying ΔU, the damping coefficient, comprised of the sum of the $\rho A C_T(U_M) U_M$ product and the $\rho A(\partial C_T(U_M)/\partial U) U_M^2/2$ product. The first and dominant term, is larger for the prototype by a factor of 1.7 for this example. However, the second product, which contributes negatively to the sum as the partial derivative is negative, is also larger in magnitude for the prototype by a factor of 1.5 yielding comparable damping coefficients for the two scales. The end result is similar wind turbine motion damping for the prototype and the model despite the fact that the model wind speed is 81% larger than the prototype.

As noted earlier in this section, an additional measure which may be taken to improve model wind turbine thrust forces in a Froude scale experiment is to roughen the leading edges of the blade sections. To help quantify the effect of this correction, performance tests are conducted for the model wind turbine with a 25 mm wide strip of 250-290 μm calibrated sand applied to the leading edge of the turbine blades, as shown in Figure 21.

Figure 21: Image of roughened leading edge of model wind turbine blade.

These particular values are selected based on MARIN experience and preferred protocol (e.g. see (van Walree and Yamaguchi, 1993)). The wind conditions for the roughened blade performance tests are identical to earlier turbine testing with a 20.8 m/s wind inflow speed. The results for C_P and C_T as a function of TSR for the roughened edge blade, as well as the results for the original untreated blades, are shown in Figure 22.

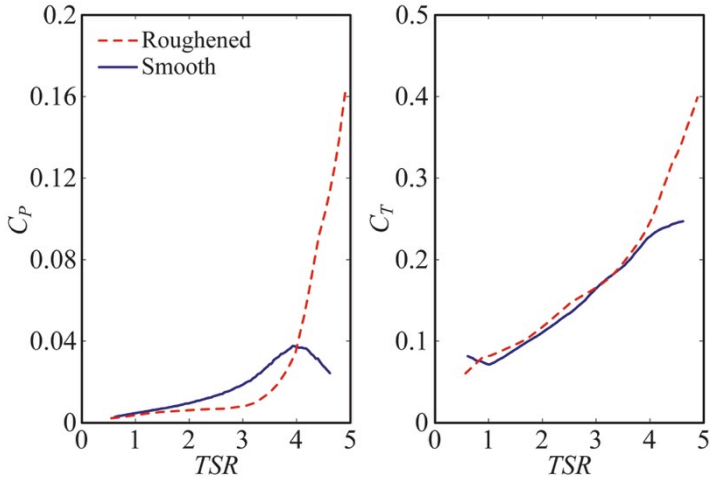

Figure 22: Comparison of model wind turbine performance with and without roughness on the wind blade leading edge.

As can be seen in the figure, the performance and thrust coefficients improve greatly once the TSR exceeds a value of roughly 4. At this point, the combination of a roughened leading edge and large enough rotor speed trip the transition from laminar to turbulent boundary layer flow, eliminating the laminar stall condition of the thick untreated blades depicted in Figure 1. As a result, the airfoil begins producing significantly improved lift forces evidenced by the increased C_P and C_T responses.

While the performance improves from this treatment, there are some important points worth mentioning. First, the wind turbine performance is not sufficiently improved to the point of being comparable with the prototype. Therefore, thrust matching of a treated model wind turbine with commercial scale geometry would still require increased wind speeds. Second, the peak performance coefficient is not obtained for the roughened blades in Figure 22 as sufficiently large TSR values cannot be achieved with the model wind turbine employed for testing here. This is due to a combination of wind turbine rotor speed safety limitations, and the fairly high 20.8 m/s wind speed used to generate the curves. At lower wind speeds, and even for lower rotor speeds for the 20.8 m/s wind case, the transition from laminar to turbulent flow of the boundary layer does not occur, and thus, performance is not improved. In addition to the airfoils still experiencing laminar separation in these cases, there also exists added drag due to the leading edge roughness producing even poorer performance than if the blade is left untreated. Also, it is observed during the testing that the transition out of laminar stall for the turbine blades is fairly dramatic, leading to sudden increases in rotor thrust force despite only small changes in rotor speed. This situation, of course, is not representative of the prototype's response and is not ideal for model testing. In short, it is recommended that leading edge roughness be employed carefully, ideally as a small tuning adjustment and not as the sole means to emulate the prototype turbine response.

The final recommended practice for matching aerodynamic rotor thrust forces for floating wind turbines is to design a rotor using low Reynolds number airfoil sections that properly mimics the prototype thrust coefficient curves when subjected to Froude scale winds. If properly designed, the airfoil will not need to employ much, if any, leading edge roughness preventing the possibility of the aforementioned erratic rotor performance. Also, a properly designed low Reynolds number specific blade will not need to rely on increased wind speeds, as the C_T for model and prototype will be the same. This will in turn yield a model turbine that better captures the aerodynamic damping of the prototype, not only due to motion of the floating structure at its natural period, but also due to other changes such as variations in the inflow wind speed. This is a result of the similarity between the model and prototype terms, such as U_M and $C_T(U_M)$, in the Taylor series expansion equation. A final important note is that such a turbine will be best suited for blade pitch control studies. When an airfoil is performing correctly in its operational range, the variation of the lift coefficient is nearly proportional to the angle of attack, α, this variable being determined in part by the blade pitch angle. In addition, the lift force F_L is proportional to the product of the chord length c, square of the apparent velocity V^2 and the lift coefficient C_L. A model that minimizes the distortion of the airfoil apparent velocity, C_L curve slope and airfoil chord length will be best suited for blade pitch studies as it will preserve the sensitivity of the blade lift forces to changes in blade pitch angle.

To complete this section, an example of a redesigned low Reynolds number model blade is given. A redesigned turbine should employ low Reynolds number specific airfoils throughout the rotor, and no thick airfoils should be included as is common on commercial machines. An example of such a foil, the Drela AG04, is given in Figure 23. Thin Airfoils of

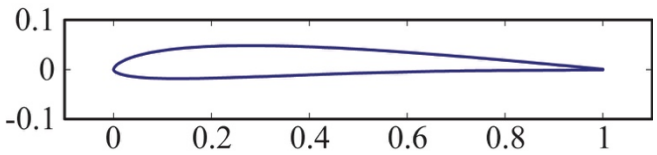

Figure 23: Drela AG04 low-Reynolds number airfoil.

this type are not as susceptible to the laminar separation problem of the thick airfoils employed on commercial machines at the low Reynolds numbers of the Froude scale environment. This is evidenced by the improved lift and drag coefficient behavior of the Drela AG04 airfoil at low

Reynolds numbers as compared to the NACA 64-618 used in the outer portion of the NREL 5 MW Reference wind turbine. The comparison of the NACA 64-618 airfoil from Figure 17 and the XFOIL predicted performance of the Drela AG04 airfoil is shown in Figure 24. At the low model Reynolds number, the Drela AG04 greatly outperforms the NACA 64-618 with much larger lift coefficients and significantly reduced drag coefficients due to a lack of separation at low α. In addition, the Drela AG04 airfoil performance is moderately representative of the prototype Reynolds number performance of the NACA 64-618 for small angles of attack, which is desirable.

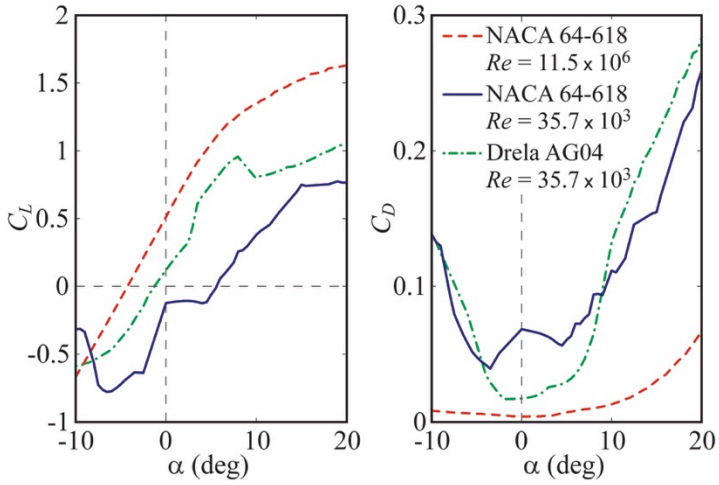

Figure 24: Lift and drag coefficients of the NACA 64-618 airfoil under high and low-Reynolds number conditions and of the Drela AG04 airfoil under low-Reynolds number conditions.

To redesign the blade, the Drela AG04 airfoil is employed over the complete length of the blade. In addition, the structural twist of the NREL 5 MW Reference Wind Turbine blade is mimicked, with the exception of the root sections which more closely follow an ideal twist distribution (e.g. see (Manwell *et al.*, 2009)). The relative chord distribution is maintained from the NREL machine, but the chord length is uniformly increased by 25% in order to compensate for the slightly lower lift coefficient allowing for production of the appropriate thrust forces under unaltered Froude scale winds. Ideally, the chord lengths of the airfoils should be as close to the prototype as possible in order to preserve the sensitivity of the thrust force to blade pitch angle. That said, an analysis of this blade using the lift and drag coefficients of Figure 24 with FAST yields the non-dimensional performance curves shown in Figure 25.

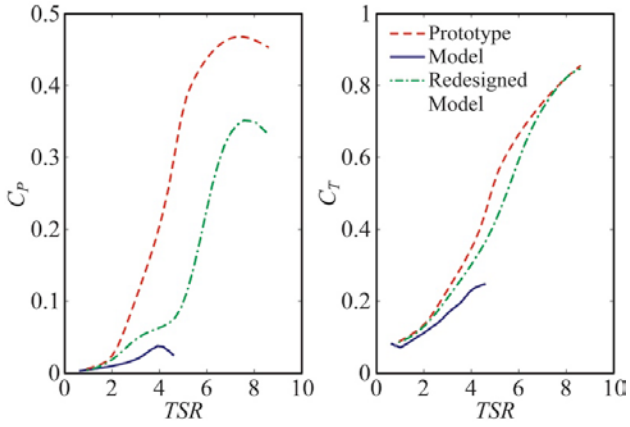

Figure 25: Power and thrust coefficient curves for the prototype, original model, and redesigned model rotor.

As can be seen in the figure, the performance is markedly better than the original model. The C_T response is nearly the same as the prototype, and the less important power coefficient, while not ideal, is drastically improved. In short, the low-Reynolds number specific blade design presented here would perform admirably when subjected to Froude scale winds, yielding correct thrust forces, modest power output and aerodynamic damping very similar to the prototype as a result of preserving the terms laid out in Taylor series expansion equation of this section.

While the three corrective measures outlined in this section all possess some potential for improving the thrust scaling problem, the option for increasing the wind speed was selected as the turbine blade could not be modified once the testing had begun and the addition of leading edge roughness lead to erratic wind turbine performance. However, as demonstrated in this section, this choice does not appear to severely hamper the value of the test data as the dynamic wind response of the floating wind turbine is very similar for both the prototype and poorly-performing model-scale wind turbine for comparable mean thrust conditions. Regarding the redesigned wind turbine option, this scenario will be investigated further in a later section in this report.

3 Test Program Overview

In this section, an overview of the floating wind turbine model test program performed at MARIN is given. Topics covered include descriptions of the floating wind turbine models, instrumentation and lastly, the matrix for the floating wind turbine model tests.

3.1 Definition of Floating Wind Turbine Systems

For the model tests, the horizontal axis wind turbine chosen for scale model construction is the NREL designed 5 MW Reference Wind Turbine (Jonkman *et al.*, 2009). An image of the wind turbine is shown in Figure 26.

Figure 26: Wind turbine model.

The wind turbine possesses a 126 m rotor diameter and is located with a hub height of 90 m above the still water line (SWL). The flexible tower, which begins 10 m above SWL, is designed to emulate the fundamental bending frequency of the OC3 Hywind tower (Jonkman, 2010). The wind turbine deviates from the standard NREL 5 MW Reference Wind Turbine in a few notable areas (Martin, 2011). For the model wind turbine, the shaft tilt is 0°, the blade precone is 0° and the blades are rigid. The last difference is the result of two factors. First, fabricating the 17.7 mt blades at 1/50th scale requires a very light woven carbon fiber construction which is inherently stiff. Second, eliminating the added aeroelastic dynamic phenomena associated with a flexible rotor is deemed to be desirable as these effects are perceived as being beyond the scope of these tests. To mimic the

first bending frequency of the OC3 Hywind tower, the tower is constructed from specifically sized aluminum tubing. Furthermore, the lower 11.3 m of the tower is of a larger diameter than the remainder of the tower in order to more closely match the OC3 Hywind tower center of gravity and fundamental bending mode shape. The total topside mass, which includes the wind turbine, tower and all accompanying instrumentation, is 699.4 mt. This value is 16.6% larger than the standard specifications for the NREL 5 MW Reference Wind Turbine and OC3 Hywind tower.

While most floating wind turbine concepts under consideration employ a horizontal axis wind turbine, the platforms employed in current concepts vary widely. Therefore, to make the test results useful to as broad an audience as possible, the previously described wind turbine and tower is tested atop three different floating platforms. The platforms, each modeled after viable offshore oil and gas platform technology, derive stability from differing mechanisms. The platforms consist of a TLP (mooring stabilized), a spar-buoy (ballast stabilized) and a semi-submersible (buoyancy stabilized). Images of the platforms employed during testing, including the wind turbine, are shown in Figure 27.

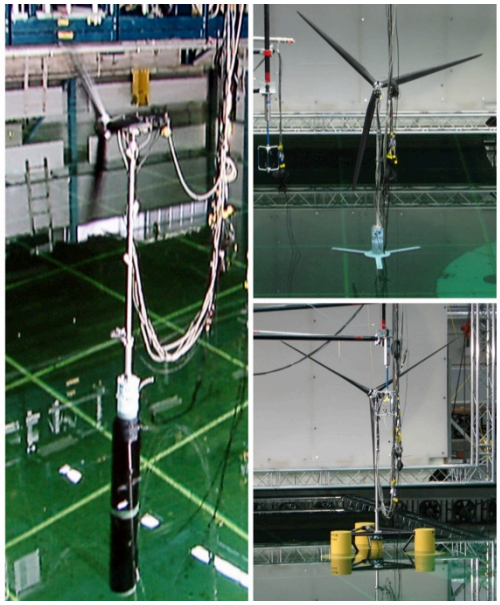

Figure 27: Clockwise from left: spar-buoy, TLP and semi-submersible floating wind turbines utilized in model testing.

Like the blades, each platform is designed to be rigid to eliminate the added complexity of a flexible platform. Each of the designs is tested in a water depth of 200 m. The first design, the TLP, is restrained by three stiff vertical tendons. The spar-buoy is moored by a spread mooring consisting of taught lines attached to the spar-buoy via a delta connection similar in nature to the type employed on the actual Statoil Hywind (Jonkman, 2010). The last design, the semi-submersible, is restrained by three slack catenary lines with fairlead attachments located at the top of the lower bases. Images of the floating foundations alone are given in Figure 28. The principle dimensions of the spar-buoy, TLP and semi-submersible are given in Figure 29, Figure 30 and Figure 31, respectively.

Figure 28: Selected floating platforms.

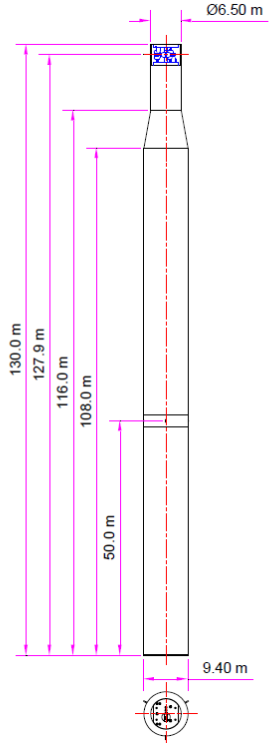

Figure 29: Principal dimensions of the spar-buoy.

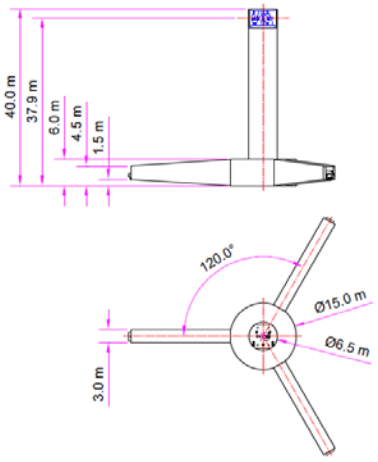

Figure 30: Principal dimensions of the TLP

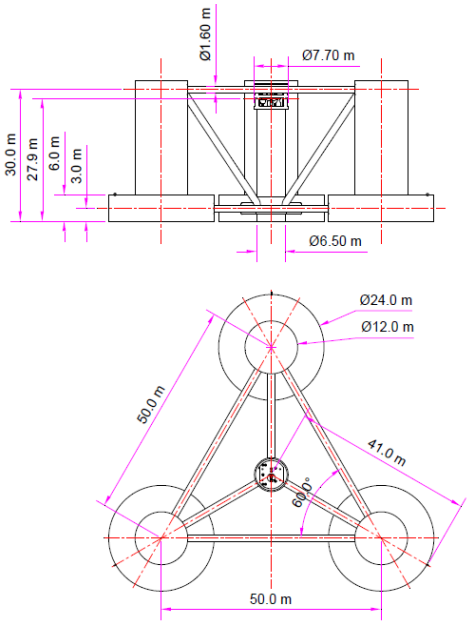

Figure 31: Principal dimensions of the semi-submersible.

Table 7, Table 8 and Table 9 for the spar-buoy, semi-submersible and TLP, respectively. A depiction of the delta connection employed for the taut mooring system of the spar-buoy is shown in **Error! Reference source not found.**.

For each design, the freeboard at the tower base is 10 m. As can be seen in the table, the TLP is by far the smallest of the designs with the semi-submersible being the largest. Note, however, that these structures are generic, not optimized and are intended to exhibit the main characteristics of each concept. In addition, the TLP system does not contain any ballast unlike the other two designs. As can be seen in Table 6, the primary mass properties and motion characteristics for each of the designs, including a mounted wind turbine and tower, are also given. Examining the table, the natural periods of roll, pitch and heave motion for the moored structures indicate that the TLP system is very stiff as opposed to the spar-buoy and semi-submersible systems. In all cases,

however, the natural periods of motion for these noted rigid body modes do not lie in the range of typical wave energy peak spectral periods, these being from approximately 5 to 17 seconds. Lastly, the fundamental tower bending frequencies in the fore-aft (surge) and side-side (sway) directions are also given for the three designs. It is evident from Table 6 that floating platform characteristics significantly influence the bending frequencies, with the foundations stiffer in pitch and roll exhibiting a lower bending frequency than the compliant foundations.

Table 6: Select specifications for each of the platforms tested.

Platform Type	TLP	Spar	Semi
Mass w/ Turbine (mt)	1361	7980	14040
Displacement (mt)	2840	8230	14265
Draft (m)	30	120	20
CG Above Keel (m)	64.1	43.7	10.1
Mooring Spread Diameter (m)	60	890	1675
Roll Radius of Gyration (m)	52.6	53.5	31.6
Pitch Radius of Gyration (m)	52.7	53.6	32.3
Natural Surge Period (s)	39.3	43.0	107
Natural Sway Period (s)	39.3	42.8	112
Natural Heave Period (s)	1.25	28.1	17.5
Natural Roll Period (s)	3.7	32.0	26.9
Natural Pitch Period (s)	3.7	31.5	26.8
Natural Yaw Period (s)	18.2	5.5	82.3
Tower Fore-Aft Fundamental Bending Frequency (Hz)	0.28	0.43	0.35
Tower Side-Side Fundamental Bending Frequency (Hz)	0.29	0.44	0.38

Table 7: Taut mooring system properties (spar-buoy).

Item	Unit	Designations
Anchor Radius	(m)	445.0
Anchor Depth	(m)	200.0
Radius of Fairlead	(m)	5.2
Fairlead Depth	(m)	70.0
Unstretched Line Length A	(m)	424.35
Unstretched Line Length B & C	(m)	30.0
Line A Diameter	(m)	0.167
Line B & C Diameter	(m)	0.125
Mass per Length Line A (dry)	(kg/m)	22.5
Mass per Length Line B & C (dry)	(kg/m)	12.6
Mass per Length Line A,B & C (wet)	(kg/m)	0.0
Axial Stiffness Line A (EA)	(MN)	121.0
Axial Stiffness Line B & C (EA)	(MN)	68.0

Table 8: Catenary mooring system properties (semi-submersible).

Item	Unit	Designations
Anchor Radius	(m)	837.6
Anchor Depth	(m)	200.0
Radius of Fairlead	(m)	40.9
Fairlead Depth	(m)	14
Unstretched Line Length	(m)	835.5
Line Diameter	(m)	0.0766
Mass per Length (dry)	(kg/m)	113.35
Mass per Length (wet)	(kg/m)	108.63
Axial Stiffness(EA)	(MN)	753.6

Table 9: TLP tendon properties.

Item	Unit	Designations
Anchor Radius	(m)	30.0
Anchor Depth	(m)	200.0
Radius of Fairlead	(m)	30.0
Tendon Porch Depth	(m)	28.5
Unstretched Tendon Length	(m)	171.39
Tendon Diameter	(m)	0.6
Mass per Length (dry)	(kg/m)	289.8
Mass per Length (wet)	(kg/m)	0.0
Axial Stiffness (EA)	(MN)	7430.0

.This is not unexpected as stiffer foundations are more representative of a fixed boundary condition for the base of the tower, while the softer foundations are more akin to a free condition at the tower base (e.g. see (Rao, 2004)).

3.2 Instrumentation

In order to measure loads and motions of the floating wind turbines, a total of about 40 to 50 channels were used in the model tests depending on the floater. The six DOF motions of the floating wind turbine were measured by the optical tracking system. Three accelerometers were located at the base, middle and top of the turbine tower to measure accelerations. The structural mode shapes and natural periods of the wind turbine tower were derived from these accelerometers. The nacelle was connected to the tower by means of a six component load cell that measured the six DOF forces and moments between the tower and nacelle. The global connection loads between the wind turbine and the platform were measured by another six component load cell between the tower base and platform top. The turbine performance was measured by the torque sensor between the motor and the blades. Figure 32 and Figure 33 show instrumentation for the wind turbine and floating platform. The mooring top tension was measured by a ring type transducer at the fairlead location. A z-shaped strain gauge was installed at each tendon porch to measure tendon top tensions.

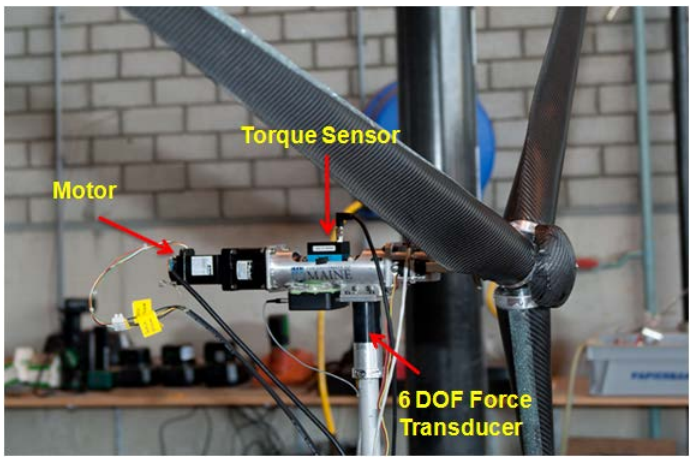

Figure 32: Instrumentation on wind turbine.

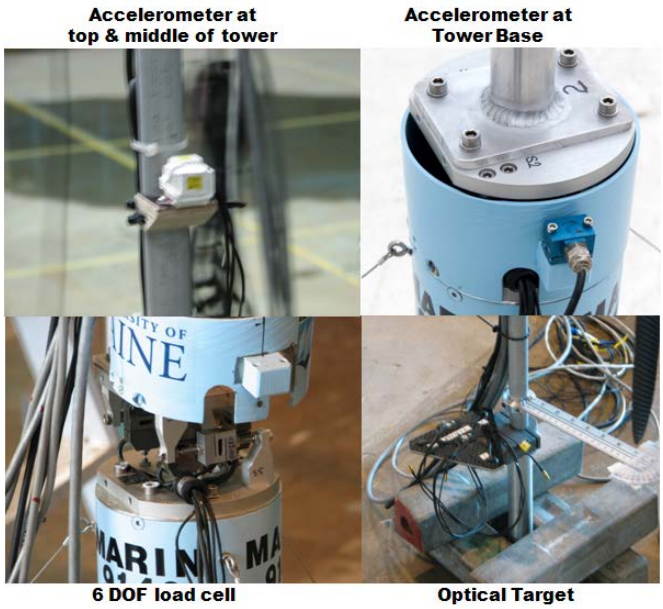

Figure 33: Instrumentation on turbine tower and floating platform.

A total of three calibration probes and two reference probes were used for the wave calibration tests. The reference wave probes remained in place throughout the tests to ensure repeatability of the wave generation. A total of three ADVs were used for the wind calibration tests. During the tests, two reference ADVs were also deployed to measure the tested wind. Table 10 gives the summary of the test measurements.

Table 10: Instrumentation list

Item	Channel	Remark
Ref. wave probes (2)	2	
Ref. ADV (2)	6	Three Axes
Optical Measuring	6	
Accelerometer Top	3	below nacelle
Accelerometer Mid	2	middle at tower
Accelerometer Low	3	bottom at tower
6 DOF Load Cell Low	6	at base of tower
6 DOF Load Cell High	6	at nacelle
Mooring – Semi	3	3 mooring lines
Tendon – TLP	3	3 tendons
Mooring - Spar	9	3 mooring line + 6 delta connections
Rotor Speed	1	
Torque sensor	1	at main rotor shaft

3.3 Test Matrix

In this section, an overview of the test matrix is presented. First, details including the wind and wave environments are discussed. Subsequently, the calibration of these environments is presented. Lastly, the test procedures and matrix of tests is covered.

3.3.1 Environments

The wind speeds were selected from the NREL 5 MW wind turbine power curve. Figure 34 shows the power curve of the full-scale NREL 5 MW wind turbine. Table 11 lists the tested wind speeds. During the model tests, six steady wind conditions were simulated. The steady wind speeds are defined at hub height (i.e. 90m above MWL) of the wind turbine. In addition to steady wind conditions, three dynamic wind conditions were also simulated to test realistic ocean wind conditions. The API (i.e. NPD) wind spectrum was used for the dynamic wind simulations (API, 2000). The dynamic wind speeds are defined at 10m above MWL.

Table 12 summarizes the tested wave conditions. Three wave conditions were selected based on 9 years worth of data measurement from the NERACOOS floating buoy system in offshore Gulf of Maine. In addition to wind driven wave conditions, one swell condition was also selected to simulate a bi-directional sea state. The bi-directional sea state was simulated by superposing the operational wave condition 2 from head seas (= 180 deg) and the swell waves from quartering seas (= 225 deg).

Table 11: Selected wind conditions.

	Velocity (m/s)	Rotor rpm	Remarks
Steady Wind 1	7.0	4.95	
Steady Wind 2	9.0	5.66	
Steady Wind 3	11.4	7.78	Rated Wind
Steady Wind 4	16.0	9.19	
Steady Wind 5	21.0	12.73	Design Maximum
Steady Wind 6	30.5	-*	Survival
Dynamic Wind 1	9.5	7.78	API Spectrum
Dynamic Wind 2	17.0	12.73	API Spectrum
Dynamic wind 3	24.0	-*	API Spectrum

*feathered turbine

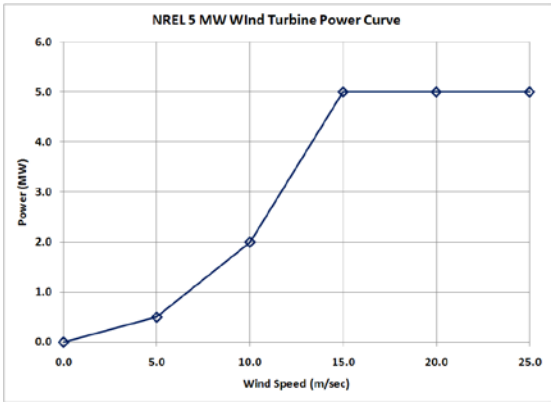

Figure 34: NREL 5 MW wind turbine performance curve.

Table 12: Selected wave conditions (JONSWAP spectrum).

	Hs (m)	Tp (sec)	Gamma	Remarks
Operation 1	2.0	7.5	2.0	
Operation 2	7.1	12.1	2.2	1 Year
Design	10.5	14.3	3.0	100 Year
Bi-directional	7.1/3.6	12.0/17.0	2.2/6.0	

3.3.2 Calibration of wind and wave environments.

Extensive wind calibrations were conducted of the wind generation machine. An image of the custom wind generation machine, unique to these model tests, is shown in Figure 35. Three Acoustic Doppler Volocimeters (ADV) were used for wind calibrations. Each ADV measures velocity in three directions. The wind calibration procedure is summarized as follows:

1. Determine spatial distribution over a calibration grid
2. Calibrate all steady wind speeds

3. Calibrate dynamic wind velocity spectrum

The wind field measurement range and locations are shown in Figure 36, and wind field measurement results are shown in Figure 37.

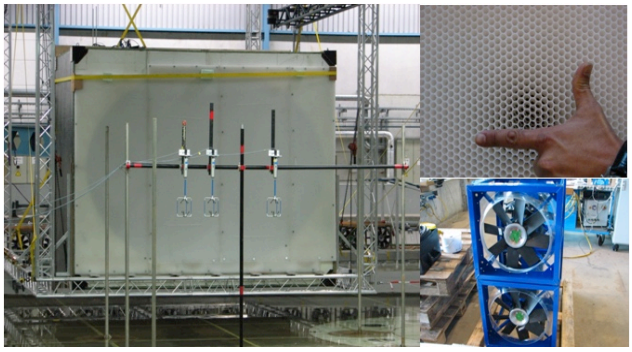

Figure 35: Wind generator.

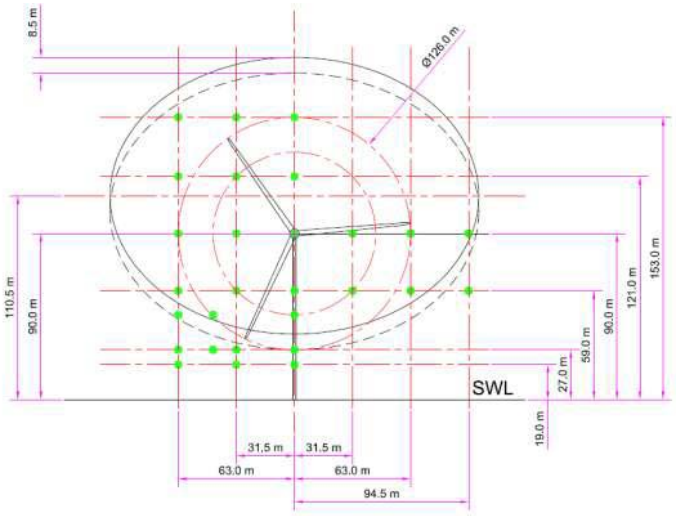

Figure 36: Wind field measurement locations.

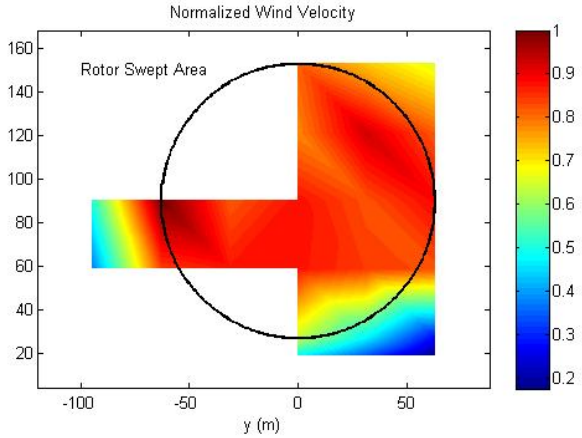

Figure 37: Wind field measurement results.

The waves were calibrated prior to installation of the model in the basin. The wave heights were measured at the location where the wind turbines will be located. In addition to calibration probe, two more wave probes were deployed at expected mean offset positions (i.e. 9m and 18m) of the floating wind turbines. Two additional reference probes were also deployed. The calibration results show that the maximum difference in standard deviation between the target waves and measured waves was less than 3%. Table 13 summarizes comparison results between target waves and measured waves. As shown in Figure 38, the basin generated wave spectra shows good agreement with the theoretical JONSWAP spectrum.

Table 13: Comparisons between target and measured waves

		Target	Measured	Diff. (%)
Operation 1	STD (m)	0.50	0.49	2.34
	Tz (sec)	5.74	6.16	7.43
Operation 2	STD (m)	1.79	1.77	1.15
	Tz (sec)	9.18	9.72	5.81
Design	STD (m)	2.62	2.62	0.21
	Tz (sec)	11.09	11.56	4.31
Swell	STD (m)	0.88	0.91	2.84
	Tz (sec)	13.83	12.9	6.75

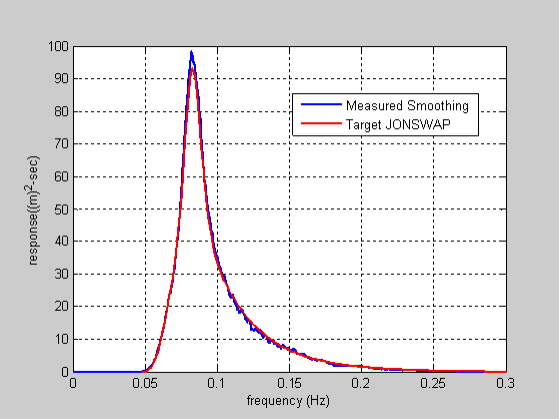

Figure 38: Operational wave 2 comparisons (measured Vs theory).

3.3.3 Test Procedures

The model tests started with calibration of the selected environmental conditions. After completing the calibration tests, the system identification tests were conducted. The purposes of the system identification tests are to verify physical properties such as system stiffness, natural periods, total system damping, and linear (RAOs) and non-linear (low & high frequency) response characteristics of the floating wind turbine models. Table 14 summarizes the system identification tests.

After the system identification tests, the station keeping tests were carried out. In order to identify coupling between the wind turbine and the floating platform, four different in-place test phases were conducted.

Table 14: Summary of system identification tests.

Test Types	Measurements
Hammer Tests	Structural natural periods
Static Offset Tests	Mooring stiffness
Free Decay Tests	System natural periods and total damping
Free Decay + Steady Wind	Damping contribution from wind
Regular Wave Tests	Linear response characteristics (RAOs)
Regular Wave + Steady Wind	Linear response characteristics include wind
White Noise Wave Tests	Linear response characteristics (RAOs) & Non-linear response characteristics (low frequency & high frequency)
White Noise Wave + Steady Wind	Wind damping contribution on system response

After the system identification tests, the station keeping tests were carried out. In order to identify coupling between the wind turbine and the floating platform, four different in-place test phases were conducted.

The first phase was wind only tests for the fixed wind turbine configuration. These tests served as benchmark for calibrating and verifying the aerodynamic load coefficients such as drag (C_D), lift (C_L), thrust, and torque of the wind turbine model.

The second phase was wind only tests for the floating wind turbine configuration. In this phase, the wind turbine was responding to wind and to "calm" water. The test isolated the wind effects on the floating wind turbine response.

The third phase was wave only tests for the floating wind turbine configuration. This phase served as benchmark for calibrating and verifying the hydrodynamic coefficients and station keeping characteristics of the floating wind turbines. The final phase was wind and wave tests. These tests were carried out with steady and dynamic winds, and regular and random wave environments. The station keeping test types and load cases are summarized in Table 15 and Table 16, respectively. Since the current speed is low in Gulf of Maine, currents were not simulated in these tests.

Table 15: Summary of station keeping test types.

Test Types	Test Description
Wind only	Wind tests for fixed wind turbine
	Wind tests for floating wind turbines
Wave only	Head seas
	Oblique seas
	Bi-directional seas (swell & local waves)
Wind & Wave	Operation wave with wind speed 1,2 & 3
	1year storm wave with wind speed 3,4 & 5
	100 year storm wave with wind speed 5
	100 year storm wave and wind speed 6
	Bi-directional wave + steady wind 5
	Bi-directional wave + dynamic wind 2

Table 16: Summary of load cases

	Operational Wave 1	Operational Wave 2	Design Wave	Bi-Directional
Steady Wind 1	Operation Low 1			
Steady Wind 2	Operation Low 2			
Steady Wind 3	Operation Low 3	Operation High 1		
Steady Wind 4		Operation High 2		
Steady Wind 5		Operation High 3	Design	Swell 1
Steady Wind 6			Survival	
Dynamic Wind 1		Operation High 1		
Dynamic Wind 2		Operation High 2	Design	Swell 2
Dynamic Wind 3		Operation High 3	Survival	

4 Experimental Comparison of the Three Floating Wind Turbine Systems

In this section, the experimental data for the three floating wind turbine systems is investigated. First, data pertaining to the system identification tests will be discussed. The system identification tests outline key characteristics of the floating wind turbine systems, such as non-dimensional wind turbine performance, tower bending natural frequencies, mooring restoring forces, motion natural periods and response amplitude operators (RAOs). Subsequently, the performance of the three floating wind turbines in several coupled wind and wave environments is analyzed and the results presented.

4.1 System Identification of the Floating Wind Turbine Systems

The first system identification test performed was a fixed-base test of the wind turbine under steady winds. During these tests, a sweep through various rotor speeds at a fixed wind speed was conducted to measure the variation of performance coefficient and thrust coefficient as a function of tip speed ratio. The results of the tests are given in Figure 39.

The turbine tower structural natural periods were measured with hammer tests. Hammer tests were executed by exciting the model with an impulse forces. Hammer test results are summarized and shown in Table 17 and Figure 40. The hammer test results show that the floating platform characteristics significantly influence the bending frequencies of the turbine tower. As expected, the stiffer foundation such as a TLP provides lower tower bending natural frequency than the compliant foundations such as a Spar-Buoy and Semisubmersible. The stiffer foundations represent free-fixed boundary condition such as cantilever beam, while softer foundation represents free-free boundary condition at the tower base.

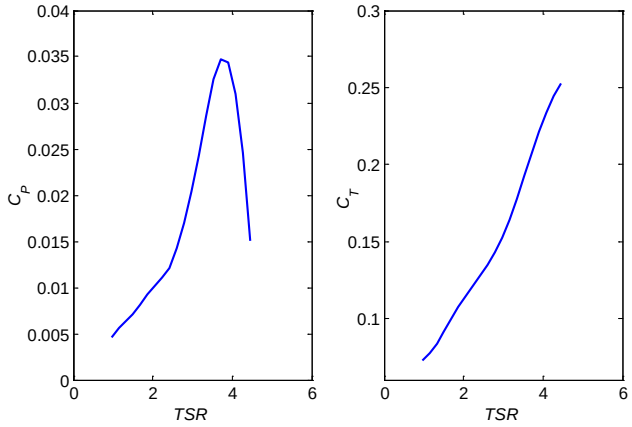

Figure 39: Performance coefficient and thrust coefficient as a function of tip-speed ratio for the wind turbine used in the model test program.

The total stiffness of the mooring system was measured by the static offset tests. Static offset test results are shown in Figure 41. As expected, softening was observed with the synthetic mooring system. On the other hand, hardening was observed with the catenary mooring system. The tendon system shows a linear stiffness trend. Setdown of the TLP was also measured during the horizontal static offset tests. Figure 42 shows setdown measurement of the TLP.

Table 17: Measured tower bending natural frequencies.

	Natural Frequency (Hz)		
	1st FA*	1st SS**	2nd FA*
Fixed Turbine	0.29	0.29	1.24
TLP	0.28	0.29	1.16
Spar-Buoy	0.43	0.44	1.29
Semi-Submersible	0.35	0.38	1.26

*fore - after mode
**side - side mode

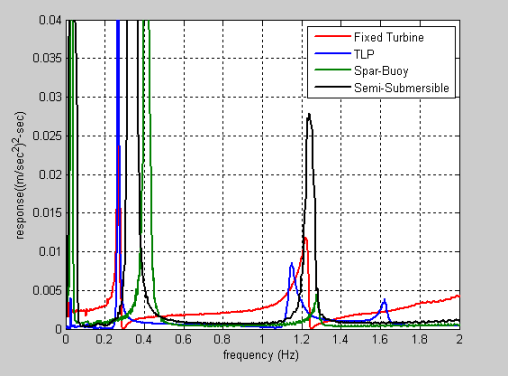

Figure 40: Hammer test results.

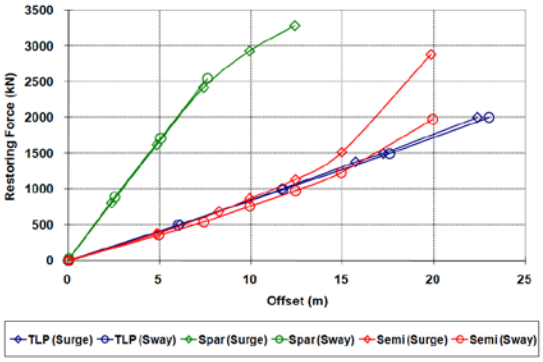

Figure 41: Comparison of static offset test results.

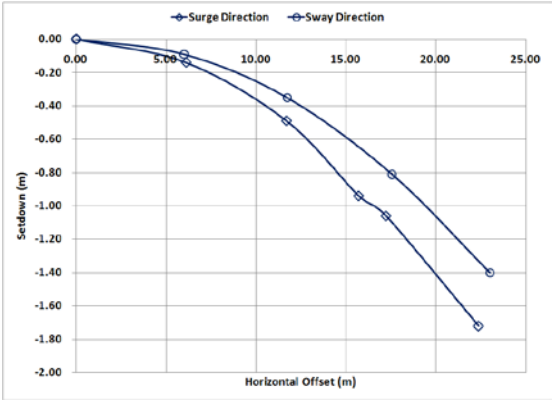

Figure 42: TLP setdown.

The natural periods and total damping of the floating platform system were obtained from free decay tests. In order to measure damping for the floating wind turbines, two types of free decay tests were carried out. The first type was calm water free decay test that measures system natural periods and hydrodynamic damping. The second type was free decay test with steady wind that measures aerodynamic damping from the wind turbine. The six DOF natural periods of the floating wind turbines are listed in Table 18.

Damping ratios with respect to motion amplitudes for all three floating wind turbines are shown in Figure 43, Figure 44 and Figure 45. Damping analysis results show that steady wind substantially increases pitch damping of the Spar-buoy and Semi-submersible. Due to slender and deep draft shape, relatively low heave, roll and pitch damping were measured with the Spar-buoy.

Table 18: Comparisons of natural periods.

DOF	Unit (sec)		
	TLP		
	Measured	Measured	Predicted
	No wind	Steady wind	No wind
Surge	39.30	39.48	40.2
Sway	39.30	-	40.2
Heave	1.25	-	1.05
Roll	3.70	-	3.11
Pitch	3.70	-	3.08
Yaw	18.20	-	16.8
DOF	Spar – Buoy		
	Measured	Measured	Predicted
	No wind	Steady wind	No wind
Surge	43.0	42.6	41.3
Sway	42.8	42.8	41.3
Heave	28.1	-	28.4
Roll	32.0	-	30.4
Pitch	31.5	31.2	30.4
Yaw	5.5	-	8.1
DOF	Semi-Submersible		
	Measured	Measured	Predicted
	No wind	Steady wind	No wind
Surge	107.0	102.0	107.5
Sway	112.0	-	107.5
Heave	17.5	-	17.2
Roll	26.9	-	26.6
Pitch	26.8	26.9	26.6
Yaw	82.3	-	84.3

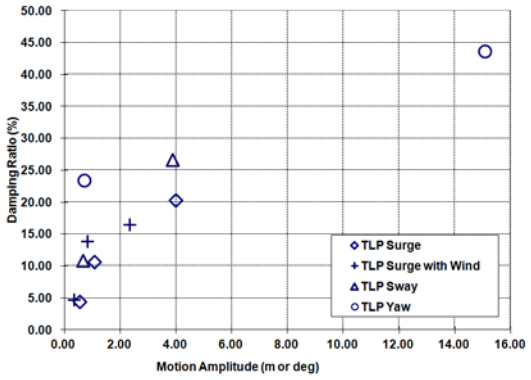

Figure 43: Comparisons of damping ratios (TLP).

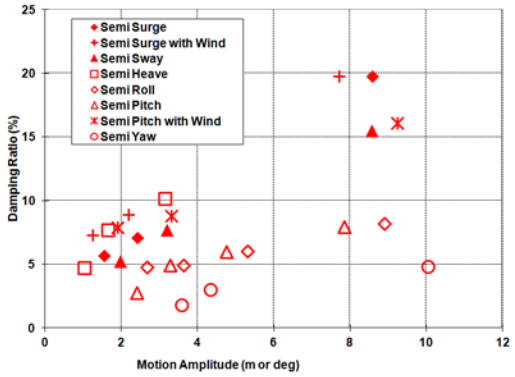

Figure 44: Comparisons of damping ratios (semi-submersible).

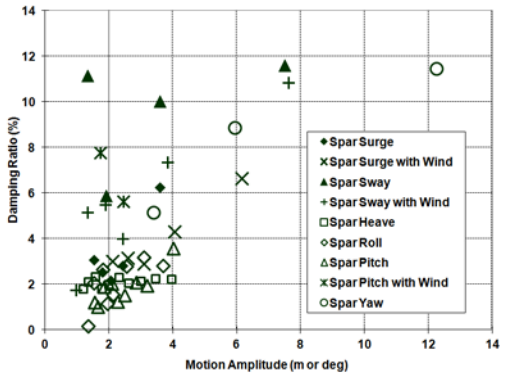

Figure 45: Comparisons of damping ratios (spar-buoy).

The linear and nonlinear wave response characteristics of the floating wind turbines were measured by the regular and white noise wave tests. In order to identify wind effects on the global performance of the floating wind turbines, the regular wave and white noise tests were conducted with and without steady wind.

4.1.1 TLP Response Amplitude Operators

Figure 46 shows surge RAOs of the TLP. The surge natural period of the TLP is longer than the linear wave frequency range, and therefore the damping effect from wind is not shown in the surge RAO. However, as shown in Figure 47, the response spectra comparisons clearly show wind damping effect at the TLP surge natural period (= 39.3 sec) response.

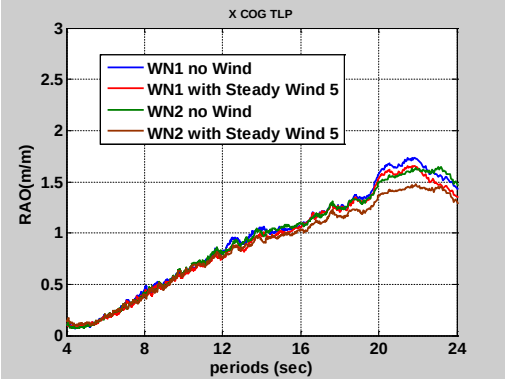

Figure 46: Surge RAOs of the TLP.

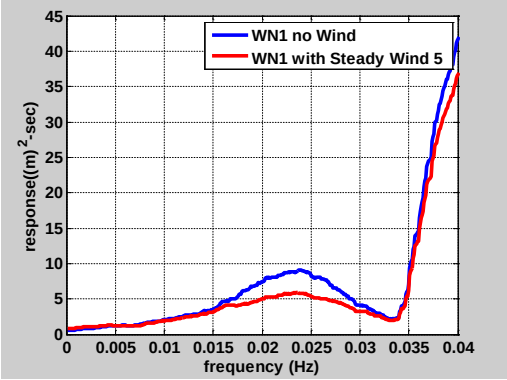

Figure 47: TLP Surge response spectra.

Figure 48 shows pitch RAOs of the TLP. Since pitch natural period of the TLP is near the linear wave excitation periods, the RAOs clearly show wind damping effects on the TLP pitch response. As shown in Figure 49, the response spectra comparison clearly shows reduction of the TLP pitch natural period motion.

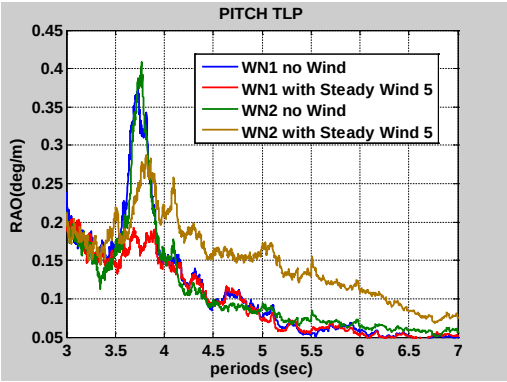

Figure 48: Pitch RAOs of the TLP.

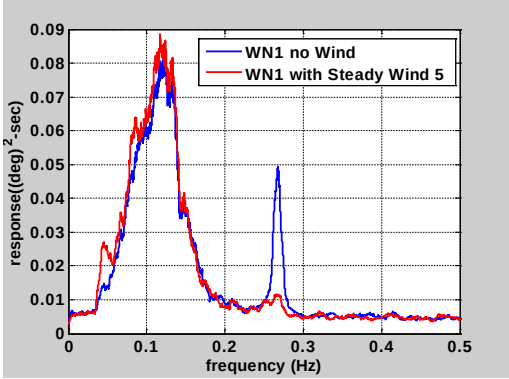

Figure 49: Pitch responses of the TLP.

4.1.2 Spar-buoy Response Amplitude Operators

Figure 50, Figure 51 and Figure 52 show the surge, heave and pitch RAOs of the Spar-Buoy, respectively. Since all six DOF motion natural periods of the Spar-buoy are longer than linear wave excitation period range, the damping effect from wind is not shown in the RAOs. On the other hand, Figure 53 and Figure 54 show response spectra of the Spar-Buoy, and both surge and pitch

responses show that the wind reduces the surge and pitch responses at the natural periods, while the wind increases the linear wave frequency responses of the Spar-Buoy in surge and pitch modes.

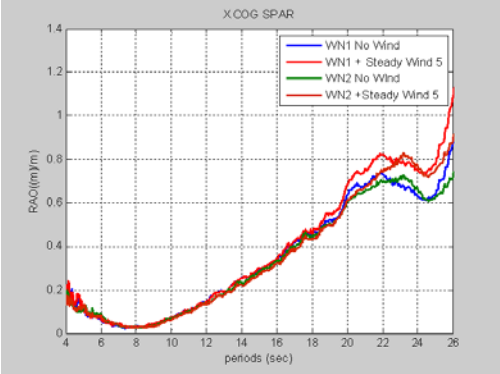

Figure 50: Surge RAOs of the spar-buoy.

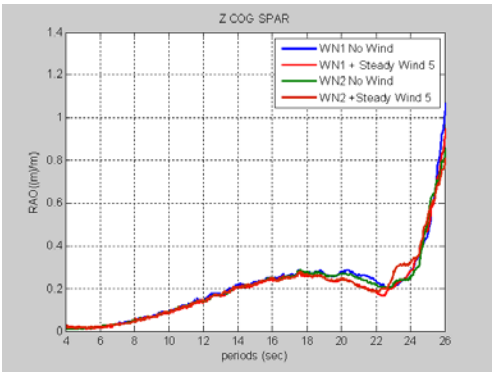

Figure 51: Heave RAOs of the spar-buoy.

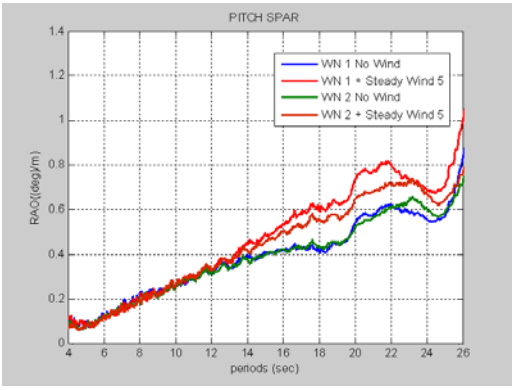

Figure 52: Pitch RAOs of the spar-buoy.

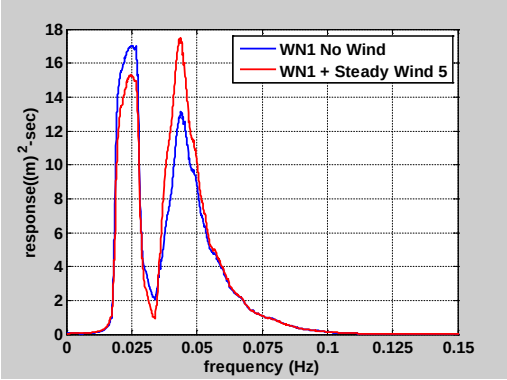

Figure 53: Surge response of the spar-buoy.

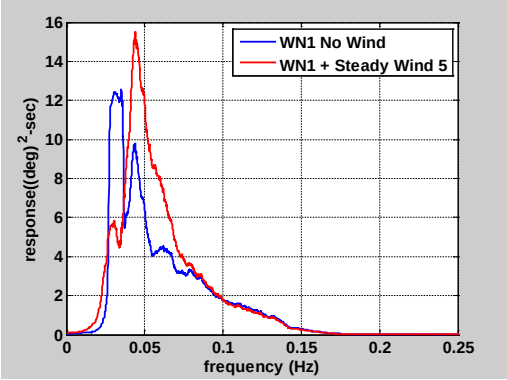

Figure 54: Pitch response of the spar-buoy.

4.1.3 Semi-submersible Response Amplitude Operators

Figure 55, Figure 56, and Figure 57 show the RAOs of the Semi-submersible. Since the heave natural period of the semi-submersible is close to linear wave energy, the heave RAO comparisons show nonlinear damping effect near the heave natural period (= 17.5 sec).

Figure 58 and Figure 59 show the surge and pitch response spectra of the semi-submersible. It is interesting to note that the surge and pitch linear wave frequency responses remained same for both with and without wind, while the steady wind reduces the low frequency surge and pitch responses.

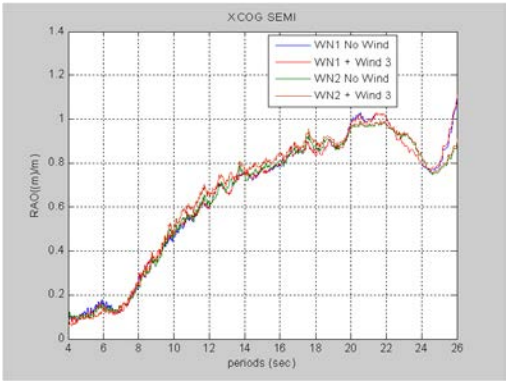

Figure 55: Surge RAOs of the semi-submersible.

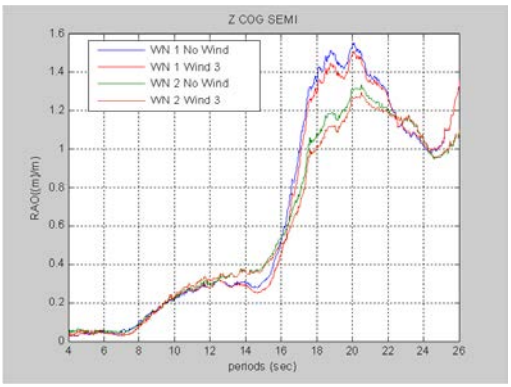

Figure 56: Heave RAOs of the semi-submersible.

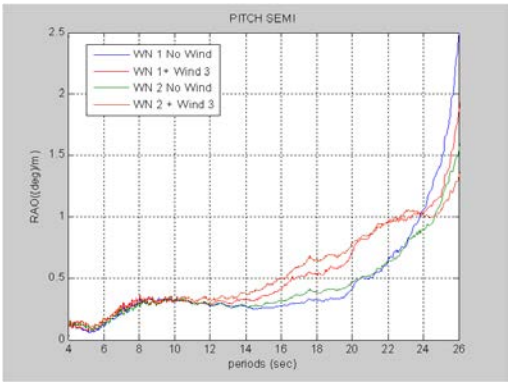

Figure 57: Pitch RAOs of the semi-submersible.

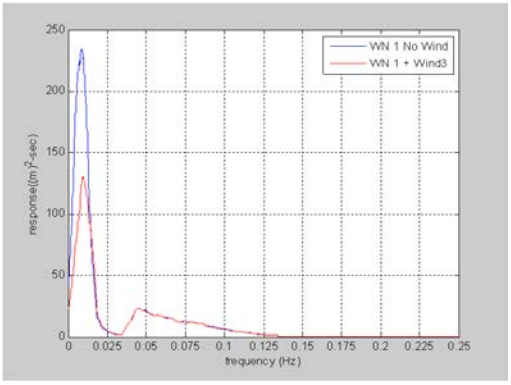

Figure 58: Surge response of the semi-submersible.

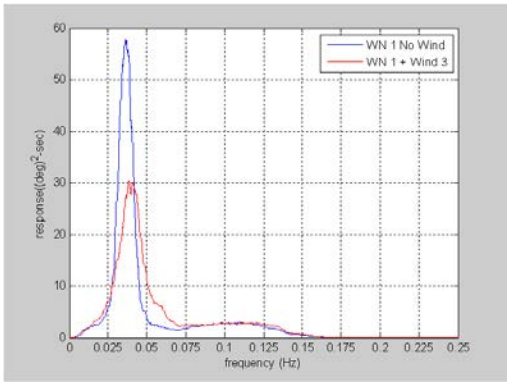

Figure 59: Pitch response of the semi-submersible

4.2 Performance of the Floating Wind Turbine Systems in Dynamic Winds and Irregular Waves

As noted earlier, the floating wind turbine test program covers a large number of tests ranging from basic system identification to complex, coupled wind/wave tests. With these system identification tests already covered, this section only presents results for the three systems subjected to combined wind and irregular wave loading. Also, as there were numerous combinations of wind and wave environments studied, this report focuses on only a select set of environmental conditions that yield interesting results. As such, the next section will outline the specific wind and wave environmental conditions employed throughout this section. Subsequently, the response of the three floating wind turbine systems to these environments will be discussed.

4.2.1 Environmental Condtions

The metocean conditions employed during the tests are based on measurements made from the Gulf of Maine NERACOOS floating buoy system. The wind environment during testing is created via a novel wind machine suspended above the water which produces near spatially uniform winds with a turbulence intensity at hub height of 4%. Multiple steady and dynamic winds are tested that cover a majority of the wind turbine operational wind speeds in addition to extreme, 100 year winds. However, only results using two steady winds and two temporally dynamic, NPD spectrum winds (NPD, 1992) are presented in the results section. The steady winds possess mean wind speeds at the 90 m hub height of U_m = 11.2 and 21.8 m/s. The NPD spectrum winds exhibit mean wind speeds of U_{10} = 17.0 and 24.0 m/s at the NPD specification height of 10 m above SWL. All winds are directed at 180 degrees and last for 3 hours. A depiction of the orientations and degrees of freedom (DOF) employed during model testing is shown in Figure 60.

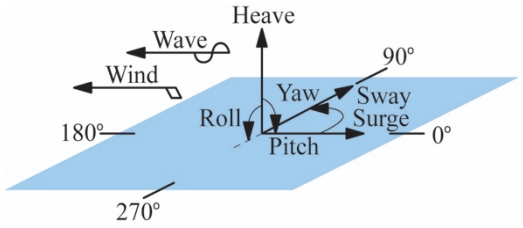

Figure 60: Orientations and degrees of freedom used during model testing.

The wind turbine operates at a rotor speed of 7.8 rpm for the U_m = 11.2 m/s condition and at a speed of 12.7 rpm for the steady U_m = 21.8 m/s and U_{10} = 17.0 m/s NPD winds. For the higher NPD wind speed, U_{10} = 24.0 m/s, the rotor is parked (0 rpm) with the blades feathered to minimize the aerodynamic drag loads. No active blade pitch control schemes are attempted and all tests utilize a fixed blade pitch setting in order to keep the number of variables that influence the global response of the floating wind turbine systems to a manageable level. For the dynamic winds, a comparison of the theoretical and obtained wind spectrums is shown in Figure 61. As can be seen in the figure, the match between the theoretical and measured spectra is quite good. The hub height statistics for the two dynamic winds are displayed in Table 19. For each of the steady and dynamic wind cases, the primary aerodynamic load contributing to global motion, thrust, varies significantly. The average thrust force for all three structures from wind only testing is found in Table 20. Note that even though the U_{10} = 24.0 m/s wind possesses the largest mean wind speed of all the winds presented, the average thrust load is the least due to the drag reducing effect of parking the turbine rotor and feathering the blades.

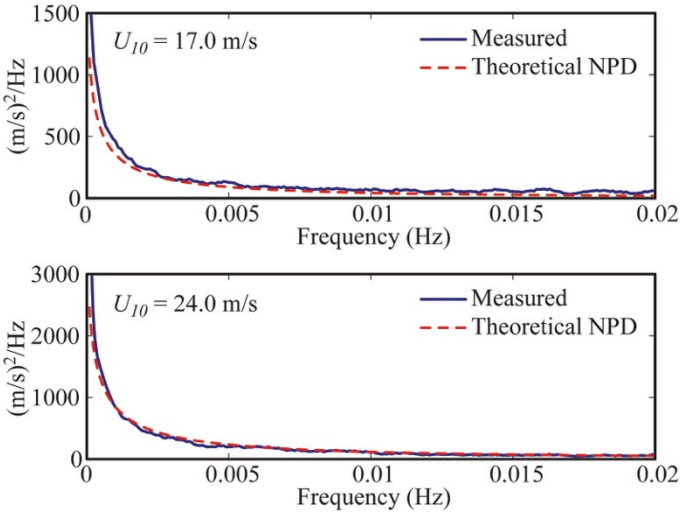

Figure 61: Theoretical and measured spectra for the U_{10} = 17.0 and 24.0 m/s NPD dynamic winds.

Table 19: Hub height (90 m) statistics for the U_{10} = 17.0 and 24.0 m/s NPD dynamic winds.

U_{10} (m/s)	Mean (m/s)	Std (m/s)	Max (m/s)	Min (m/s)
17.0	20.7	2.04	28.7	12.9
24.0	30.1	2.71	41.3	20.4

Table 20: Average thrust forces from wind only tests.

Wind Case	TLP (kN)	Spar (kN)	Semi (kN)
U_m = 11.2 m/s	263	255	203
U_m = 21.8 m/s	775	870	749
U_{10} = 17.0 m/s	642	755	683
U_{10} = 24.0 m/s	171	190	202

Similar to the winds, multiple regular and irregular waves are tested during the model floating wind turbine experiment. However, this section presents data from only three unidirectional irregular waves. The waves follow a JONSWAP spectrum (IEC, 2009) with significant wave heights of H_s = 2.0, 7.1 and 10.5 m. The peak spectral periods for these waves are T_p = 7.5, 12.1 and 14.3 s, respectively. Each of these waves is applied at 180 degrees, and thus, is aligned with the wind direction. All of these irregular waves are 3 hours in length. A comparison of the theoretical and measured spectra is shown in Figure 62.

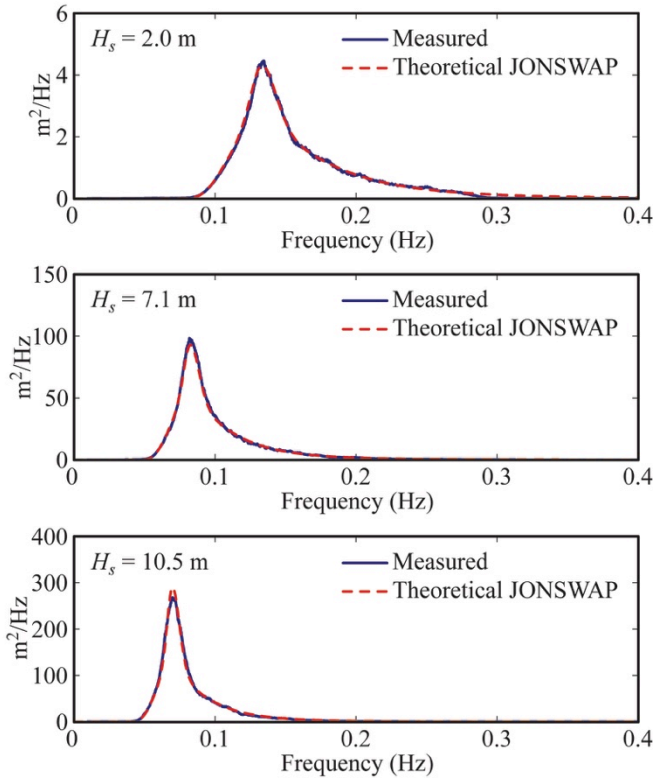

Figure 62: Theoretical and measured spectra for the H_s = 2.0, 7.1 and 10.5 m JONSWAP irregular waves.

Similar to the dynamic wind results, the comparisons shown in Figure 62 show a very good agreement between the theoretical and measured spectra. The statistics for the three irregular waves, consisting of standard deviation, maximum crest height, minimum trough and maximum wave height, are shown in Table 21. As can be seen in the table, the maximum crest heights are slightly larger than the value of H_s, while the maximum wave heights are roughly double H_s for each of the waves shown.

Table 21: Statistics for the H_s = 2.0, 7.1 and 10.5 m JONSWAP irregular waves.

H_s (m)	T_p (s)	Std (m)	Max Crest (m)	Min Trough (m)	Max Wave (m)
2.0	7.5	0.49	2.14	1.87	3.64
7.1	12.1	1.79	7.20	6.37	13.58
10.5	14.3	2.62	13.59	9.58	22.01

4.2.2 Wave Only Performance Comparison

In this section, a performance comparison of the three floating wind turbine systems is presented in wave only conditions. Response spectra and statistical surge and pitch results are provided for the systems subjected to each of the three, aforementioned irregular waves to illustrate the relative motion performance of the three floating systems in irregular seas. To begin, the response spectra for the surge DOF is shown in Figure 63. The surge coordinate is reported at the structure center of gravity (CG) for all three systems, as this location provides greater physical understanding of the system translational motion.

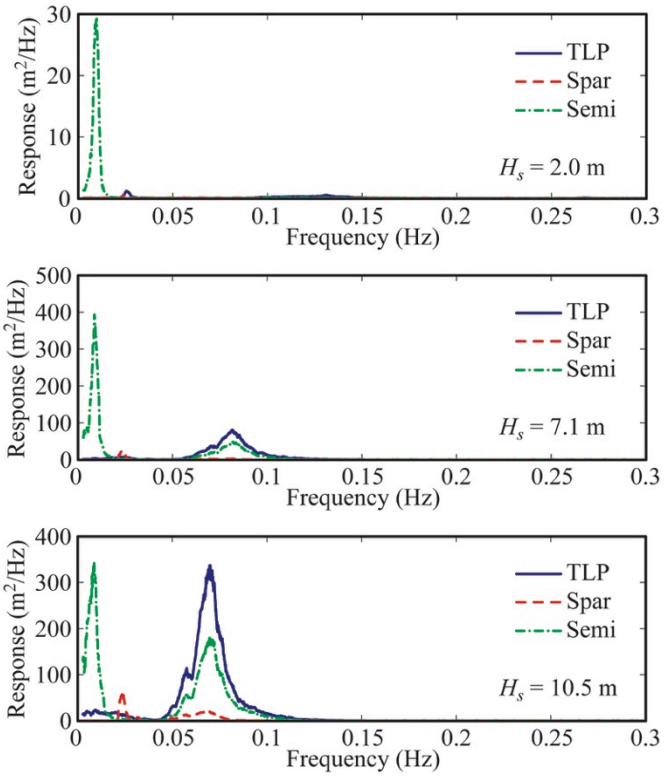

Figure 63: Surge response spectra for all three systems under wave only loading.

As can be seen in Figure 63, the TLP exhibits the greatest surge response in the wave energy range (0.05 to 0.15 Hz) about its CG for the three systems. The spar-buoy response is the least of the three, however, this is due in large part to the fact that the CG is very low on the structure and does not move much relative to the portion of the structure located near the waterline. The semi-submersible response is slightly less than the TLP in the wave energy range, but the semi-submersible exhibits by far the largest second-order difference-frequency associated surge motion of any of three floating turbine systems as evidenced by the significant response near the surge natural frequency of 0.009 Hz.

The second wave only comparison presented is the response spectra for the pitch motion of the structures, given in Figure 64. As one would expect, the stiff pitch restoring stiffness of the TLP is evidenced by the very low response of this system compared to the other two. Comparing the other two systems, the response is greatest for the spar-buoy in the wave energy regime, excepting the H_s = 2.0 m sea state where the semi response is slightly greater. The second-order difference-frequency response is once again greatest for the semi-submersible, with the disparity between the spar-buoy and semi-submersible being greatest as the sea state is diminished.

To complete the wave only comparison, the statistics for the surge and pitch motion are presented in Table 22. Many of the previous observations made from the frequency domain results are reinforced by the statistics of Table 22. The TLP and semi-submersible exhibit the largest minimum and maximum surge motions, with the TLP possessing the largest maximum surge for any design, 6.91 m, and the semi- submersible, the largest magnitude minimum for any of the designs, -13.72 m.

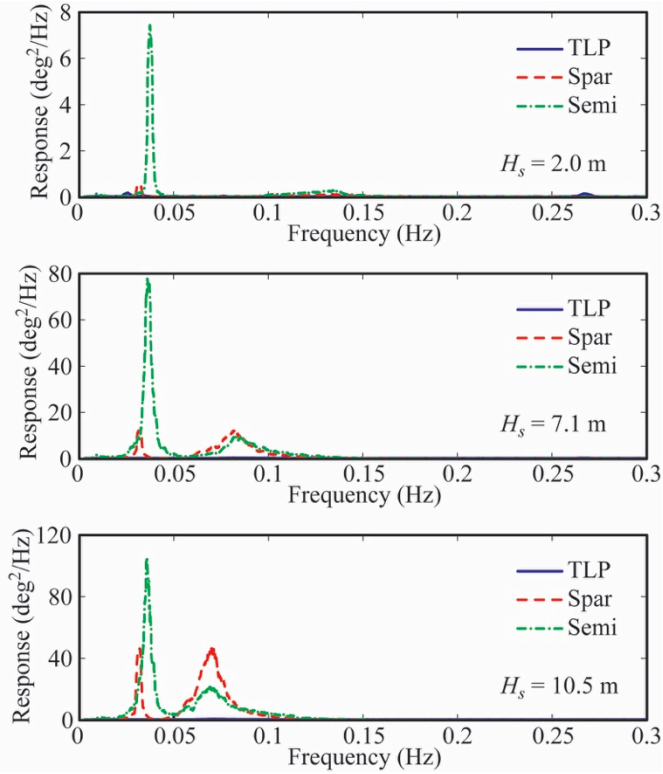

Figure 64: Pitch response spectra for all three systems under wave only loading.

Table 22: Statistics for the surge and pitch motion for the TLP, spar-buoy and semi-submersible.

DOF	H_s	Mean	Std	Max	Min
TLP					
Surge (m)	2.0 m	0.07	0.21	0.86	-0.70
Pitch (deg)	2.0 m	-0.20	0.19	0.24	-0.67
Surge (m)	7.1 m	-0.11	1.37	4.49	-8.22
Pitch (deg)	7.1 m	-0.18	0.15	0.42	-0.81
Surge (m)	10.5 m	-0.33	2.53	6.91	-12.73
Pitch (deg)	10.5 m	-0.18	0.16	0.64	-1.37
Spar-buoy					
Surge (m)	2.0 m	0.18	0.21	0.97	-0.50
Pitch (deg)	2.0 m	-0.11	0.13	0.42	-0.61
Surge (m)	7.1 m	0.17	0.45	2.00	-1.87
Pitch (deg)	7.1 m	-0.12	0.57	2.13	-2.54
Surge (m)	10.5 m	0.16	0.81	3.13	-3.42
Pitch (deg)	10.5 m	-0.13	1.01	-3.65	-5.43
Semi-submersible					
Surge (m)	2.0 m	-0.73	0.38	0.70	-2.36
Pitch (deg)	2.0 m	0.05	0.24	0.97	-0.90
Surge (m)	7.1 m	-1.83	1.71	3.44	-9.68
Pitch (deg)	7.1 m	0.06	0.86	3.35	-3.92
Surge (m)	10.5 m	-2.38	2.41	5.16	-13.72
Pitch (deg)	10.5 m	0.06	1.11	4.27	-4.71

Uniquely enough, the mean surge value for the TLP is quite small for all the environments, while the mean surge value for the semi-submersible grows modestly as the structure is subjected to increasing sea states. For the pitch motion, the TLP motion is by far the smallest of the three, as expected. For the other two systems, the pitch response range of the semi-submersible is largest in the H_s = 7.1 m sea state, as is the pitch standard deviation. In the H_s = 10.5 m condition, the spar-buoy and semi-submersible pitch ranges are nearly identical (approximately 9 degrees) with a slightly larger pitch standard deviation for the semi-submersible as opposed to the spar-buoy.

4.2.3 Effect of Wind on Global Performance

In this section, the effect of wind turbine aerodynamic loading on the global motion of the three structures is investigated. For all three structures, the response spectra and statistics of the surge and pitch DOF are investigated for three cases with an H_s = 10.5 m sea state: no wind, an operating turbine subjected to a U_{10} = 17.0 m/s wind and a parked and feathered turbine subjected to U_{10} = 24.0 m/s winds.

4.2.3.1 TLP

The response of the TLP floating wind turbine in these three conditions is investigated first. The response spectra for the surge and pitch DOF for the three cases are given in Figure 65. For both DOF, the response of the no wind and U_{10} = 24.0 m/s cases are very similar. This indicates that even under high wind speeds, a parked and feathered rotor minimizes the impact of the wind loading on the structure's response.

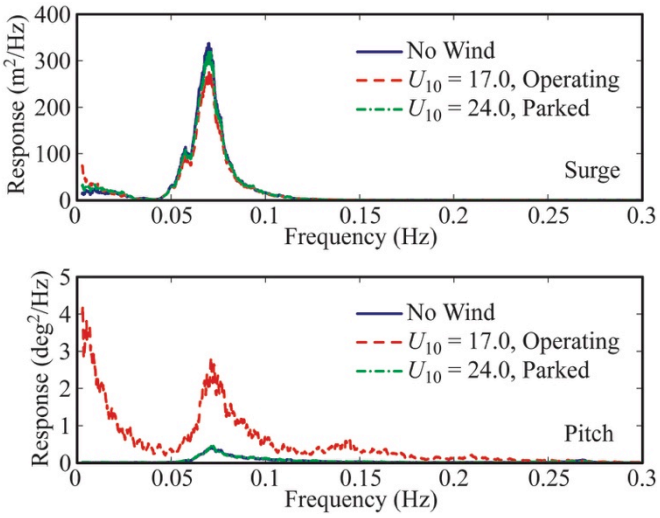

Figure 65: TLP surge and pitch response spectra for an H_s = 10.5 m sea state with three different wind conditions.

When the turbine is operating and the thrust loads are high in the U_{10} = 17.0 m/s case, the surge DOF exhibits increased response in the wind energy frequency range (<0.02 Hz) and is slightly damped in the wave frequency range (0.05 to 0.1 Hz). For the pitch response, the operating turbine increases the pitch response over all frequencies shown, with the greatest increases near the wind and wave energy frequencies. This is due to the fact that the TLP employed during model testing is of a small design and is not large enough to support the large overturning moment created by the thrust of the operating wind turbine in high seas, resulting in multiple slack line events. These slack line events result in infrequent, but violent pitch motions that excite a broad range of structural vibrations as evidenced by the increased pitch response shown in Figure 65. It should be noted

though, that the TLP pitch response is very small, and hence, the disparity between the TLP pitch response curves in Figure 65 does not represent a great deal of energy. The statistics for the three cases are given in Table 23. For the no wind and U_{10} = 24.0 m/s cases, the statistics are very similar, with the U_{10} = 24.0 m/s case yielding a larger magnitude mean surge and on average slightly larger magnitude extreme statistics.

Table 23: TLP surge and pitch statistics for an H_s = 10.5 m sea state with three different wind conditions.

DOF	U_{10}	Mean	Std	Max	Min
Surge (m)	0.0 m/s	-0.33	2.53	6.91	-12.73
Pitch (deg)	0.0 m/s	-0.18	0.16	0.64	-1.37
Surge (m)	17.0 m/s	-11.03	2.46	-3.62	-22.21
Pitch (deg)	17.0 m/s	-0.52	0.41	1.48	-6.86
Surge (m)	24.0 m/s	-3.23	2.52	4.31	-15.75
Pitch (deg)	24.0 m/s	0.28	0.16	1.44	-1.72

For the U_{10} = 17.0 m/s scenario, the mean value for surge is increased, but the standard deviation is similar to the other cases. The evidence for the slack tendon in the operating turbine case is the minimum pitch value of -6.86 degrees, this being abnormally large pitch motion for a TLP platform. If the TLP were of a sufficiently large size to prevent slack tendons, than the minimum pitch value for the U_{10} = 17.0 m/s scenario would likely decrease in magnitude by a significant amount.

4.2.3.2 Spar-buoy

Next, the results for the spar-buoy floating wind turbine are discussed. The response spectra for the surge and pitch DOF are displayed in Figure 66. For both surge and pitch DOF, the no wind and parked wind turbine cases are quite similar. As seen in Figure 66, the operating turbine increases only the second- order difference-frequency surge response of the spar-buoy, this being near the spar surge natural frequency of 0.023 Hz.

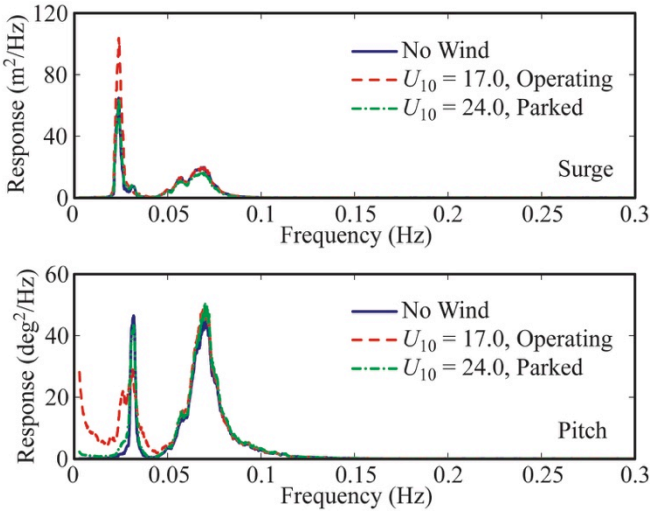

Figure 66: Spar-buoy surge and pitch response spectra for an H_s = 10.5 m sea state with three different wind conditions.

The pitch response, however, is increased significantly in the wind energy frequency range, with the sole exception being some damping of the pitch second-order difference-frequency response, near 0.032 Hz. The spar-buoy statistics for the two DOF for all three environments are given in Table 24.

Table 24: Spar-buoy surge and pitch statistics for an H_s = 10.5 m sea state with three different wind conditions.

DOF	U_{10}	Mean	Std	Max	Min
Surge (m)	0.0 m/s	0.16	0.81	3.13	-3.42
Pitch (deg)	0.0 m/s	-0.13	1.01	3.65	-5.43
Surge (m)	17.0 m/s	0.14	0.92	11.23	-4.41
Pitch (deg)	17.0 m/s	-4.36	1.25	0.04	-15.26
Surge (m)	24.0 m/s	-0.08	0.76	2.93	-3.48
Pitch (deg)	24.0 m/s	-1.25	1.07	2.39	-6.13

The statistics for the surge DOF for all three conditions are very similar with the lone exception being a larger range of motion for the U_{10} = 17.0 m/s case than the other two conditions. For the pitch motion, the mean value is much larger for the operating turbine than the no wind and parked turbine cases, as expected. The range of motion is also increased, however, the standard deviation is only 17% larger than the parked and feathered rotor subjected to U_{10} = 24.0 m/s winds.

4.2.3.3 Semi-submersible

Finally, the surge and pitch response spectra for the semi-submersible floating wind turbine are presented in Figure 67.

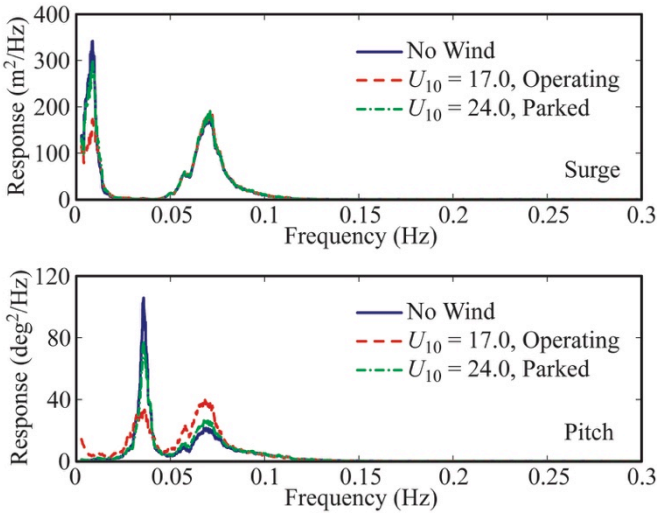

Figure 67: Semi-submersible surge and pitch response spectra for an H_s = 10.5 m sea with three different wind conditions.

Observing the figure, the parked wind turbine under U_{10} = 24.0 m/s winds provides marginal damping of the second-order difference-frequency response (0.009 Hz surge, 0.037 Hz pitch), and marginal excitation of the wave energy frequency response for pitch motion. The operating wind turbine case significantly damps the second-order response in surge and pitch, but noticeably amplifies the response in the wind and wave energy frequency ranges for pitch motion. The statistics for the cases shown in Figure 67 are given in Table 25.

Table 25: Semi-submersible surge and pitch statistics for an H_s = 10.5 m sea state with three different wind conditions.

DOF	U_{10}	Mean	Std	Max	Min
Surge (m)	0.0 m/s	-2.38	2.41	5.16	-16.72
Pitch (deg)	0.0 m/s	0.06	1.11	4.27	-4.71
Surge (m)	17.0 m/s	-9.28	2.30	-2.31	-22.28
Pitch (deg)	17.0 m/s	-3.48	1.25	1.55	-8.91
Surge (m)	24.0 m/s	-4.61	2.41	2.99	-17.78
Pitch (deg)	24.0 m/s	-0.69	1.12	3.73	-5.69

Similar to the other two floating wind turbine systems, the statistics are very similar for the no wind and parked turbine cases. The operating turbine case exhibits the largest magnitude mean pitch and surge values in Table 25, but the ranges of motion for both DOF are quite similar to the no wind and parked rotor cases.

4.2.4 Nacelle Acceleration

In this section, a study of the relative performance of the three floating wind turbine systems as measured by the nacelle surge acceleration is presented. The nacelle acceleration, which is a function of platform motion and flexible tower dynamics, is of great interest as it is indicative of the inertial loading that the wind turbine gearbox, bearings, and other complex parts will experience. For the comparison, the nacelle surge acceleration measured at 88.25 m above SWL is investigated for all three floating wind turbine systems under three distinct environmental conditions. The environmental conditions consist of H_s = 2.0, 7.1 and 10.5 m irregular sea states, each with an operating wind turbine. The H_s = 2.0, 7.1 m sea states are subjected to steady U_m = 11.2 m/s winds while the H_s = 10.5 m sea state case is subjected to U_m = 21.8 m/s steady winds. The response spectra for all three systems in each of the three conditions are displayed in Figure 68. There are several noteworthy observations to be made from the results shown in Figure 68. First, for the modest, H_s = 2.0 m sea state environment, the performance of the three systems is very similar in the wave energy frequency range (0.1 to 0.2 Hz). However, the TLP exhibits significant response at frequencies larger than the wave energy, which the other two systems do not. This energy is associated with the TLP coupled platform pitch/tower bending frequency of 0.28 Hz which is excited by the second-order sum-frequency wave loading from the small, T_p = 7.5 s sea state. While the response of all three systems is quite low in energy for the H_s = 2.0 m sea state, the prevalence of these mild sea environments indicates that this TLP may be prone to greater wind turbine and tower fatigue issues than the other systems.

Moving to the intermediate sea state of H_s = 7.1 m, the figure shows that the performance of the three systems are quite distinct. The spar-buoy system possesses the maximum peak response of the three systems with a peak that is nearly double that of the second most excited system, the TLP. While the TLP motion is primarily pure surge translation, the spar pivots about a point located low on the spar, near the CG, translating modest wave induced motions at the water line into large translational motions at the nacelle location. The result is the large nacelle surge accelerations seen in Figure 68 for this environmental condition. Surprisingly for this environment, the semi-submersible system nacelle surge acceleration response is greatly diminished to negligible levels over most of the wave energy range (0.05 Hz to 0.2 Hz). This is unexpected as the platform motion is substantial for this sea state with motion similar to the responses given in Figure 63 and Figure 64. The low surge acceleration at the nacelle location is a result of the unique interplay of the surge and pitch motion characteristics for this semi-submersible in the H_s = 7.1 m environment.

The nacelle surge acceleration response comparison for the most severe environment in Figure 68, H_s = 10.5 m, shows that the response of the semi-submersible is once again the smallest, albeit only

slightly less than the TLP floating wind turbine system. The spar-buoy floating wind turbine exhibits the largest response of the three, with a peak response in the frequency domain of approximately three times the TLP and semi-submersible. The reasons for the large response are similar to those identified for the H_s = 7.1 m condition, only magnified.

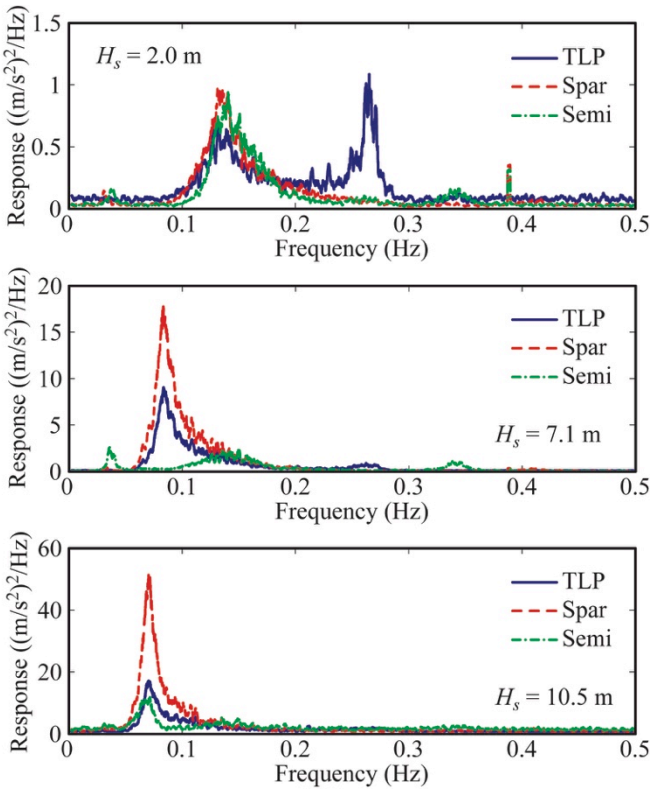

Figure 68: Nacelle surge acceleration spectra for all three systems under three distinct environmental conditions.

4.2.5 System Loads Comparison

In this section, a comparison of a few of the floating wind turbine system loads is presented. First, the tower base bending moment about the sway axis (pitch DOF) is presented for two different environments. This bending moment is the largest moment induced in the tower and is major design driver in the sizing of the tower. The second comparison involves the mooring line tensions for each of the designs subjected to the same wind and wave loading. These loads will indicate the relative demands of the floating wind turbine systems on the mooring and anchoring systems.

4.2.5.1 Tower Loads

For the comparison of the tower base bending moment, two environments are considered, both with an operating wind turbine subjected to a U_{10} = 17.0 m/s dynamic wind. The first possesses an H_s = 2.0 m irregular sea while the second consists of an H_s = 10.5 m sea state. The response spectra for the two conditions are shown in Figure 69. For the low energy sea state, all three systems exhibit a moderate response in the wave energy frequency regime (0.1 to 0.2 Hz), with the semi possessing the greatest response and the TLP the least. The largest discrepancy in the three systems is the response in the frequency ranges above and below the wave energy frequency range. For low frequencies in the wind energy regime, the TLP exhibits very little response, unlike the spar-buoy and semi-submersible. The wind loading excites the rigid body pitching motion of these

two systems which in turn induces significant moments at the base of the tower as a result of supporting the large nacelle and rotor weight on a tilted tower. As can be seen in Figure 69, the response at the spar-buoy and semi-submersible natural pitch frequencies (0.032 And 0.037 Hz, respectively) is quite prominent as a result of this phenomenon. At frequencies above the wave energy range, the TLP shows by far the greatest response. The response, located near the coupled platform pitch/tower bending frequency of 0.28 Hz, is excited primarily by the second-order sum-frequency wave loading of the TLP platform. The spar-buoy and semi-submersible also exhibit some tower base bending energy at their respective tower bending frequencies of 0.43 and 0.35 Hz, albeit, at a much reduced level as compared to the TLP. A final note for this condition is that the stiff TLP system allows transmission of the turbine's once per revolutions excitation at 12.7 rpm (0.21 Hz) all the way down the tower, as evidenced by the strong peak in the signal at this frequency.

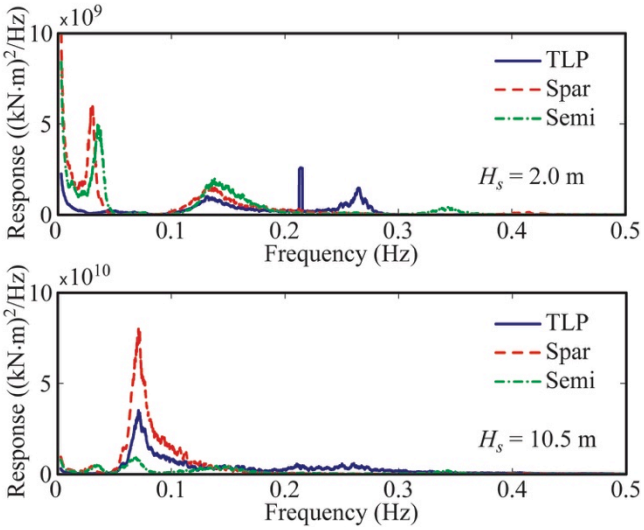

Figure 69: Tower base bending moment spectra for all three systems for two combined wind/wave loading conditions.

Moving to the environment with the larger H_s = 10.5 m sea state, it is evident from Figure 69 that the majority of the response for all three systems is in the wave energy frequency range (0.05 to 0.1 Hz). The spar-buoy possesses the most energy in the tower base bending, with the semi-submersible the least. Since the inertial forces created by motion of the nacelle and rotor contribute greatly to the tower base moment, it is not surprising that the response trends for this sea state are similar to the Figure 68 trends for the nacelle surge acceleration in the H_s = 10.5 sea.

To complete the moment comparison, the statistics for the two conditions for all three systems are shown in Table 26. It should be noted that the extreme minimum and maximum values for the TLP system in the H_s = 10.5 m condition are the result of tendon snapping events which cause violent pitch motions of the TLP floating wind turbine.

Table 26: Tower base bending moment statistics for all three systems for two combined wind/wave loading conditions.

H_s	Mean (kN)	Std (kN)	Max (kn)	Min (kN)
TLP				
2.0	-73,922	10,731	-23,047	-121,784
10.5	-74,291	38,757	356,510	-301,933
Spar-buoy				
2.0	-87,468	15,990	-27,787	-156,258
10.5	-79,064	45,332	91,815	-301,657
Semi-submersible				
2.0	-86,929	15,804	-28,538	-161,873
10.5	-84,358	24,572	53,555	-221,031

For a properly sized (i.e., larger) TLP platform, the extreme values for the TLP system in large seas would be significantly smaller, likely less than the spar-buoy and semi-submersible. This stated, the TLP has the smallest magnitude mean, standard deviation, minimum and maximum for the H_s = 2.0 m condition. While more severe, the moment statistics for the other two systems are very similar in the smaller energy environment. For the larger sea state, the TLP appears to be the poorest performer, again, as a result of the slack tendon events encountered during testing for this TLP design. For the other two systems, the spar-buoy has a moderately larger magnitude standard deviation, minimum and maximum bending moment due mostly to the larger variations in pitch angle of the structure as displayed in Table 23, Table 24 and Table 25.

4.2.5.2 Mooring Loads

To complete the loads comparison, the fairlead mooring line tensions for the three designs is investigated next. Note that for the spar-buoy system, only the main mooring lines are shown and the lines comprising the delta connection are omitted here. The environment investigated consists of U_{10} = 17.0 m/s winds and H_s = 2.0 m seas. The response spectra for the three mooring lines per design, denoted by orientation in degrees, are shown in Figure 70. From the figure, it is clear to see that the energy in the response of the TLP tendons is an order of magnitude greater than the response for the other two systems. This is not entirely unexpected as the TLP system gains its stability from highly loaded, stiff mooring tendons. For the spar-buoy, the mooring load response is tied closely to the surge natural period, as is the peak response of the semi-submersible. The TLP, on the other hand, exhibits significant response at frequencies associated with the wind energy, wave energy, and platform pitch/tower bending natural frequency. Surprisingly, all three TLP tendons also display a sharp response at the once per revolution rotor excitation frequency of 12.7 rpm (0.21 Hz). This is likely a result of the vertically stiff and lightweight nature of the floating TLP wind turbine system tested here.

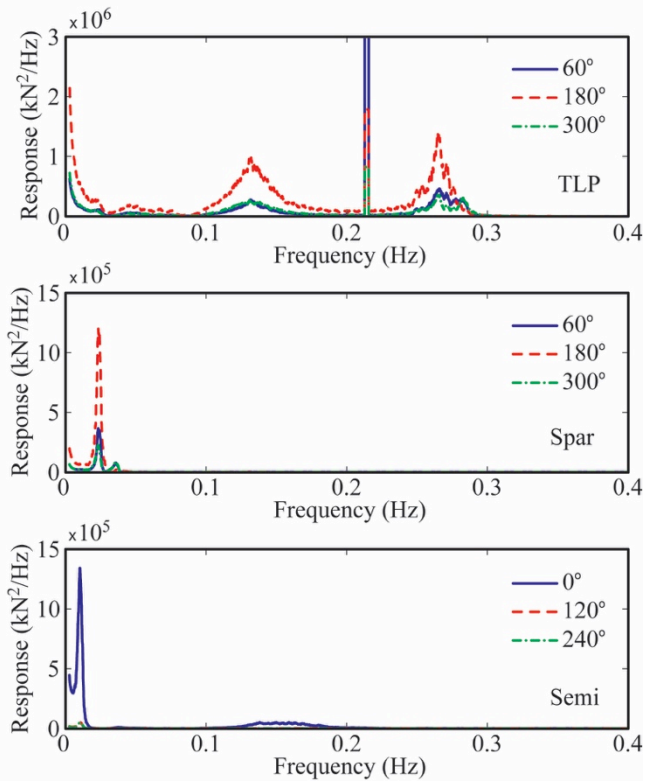

Figure 70: Fairlead mooring tension response spectra for all three systems in a combined wind and wave environment.

5 Calibration and Validation of Floating Wind Turbine Numerical Simulators Using Model Test Data

In this section, the calibration and validation of FAST models of the three floating wind turbine models is presented. First, the calibration of the wind turbine model as well as the coupled semi-submersible floating wind model is presented. Subsequently, the calibration and validation of the tension-leg platform floating wind turbine is discussed. Next, the calibration and validation of the spar-buoy floating wind turbine is reviewed. Lastly, a discussion is given presenting various improvements to FAST's hydrodynamic and mooring simulation capabilities.

5.1 Calibration and Validation of a Semi-submersible Floating Wind Turbine Model

5.1.1 Model Description

In this section, a description of the DeepCwind semi-submersible floating wind turbine is presented. Froude scaling was used to create the 1/50th-scale model, shown in Figure 71, and a variety of corresponding 1/50th-scale environmental loading conditions.

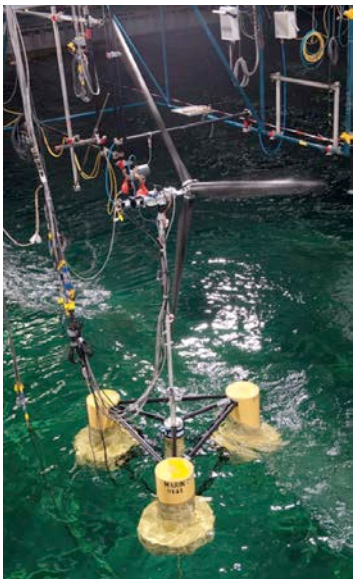

Figure 71: Image of the 1/50th-scale DeepCwind semi-submersible floating wind turbine.

Descriptions of pertinent system properties will be given for the wind turbine, tower, floating platform, and mooring system. The properties, which will include mass, elastic, aerodynamic and hydrodynamic quantities, are all presented at full-scale. It should also be noted that all test data and validation work is also presented at full-scale, as is customary for Froude-scale wave basin model testing. For more information regarding the scaling methods utilized to present the model test data at full-scale, please see the works of (Jain *et al.*, 2012) and (Martin *et al.*, 2012).

5.1.1.1 Wind Turbine

This subsection describes pertinent properties of the rotor blades, hub, nacelle, and control system. The rotor diameter and hub height dimensions are identical to the NREL 5-MW reference wind turbine at 126.0 m and 90.0 m above the still water line (SWL), respectively. However, the wind turbine tower top mass is larger than the NREL turbine by 13.47%. This resulted from physical design constraints when producing the scale model, which necessitated a significant amount of electronic and instrumentation gear to be housed inside the nacelle (Martin, 2011). After final design, accommodation of this equipment required a top-side mass of 397,160 kg, a total in excess of the desired 350,000-kg original target specification from the NREL 5-MW reference wind turbine. The gross properties of the model wind turbine are given in Table 27.

Table 27: Wind turbine gross properties.

Rotor Orientation, Configuration	Upwind, 3 Blades
Rotor, Hub Diameter	126.0 m, 3.0 m
Hub Height Above SWL	90.0 m
Height of Tower-Top Flange Above SWL	87.6 m
Overhang, Shaft Tilt, Precone	10.58 m, 0°, 0°
Vertical Distance Along Tower Centerline Between Tower Top and Shaft	2.4 m
Total Tower-Top Mass	397,160 kg

Table 28: Hub and nacelle gross properties.

Nacelle Mass	274,940 kg
Nacelle Center of Mass (Above Tower)	2.4 m
Nacelle Center of Mass (Downwind)	4.56 m
Nacelle Roll Inertia	284,100 kgm^2
Nacelle Pitch Inertia	22,440,000 kgm^2
Nacelle Yaw Inertia	22,440,000 kgm^2
Hub Mass	72,870 kg
Hub Inertia About Rotor Axis	Negligible (0)

In Table 28, additional details for the hub and nacelle required for generating a FAST numerical model are given. Note that the hub inertia about the rotor shaft axis is a very small contribution to the total rotor inertia and is taken to be zero. The experimentally derived rotor inertia and the total rotor inertia about the rotor axis utilized in the FAST model compare extremely well. A final detail worth noting is that the shaft tilt and blade precone are eliminated from both the physical and numerical models.

For the model tests, the rotor blades were designed to closely emulate the geometry of the NREL 5-MW reference wind turbine as is typical of a Froude-scaled model (Martin, 2011). In addition, the total mass of the blade was targeted to be roughly equal to the NREL 5-MW reference wind turbine. However, the wind turbine blades were designed to be nearly rigid to eliminate the aeroelastic complexities resulting from flexible blades. As a result, the nine degrees of freedom (DOF) associated with blade flexibility in FAST are turned off for all calibration and validation efforts in this work. The gross wind blade properties are given in Table 29 and the distributed blade mass properties employed in the analyses are given in Table 30.

Table 29: Blade gross properties.

Blade Length	61.5 m
Blade Mass	16,450 kg
Location of Blade Center of Mass (Measured from Blade Root)	23.4 m
Blade First Mass Moment of Inertia	385,150 kgm
Blade Second Mass Moment of Inertia	13,940,000 kgm^2

Moving to Table 31, details concerning the wind blade aerodynamics are presented, including blade twist, chord length, and airfoil designation. It is important to note that while the information in Table 31 is nearly identical to that for the NREL 5-MW reference wind turbine, the airfoil performance of the Froude-scaled blade geometry was significantly altered. This is because Froude scaling produces aerodynamic Reynolds numbers much smaller than what would be seen in a full-scale system. As such, new airfoil lift and drag coefficients were created for the model-scale wind turbine through a calibration process that employed model test wind turbine performance data. The details of this procedure are outlined in the calibration section of this section.

Table 30: Blade-distributed mass properties.

Radius (m)	Structural Twist (°)	Aerodynamic Center (-)	Mass (kg/m)
1.50	13.308	0.250	5868.9
1.95	13.308	0.250	350.1
3.40	13.308	0.228	345.9
5.54	13.308	0.199	338.7
8.63	13.308	0.173	334.5
11.78	13.308	0.125	337.8
15.88	11.480	0.125	331.2
19.97	10.162	0.125	309.7
24.07	9.011	0.125	289.8
28.16	7.795	0.125	270.8
32.26	6.544	0.125	251.4
36.35	5.361	0.125	233.3
10.45	4.188	0.125	215.7
44.54	3.125	0.125	198.1
48.64	2.319	0.125	182.0
52.73	1.526	0.125	165.8
56.20	0.863	0.125	152.3
58.91	0.370	0.125	137.3
61.61	0.106	0.125	93.4
63.00	0.000	0.125	13.2

Table 31: Blade-distributed aerodynamic properties.

Node Radius (m)	Aerodynamic Twist (°)	Chord Length (m)	Airfoil Designation*
2.867	13.308	3.542	Cylinder
5.600	13.308	3.854	Cylinder
8.333	13.308	4.167	Cylinder
11.750	13.308	4.557	DU 40
15.850	11.480	4.652	DU 35
19.950	10.162	4.458	DU 35
24.050	9.011	4.249	DU 30
28.150	7.795	4.007	DU 25
32.250	6.544	3.748	DU 25
36.350	5.361	3.502	DU 21
40.450	4.188	3.256	DU 21
44.550	3.125	3.010	NACA 64-618
48.650	2.319	2.764	NACA 64-618
52.750	1.526	2.518	NACA 64-618
56.167	0.863	2.313	NACA 64-618
58.900	0.370	2.086	NACA 64-618
61.633	0.106	1.419	NACA 64-618

*DU = Delft University, NACA = National Advisory Committee for Aeronautics

Moving to the operating details of the wind turbine, the control system used for the model wind turbine was very basic compared to the variable-speed, active blade-pitch systems encountered in many existing commercial-scale wind turbines. The tested system did not use variable-speed

control or active pitch control in an effort to manage the complexity of the model testing campaign. In operational test modes, the blades on the turbine were each fixed at a collective pitch of 6.4° and in parked test modes the blades were each fixed at 85°. Because of the aforementioned altered airfoil performance of the wind blades, the collective blade-pitch values utilized for operating and feathered modes differ from those employed in (Jonkman *et al*., 2007). During each test, the rotor speed was held constant, although the speed did change from test to test. Table 32 shows the various environmental and operating conditions for the model wind turbine studied in this work. Aside from a range of environments with an operating wind turbine, this work considered one extreme environment with a parked wind turbine and a mean wind speed of 30.5 m/s corresponding to a 100-year event in the Gulf of Maine (University of Maine, 2011).

Table 32: Wind turbine operating parameters.

Mean Wind Speed (m/s)	Reference Height (m)	Wind Condition	Rotor Speed (RPM)	Collective Blade Pitch Angle (°)
7.32	90.0	Steady	4.95	6.4
8.94	90.0	Steady	5.66	6.4
11.23	90.0	Steady	7.78	6.4
16.11	90.0	Steady	9.19	6.4
21.80	90.0	Steady	12.73	6.4
30.50	90.0	Steady	0.0	85.0
16.98 (20.60)	10.0 (90.0)	Dynamic	12.73	6.4

5.1.1.2 Tower

The tower for the DeepCwind semi-submersible platform was designed to emulate the fundamental bending frequencies of the OC3-Hywind tower (Jonkman, 2010) when supporting the previously described wind turbine mounted atop the OC3-Hywind spar-buoy. Successful achievement of this target is demonstrated in (Martin, 2011).

The mass and stiffness properties of the tower were calculated using the tower geometry and material properties of aluminum, of which the tower is made. As can be seen in Figure 71, there was a significant bundle of instrumentation cables that runs along a majority of the tower for the physically tested model. The weight of these cables that the floating platform had to support was calculated during testing, and this additional mass was evenly distributed along the entire length of the tower for numerical modeling. The cables were assumed to add negligible bending stiffness to the tower. The gross properties of the tower are given in Table 33 and the distributed properties are found in

Table 34. Note that

Table 34 only provides bending stiffness and excludes tower torsional and extensional stiffnesses as these quantities are not utilized by the FAST code.

Table 33: Gross tower properties.

Tower Height	77.6 m
Tower Base Elevation Above SWL	10.0 m
Tower Top Elevation Above SWL	87.6 m
Total Mass	302,240 kg
Center of Mass Above SWL	44.6 m

Table 34: Tower distributed properties.

Elevation (m)	Mass (kg/m)	Fore-aft Stiffness (Nm^2)	Side-side Stiffness (Nm^2)
10.00-10.31	55,671.5	1.123×10^{12}	1.123×10^{12}
10.31-18.54	4599.0	1.123×10^{12}	1.123×10^{12}
18.54-21.56	5808.1	1.371×10^{12}	1.371×10^{12}
21.56-22.26	16,044.3	1.371×10^{12}	1.371×10^{12}
22.26-81.63	2982.9	2.485×10^{11}	2.485×10^{11}
81.63-82.87	5128.5	2.485×10^{11}	2.485×10^{11}
82.87-83.49	11,821.4	2.485×10^{11}	2.485×10^{11}
83.49-84.42	10,433.7	2.485×10^{11}	2.485×10^{11}
84.42-87.60	5710.8	1.104×10^{12}	1.104×10^{12}

In addition to distributed properties, FAST also requires the first two modes of vibration for both fore-aft and side-side bending as well as modal damping quantities. The generation of mode shapes, estimation of modal damping, and reconciliation of FAST tower response with test data will be covered in the calibration section of this work.

5.1.1.3 Floating Platform

The floating platform for this model is a semi-submersible. It is considered to be buoyancy-stabilized because rotational displacements induce large buoyant-restoring forces from the volumes of water that are displaced. Dimensioned drawings of the DeepCwind semi-submersible platform are given in Figure 72 along with the coordinate system employed in this study.

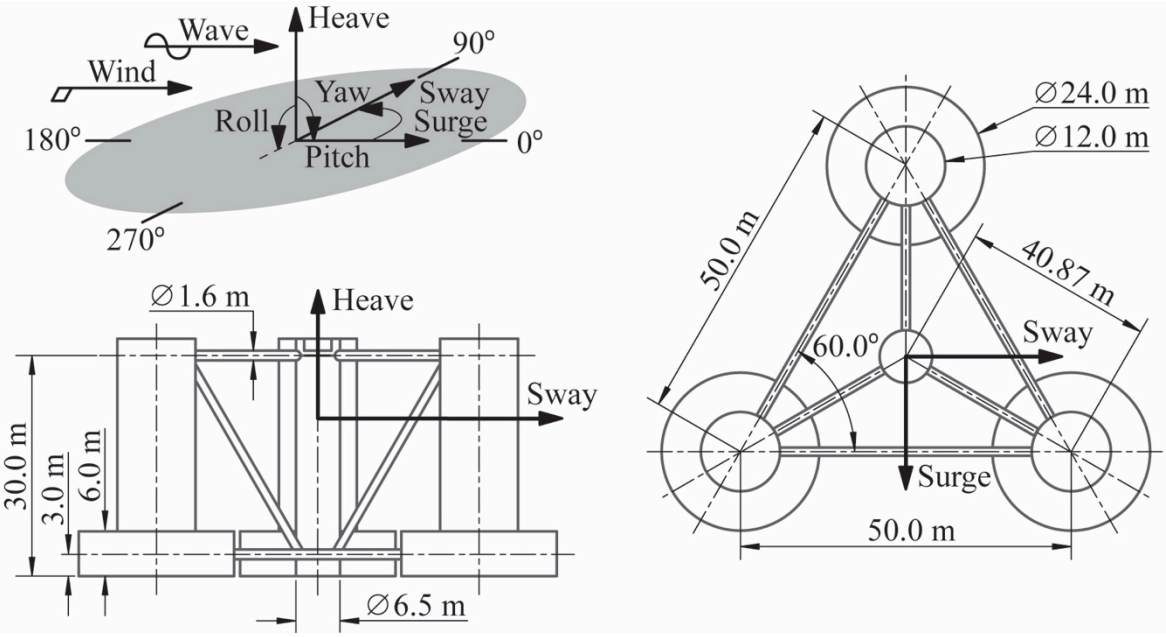

Figure 72: Coordinate system and dimensions of the DeepCwind semi-submersible platform.

The platform is made up of three offset columns with larger diameter lower bases, one center support column for the turbine, and a series of horizontal and diagonal cross bracing. The 1.6-m-diameter cross bracing consists of two sets of three pontoons connecting the outer columns with each other, two sets of three pontoons connecting the outer columns to the center column and three diagonal braces connecting the top of the outer column to the bottom of the center column. An overview of the full-scale dimensions and gross properties of the platform are given in Table 35.

Concerning platform flexibility, the 1/50th-scale platform was designed to be very stiff and was assumed to be rigid for the analyses conducted in this work.

Table 35: Platform gross properties.

Depth to Platform Base Below SWL (Total Draft)	20.0 m
Elevation to Platform Top (Tower Base) Above SWL	10.0 m
Platform Mass, Including Ballast	13,444,000 kg
Displacement	13,986.8 m^3
Center of Mass (CM) Location Below SWL Along Platform Centerline	14.4 m
Platform Roll Inertia About CM	8.011×10^9 kgm^2
Platform Pitch Inertia About CM	8.011×10^9 kgm^2
Platform Yaw Inertia About Platform Centerline	1.391×10^{10} kgm^2

This is consistent with the modeling approach employed in FAST. A full-scale platform built with these dimensions would likely have some compliance and therefore require larger bracing components to be considered rigid. It is important to note that the model tests performed were intended to capture the global performance characteristics of a generic semi-submersible platform, not to analyze an optimal design. Certainly more efficient semi-submersible designs can be created through optimization.

Regarding hydrodynamics, FAST implements a linear, time-domain formulation in which the problem is separated into three separate problems: hydrostatics, diffraction, and radiation (Jonkman, 2007; Faltinsen, 1990, Newman, 1997). The quantities required for executing the time-domain hydrodynamic load simulation are obtained from WAMIT (Lee and Newman, 2006), a three-dimensional frequency-domain potential-flow numerical panel method. For WAMIT analysis, a higher-order representation geometric description file for the DeepCwind semi-submersible platform was created using MultiSurf (MultiSurf, 2011). In the higher-order geometric description, the velocity potential on the body surface is represented using B-splines. One geometric plane of symmetry was exploited in the analysis, and the average panel size utilized was 2.0 m. To further improve the accuracy of the WAMIT results, options were selected to integrate the logarithmic singularity analytically, solve the linear system of equations using a direct solver, and remove the effects of irregular frequencies by manually paneling the free surface. These settings were beneficial because of the requirement for high-frequency output for time-domain analysis. The semi-submersible platform was analyzed in its undisplaced position and with a water depth of 200.0 m. The origin for the analysis was taken to be the intersection of the platform centerline and waterline because this point coincides with the location of FAST platform DOF. As such, all hydrodynamic quantities in this section are referenced from this point.

With the numerical solution parameters established, the output of the WAMIT analysis is now presented and discussed. The linear hydrostatic restoring forces account for contributions due to system weight and center of gravity location, buoyancy and center of buoyancy location, and lastly, water plane stiffness. In FAST, the contribution due to weight is handled separately and the hydrostatic restoring force is characterized via a stiffness matrix, C_{ij}^H, which includes only buoyancy and water plane effects. The hydrostatic forces F_i^H are computed as

$$F_i^H = \rho g V_o \delta_{i3} - C_{ij}^H q_j, \quad i,j = 1,2,\ldots,6,$$

where ρ is the density of water (1025.0 kg/m^3), g is the local acceleration due to gravity (9.80665 m/s^2), V_o is the displaced volume in the undisplaced position, δ_{i3} is the Kronecker delta, q_j are the six rigid-body DOF located at the waterline and C_{ij}^H is

$$\boldsymbol{C}^{H} = \begin{bmatrix} 0 & 0 & 0 & 0 & 0 & 0 \\ 0 & 0 & 0 & 0 & 0 & 0 \\ 0 & 0 & 3.836\ N/m & 0 & 0 & 0 \\ 0 & 0 & 0 & -377.6\ Nm/rad & 0 & 0 \\ 0 & 0 & 0 & 0 & -377.6\ Nm/rad & 0 \\ 0 & 0 & 0 & 0 & 0 & 0 \end{bmatrix} \times 10^{6}.$$

The diffraction forcing, which considers the hydrodynamic loads associated with incident waves, is characterized by wave frequency- and direction-dependent first-order transfer functions, $X_i(\omega, \beta)$, where ω is the wave frequency and β is the wave direction. The complex valued $X_i(\omega, \beta)$ vector contains the platform forces and moments per unit wave amplitude and the interplay of the real and imaginary components determine the phase lag between the wave crest and the peak forces.

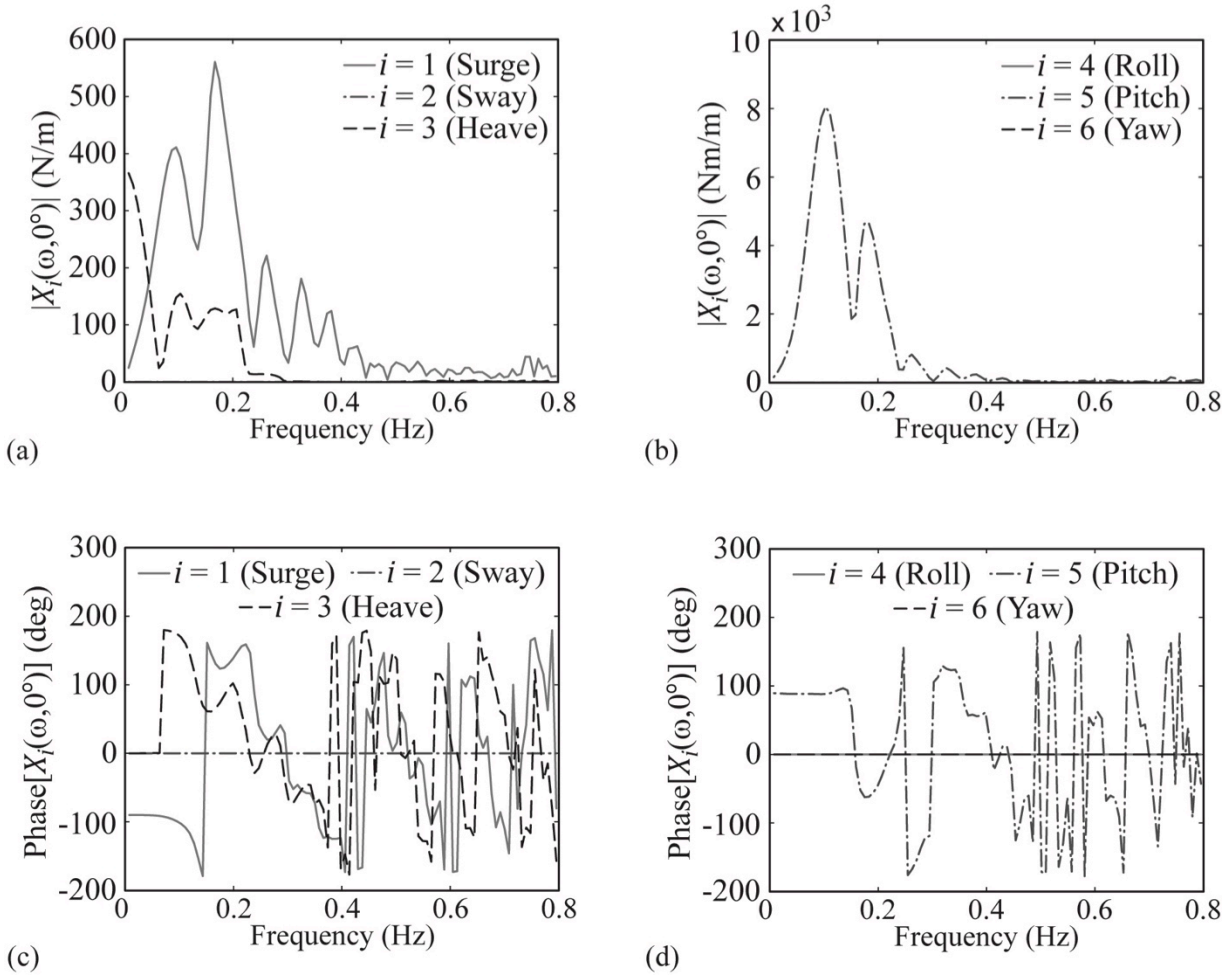

Figure 73: Plots of first-order transfer functions at a zero-degree wave heading for (a) forces and (b) moments, along with phase lag angles for forces and moments in (c) and (d), respectively, as a function of frequency.

A plot of the first-order transfer function magnitudes and phase angles for a zero degree wave heading is given in Figure 73.

The last hydrodynamic force considered in the linear implementation is the radiation force that accounts for platform forces associated with the oscillation of the platform. To compute forces

associated with radiation in the time domain, FAST requires knowledge of the infinite-frequency, added-mass matrix, $A_{ij}(\infty)$, and the oscillation-frequency-dependent damping matrix, $B_{ij}(\omega)$ (Jonkman, 2007). The WAMIT-derived, infinite-frequency, added-mass matrix for the DeepCwind semi-submersible platform is

$$\boldsymbol{A}(\infty) = \begin{bmatrix} 6.504 & 0 & 0 & 0 & -85.44\ m & 0 \\ 0 & 6.504 & 0 & 85.44\ m & 0 & 0 \\ 0 & 0 & 14.71 & 0 & 0 & 0 \\ 0 & 85.44\ m & 0 & 7257\ m^2 & 0 & 0 \\ -85.44\ m & 0 & 0 & 0 & 7257\ m^2 & 0 \\ 0 & 0 & 0 & 0 & 0 & 4894\ m^2 \end{bmatrix} \times 10^6\ kg. \qquad (3)$$

Plots of the non-zero damping-matrix components for the DeepCwind semi-submersible platform as a function of frequency are given in Figure 74.

In addition to linear hydrodynamic forces, a quadratic drag model is implemented in this work to account for flow-separation-induced drag. FAST has the ability to compute drag forces using Morison's equation for the main column; however, the formulation does not permit inclusion of all the members of the semi-submersible platform. Therefore, the coefficients employed in this quadratic drag model are determined from experimental data to represent the additional damping present in the system. A discussion of the quadratic drag model and derivation of coefficients is presented in the subsequent calibration section.

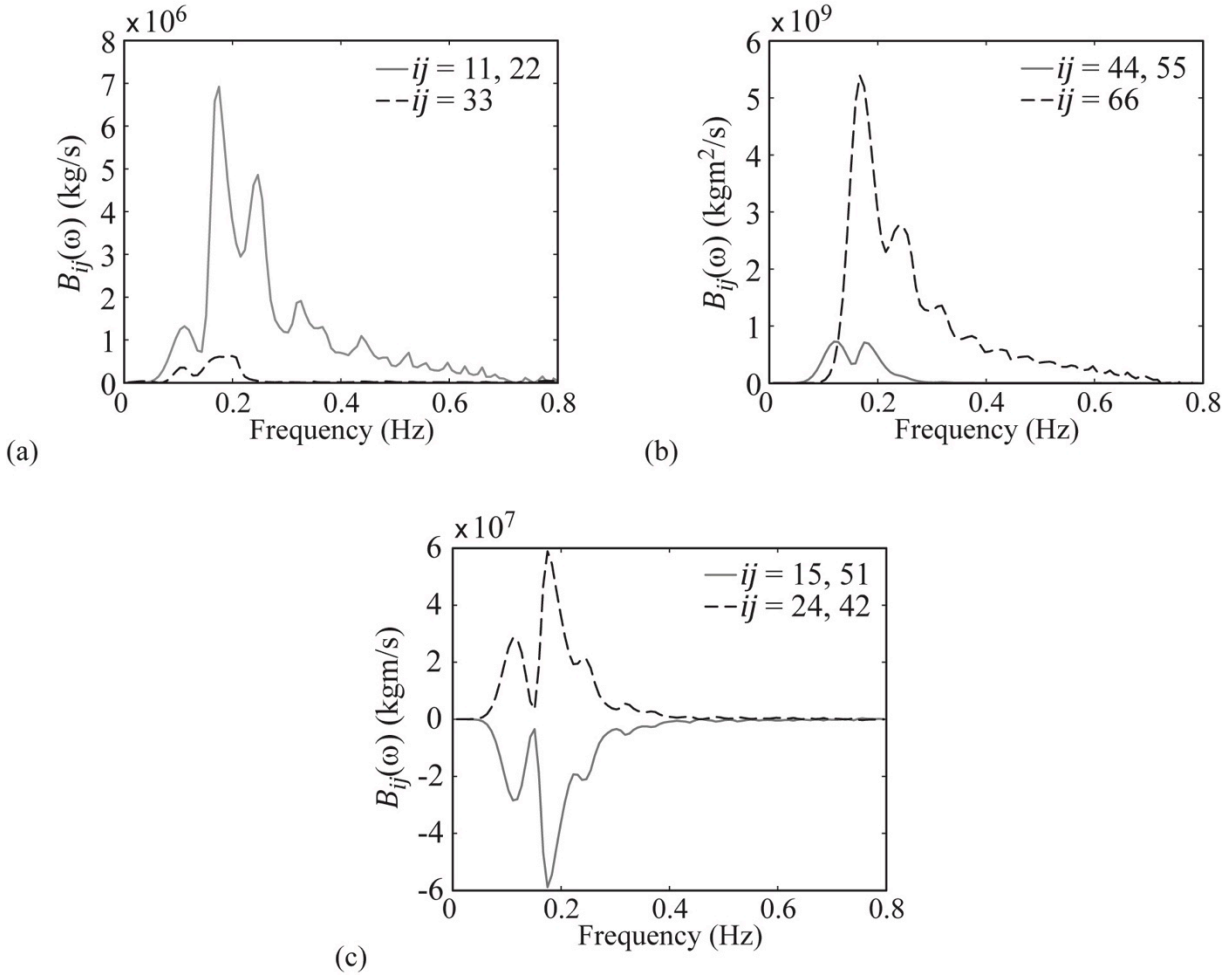

Figure 74: Plots of the nonzero entries of the damping matrix as a function of frequency for the (a) translational modes, (b) rotational modes, and (c) coupled translation-rotation modes.

5.1.1.4 Mooring System

The mooring system for the DeepCwind semi-submersible platform consists of three slack, catenary lines that provide the primary global restoring forces for motion in surge, sway, and yaw, and additional, albeit marginal, global restoring forces for heave, roll, and pitch motion. The default quasi-static mooring module from FAST is employed in this work, and the details of how the non-linear catenary equations are solved can be found in (Jonkman, 2007). The relevant information for the mooring system is found in Table 36. The three mooring lines are orientated at 60°, 180°, and 300° (lines 1, 2, and 3 respectively) about the heave axis with 0° being aligned with the surge axis. A comparison of the numerical model and the tuned physical mooring system employed for testing is covered in the calibration section.

Table 36: Mooring system properties.

Number of Mooring Lines	3
Angle Between Adjacent Lines	120°
Depth to Anchors Below SWL (Water Depth)	200 m
Depth to Fairleads Below SWL	14 m
Radius to Anchors from Platform Centerline	837.6 m
Radius to Fairleads from Platform Centerline	40.868 m
Unstretched Mooring Line Length	835.5 m
Mooring Line Diameter	0.0766 m
Equivalent Mooring Line Mass Density	113.35 kg/m
Equivalent Mooring Line Mass in Water	108.63 kg/m
Equivalent Mooring Line Extensional Stiffness	753.6×10^6 N

5.1.2 Model Calibration

In this section, the calibration of various tunable aspects of the wind turbine model is presented. These tunable aspects rely on test information from simple, fundamental tests of the floating wind turbine that focus on characterizing a particular facet of system behavior. These tests, called system identification tests, are used to tune the FAST wind turbine aerodynamics, first tower-bending mode frequencies, and viscous damping parameters. The tests also verify the system restoring forces provided by the mooring system. The data employed for use in the calibration process can be found in (Koo *et al*., 2012). This step is necessary because of unknown testing parameters and some imperfections in the numerical model.

5.1.2.1 Wind Turbine Performance

During model testing, the low wind speeds of the Froude-scale environment created Reynolds numbers that were nearly three orders of magnitude lower than full-scale. This resulted in altered airfoil lift and drag performance with overall lower thrust loads and power production relative to the full-scale NREL 5-MW reference wind turbine for a given wind speed. Because thrust loading is the major aerodynamic driver for global motion of the system, higher wind speeds were selected for testing, which yielded proper, Froude-scale rotor thrust values. The details of the wind turbine performance deficiency and accompanying adjustments are discussed in (Martin *et al*., 2012).

For completeness, it is noted that a high-quality wind environment was generated in MARIN's offshore basin using a suspended rectangular rack with 35 fans, a series of screens, and an elliptically shaped nozzle. The nozzle outlet used was 200 m wide and 150 m tall (full scale), this being larger than the rotor swept area. Turbulence intensity at the hub location was measured to be 4% and modestly higher at the boundaries of the outlet nozzle. Swirl in the flow field was less than 1% of the free stream velocity. A more thorough description of the wind generation machine can be found in (Goupee *et al*., 2012 OTC).

For numerical modeling in FAST, the altered performance of the wind turbine necessitated a new aerodynamic model because the one associated with the standard NREL 5-MW reference wind turbine was no longer applicable. To begin the process, new coefficients of lift and drag for the airfoils of Table 31 at various angles of attack were generated by building a model of the airfoils in XFOIL, a high-order, viscous-analysis panel code (Drela 1989). The resulting lift and drag curves were then processed using NREL's AirfoilPrep tool (Hansen, 2012) to expand the data over the entire 360° range of possible angles of attack required by FAST. This produced simulation results that correlated poorly to model test data because of the questionable applicability of XFOIL solutions for

the separated flows experienced in the tested model wind turbine. Hence, the XFOIL lift and drag curves for the airfoils were parameterized and tuned using multi-objective genetic algorithm optimization techniques (e.g. see (Deb, 2001)) to simultaneously minimize the error between FAST simulations and test data curves for the wind turbine thrust and power as a function of rotor speed under a steady hub height wind speed of 21.80 m/s. Options utilized in FAST for the optimization included disabled dynamic stall, elimination of the pitching moment model, selection of the swirl equilibrium inflow model, and selection of the Prandtl tip- and hub-loss models.[1] The air density was taken to be 1.225 kg/m^3. The wind profile generated in the wind/wave basin used a simple wind file, which contained one hub-height wind speed for steady winds and a time-series of varying wind speeds for dynamic winds studied later in this work. To best represent this wind profile, the measured hub height wind speed was multiplied by a factor of 0.952 and a vertical power law wind shear exponent of 0.0912 was employed. These parameters yielded the best comparison between measured hub-height wind speeds and information gleaned from spatial surveys of the wind generation machine output used for testing. Details of the wind machine surveys can be found in (Goupee *et al*., 2012 OTC) and (Koo *et al*., 2012. Regarding parameterization of the airfoil coefficients, variables were introduced that permitted perturbations of lift curve slope and zero-lift angle of attack, as well as more moderate alterations of the lift curve stall point, lift curve post-stall behavior, and general nature of the drag coefficients. Because the multi-objective optimization generated several pareto-optimal solutions, a solution was chosen for use in the numerical model that exhibited nearly identical thrust behavior to the test model and a reasonably fair prediction of wind turbine power. This bias towards more accurately capturing the thrust response is due to the aforementioned fact that wind turbine thrust is the aerodynamic driver in global motion and load response.

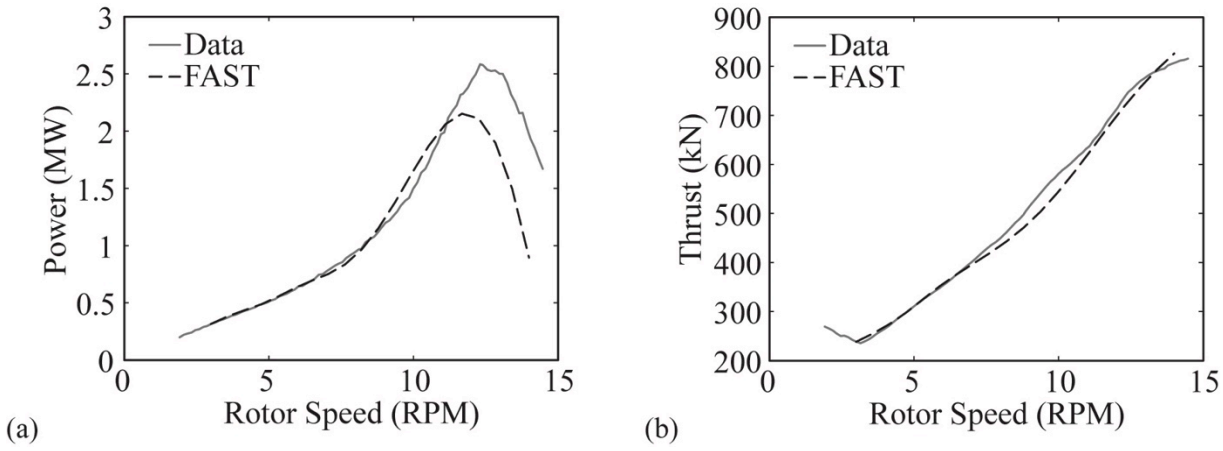

Figure 75: Comparison of calibrated FAST and tested wind turbine performance as a function of rotor speed for (a) rotor power and (b) thrust under steady 21.80-m/s winds.

Table 37: Comparison of calibrated FAST model and tested wind turbine thrust.

Mean Wind Speed (m/s)	Rotor Speed (RPM)	Tested Thrust (kN)	FAST Thrust (kN)
7.32	4.95	126.1	102.6
8.94	5.66	156.9	143.4
11.23	7.78	202.7	247.2
16.11	9.19	381.7	413.0
21.80	12.73	749.8	779.3
30.50	0	156.8	153.2

A comparison of the calibrated FAST and model test wind turbine performance is given in Figure 75. In addition, Table 37 shows the thrust values corresponding to the steady wind cases of Table 32. As can be seen in Figure 75 and Table 37, the thrust behavior that is critical for properly simulating global response is captured very well by the calibrated FAST wind turbine model. In addition, the range of thrust values captured during testing is very similar to the true NREL 5-MW reference wind turbine with peak thrust loads in the neighborhood of 800 kN, as shown in Table 37. It should be noted that the peak thrust load occurs at a different wind speed for model-scale compared to an ideal full-scale wind turbine because of the inherently low Reynolds numbers seen at model-scale. The aerodynamic lift ($\boldsymbol{C_L}$) and drag ($\boldsymbol{C_D}$) coefficients corresponding to the calibrated wind turbine model for the airfoil sections noted in Table 31 are given in Figure 76. For the Cylinder section, the lift coefficient was set to 0.0 and the drag coefficient to 1.0 for all angles of attack.

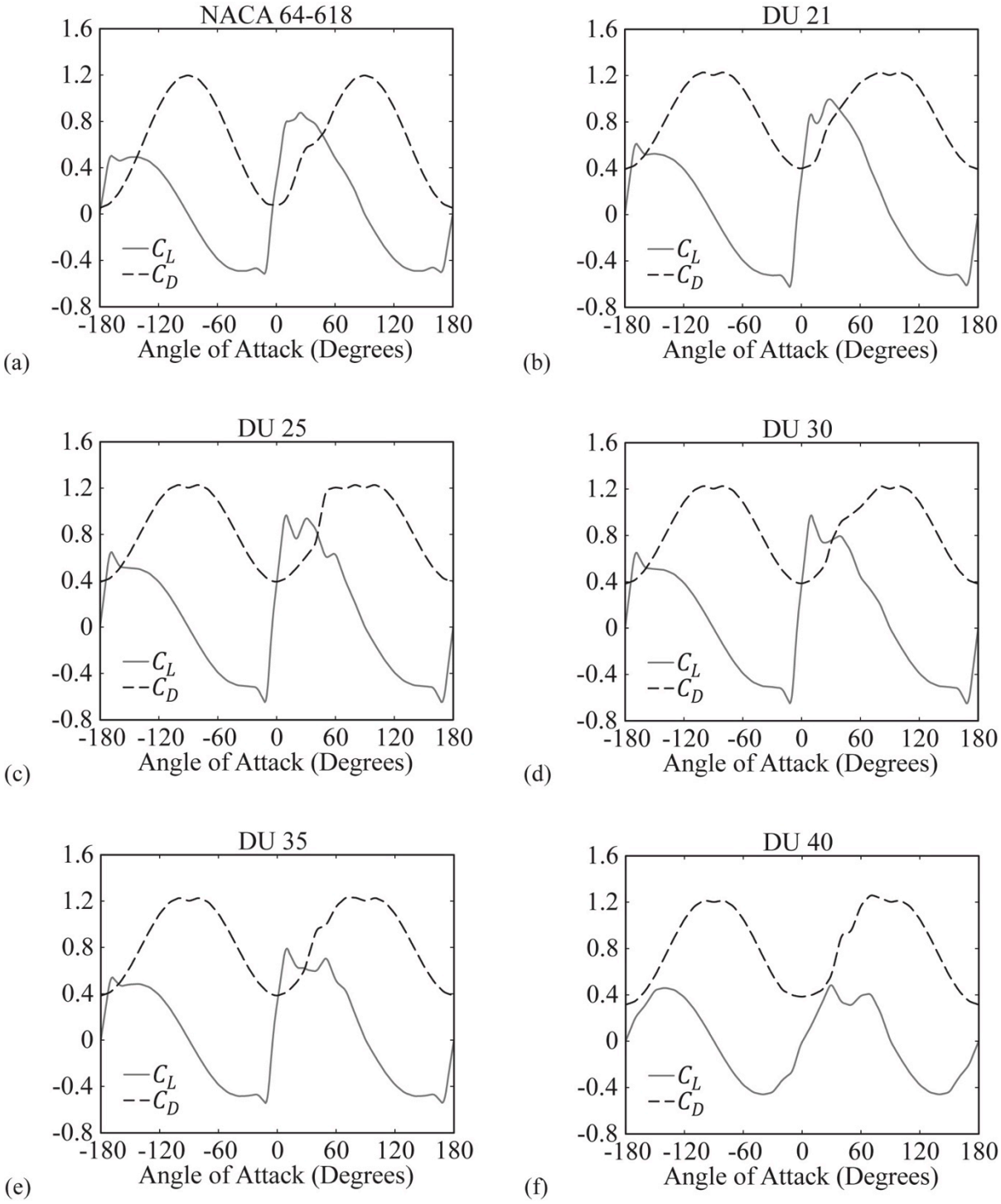

Figure 76: Plots of airfoil lift and drag coefficients at low Reynolds number for (a) NACA 64-618, (b) DU 21, (c) DU 25, (d) DU 30, (e) DU 35 and (f) DU 40 airfoils for the tuned FAST aerodynamic model.

5.1.2.2 Tower Mode Shapes and Frequencies

To model tower flexibility, FAST's modal representation requires the first two elastic bending mode shapes for both the fore-aft and side-side tower-bending DOF. Factors that influence the tower vibration mode shapes include distributed tower mass and stiffness properties, tower-top mass properties, gravity, floating foundation mass, added-mass, hydrostatic stiffness, and mooring stiffness properties.

To estimate these mode shapes, a simple custom finite-element tool was developed that employed three-dimensional Euler-Bernoulli beam elements (e.g., see (Cook *et* al., 2002)) to discretize the tower. After inputting the aforementioned distributed tower, turbine mass, platform mass, and stiffness properties, the finite-element system mass and stiffness matrices were constructed and the eigenvalue problem was solved using standard techniques. The appropriate first and second bending mode shapes for the fore-aft and side-side tower-bending DOF were extracted, and normalized ninth-order mode shapes were constructed for input into FAST. The mode shapes are plotted in Figure 77. The higher-order polynomials were employed because the standard sixth-order polynomials do not accurately capture the finite-element-estimated mode shapes resulting from the multiple discontinuities in the distributed tower properties.

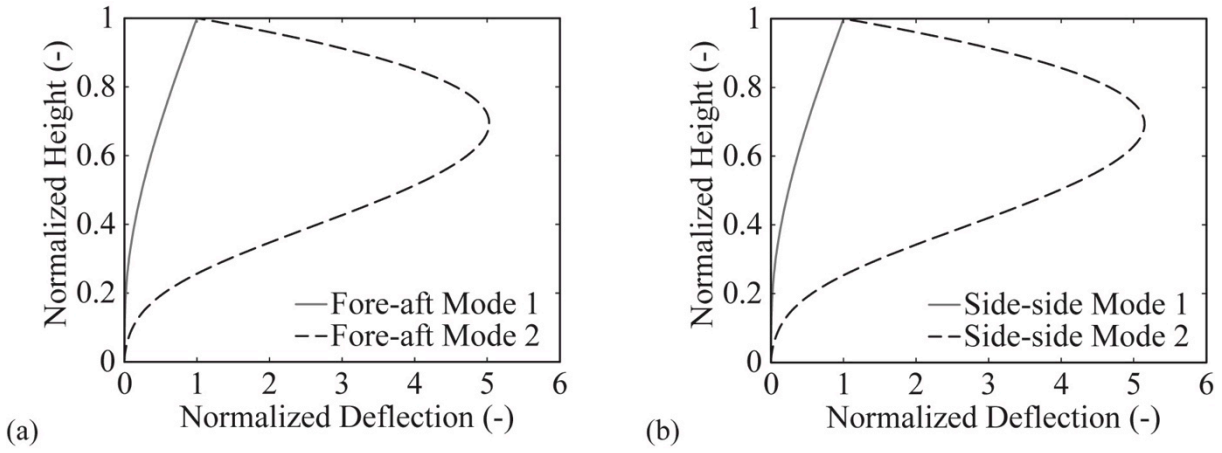

Figure 77: Plots of the FAST normalized ninth-order tower mode shapes for (a) fore-aft and (b) side-side bending DOF.

Upon inserting the mode shapes into the FAST model and running a linearization analysis to determine the tower-bending frequencies (Jonkman and Buhl, 2005), it was found that the finite element and FAST tower frequencies were in relative agreement. However, the FAST fundamental tower-bending frequencies were approximately 10% higher than measured from hammer tests conducted on the DeepCwind semi-submersible. While it is unknown why the discrepancy occurred, it could be due to, for example, a greater compliance between the tower base and floating platform connection for the DeepCwind semi-submersible. Another possibility is that the DeepCwind semi-submersible was the last specimen tested and that the base, mid-tower, and top joints on the tower could have relaxed or loosened slightly after weeks of double-shift, repeated testing. In any event, the tower stiffness properties of

Table 34 were reduced by 21.0% to better match the test data. The individual fore-aft and side-side fundamental tower-bending natural frequencies were fine tuned to match test data by adjusting FAST's modal stiffness tuners. The final stiffness tuner values used in fore-aft and side-side DOFs were 0.905 and 1.049, respectively. After final calibration of the tower stiffnesses, the FAST fore-aft

and side-side tower-bending frequencies match experimental measurements and are 0.35 Hz and 0.38 Hz respectively.

In addition to mode shapes, FAST also requires damping ratios for each of the tower bending modes. The damping ratios of the tower-bending modes were estimated using the half-power bandwidth method (e.g., see (Bendat and Piersol, 1980)) in conjunction with acceleration records from hammer tests. A value of 2.1% was determined for first mode fore-aft and side-side structural damping, and a value of 1.5% was determined for second mode fore-aft and side-side structural damping.

5.1.2.3 Hydrodynamic Viscous Damping

For the DeepCwind semi-submersible platform, flow-separation-induced drag is a large component of the total hydrodynamic damping. As such, the linear time-domain radiation damping included in FAST was augmented with a quadratic damping model that captures the effects of this viscous damping. The platform viscous damping forces and moments, F_i^v, are computed as

$$F_i^v = -B_{ij}^v \dot{q}_j \left|\dot{q}_j\right|, \quad i,j = 1,2,\ldots,6,$$

where B_{ij}^v are the quadratic damping coefficients, q_j are the six rigid-body DOF located at the waterline, and a superimposed dot indicates the first time derivative. This model assumes no directional coupling of drag terms, so only diagonal terms of B_{ij}^v are nonzero.

The coefficients B_{ij}^v were determined using the rigid-body motion free-decay tests conducted in the wind/wave basin. Simulation free-decay results for each of the six platform degrees of freedom were tuned by varying B_{ij}^v for each DOF until fair agreement existed between FAST and the test data. The free-decay test data was also employed to estimate the additional global surge stiffness provided by the cable bundle shown in Figure 71. The computed additional surge stiffness is 7.39 kN/m and was employed in all subsequent numerical experiments. The derived global drag coefficients are given in Table 38. A comparison of the FAST predictions and test data for free-decay damping ratio response is given in Figure 78 for platform surge, heave, and pitch DOF. The free-decay damping ratios are presented as the damping ratio over one cycle as a function of initial cycle amplitude. As can be seen in the figure, the overall nonlinear hydrodynamic damping behavior is captured very well for small to moderate amplitude oscillations. For large amplitudes, the quadratic damping model employed here over-predicts heave and pitch damping and under-predicts surge damping.

Table 38: Platform quadratic drag coefficients.

DOF	Global Quadratic Coefficient
Surge	1.25×10^6 Ns^2/m^2
Sway	0.95×10^6 Ns^2/m^2
Heave	3.88×10^6 Ns^2/m^2
Roll	3.35×10^{10} Nms^2/rad^2
Pitch	3.35×10^{10} Nms^2/rad^2
Yaw	1.15×10^{10} Nms^2/rad^2

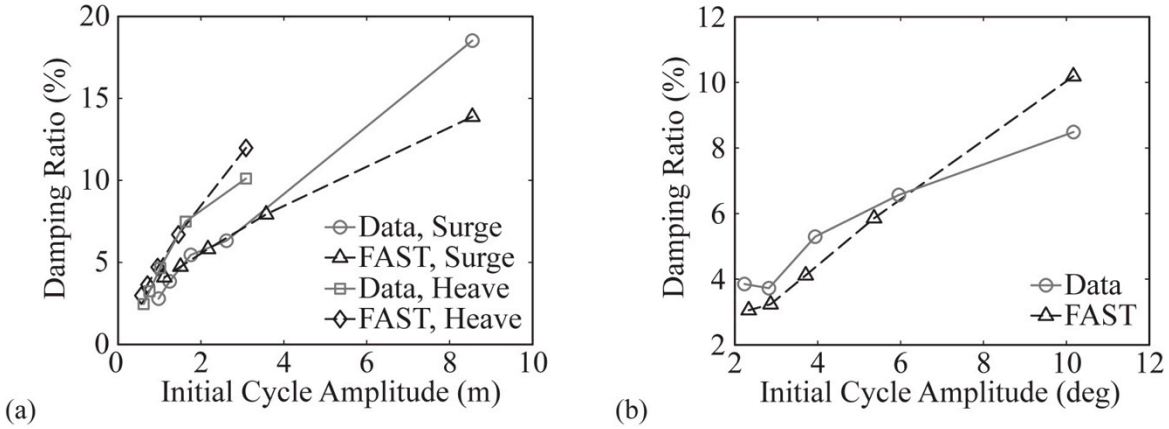

Figure 78: Comparisons for FAST prediction and test data free-decay damping ratios for (a) surge and heave as well as (b) pitch DOF.

5.1.2.3 Mooring Restoring Forces

Unlike the previously discussed quantities in this calibration section, the mooring system parameters were not tuned in order to reconcile differences in system restoring forces between FAST and the test data. In fact, the mooring module in FAST was utilized to set the target global restoring forces for the model test, and the physical model was tuned to reach these targets. The physical mooring system that was tested, which was full length and not truncated, utilized chain that yielded the correct mooring line wet weight with carefully selected springs placed at the anchors to capture the appropriate extensional stiffness of the mooring line. A comparison of mooring restoring in surge and sway DOF for both FAST simulations and test results are given in Figure 79. As can be seen in the figure, there is excellent agreement between the simulation and test data. There is further evidence that the numerical model mooring system stiffness is correct; in addition to hydrostatic stiffness, system mass, and added-mass, a comparison of FAST simulation and tested rigid-body motion natural periods is given in Table 39. As the table shows, the agreement between the simulation and test data is excellent.

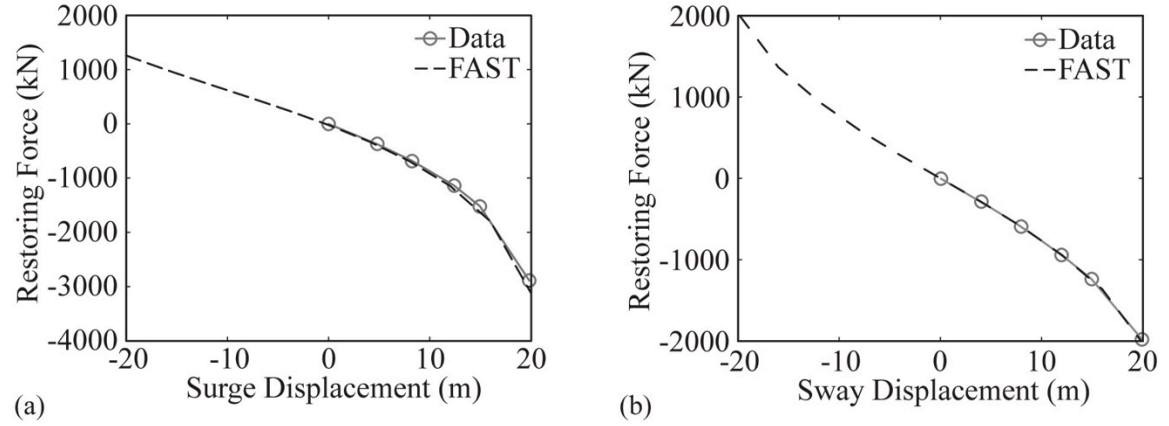

Figure 79: Comparisons for FAST prediction and test data for (a) surge mooring restoring force and (b) sway mooring restoring force.

Table 39: Comparison of FAST prediction and test data for the six rigid-body motion natural periods.

DOF	FAST (s)	Data (s)
Surge	107	107
Sway	113	112
Heave	17.3	17.5
Roll	26.7	26.9
Pitch	26.8	26.8
Yaw	82.7	82.3

5.1.3 Model Validation

In this section, the output of the calibrated FAST model from Section II will be compared to wind/wave basin model test data for the DeepCwind semi-submersible. Cases that are considered include steady wind only, dynamic wind only, free-decay under steady wind, regular waves only, irregular white noise waves only, and lastly, combined dynamic wind and irregular wave conditions. This systematic approach allows for an easier identification of root causes for discrepancies between test data and FAST simulations. This noted, the results highlight the many merits of FAST's predictive capabilities in addition to potential shortcomings in the test data, as well as possible areas of improvement for FAST. Lastly, it should be noted that all the relevant global motion results presented in subsequent sections are given with respect to the center of gravity of the total system. The FAST global motions results are initially obtained at the waterline and have been transformed accordingly.

5.1.3.1 Steady Wind Only

Simulations of the DeepCwind semi-submersible platform subjected to the six steady wind environments noted in Table 32 were conducted and compared to model test data. All winds were directed along the positive surge direction. As was done in the calibration portion for tuning wind turbine aerodynamics, the steady wind files required for simulation were produced by multiplying the mean hub height wind speed of Table 32 by 0.952 and using a wind shear coefficient of 0.0912. The metric targeted for comparison between simulation and test data was the steady-state solution. While the model test cases were run for one hour, the FAST simulations results were terminated at 2000 seconds because any significant transient global motions had diminished well in advance of this time.

For these particular loading scenarios, responses associated with surge and pitch motion receive the most excitation. As such, the mean platform surge and pitch angle are presented in Figure 80, as are the tower base fore-aft bending moment and mooring line 2 fairlead tension. As can be seen in the figure, the comparison between the simulation and test data is quite favorable. One obvious trend shown in the figure is that FAST appears to under-predict the mean surge offset with the largest discrepancies, from a percentage point of view, occurring at low operational winds and at the highest wind speed where the blades are feathered and the rotor is parked. For these aforementioned conditions, the thrust load on the rotor is low and aerodynamic drag loads on the tower, floating platform, and instrumentation cable bundle, which are not included in this FAST model, may be contributing a substantial portion to the total overall system surge force. Because the comparison between FAST and the test data is quite good with regard to tower-base fore-aft bending moment, it is likely that the largest contribution is additional aerodynamic drag on the platform.

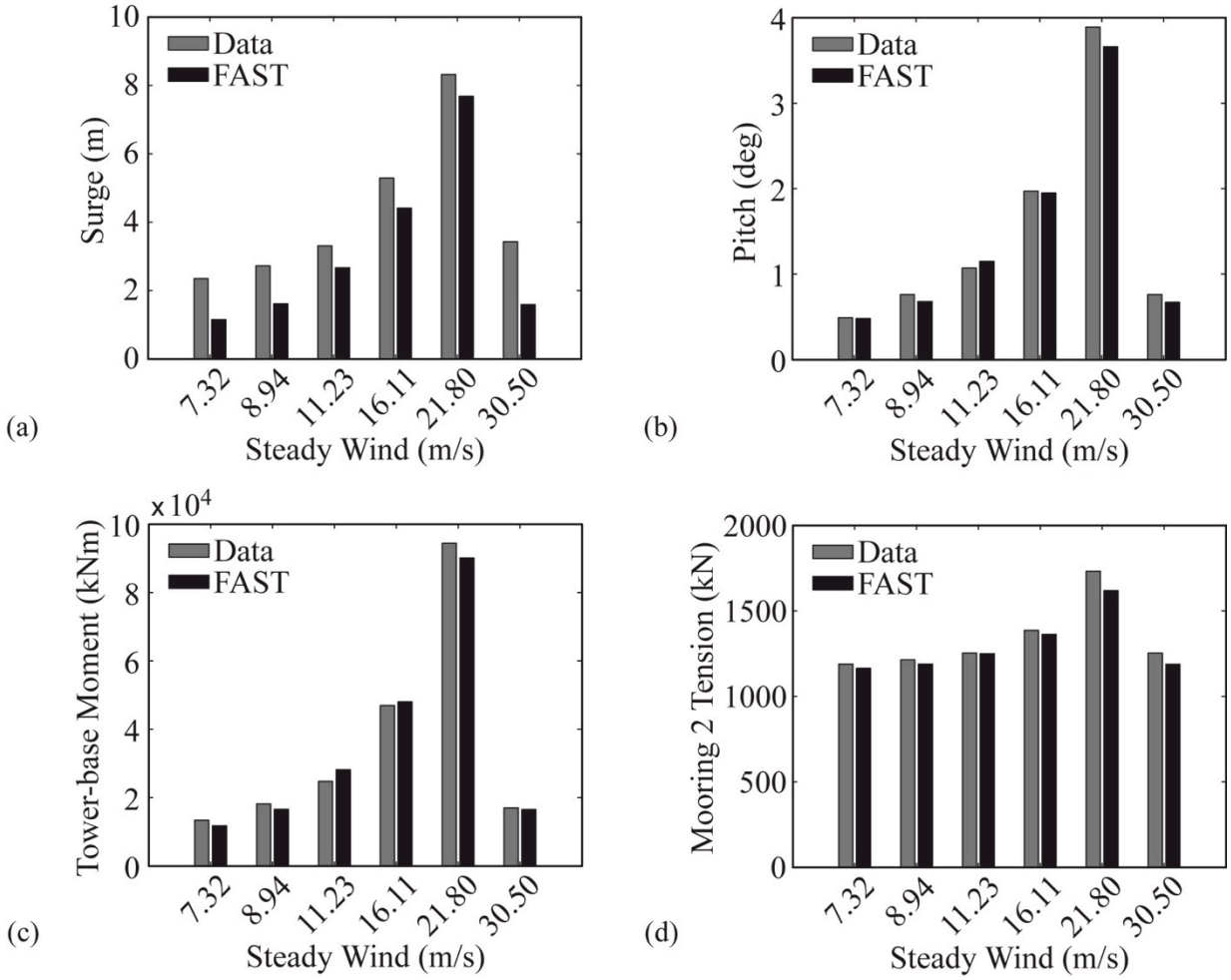

Figure 80: Comparison of simulation and test data steady-state response under steady winds for (a) surge, (b) pitch, (c) tower-base fore-aft bending moment and (d) mooring line 2 fairlead tension.

In addition, this situation is exacerbated by the fact that the low rotor thrust coefficient, resulting from poor airfoil performance (Martin *et* al., 2012) at the low test Reynolds numbers, required higher wind speeds to produce an equivalent full-scale rotor thrust, thus creating greater drag on non-rotor structures (e.g., the platform) than would be seen in a true full-scale system. Lastly, the surge-restoring stiffness is in general quite low, yielding significant discrepancies in surge position despite only small differences in total system surge loading. As an example, even in the 30.5-m/s case where the worst discrepancy occurs, the 1.84-m difference in predicted surge position is caused by a relatively small 140-kN difference in overall system surge loading. Unlike the total system surge loading, the system overturning moment leading to pitch and tower bending moment response is dominated by the rotor, because it is higher above the SWL than the center of pressure for the tower, cable bundle, or platform. The FAST rotor thrust is fairly well predicted as a result of the calibration shown in Figure 75, so it stands to reason that the simulation and test data pitch responses are very similar in Figure 80. In addition, while the agreement for mean pitch offset is good, there is an under-prediction by FAST that is consistent with the simulation, ignoring the aforementioned, additional aerodynamic drag loads.

5.1.3.2 Steady Wind Free-decay

As the second phase of model validation, the ability of FAST to capture the wind turbine rotor's aerodynamic damping forces is assessed. This was evaluated by simulating free-decay while the wind turbine was operating in a steady wind, with no waves, and comparing the motion response between FAST simulations and test data. The surge and pitch platform DOF, which are most affected by aerodynamic forces on the wind turbine, are the focus of this section.

For the two free-decay scenarios investigated, the wind turbine was subjected to the third smallest steady wind from Table 32. Consistent with the treatment of the wind in previous simulations, the steady wind file was generated by multiplying the experimentally measured 11.23-m/s wind by 0.952 and utilizing a 0.0912 wind shear exponent. Recall that this was done to best replicate the experimental wind velocity distribution using only a single, steady wind file. A comparison of the simulation and test data surge and pitch motion damping ratios as a function of initial cycle amplitude is given in Figure 81 for the no-wind and 11.23-m/s wind cases.

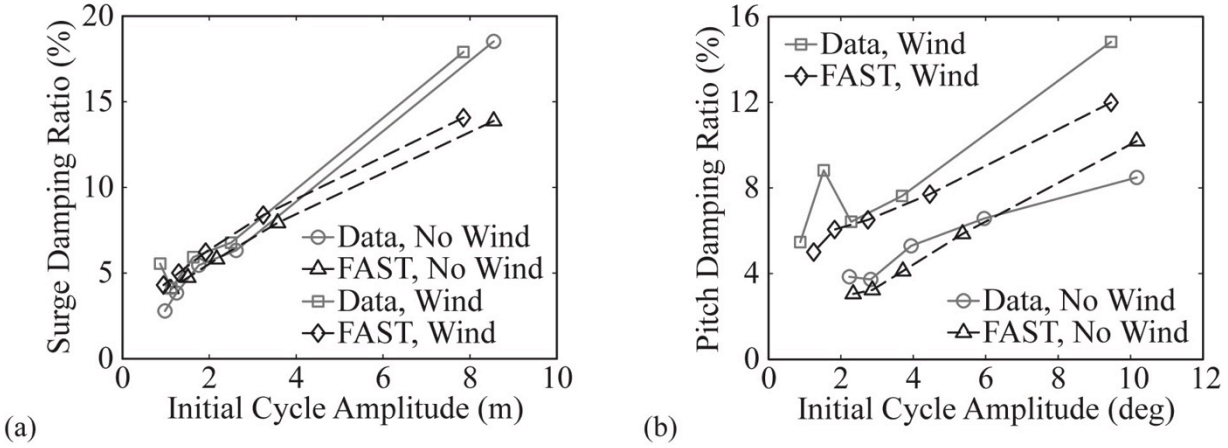

Figure 81: Comparison of simulation and test data damping ratios for (a) surge and (b) pitch motion for no wind and 11.23-m/s steady wind cases.

For both surge and pitch free-decay, regardless of the wind condition, the comparison between FAST and the test data is quite good overall, especially for small to moderate motion amplitudes. More importantly, FAST accurately captures the additional motion damping, approximately 1% in surge and 3% in pitch for this scenario, provided by the operating wind turbine in steady winds.

5.1.3.3 Dynamic Wind Only

To complete the wind only comparisons, the response of the DeepCwind semi-submersible subjected to a strong, dynamic wind in the absence of waves was simulated and compared to experimental data. The wind field, which was temporally dynamic, followed a National Petroleum Directorate (NPD) spectrum (API, 200) and was oriented along the positive surge direction. In the wind/wave basin, the temporally dynamic NPD wind possessed a mean wind speed at hub height of 20.6 m/s, a standard deviation of 2.04 m/s, a maximum wind speed of 28.7 m/s, and a minimum wind speed of 12.9 m/s. A power spectral density (PSD) plot of the wind time-series, which was three hours in length, is given in Figure 82.

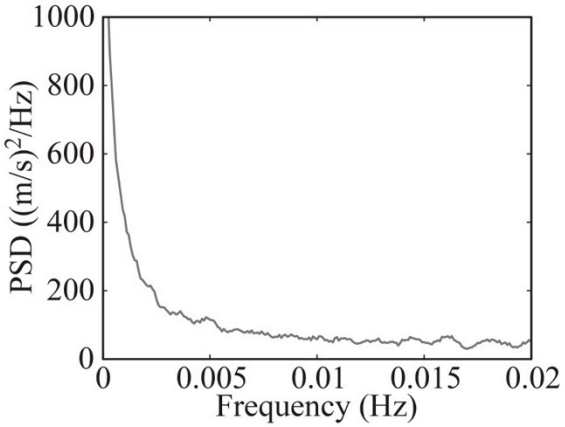

Figure 82: PSD plot for NPD wind spectrum with mean wind speed of 20.6 m/s at 90 m above SWL.

For simulation, a dynamic wind file was created in the usual manner by multiplying the recorded hub height wind velocity time history by 0.952 and utilizing a wind shear exponent of 0.0912 to better represent the measured spatial distribution of wind generated during testing. This yielded winds for simulation with a mean of 19.6 m/s, a standard deviation of 1.94 m/s, a maximum of 27.4 m/s, and a minimum of 12.3 m/s at the hub-height location (90 m above SWL).

A comparison of the FAST predictions and experimental data for platform pitch and mooring line 2 fairlead tension is given in Figure 83 and Figure 84. Figure 83 provides comparisons via PSDs, while Figure 84 displays sample time-series comparisons. As can be seen in Figure 83, the PSD comparison is fair for platform pitch with similar total energy; however, the FAST response is more peaked at the platform natural pitch frequency (0.037 Hz) with less response at frequencies immediately above this particular point. Despite this difference in platform-pitch PSD response, Figure 84 shows good agreement between the FAST simulation and test data time-series consistent with the steady state offset findings in Figure 80.

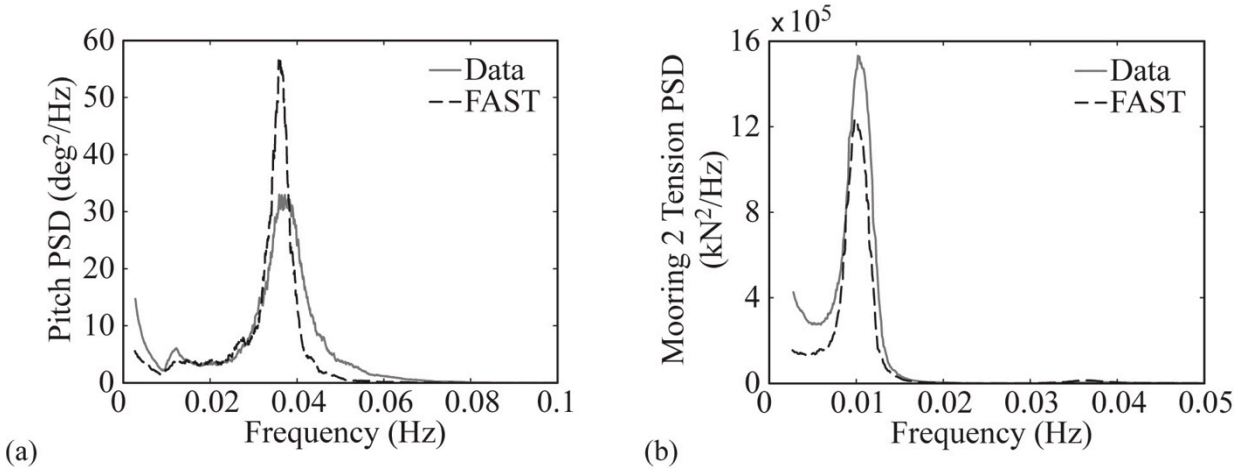

Figure 83: Comparisons of PSDs from FAST and test data for (a) pitch and (b) mooring line 2 fairlead tension for a dynamic wind-only case with a mean hub-height wind speed of 20.6 m/s.

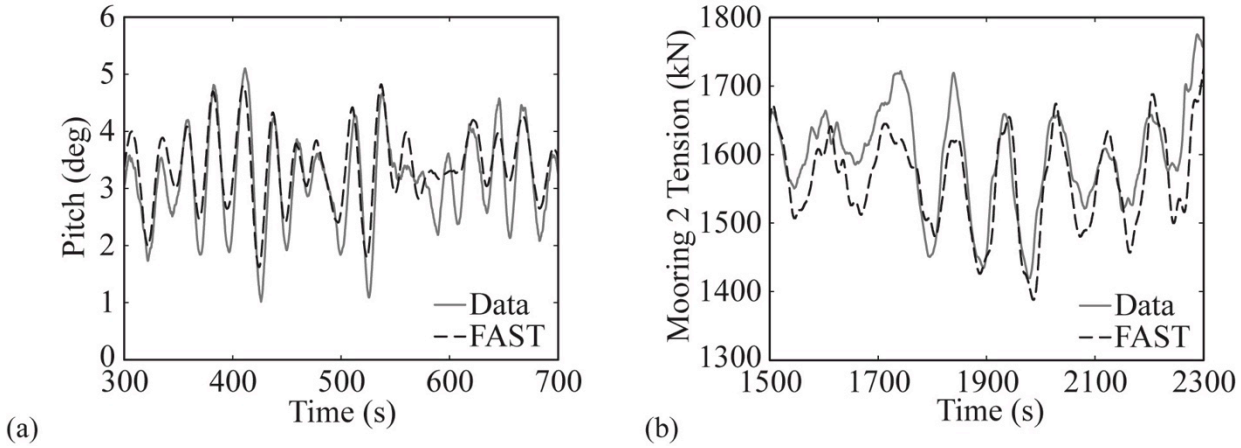

Figure 84: Comparisons of time-series from FAST and test data for (a) pitch and (b) mooring line 2 fairlead tension for a dynamic wind-only case with a mean hub-height wind speed of 20.6 m/s.

Regarding the mooring line 2 fairlead tension, the PSD and time-series comparisons given in Figure 83 and Figure 84, respectively, are also quite favorable. While there was good agreement, FAST generally produces slightly less response for both the PSD and time-series.

In addition to sample PSD and time-series, Table 40 provides statistical comparisons of the FAST simulation and test data for field variables that experience significant excitation for this dynamic wind-only condition. After a review of Table 40, it is clear that the surge, pitch, tower-base bending moment and mooring line 2 fairlead tension statistics are in very good agreement between FAST and the test data. Of all the comparisons provided, the largest difference is for the platform surge with FAST predicting the maximum value to be 8.54% smaller than the true value. However, the mean platform surge is accurately predicted.

Table 40: Comparison of FAST prediction and test data statistics for a dynamic wind-only case with a mean hub height wind speed of 20.6 m/s.

DOF	Source	Mean	Std. Dev.	Maximum	Minimum
Surge (m)	FAST	7.22	0.93	9.96	4.07
	Data	7.26	1.18	10.89	3.64
Pitch (deg)	FAST	3.43	0.69	5.45	0.97
	Data	3.34	0.67	5.65	1.04
Fore-Aft Bending (kNm)	FAST	8.45×10^4	1.12×10^4	12.21×10^4	3.66×10^4
	Data	8.09×10^4	1.17×10^4	11.84×10^4	4.03×10^4
Fairlead 2 Tension (kN)	FAST	1.58×10^3	0.075×10^3	1.83×10^3	1.35×10^3
	Data	1.64×10^3	0.094×10^3	1.96×10^3	1.36×10^3

5.1.3.4 Regular Waves Only

To begin the validation of FAST to test data due to wave excitation, the response of the DeepCwind semi-submersible platform to regular waves in the absence of wind was investigated. Since there was no wind, the blades were feathered and the rotor was parked. Seven different regular waves were considered, the amplitudes and periods of which are given in Table 41. All waves propagated in the positive surge direction.

Table 41: Regular wave amplitudes and natural periods.

Amplitude (m)	Period (s)
0.96	7.5
3.79	12.1
3.57	14.3
3.79	20.0
5.15	12.1
5.37	14.3
5.56	20.0

It should be noted that two distinct amplitudes were investigated for periods of 12.1, 14.3, and 20.0 seconds for the purpose of assessing any nonlinearity in system response. The DeepCwind semi-submersible platform performance in the presence of regular waves is characterized by response amplitude operators (RAO) magnitudes, which normalize the amplitude of a periodic response of a field variable by the amplitude of the regular wave. In both the time-domain simulation and model test, the RAO values were computed from the nearly harmonic, steady-state response. For FAST, simulations were run for 1600 seconds to achieve the desired steady-state result.

The RAO magnitudes for surge, heave, pitch, tower-base fore-aft bending moment, and fairlead tension for mooring lines 1 and 2 are given in Figure 85 for the seven regular waves investigated. Many of the comparisons in Figure 85 are quite good, as evidenced by FAST's ability to capture the increase in normalized pitch response for a given wave period with increasing wave amplitude. However, there are some notable discrepancies between the FAST simulation and test data. First, the FAST simulation modestly under-predicts the heave RAO for the two 20.0-s cases investigated. Because this period is in close proximity to the DeepCwind semi-submersible's heave natural period (causing some resonance), the normalized response will be sensitive to system damping. The discrepancy is likely a result of the quadratic damping model employed in this study, which over-predicts the damping in large amplitude heave scenarios at the expense of properly modeling the damping for small to moderate motions. The second discrepancy, which is very significant, is the mooring line fairlead tensions, especially for mooring line 2, which is aligned with the wave propagation direction. For the worst scenario, the 5.56-m amplitude, 20.0-s regular wave, the FAST mooring line 2 fairlead tension RAO is only 13.4% of the test data value. It is suspected that this is caused by the exclusion of dynamic mooring line effects in the simulation, because FAST employs a quasi-static mooring solver. Further investigation would be required to confirm this hypothesis.

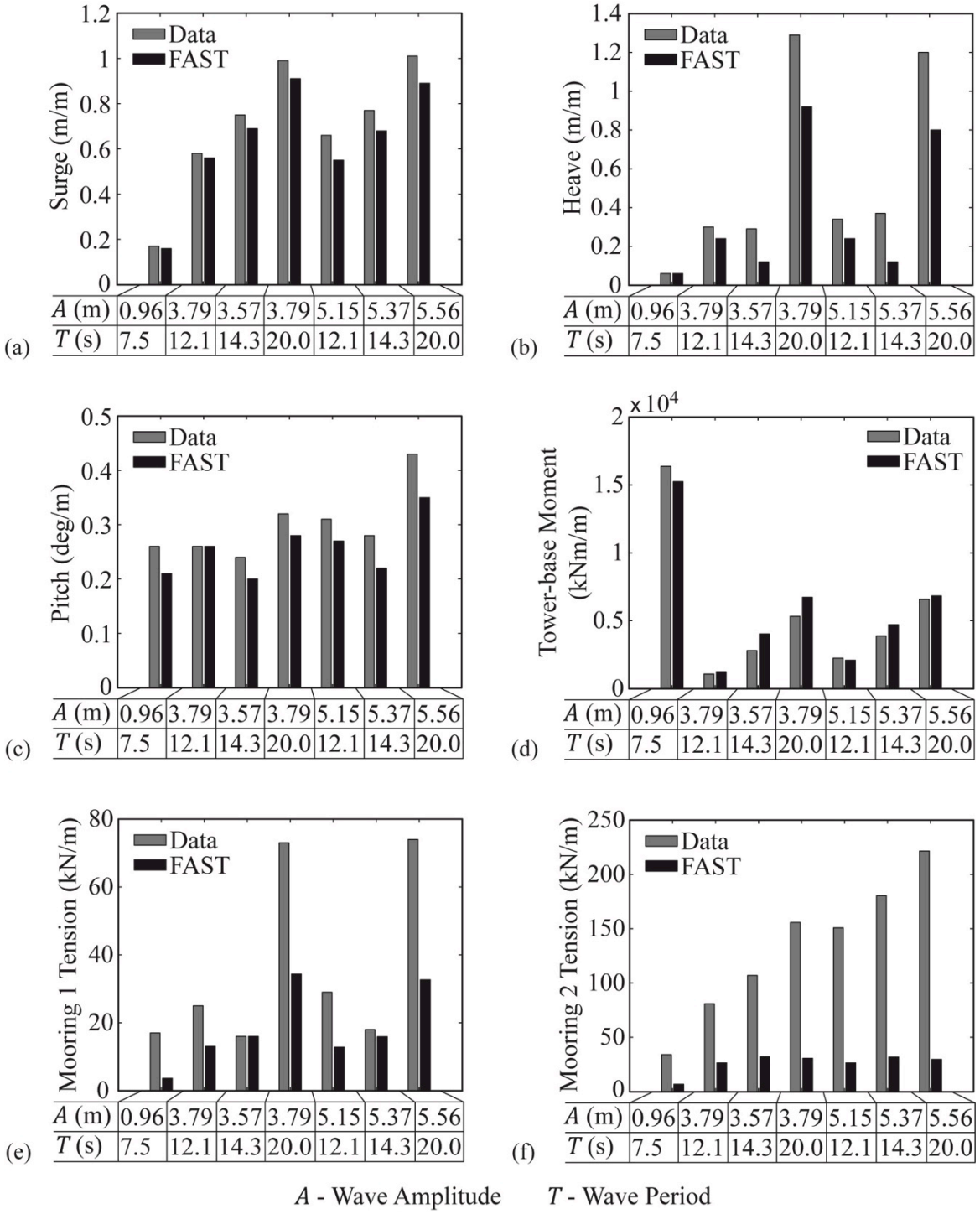

Figure 85: Comparisons of RAOs from FAST and test data for (a) surge, (b) heave, (c) pitch, (d) tower base fore-aft bending moment, (e) mooring line 1 fairlead tension and (f) mooring line 2 fairlead tension.

5.1.3.5 Irregular Waves Only

To continue the validation study, the behavior of the DeepCwind semi-submersible platform subjected to a severe irregular wave in the absence of wind was simulated with the calibrated FAST

model, and the simulation results were compared to test data. There was no wind, so the blades were feathered and the rotor was parked. The wave that was investigated possessed a broad-band, white noise spectrum, shown in Figure 86, with a significant wave height of 11.3 m.

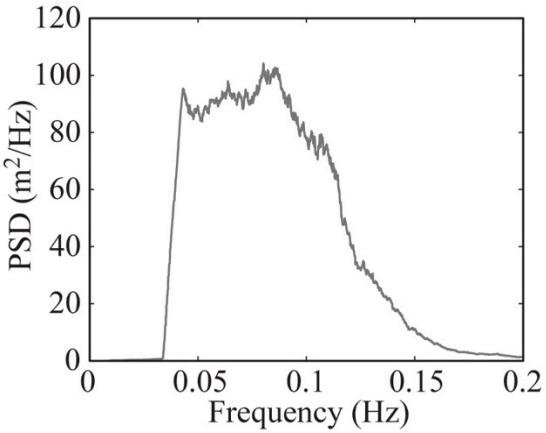

Figure 86: PSD for 11.3 m significant wave height white noise wave.

This significant wave height is in excess of that corresponding to a 100-year event in the Gulf of Maine (University of Maine, 2011). The wave propagated along the positive surge direction. For the 3-hr wave, the maximum crest was 12.8 m, the minimum trough was -11.0 m, and the maximum wave height was 21.5 m. The broad-band spectrum utilized here is advantageous for computing RAOs as well as for amplifying, and thus highlighting, the floating wind turbine's response to second-order wave diffraction forces (e.g., see (Kim and Yue, 1991)). To make the comparison between FAST and the model test data a fair one, a modified version of FAST was employed that could compute the linear wave diffraction forces directly from the tested wave-elevation time-series.

The first results shown are the FAST simulation and test data RAO magnitude and phase angles for the surge, heave, and pitch DOF in the wave energy range (5 to 25 seconds). The plots, given in Figure 87, show that the motion RAO magnitudes are for the most part quite good. The same cannot be said, however, of the phase angles in general. This could be a result of the wave measurement, which was located at the undisplaced position, not coinciding with the true position of the platform as a result of mean drift forces. Regarding the RAO magnitudes, the worst discrepancy between FAST and the test data occurs in the heave DOF for periods near the resonant system heave period of 17.5 seconds, with FAST modestly under-predicting the heave response. This observation is consistent with those made for the regular waves investigated.

To further assess FAST's hydrodynamics abilities, PSD comparisons are presented in Figure 88 for surge, heave, tower-base fore-aft bending moment, and mooring line 2 fairlead tension. Referring to the surge comparison in Figure 88, it is clear that FAST accurately captures the response in the wave energy range (0.04 to 0.15 Hz); however, the prediction of the second-order difference-frequency associated response at the surge natural period of 0.0093 Hz is very poor. This is understandable because FAST neglects this aspect of the wave loading.

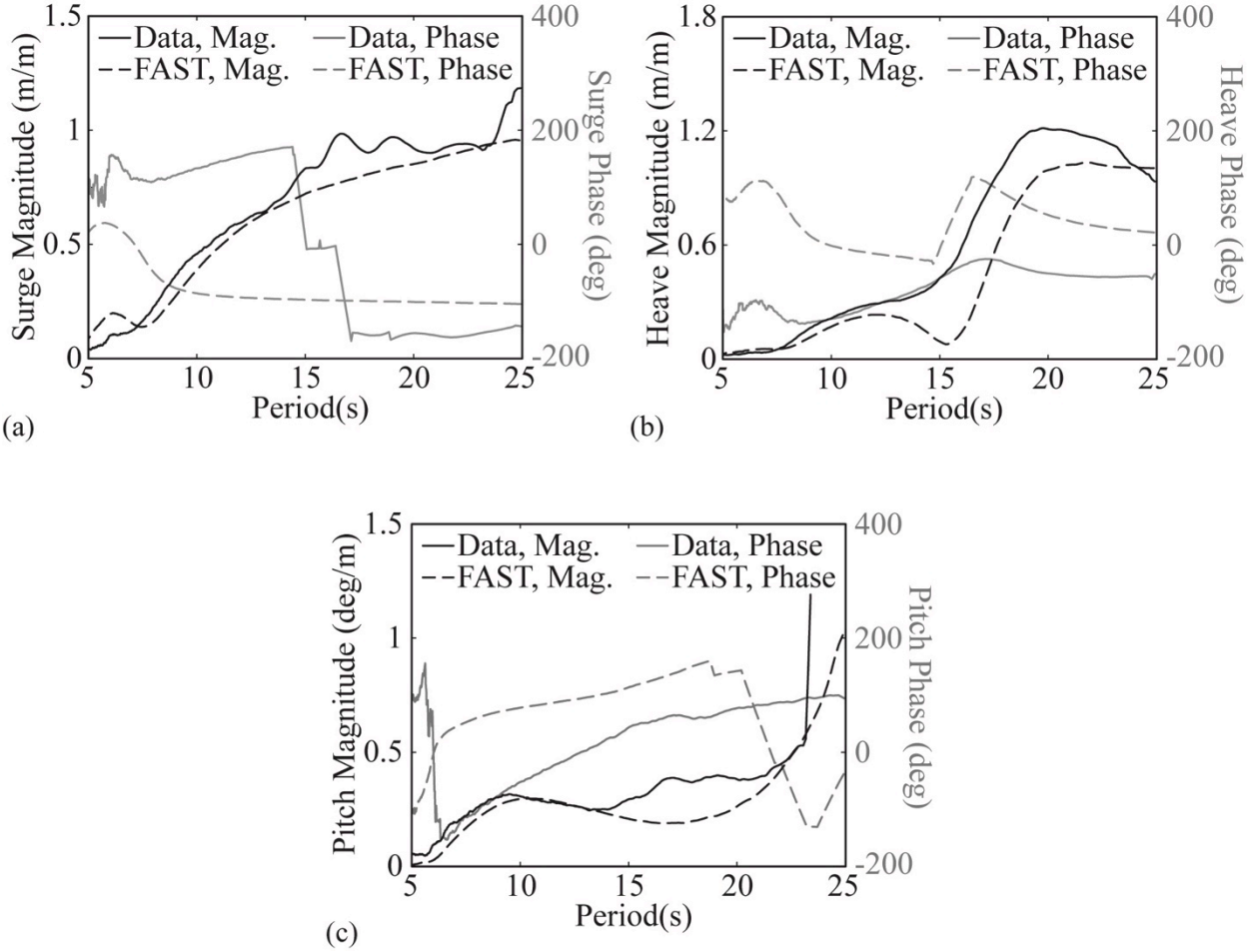

Figure 87: Comparison of RAO magnitudes and phase angles from FAST and test data for (a) surge, (b) heave, and (c) pitch.

Moving to the PSD of the tower-base fore-aft bending moment, it can be seen in Figure 88 that the comparison is fairly good between the FAST simulation and test data. FAST captures the large response at the platform-pitch natural period of 0.037 Hz, as well as the response in the wave-energy range. This stated, the response at the fore-aft fundamental tower bending frequency of 0.35 Hz is severely under-predicted. If the tower modal damping is reduced to negligible levels, the comparison between FAST and the test data at this frequency improves, capturing nearly one third of the measured response as opposed to less than 10% for the calibrated FAST model. Thus, a partial explanation for the difference may be a poor calibration of the tower modal damping. Another explanation is that second-order sum-frequency wave loads, neglected in FAST, may be sufficient to excite tower motion near the fundamental bending frequency. A further explanation for the large difference may be that dynamic loads from the instrumentation cables, which were attached to an automated following system, may be providing additional excitation of the tower that would not exist for commercial, field-deployed systems, and is not accounted for in this FAST model. The final PSD considered, the mooring line 2 fairlead tension, shows a large discrepancy between the FAST simulation test data over a broad range of frequencies.

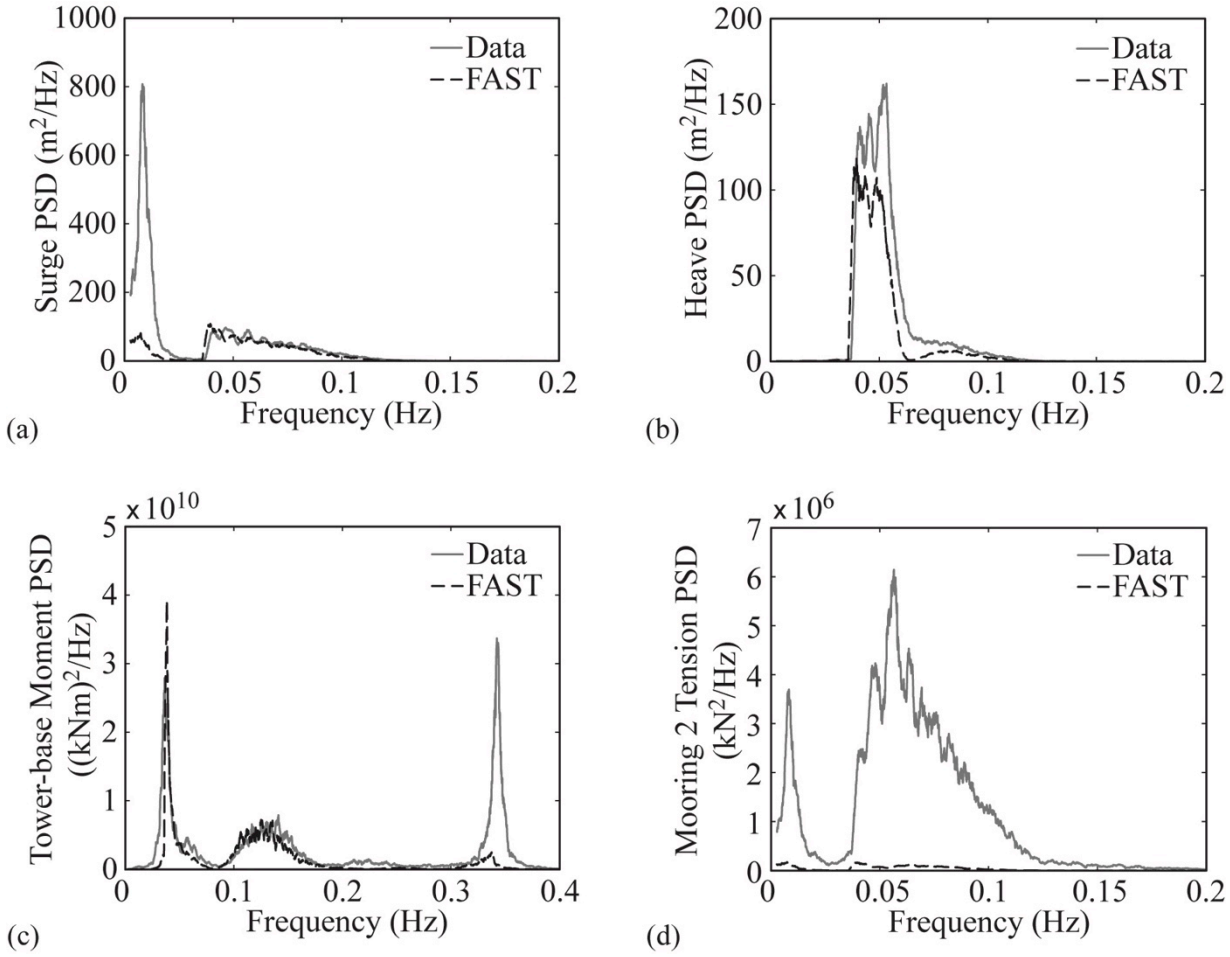

Figure 88: Comparisons of PSDs from FAST and test data for (a) surge, (b) heave, (c) tower-base fore-aft bending moment and (d) mooring line 2 fairlead tension for an irregular white noise wave only case with a significant wave height of 11.3 m.

As can be seen by comparing the surge and mooring tension PSDs in Figure 88, the relative difference between the FAST simulation and test data are nearly identical in the vicinity of the surge natural frequency of 0.0093 Hz.

This indicates that if FAST was able to account for the second-order, difference-frequency associated surge motion, it is likely that FAST's quasi-static catenary mooring line solver could capture the mooring tension behavior associated with slowly-varying drift motion. However, FAST's admirable performance with regard to emulating the correct surge motion response in the wave-energy range does not translate into accurate prediction of mooring tensions in the wave energy frequency range. As can be seen in Figure 88, the mooring line 2 fairlead tension dynamic response is grossly under-predicted by FAST. This clearly demonstrates that mooring line tension is not arising from platform motion alone and the sharp increase in mooring line 2 fairlead tension response in the wave energy frequency range is likely the result of dynamic mooring effects that are excluded in the FAST simulation. It is suspected that the inclusion of a more sophisticated, finite-element-method based dynamic mooring module (e.g., see (Garrett, 1982; Paulling and Webster, 1986)) into FAST might rectify much of the discrepancy between FAST and the test data for mooring tension response in the wave-energy frequency range.

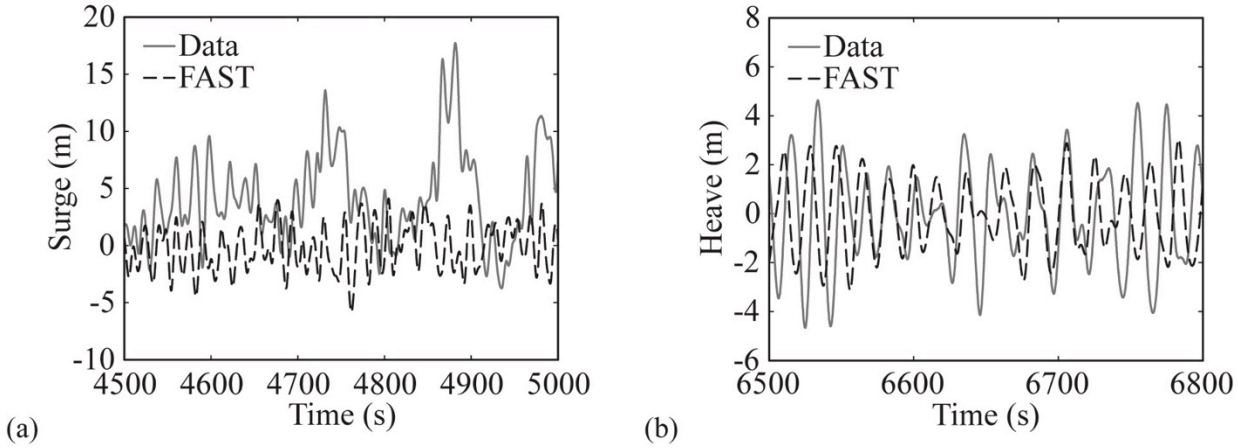

Figure 89: Comparisons of time-series from FAST and test data for (a) surge and (b) heave for an irregular white noise wave only case with a significant wave height of 11.3 m.

To complement previous results in the section, a comparison of FAST simulation and test data time-series for surge and heave motion is given in Figure 89. Turning to the surge time-series, it is clear that the higher frequency wave response is captured commendably by FAST; however, the mean drift and slowly-varying response of the real system is visibly ignored. This observation, consistent with previous statements, indicates that the inclusion of mean drift and second-order difference-frequency wave diffraction models into FAST would likely yield high quality hydrodynamic simulations. Moving to the second comparison, the heave time-series are similar in nature, with FAST occasionally under-predicting the magnitude of the heave motion excursion. This is consistent with the heave motion RAO and PSD previously presented. As noted earlier, this is most likely due to too much damping in the FAST model for heave motions with large amplitudes.

To complete this section, a comparison of the simulated and measured statistics for surge, heave, pitch, tower-base fore-aft bending moment, and mooring line 1 and 2 fairlead tensions is given in Table 42. It is observed from Table 42 that FAST under-predicts the standard deviation and range for the six field variables presented. Other key points worth noting include FAST's inability to predict the surge mean drift position and a maximum mooring line 2 fairlead tension that is only 26.7% of the measured value.

Table 42: Comparison of FAST prediction and test data statistics for an irregular white noise wave only case with a significant wave height of 11.3 m.

DOF	Source	Mean	Std. Dev.	Maximum	Minimum
Surge (m)	FAST	-0.14	2.01	8.09	-6.79
	Data	3.78	2.99	18.01	-4.41
Heave (m)	FAST	0.00	1.42	4.27	-4.17
	Data	-0.07	1.73	5.87	-6.50
Pitch (deg)	FAST	-0.01	1.20	4.83	-3.75
	Data	-0.02	1.55	6.94	-6.09
Fore-Aft Bending (kNm)	FAST	0.0×10^4	2.40×10^4	9.36×10^4	-10.53×10^4
	Data	0.16×10^4	3.31×10^4	19.89×10^4	-19.49×10^4
Fairlead 1 Tension (kN)	FAST	1111	60.05	1338	918.6
	Data	990.6	91.91	1403	431.8
Fairlead 2 Tension (kN)	FAST	1105	82.68	1541	879.5
	Data	1344	468.0	5774	95.25

This last discrepancy is in part due to FAST estimating insufficient surge motion, with the remainder likely due to a neglect of dynamic mooring effects. Nonetheless, many of the statistical comparisons are fair and differences between the FAST simulation and test data are in keeping with previous observations in this section.

5.1.3.6 Combined Dynamic Wind and Irregular Wave

To complete this validation study, a combined dynamic wind and irregular wave case of three hours in length was studied. The wave and wind were aligned and directed along the positive surge direction. The dynamic wind was the same as that described in Section IV, Subsection C. The wave considered was a 10.5-m significant wave height, 14.3-s peak spectral period wave based on a JONSWAP (IEC, 2009) spectrum, shown in Figure 90, with a shape parameter of 3.0.

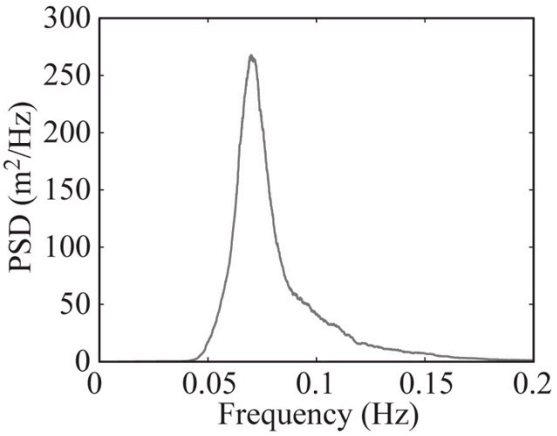

Figure 90: PSD for 10.5-m significant wave height JONSWAP wave condition.

This wave corresponds to a 100-year event in the Gulf of Maine (University of Maine, 2011). The wave condition possessed a maximum crest of 13.6 m, a minimum trough of -9.6 m, and a maximum wave height of 22.0 m. Unlike the white noise spectrum wave studied in the previous section, the JONSWAP wave considered here is more representative of a real sea condition. For comparison purposes, the custom FAST tool was again employed such that the wave diffraction forces could be computed based on the wave produced in the wind/wave basin during model testing. It is worth noting that while a sea condition of this magnitude would likely be encountered with much more severe winds that would necessitate a parked or idling turbine, the combination studied here of an operating wind turbine in a severe wave environment is still of interest because it is representative of an IEC design load case (IEC, 2009) (DLC 1.6a).

For comparison, this section will focus primarily on the tower-base fore-aft bending moment; however, statistics will also be given for surge, pitch, and mooring line 2 fairlead tension. The response of the fore-aft bending moment is influenced by most of the relevant physics of interest, including wind, waves, tower structural vibration frequencies, and lastly, second-order difference-frequency diffraction wave forcing. Regarding this last effect and its influence on tower-bending, it should be noted that all platform pitch motion, whether as a result of wind, linear wave, or second-order wave forcing, creates tower-base bending moments as a result of supporting the weight of the heavy wind turbine atop a tilted tower. In addition to comparing FAST and the test data for the combined wind and wave case, the bending moment comparison will also be presented for the dynamic wind only and the JONSWAP wave only. This will permit assessment of the importance of a few of the wind-only or wave-only deficiencies noted previously, and whether or not they are still present in the combined wind and wave case.

The PSDs of the tower-base fore-aft bending moment for the dynamic wind only, irregular wave only, and combined dynamic wind and irregular wave case are given in Figure 91. For the dynamic wind only condition, the comparison is very good, with FAST accurately predicting the increase in response resulting from wind-induced system pitch motion (0.037 Hz). Both the FAST and test data show some minor response at the tower fore-aft fundamental bending frequency of 0.35 Hz, with FAST marginally over-predicting the response. Note that Figure 83 and Figure 84 and Table 40 contain additional plotted results and statistics, respectively, for the dynamic wind only condition used in the combined case.

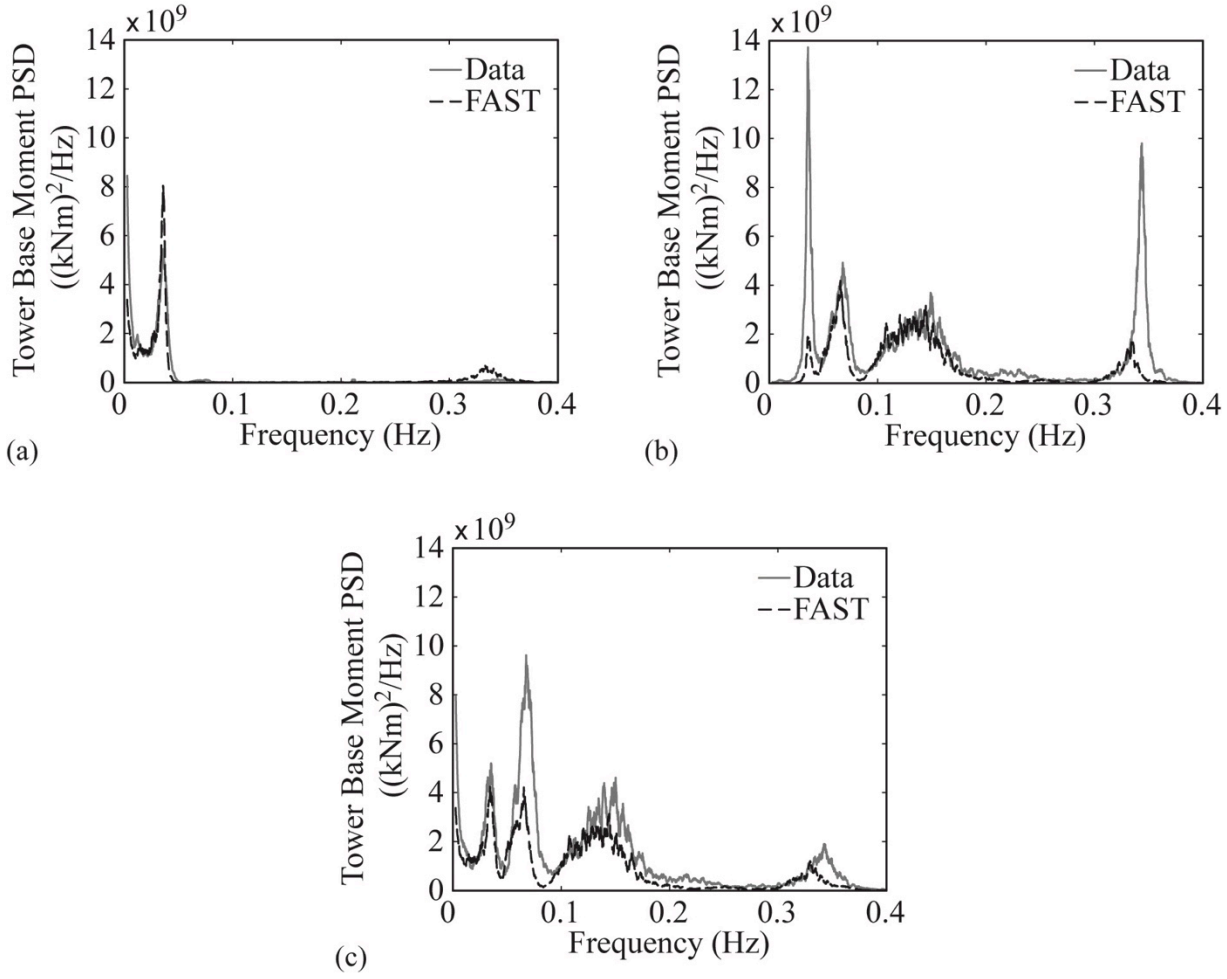

Figure 91: Comparisons of tower-base fore-aft bending moment PSDs from FAST and test data for (a) 20.6 m/s mean wind speed dynamic wind only, (b) 10.5-m significant wave height irregular wave only and (c) combined dynamic wind and wave cases.

Moving to the wave-only bending moment PSD, the comparison is fairly good in the wave-energy range (0.05 to 0.2 Hz), but less so outside of these bounds. FAST poorly predicts the sharp rise in bending moment response associated with platform-pitch motion resulting from second-order difference-frequency wave diffraction forces at 0.037 Hz. The response at the fore-aft fundamental bending frequency is also severely under-predicted by FAST, the possible reasons being highlighted in the previous subsection. On a positive note, the strong correlation between FAST and test data in the wave-energy range is very encouraging because the response for the tower-base fore-aft bending moment is rather complex. Note that in Figure 91 there is a marked decrease in response near 0.08 Hz, despite the fact that the peak wave energy occurs at 0.07 Hz. This results from the

unique platform motion of this system for this particular sea. Despite significant platform motion, the nacelle motion is very low. This results in lower inertial forces at the tower-top and hence, lower tower-base bending moments. As Figure 91 clearly shows, this behavior is accurately captured by FAST. To continue the discussion of wave-only response to the JONSWAP wave, Table 43 below shows statistics for the field variables of interest. The results comparison is fair, with similar discrepancies and possible explanations as those given for the irregular wave-only study with the 11.3-m significant wave height white noise wave.

Table 43: Comparison of FAST prediction and test data statistics for an irregular wave-only case with a significant wave height of 10.5 m.

DOF	Source	Mean	Std. Dev.	Maximum	Minimum
Surge (m)	FAST	-0.08	1.75	6.89	-7.37
	Data	2.35	2.37	16.29	-4.98
Pitch (deg)	FAST	0.00	0.68	3.15	-3.10
	Data	-0.06	1.08	4.50	-4.15
Fore-Aft Bending (kNm)	FAST	0.0×10^4	1.61×10^4	7.69×10^4	-6.83×10^4
	Data	0.13×10^4	2.14×10^4	17.85×10^4	-13.55×10^4
Fairlead 2 Tension (kN)	FAST	1106	75.41	1487	862.0
	Data	1256	406.9	5469	36.05

Moving to the combined dynamic wind and irregular wave condition of Figure 91, the comparison between FAST and the test data shows a fairly good agreement over the entire range of frequencies investigated. The figure indicates that the tower-base fore-aft bending moment response at the platform-pitch (0.037 Hz) and fundamental tower-bending (0.35 Hz) frequencies is dominated by wind rather than second-order wave diffraction or other effects and is therefore predicted very well by FAST. Over the wave-energy range of 0.05 to 0.2 Hz, FAST captures the appropriate trend in the response, albeit with less energy than measured during testing. Because the measured response in the wave-energy frequency range is greater for the combined wind and wave condition than just for waves alone, the data suggests that the combined case yields additional excitation to the system. This could be caused by wave-induced motion creating additional aerodynamic loads as a result of altering the wind turbine rotor relative velocity at frequencies in the wave energy range. It is possible that this calibrated model of FAST may be unable to capture these higher frequency changes in rotor aerodynamic load as a result of choosing simplistic aerodynamic calculation options, for example, by eliminating the dynamic stall model.

Table 44: Comparison of FAST prediction and test data statistics for the combined case consisting of an irregular wave with a significant wave height of 10.5 m and a dynamic wind with a mean hub height wind speed of 20.6 m/s.

DOF	Source	Mean	Std. Dev.	Maximum	Minimum
Surge (m)	FAST	7.13	1.81	13.87	0.28
	Data	9.28	2.29	22.26	2.33
Pitch (deg)	FAST	3.42	0.89	6.70	-0.05
	Data	3.49	1.23	8.66	-1.33
Fore-Aft Bending (kNm)	FAST	8.44×10^4	1.85×10^4	16.16×10^5	1.76×10^4
	Data	8.45×10^4	2.42×10^4	21.70×10^4	-5.01×10^4
Fairlead 2 Tension (kN)	FAST	1580	135.1	2231	1173
	Data	1825	697.6	8109	23.42

By employing a wind turbine model that exploits the full features of FAST's aerodynamic calculation abilities, a better comparison in the wave-energy range could result for the tower-base fore-aft bending moment for the combined dynamic wind and irregular wave case.

That aside, this case is much more realistic because it is unlikely the system would see either a high wave or wind loading alone; they would be expected to occur simultaneously. To finish the comparison, Table 44 presents the statistics for the combined wind and wave case. While discrepancies are still present for the field variables shown, the presence of the wind loads reduces some of the error compared to the wave-only case. The surge response compares much better in this case, with FAST capturing 76.8% of the mean offset without the inclusion of any second-order wave forcing. The discrepancies in the predicted ranges of the surge, pitch, and tension in mooring line 2 responses are similar to the wave-only case, and the predicted range of tower-base bending moments is improved. Overall, FAST demonstrates a fair prediction in this combined wind and wave loading scenario, which is promising.

5.2 Calibration and Validation of a Tension-leg Platform Floating Wind Turbine Model

This section will focus on the calibration and validation of the UMaine-designed TLP. This TLP design was inspired by the Glosten Associates' design (Moon and Nordstrom, 2010). The simulation tool used in this research to create the model of the TLP experiment was FAST. FAST is a coupled aero-hydro-servo-elastic code that simulates the dynamics of wind turbines in the time domain (Jonkman, 2007). It uses Blade-Element/Momentum theory (BEM) or Generalized Dynamic Wake (GDW) theory with static or dynamic stall to calculate aerodynamic loads, a combined nonlinear multibody dynamics and modal superposition formulation for structural components, a quasi-static mooring line model based on continuous cable theory with stretching, turbine control algorithms, and a hydrodynamic module that calculates wave loading on the platform based on linear radiation and diffraction as well as nonlinear viscous drag for offshore applications.

5.2.1 Model Description

Floating platforms lose the stiffness associated with the fixed-ground foundations, and gain new degrees of freedom (DOF). The naming convention for the floating platforms' DOF used for the TLP study can be seen in Figure 92. The wind turbine used in the MARIN tests was modeled after the NREL 5-megawatt (MW) reference turbine (Jonkman et al., 2009). Froude scaling is used both to provide the geometry and other properties of the 1/50th-scale experiment as well as the scaling of the output data from the tests. All of the analysis in this TLP section was done using data and modeling at full scale. For the test data, this means that it must be scaled up to full scale before comparisons are made. Figure 93 shows a diagram of the TLP used in the experiments, including sensor locations. Table 45 describes the full-scale physical dimensions of the TLP. The experimental apparatus includes accelerometers in the nacelle and three locations along the tower. There is also an optical displacement sensor located near the tower base, labeled "Motions" in Figure 93. Load cells are installed between the tower and the platform, between the tower and the nacelle, and on the mooring line fairleads to provide mooring line tension data. The goal of this research was to create, calibrate, and validate a full-scale FAST model of this TLP. The calibration step involved tuning the platform, tower, and aerodynamic parameters in the simulation of the wind turbine to match the data produced by the static equilibrium, decay, regular wave tests, and tests with only aerodynamic loading. The calibrated model was then used to compare to the combined wind and wave tests in an effort to validate FAST as a modeling tool for floating wind turbines.

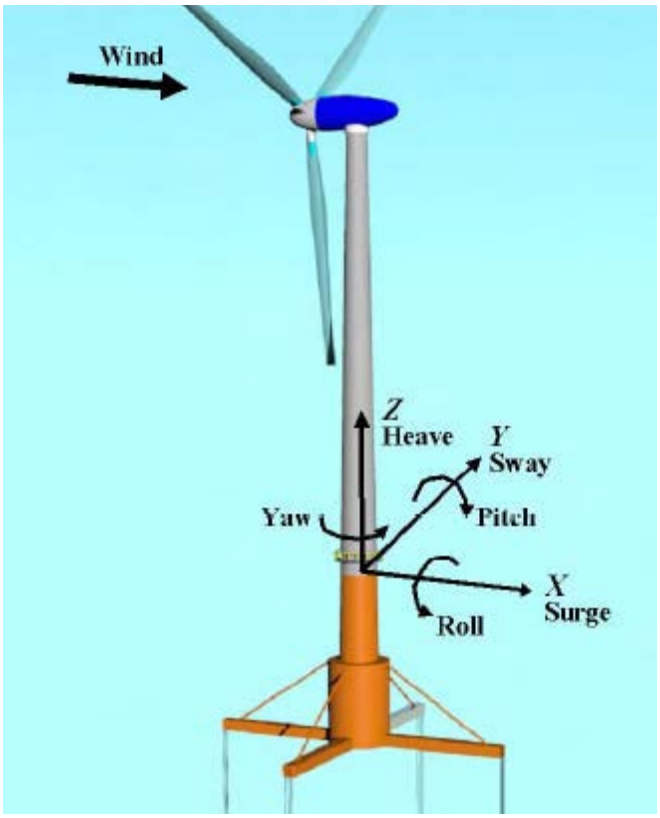

Figure 92: DOF terminology (Jonkman 2007).

Table 45: Physical Properties of the TLP.

TLP Dimensions	
Mass with Turbine (metric ton (mt))	1,361
Displacement (mt)	2,840
Draft (m)	30.0
Center of Mass above Keel (m)	64.1
Mooring Spread Diameter (m)	60.0
Roll Radius of Gyration (m)	52.6
Pitch Radius of Gyration (m)	52.7

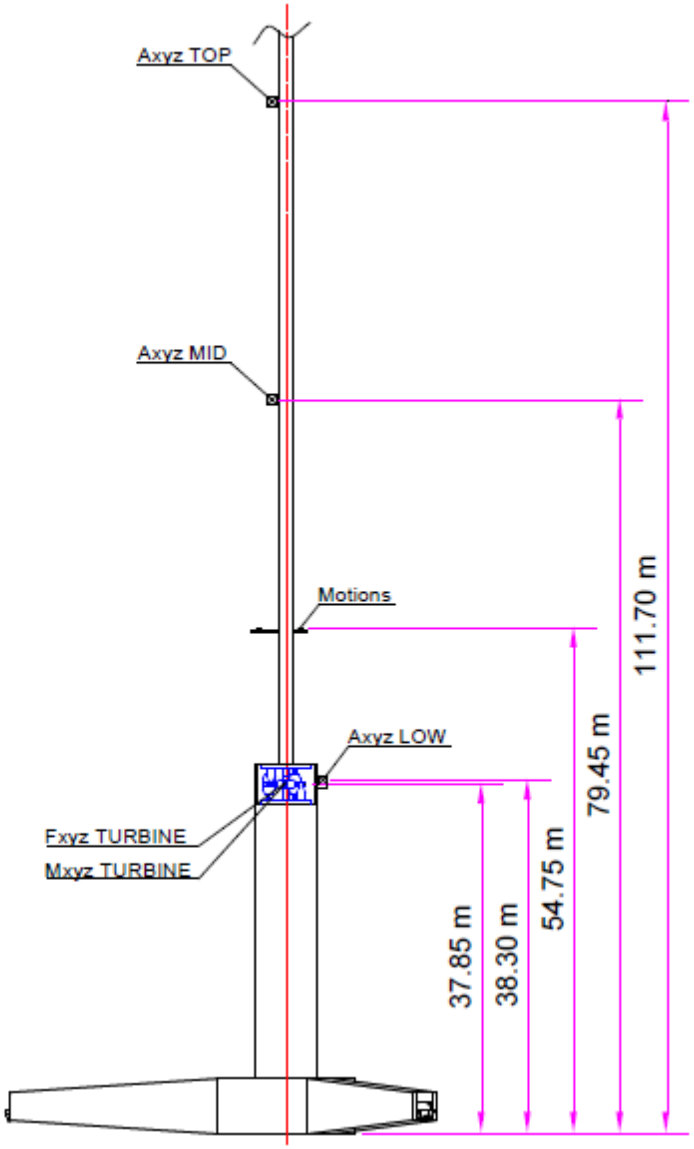

Figure 93: Sensor location on experimental TLP.

5.2.2 Model Calibration

5.2.2.1 Wind Turbine Geometry and Mass Properties

The horizontal-axis wind turbine chosen for scale-model construction is the fictitious, albeit extensively studied, NREL 5-MW reference wind turbine (Jonkman et al., 2009). The wind turbine possesses a 126-m rotor diameter and a hub height of 90 m above the still water line (SWL). The flexible tower, which begins 10 m above the SWL, is designed to emulate the mass and stiffness of the OC3-Hywind tower (Jonkman, 2010). The scale-model wind turbine deviates from the standard NREL 5-MW reference wind turbine in a few notable areas. For the model wind turbine, the shaft tilt is 0°, the blade precone is 0°, and the blades are essentially rigid, which is a reasonable approximation of the actual model. The total mass of the rotor inclusive of the hub and three blades

is a full-scale equivalent of 122,220 kilograms (kg). All values reported in this TLP section are full-scale-equivalent values. The nacelle mass is 274,940 kg.

For the physical model, instrumentation cables used for recording all of the wind turbine response data, as well as nacelle accelerations and tower-top forces, were affixed to approximately the upper two-thirds of the model tower before being looped away to run to the data acquisition system. In FAST, this instrumentation cable is not modeled directly. Instead, the apparent additional weight the platform had to support due to the cables was smeared evenly over the length of the tower for numerical modeling. The distributed stiffness of the tower was assumed to be unaltered by the presence of the cables. Therefore, the distributed bending stiffness for the tower employed for the numerical model was taken directly from the product of the tower material Young's modulus and distributed area moment of inertia. The tower area moment of inertia did not vary smoothly along the length of the tower, with the lower 11.3 m of the tower having a larger outer diameter than the remainder of the tower. The total tower mass, including the additional cable mass, was 302,240 kg. The sensor cable accounts for 137,650 kg of this tower mass. The total topside mass, which included the wind turbine and tower, was 699,400 kg. This value is 16.6% larger than the standard specifications for the combined NREL 5-MW reference turbine and OC3-Hywind tower.

5.2.2.2 Blade Aerodynamic Properties

Due to the low Reynolds numbers experienced during Froude-scale wind/wave basin testing, the aerodynamic performance of the wind turbine blade airfoil sections (which were geometrically scaled) was significantly altered. To generate the airfoil data required for numerical modeling calibration and validation studies, analyses of the airfoil sections were performed at the low Reynolds numbers for small positive angles of attack using the high-order viscous airfoil analysis panel code XFoil (Drela 1989). However, the analyses were incredibly sensitive to the particular Reynolds number and laminar-to-turbulent transition parameters. Despite the fact that the analysis replicated the general change in performance seen during the testing, the generated lift and drag coefficient curves did not accurately reproduce the model-testing-derived coefficient of thrust and coefficient of performance curves for the wind turbine when utilized in FAST. Therefore, the XFoil curves were used as a guide to create a parameterized set of curves that permitted variations in key lift and drag coefficient parameters, such as lift coefficient stall points and minimum drag coefficients. The parameterized curves were extrapolated for all angles of attack via the Viterna Method (Hansen, 2010). A multi-objective genetic algorithm (e.g. see Deb, 2001) was used to search for the lift and drag coefficient parameters that minimized the error between the FAST predictions and wind-only model test data for the wind turbine coefficient of thrust and coefficient of performance curves simultaneously.

Of the various Pareto-optimal solutions found, the result selected was one which favored a solution that achieved minimal error in the thrust coefficient curve (Ct) while still maintaining some semblance of the measured performance coefficient (Cp). This preference of matching the thrust performance was undertaken because the wind turbine thrust force, and not the rotor torque, is the key driver in the global motions of the floating wind turbine under combined wind and wave loadings. A comparison between the FAST prediction and the test data is shown in Figure 94.

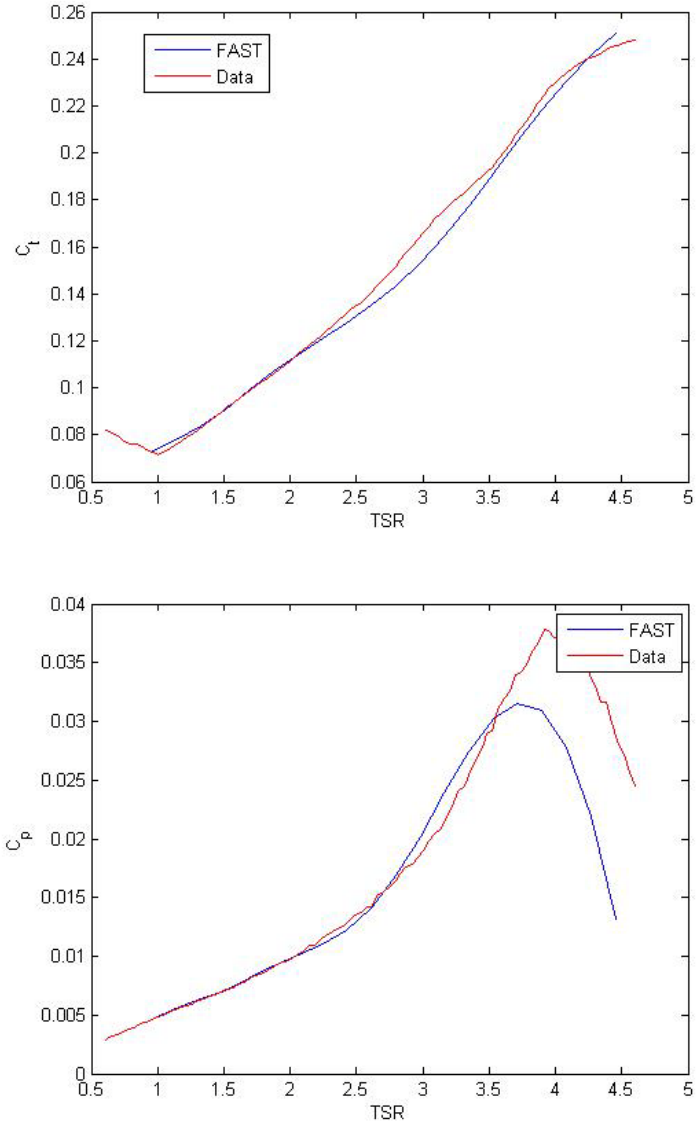

Figure 94: Comparison of model test data and aerodynamic model for coefficients of thrust and performance versus tip-speed ratio (TSR).

The FAST results in Figure 94 were generated with no aerodynamic pitching-moment coefficients. As can be seen in Figure 94, the thrust, and especially the performance coefficients are significantly lower than the NREL 5-MW reference wind turbine. The reason for this, discussed in detail in Martin (2011), is due primarily to laminar separation of the airfoil sections that drastically reduces lift and increases drag. This is especially true for the numerous thick airfoil sections found on the NREL 5-MW blade.

Figure 95: UMaine TLP model.

5.2.2.3 Initial Model and Static Equilibrium Comparison

Static equilibrium simulations were carried out in FAST with this initial model to check the global characteristics of the model. It was found that, by using the platform volumetric displacement given by MARIN, there was substantial platform heave ringing. When the platform displacement value was reduced by approximately 1% of the original value, the magnitude of this heave ringing was reduced to negligible values. Once this heave motion was eliminated, the tension values in the mooring cables were compared to the experimental values and were found to be in good agreement.

5.2.2.4 Free-decay Tests

Free-decay tests were conducted on the experimental TLP by introducing a displacement to a platform DOF and allowing the system to come to rest. Specifically, these tests were conducted to determine the natural frequencies and damping ratios of the various DOFs. Ideally, only one DOF is excited by these tests, but in practice, the tests usually excited more than one DOF. By reviewing the experimental time series, the initial displacements could be extracted and applied to the FAST model.

The data from the optical displacement sensor was found to be inaccurate for the rotational DOFs (pitch, roll, and yaw). This is most likely due to the relatively small displacement of the TLP in these DOFs compared to the rotational sensing accuracy. For this reason, the acceleration data was used instead of the displacement data as a basis for comparison between FAST and the tests.

To tune the natural frequencies and damping ratios of the platform DOFs in FAST, an additional FAST input file was created that gives the user the capability of adding stiffness and damping to each platform DOF. Using this addition, the natural frequencies and damping ratios were iteratively tuned to match the values found in the decay tests. This was done using a frequency-domain analysis of the test data and the FAST output. The stiffness and damping parameters were tuned by hand using a visual comparison of the frequency response of the experiment to the simulation.

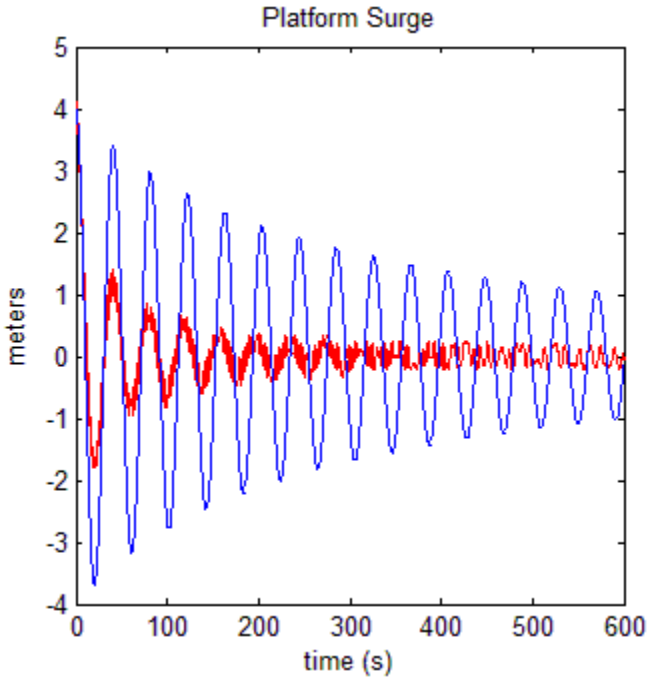

Figure 96: Un-tuned surge decay test surge displacements

5.2.2.4.1 Surge Decay Test

For the surge decay test, the comparison of the surge DOF displacement from the un-tuned FAST model and the test can be seen in Figure 96. In this test, the platform was displaced the full-scale equivalent of 4 m in the surge direction. Figure 97 and Figure 98 show the acceleration and acceleration power spectral density (PSD) of the surge DOF, respectively.

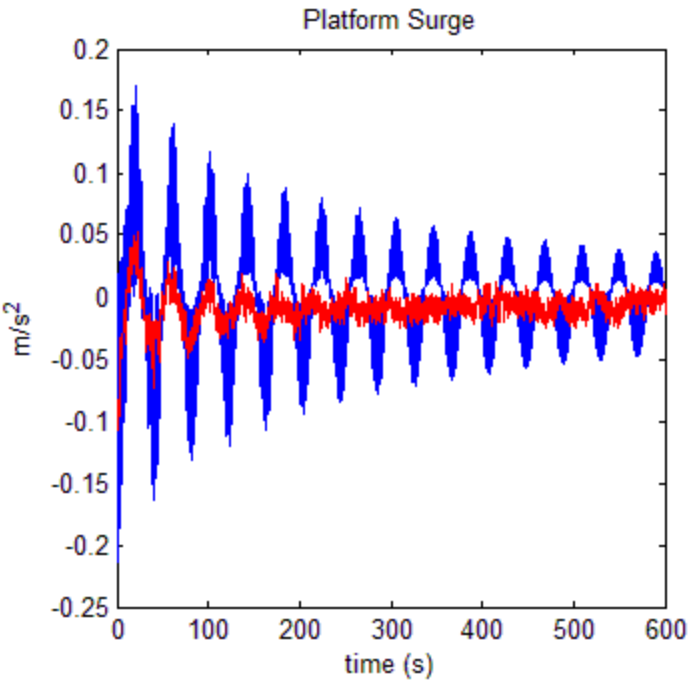

Figure 97: Un-tuned surge decay acceleration.

Figure 96, Figure 97, and Figure 98 show that the FAST model is producing a surge frequency that closely matches the test data, but the FAST simulation model is under-damped for this DOF. In addition, it can be seen in Figure 98 that the heave DOF is highly under-damped in the FAST model as well. This is most likely due to the effect of the sensor cable bundle mentioned earlier, as well as possible under-predictions of damping due to the neglecting of viscous drag in the numerical model. The simulation shows large peaks due to the coupling of the heave, pitch, and tower-bending DOFs with the surge DOF that do not show up in the test. As there is no excitation in the sway, roll, or yaw DOFs, these DOFs can be ignored for this test.

Figure 99 shows the PSD of the platform acceleration with additional damping implemented for the surge and heave DOFs. The surge damping has been increased by 1x105 Ns/m, increasing the damping ratio from 0.01 in the un-tuned case to approximately 0.094. The heave damping ratio has been changed from near zero in the un-tuned case to 0.57.

One issue with the tuned model can be seen in Figure 100. The data from the experiment indicates non-linear, amplitude-dependent damping. In other words, the value of the damping constant for the experiment is larger for larger amplitude motion, and reduces as the motion damps out. This phenomenon could be a result of the sensor cable bundle, or more likely viscous drag, where damping is proportional to velocity squared, and should be investigated in future work. For the scope of this study, the damping is approximated as linear in FAST.

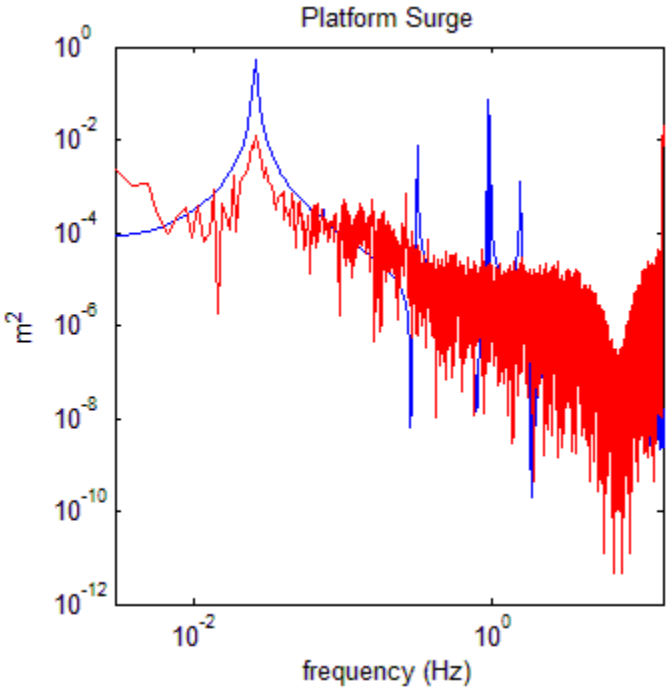

Figure 98: Un-tuned surge decay acceleration PSD.

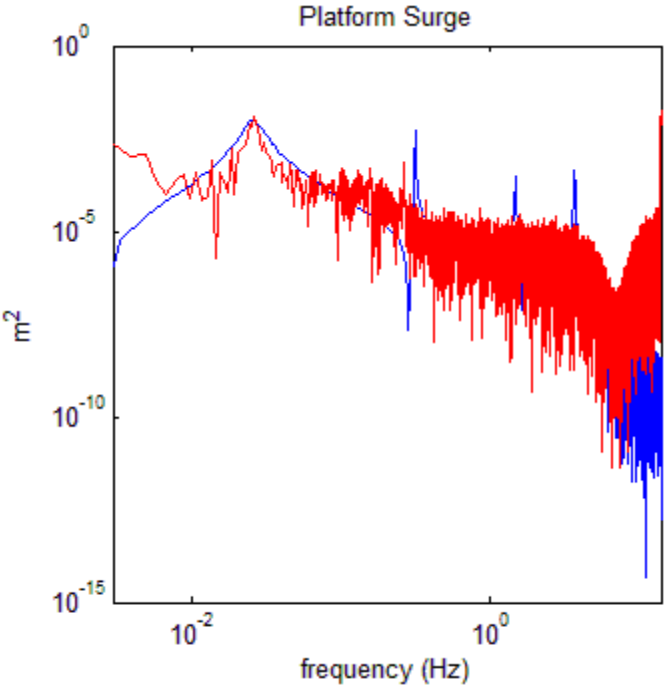

Figure 99: Tuned surge acceleration PSD.

5.2.2.4.2 Further Decay Tests

This method of tuning was carried out for the other DOF decay tests. Due to difficulties in determining the exact initial conditions of each test, only approximate constants could be

determined from the decay tests. For example, one of the pitch-decay tests was conducted by pushing the top of the tower in the pitch direction. This method of excitation produces a substantial amount of initial tower bending which is hard to quantify from the test data. The other pitch-decay test was conducted by pushing on the leg of the TLP to impart an initial pitch. Because of these inaccuracies with the free-decay tests, the plane-progressive (regular) wave tests were used for further calibration.

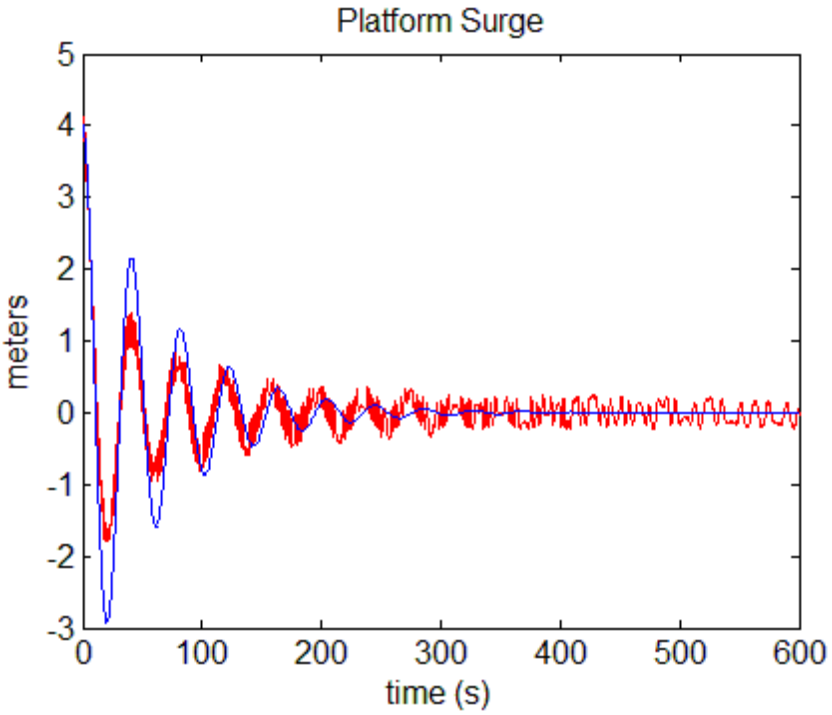

Figure 100: Tuned surge DOF displacement.

5.2.2.5 Regular Wave Tests

The tests conducted in the wave basin included seven regular wave tests with no wind excitation. These tests used a single-frequency long-crested wave input. FAST has the capability to generate these types of waves, so the inputs for the experiment and model were very similar; resulting in a stronger comparison than the decay tests. Figure 1010 shows the surge displacement for one of the regular wave tests and includes the surge damping tuning from the surge decay test. Due to the inaccuracies in the free-decay tests, some of the platform parameters were further tuned using the frequency response of one of the regular wave tests. Figure 102 shows a plot of the acceleration frequency response for all six DOFs, after tuning. In the upper left graph of the platform-surge frequency response, the simulation-surge response at the wave frequency agrees with the experiment well, and the response at the first tower-bending mode agrees as well.

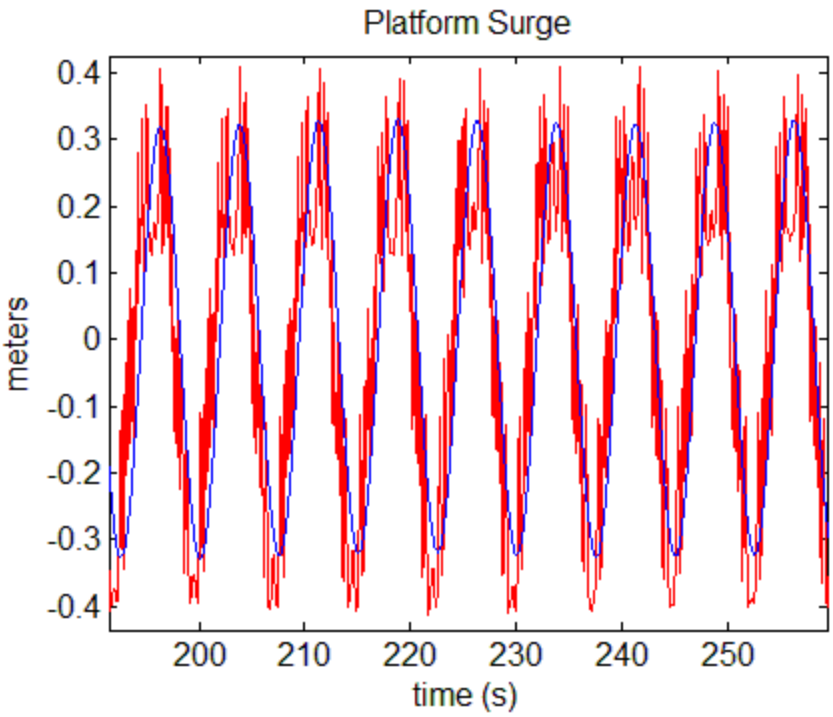

Figure 101: Surge displacement for regular wave test with Height = 1.92 m, Period = 7.5 s.

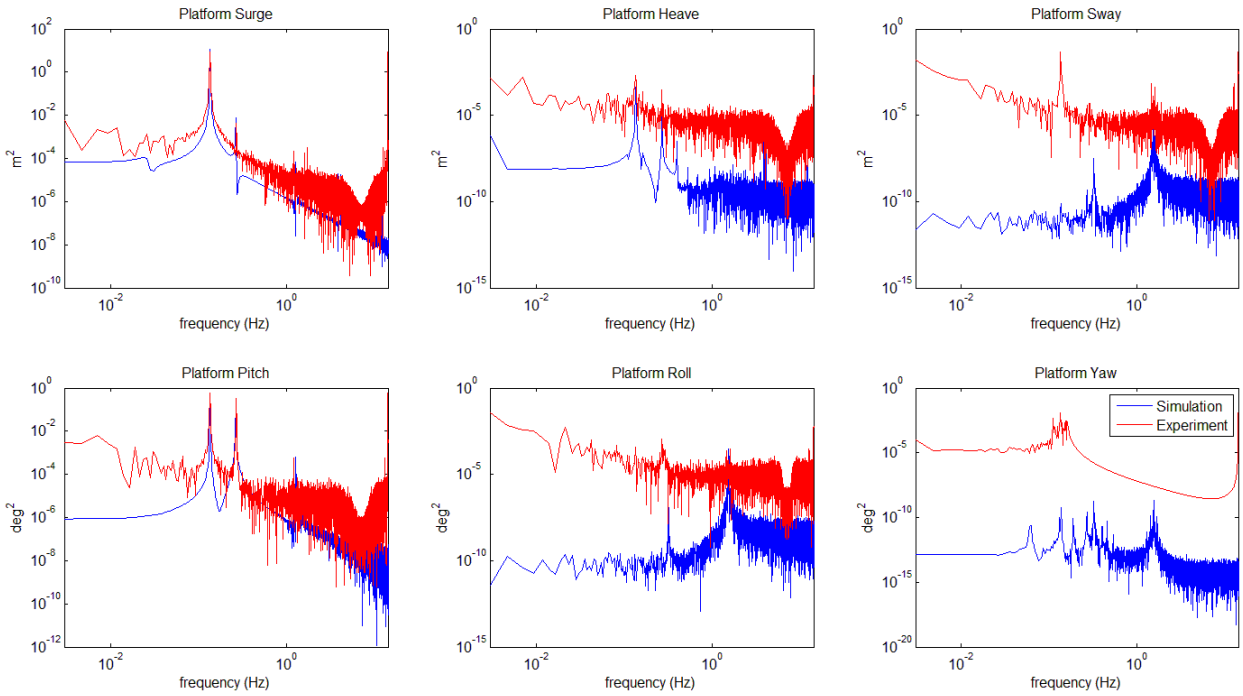

Figure 102: Acceleration frequency response for regular wave test.

In the plot of the pitch-acceleration frequency response (lower left), the wave frequency, the first tower-bending mode, and the pitching frequency are indicated. Tuning the pitch and tower-bending frequency proved to be a challenge. The mode shapes of the tower were initially

determined by the University of Maine using an in-house finite-element method (FEM) code, and as confirmation, an analysis was conducted using BModes, an NREL FEM mode shape software (Bir 2008). The difficulty with this procedure is that the tower-bending mode and the pitch mode are highly coupled. In order to find the proper mode shapes, an iterative process was conducted with BModes by reducing the pitch stiffness from 5.8x1010 Newton-meters/radian (Nm/rad) to 2.6x1010 Nm/rad until both the pitch and tower-bending frequencies aligned with the tests. The other four DOFs, heave, sway, roll, and yaw, were excited more by the waves in the experiment than in the simulations. Of note is that the magnitude of these DOFs is much smaller than the surge and pitch magnitudes. These discrepancies are most likely due to experimental imbalances in the mooring lines or in the mass symmetry of the experimental TLP.

5.2.2.6 Summary of Model Calibration

A summary of the changes to the DOF damping ratios and frequencies can be seen in Table 46. In addition to the changes seen in the table, the tower mode shapes were changed, which caused the change in tower frequency seen in the table.

Table 46: Summary of Calibration.

	Nat. Freq. (Hz)	Tuned Nat. Freq. (Hz)	Original Damping Ratio	Tuned Damping Ratio
Surge	0.025	0.025	0.01	0.098
Sway	0.025	0.025	0.01	0.098
Heave	0.96	0.96	5.1e-7	0.57
Roll	1.52	1.52	0.0050	0.0050
Pitch	1.56	1.27	0.0051	0.0050
Yaw	0.058	0.058	0.047	0.047
First Tower Fore-Aft	0.32	0.26	0.006	0.006
First Tower Side-Side	0.32	0.26	0.006	0.006

5.2.3 Model Validation

In this section, the simulations that were run to date for the model validation step are presented. Two experiments with constant wind and operational waves were simulated in FAST. More simulations will be conducted in future work on this project. In these tests, the time series of the wave input was not replicated directly, but the spectrum of the wave input was the same as the experiment. The first experiment that was simulated used a 7-m/s wind speed, and a wave spectrum with a 2- m significant height, a 7.5-s peak-spectral period, and a peak shape parameter of 2.0. The pitch of the blades was held at a constant 6.4 degrees, and the rotor was held at a constant speed of 4.95 revolutions per minute (RPM) in both the simulation and the experiment. The values for pitch and rotor speed differed from the normal NREL 5-MW specification as these values were chosen to match simulated rotor thrust with the augmented aerodynamic performance of the 1/50th-scale model.

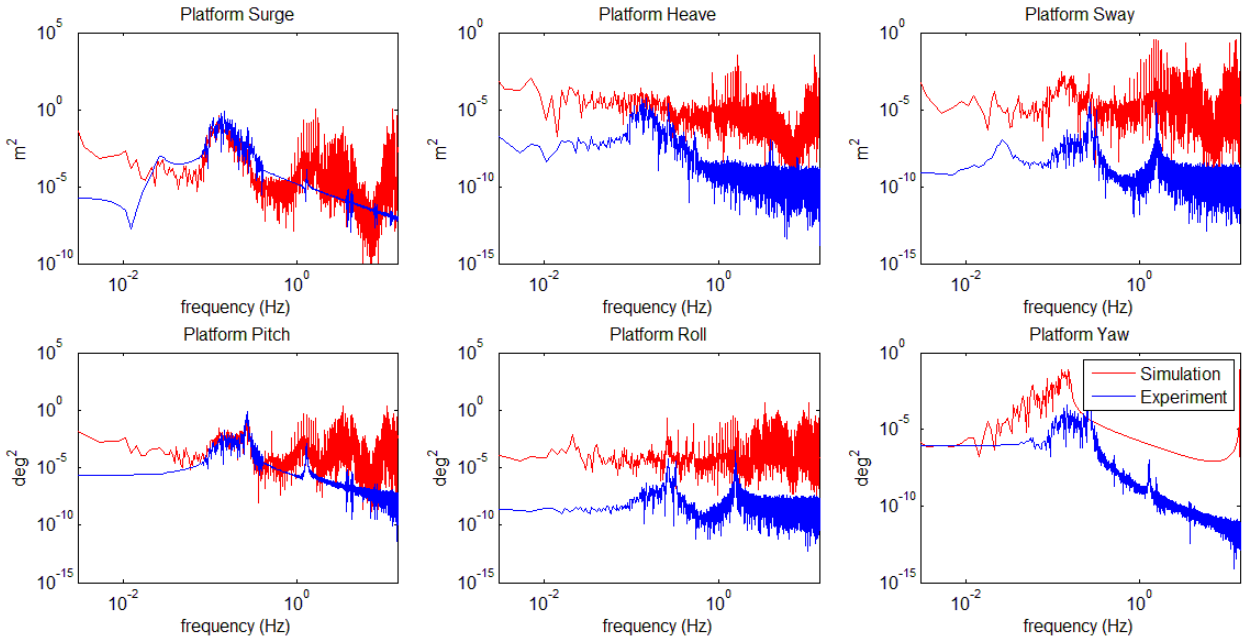

Figure 103: Acceleration frequency response for low operational wave test and steady 7 m/s wind.

Figure 103 shows the frequency response of the acceleration of the DOFs for this first validation case. The discrepancies in the frequency range lower than the wave frequencies were most likely due to fluctuations in the experimental wind speed. Similar to the regular wave response, the lower frequency modes were captured well by the simulation, but the simulation diverged from the experiment for higher frequency modes.

The difference in energy between the experiments and the simulations at these higher frequencies could mean that the FAST model needs higher frequency modes, that the simulation model was improperly calibrated, or that the sensors used in the experiments had errors or noise at these high frequencies. Further research is required to determine what combination of these three options is present.

In the pitch frequency response in Figure 103, the experiment shows a peak at the rotor frequency (1P). The FAST simulation shows no pitch excitation at this frequency. Causes of 1P excitation are indicative of a rotor imbalance in the experiment, which was not simulated in FAST. Future models may address this issue of rotor imbalance.

The second case that was simulated was an experiment with much higher wind and wave loading. The steady wind speed for this test was 21 m/s, the wave height was 7.1 m, the peak-spectral period was 12.1 s, and the shape factor was 2.2.

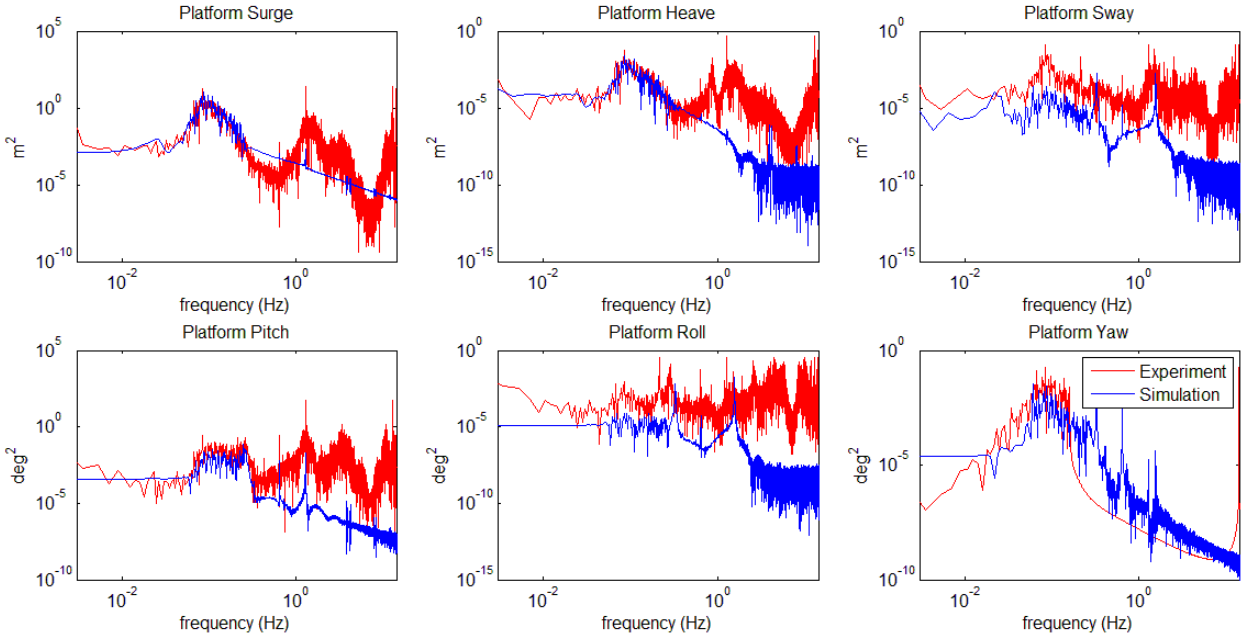

Figure 104: Acceleration frequency response for high operational wave test and steady 21 m/s wind.

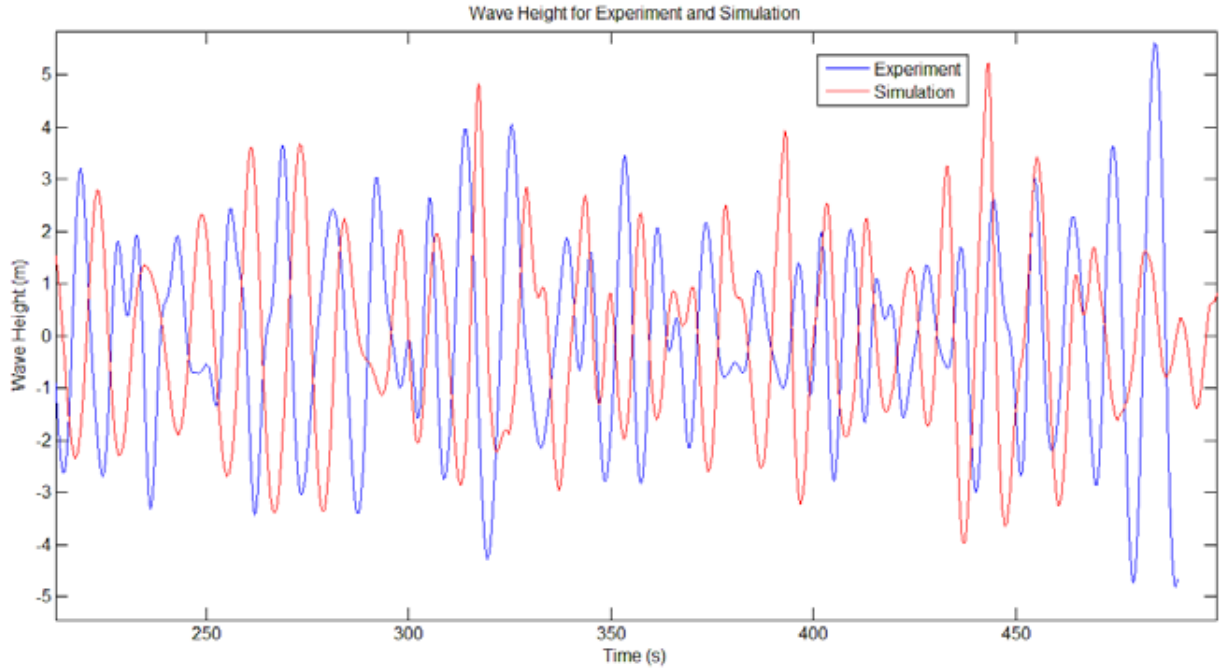

Figure 105: Wave time series

In Figure 104, there is reasonable agreement between the response of the experiment and the response of the simulation. This case produced the most consistent results seen to date for the sway, heave, roll, and yaw DOFs and could be caused by a phenomenon similar to the non-linear damping seen in Figure 100. As the amplitude of motion becomes higher, the damping values of

various degrees of freedom may increase in the experiment, which is closer to what the simulation is showing.

With the higher wind speed of this experiment, the 1P excitation is showing up in the FAST simulation, as indicated in the pitch response in Figure 104. The cause of this 1P excitation is being investigated. Figure 104 shows the acceleration frequency response in each DOF. Due to the high wind and wave loading, the simulated TLP exhibited an excessive increase in pitch angle magnitude during a large wave event, causing the simulation to end prematurely. Figure 105 shows a plot of the experimental and simulated wave heights. The simulation crashed after the large wave seen at the end of the time series. Because the blade pitch was constant in all of these tests, the rotor thrust produced by the 21-m/s wind was enough to cause a 12-m surge. These factors combined to cause excessive pitch motion. The amplitude of the pitch motion leads to a slack-line event in FAST, in which the tension in the rear mooring line goes to zero. This phenomenon was seen in the experiment as well, which is an encouraging sign for modeling accuracy.

5.3 Calibration and Validation of Spar-buoy Floating Wind Turbine Model

This section focuses on an effort to use the DeepCwind 1/50th-scale test data to calibrate and validate a FAST turbine model of a spar buoy floating wind turbine. FAST is a nonlinear time-domain simulation tool that is capable of modeling the coupled aero-hydro-servo-elastic response of floating offshore systems that are operating in an environment with combined wind and wave loading. Rotor aerodynamics are calculated using the AeroDyn software library—which relies on blade-element/momentum theory or generalized dynamic wake theory for the calculation of wake effects—and the Beddoes-Leishman model for calculation of dynamic stall, and provides the user with the option of incorporating the effects of tip losses and hub losses (Hansen and Moriarty, 2005). Structural components of the turbine are modeled as a combination of coupled rigid and flexible bodies. Flexible bodies include the blades, tower, and drive shaft (Jonkman, 2012; Jonkman and Buhl, 2005). Time-domain hydrodynamics include the effects of hydrostatic restoring, viscous drag from waves and turbine motion, added mass and damping from wave radiation, and linear wave diffraction. Mooring lines are modeled as quasi-static taut or catenary lines and include the effects of stretching, mass density, buoyancy, geometric nonlinearity, and seabed interactions. Dynamic mooring line effects and mooring line drag are not included in the model (Jonkman, 2007).

5.3.1 Model Description

The degrees of freedom (DOF) of the complete wind turbine and floating platform FAST model include edgewise and flapwise blade motions, rotor rotation, driveshaft torsion, nacelle/rotor yaw, first and second modal tower-bending motions (both side-to-side and fore-aft), as well as six degrees of platform motions, including surge, sway, heave, roll, pitch, and platform yaw. Surge, sway, and heave are translations in the X, Y, and Z directions, respectively; whereas roll, pitch, and yaw are rotations about the X, Y, and Z axes, respectively. Coordinate systems and platform DOF definitions used in this study are illustrated in Figure 106.

5.3.1.1 The Spar-type Floating Wind Turbine

The Maritime Research Institute Netherlands (MARIN)/University of Maine (UMaine) scale test model and FAST full-scale, three-bladed horizontal-axis wind turbine model are based on the National Renewable Energy Laboratory's (NREL's) offshore 5-megawatt (MW) baseline wind turbine (Jonkman *et al.*, 2009). The turbine was attached to a spar buoy platform that was adapted from a spar design developed for Phase IV of the Offshore Code Comparison Collaboration (OC3), which is based on Statoil's Hywind spar (Jonkman, 2010). The spar has three equally spaced mooring lines in a water depth of 200 meters (m). The UMaine model uses a bridle system for the attachment of the three mooring lines to the spar, providing additional yaw stiffness; whereas the

FAST model has a direct attachment to the spar of each mooring line at a radius of 5.2 m and a draft of 70 m because of FAST mooring line geometrical definition limitations. Pertinent dimensions of the FAST model are given in Table 47.

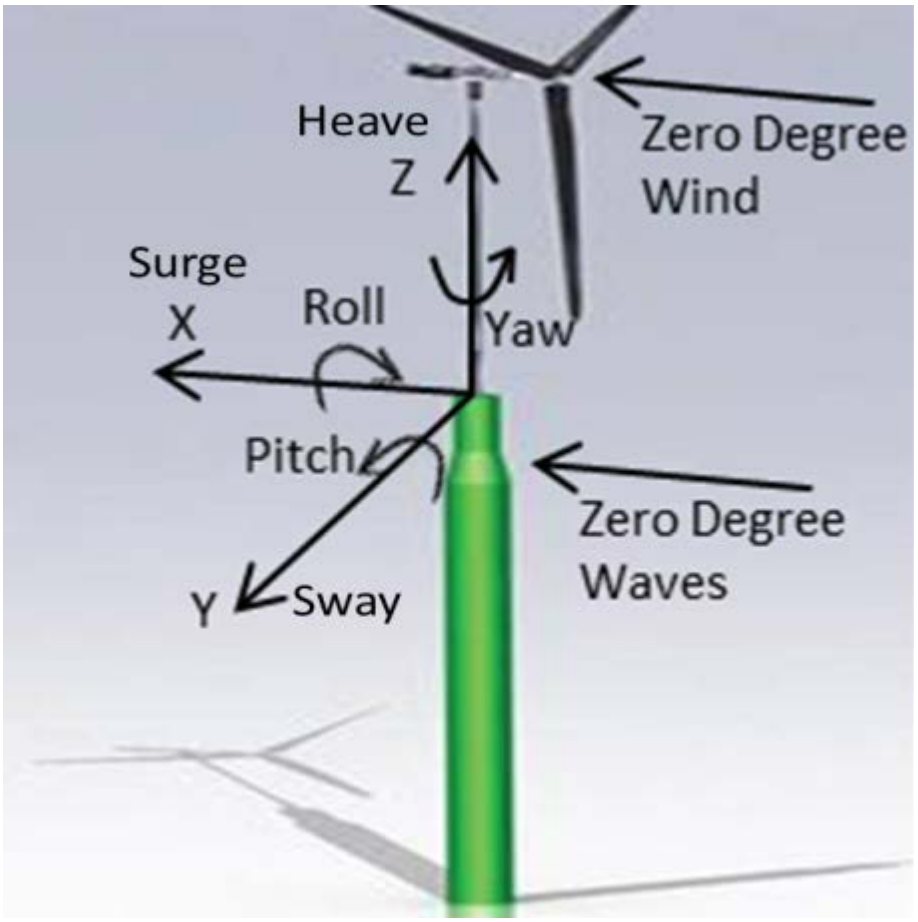

Figure 106: **Coordinate system and definitions for platform DOF used in this spar-buoy study.**

Table 47: **Dimensions of the spar type floating wind turbine model.**

Hub Height [m]	90
Flexible Tower Length [m]	77.6
Blade Length [m]	61.5
Tower Top Mass [kg]	394,000
Tower Mass [kg]	303,145
Tower Base Above MSL [m]	10
Spar Length [m]	130
Spar Center of Mass Below MSL [m]	90
Spar Mass [kg]	7,280,000
Displacement Volume [m^3]	7,948
Total System Mass [kg]	7,977,33

5.3.1.2 MARIN Wave Tank Testing (1/50th Scale)

Tests were carried out in MARIN's wind/wave basin on a 1/50th Froude-scaled model of the spar system built by UMaine and MARIN (Martin *et al*., 2012). Researchers conducted static offset tests,

six DOF decay tests, periodic wave tests with and without wind, and combinations of stochastic wind and wave conditions. In addition, hammer tests were performed on the system to obtain fundamental modal responses. Data recorded during the tests included six platform DOF positions and accelerations; rotor torque and position; accelerations at three locations spanning the tower, forces, and moments at the tower base and tower top; and mooring line tensions. The sampling frequency was 100 hertz (Hz), corresponding to a Froude-scaled sampling frequency at full scale of roughly 14 Hz. All data from the MARIN tests were converted to full scale using Froude scaling prior to analysis (Martin, 2011). All test data provided in this spar-buoy study were presented at full scale, unless otherwise noted.

5.3.1.3 Introduction to Calibration and Validation

The FAST model was calibrated prior to validation to match the UMaine test model as closely as possible by using free-decay and periodic-wave tests (a small subset of the total experimental data available). Parameters in the FAST model were calibrated to match the test model when there was a known potential for discrepancy between the two. These discrepancies took the form of simplifications in the FAST model or simulation algorithms, or uncertainties in the characteristics of the scale test model. Once calibrated, the FAST model was validated by comparing the responses of the FAST model and test model for several tests, again including the free-decay and periodic-wave tests, with the addition of tests with irregular waves and steady wind.

5.3.2 Calibration

The parameters of the FAST model, which were calibrated prior to validation, are included inTable 48, along with a brief justification for calibration. Additionally, prior to this study, the aerodynamic coefficients of the blade were calibrated to match rotor thrust between FAST full-scale simulations and scaled-up test data because of poor aerodynamic performance of the UMaine test model resulting from Reynolds number (Re) dissimilitude (Martin, 2011).

5.3.2.1 Mooring System Calibration

The mooring system used in the MARIN tests consisted of three equally spaced primary mooring lines connected to the spar via delta connections that provided additional platform yaw stiffness than a single (direct) connection. Each of the three primary lines contained an inline linear spring intended to simulate the combined stiffness caused by mooring line axial stiffness and mass density of a full-scale catenary mooring line. Because FAST was not able to simulate the more complex delta connection of the UMaine test model, and because it relied on a quasi-static catenary solution (rather than an inline spring), the FAST mooring model was calibrated, as described in the following paragraph, to mimic the steady-state reaction of the MARIN model to X-direction displacements. Static offset tests in thewas kept constant at the equilibrium value. The length, axial stiffness, and mass density of the FAST mooring lines were tuned until lines 1 and 2, at 120 and 240 degrees from the X-axis, respectively, and line 3, at zero degrees from the X-axis, matched the MARIN results for line tension at offsets of 12.4 m and at equilibrium (i.e., zero offset for all platform degrees of freedom). The anchor locations were kept fixed at a radius of 445 m for both models. The resulting line tensions at the spar connection for several offsets for the FAST model and UMaine test model are shown in Figure 107. The two models were in agreement for all offsets, with the largest discrepancy of 39 kN occurring for line 2 at an offset of 9.9 m.

Table 48: FAST model parameters calibrated prior to validation with a brief reason for calibration.

Calibrated Parameter	*Justification for Calibration*
Mooring Line Mass, Stiffness, and Length	Matching the mooring system tensions in the FAST model caused by horizontal displacement to the UMaine test model; necessary because of a delta connection in the UMaine test model that was not directly modeled in FAST
Tower Stiffness	Matching of first tower vibrational mode in the FAST model to the UMaine test model because of uncertainty in its stiffness, which was altered by sensors and sensor cables
Platform Displacement at Equilibrium	Matching zero heave at equilibrium of the FAST model and the UMaine test model because of uncertainties in mooring line fairlead angle and equilibrium displacement in the test model
Platform Yaw Stiffness	Emulating the added yaw stiffness created by the UMaine mooring system's delta connections in FAST
Heave and Yaw Damping	Fixing discrepancies between the UMaine test model and the FAST model because of FAST viscous drag simplifications

5.3.2.2 Tower Calibration

The as-tested UMaine test model included an instrument cable attached to the tower and a force and moment sensor at the base of the tower of unknown stiffness. To represent the interaction of the cable and the sensor with the structure, a single stiffness multiplier was used at all FAST tower nodes to decrease the stiffness from nominal UMaine test model design specifications. The multiplier was calibrated so that the tower's first fore-aft frequency mode matched between MARIN and FAST, as measured by a fast Fourier transform (FFT) of tower-top acceleration with the turbine operating in periodic waves. The multiplier decreased the FAST model's first tower-bending mode from 0.49 Hz to 0.42 Hz.

5.3.2.3 Platform Displacement, DOF Stiffness and Damping Calibration

Platform yaw stiffness was added to the FAST model until the yaw natural frequency matched that of the MARIN tests. The first natural frequencies in yaw for both models were measured using an FFT of a time series from a yaw decay test.

The platform draft at zero heave was reduced from the design specification value of 8,029 m3 to 7,948 m3 so that the model would float at zero heave in its equilibrium state with the calibrated mooring system.

FAST includes the capability of modeling nonlinear viscous drag on the platform in the X and Y directions via a user-specified coefficient of drag and varying platform diameter. The coefficient of drag (Cd) for the FAST spar model was calculated as the coefficient of drag for an infinite cylinder, which was determined based on the oscillatory Re of the relative water flow (Newman, 1977). Re, however, does not scale consistently with Froude scaling. Because the goal was to model the test model, the range of Re values used for calculating the appropriate Cd were based on the 1/50th-scale test data rather than the full-scale data. It was found that the likely range of Re for the scaled data corresponded to an area of low slope in a Cd versus Re curve, with a mean value of approximately 1.0. Therefore, a value of 1.0 was used for Cd in the FAST model. It should be noted that the maximum Re expected from full-scale test data (using Froude scaling) was roughly 106, corresponding to a Cd of approximately 0.6 for an infinite cylinder, thereby illustrating the importance of using Re from scale test data when approximating Cd for viscous drag for the purposes of simulating the behavior of a model-scale system.

Because viscous drag in FAST was calculated only in the X and Y directions, it had a damping effect on the surge, sway, pitch, and roll motions of the spar platform. Additional linear damping was added to the heave and yaw DOFs in the FAST model to account for damping characteristics that are currently not modeled in FAST—such as skin friction, drag on mooring lines, and the drag caused by the abrupt edge at the bottom of the spar—that would be present in the MARIN tests. During calibration, 71.0×103 N/(m/s) and 10.1×106 N·m/(rad/s) of damping were added to heave and yaw, respectively, so that the average damping ratio over several peaks from the time series of heave and yaw decay tests were consistent between FAST simulations and MARIN tests.

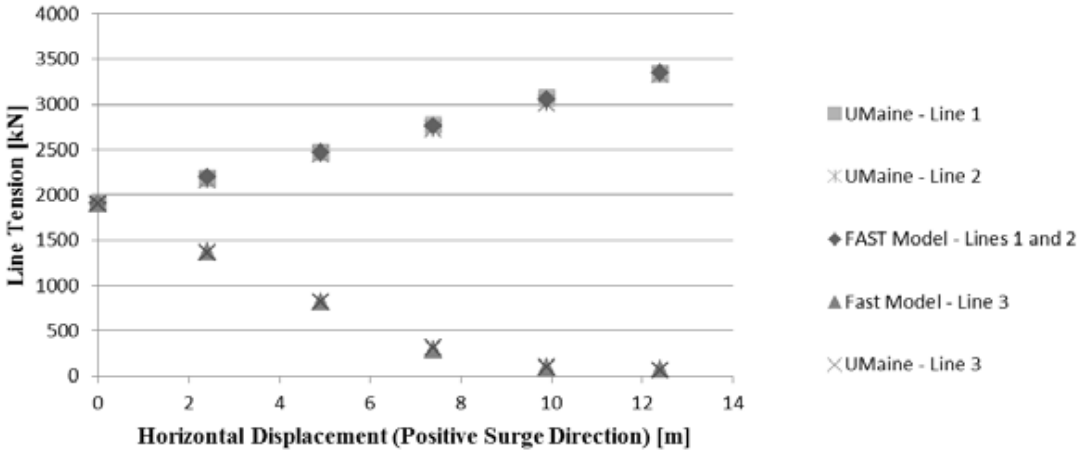

Figure 107: **Mooring line tensions at the spar connection for the FAST model and UMaine test model.**

5.3.3 Validation

After calibrating the FAST model to account for any known discrepancies between it and the UMaine test model, the FAST model was validated by comparing the results between the simulation and test for a series of tests, including free-decay tests, periodic-wave tests with no wind, and irregular-wave tests [Joint North Sea Wave Project (JONSWAP) waves] with wind.

5.3.3.1 Free-decay Tests

After calibration, damping properties and natural frequencies for the six platform DOFs were compared between the FAST model and the UMaine test model via decay tests. The tests were performed by translating or rotating the model in the direction of each of the platform DOFs and

letting the model return to equilibrium. The tests were performed with no incident waves or wind and a stationary rotor. Natural frequencies were calculated by locating the dominant frequency in the FFT of the resulting free-decay time series. Figure 108 shows the resulting natural frequencies for the FAST model and UMaine test model. As described, yaw stiffness and damping, as well as heave damping, were added to the FAST model during calibration. All frequencies matched well between FAST and the UMaine test model with the exception of pitch and roll, for which FAST exhibited a noticeably lower frequency response than the MARIN test data (0.0290 Hz and 0.0315 Hz for FAST and MARIN, respectively). This lower frequency response may have been because of incorrect placement of mass along the tower during the tower mass calibration process, which would have resulted in an incorrect moment of inertia for the system and incorrect pitch and roll restoring associated with the system center of mass.

The damping ratio for the platform motions were calculated from the average ratio of successive peaks using peaks 2–9 and peaks 9–16 from the decay tests. Averages of two ranges of time series peaks were used because the FAST model included nonlinear viscous drag, which increased with the higher platform velocities that occurred with high-amplitude oscillations; whereas damping during lower amplitude oscillation was primarily because of radiation damping. The damping ratios are presented in Figure 109. Heave and yaw were consistent between FAST and the UMaine test model for peaks 9–16. The MARIN surge damping ratio increased for lower amplitude oscillations, which may have been caused by a problem with the test procedure or the average successive peak ratio analysis procedure. FAST showed self-consistency between surge and sway (small variations were caused by different initial offset values to match MARIN tests as well as the greater influence of rotor drag in the surge direction) but did not match the MARIN test values. This inconsistency may be explained by large displacements of the mooring systems in surge and sway, leading to nonlinearities and differing behavior of the mooring systems in the FAST model and UMaine test model. This explanation would also account for the lack of self-consistency in the MARIN test data for surge and sway because the initial offset for sway was significantly larger than for surge, at 10 m and 4 m, respectively. In general, the FAST model appeared to have greater damping in surge and sway and less damping in pitch and roll relative to the UMaine model. Drag on the mooring lines was not modeled in the current version of FAST, which may have accounted for some of the discrepancy in surge and sway.

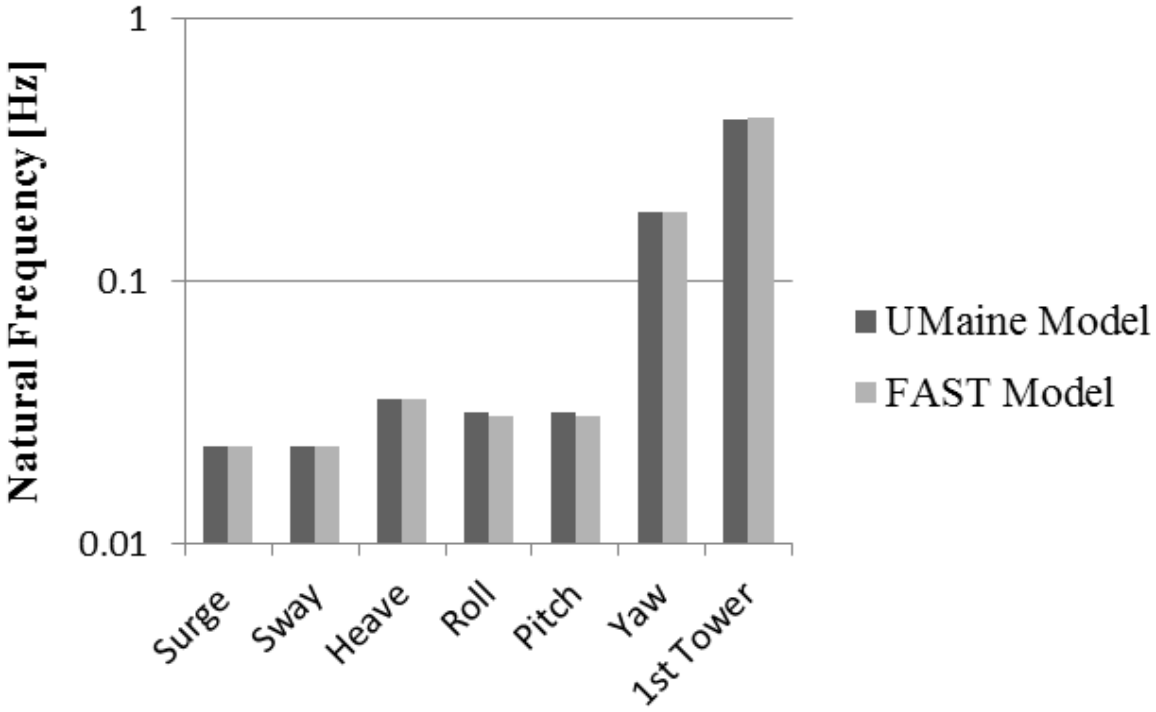

Figure 108: **Natural frequencies of platform motions for the UMaine test model and FAST model.**

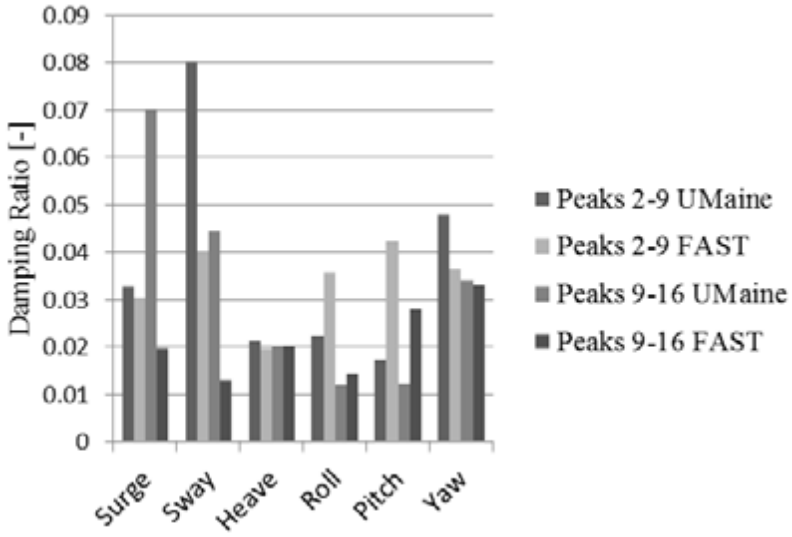

Figure 109: Average damping ratios from peaks 2–9 and peaks 9–16 of platform DOF decay tests.

5.3.3.2 Periodic Wave Tests

The results of two periodic wave tests, with wave heights of 1.92 and 7.14 m and wave periods of 7.5 and 14.3 s, were compared between the FAST model and the UMaine test model to validate the system response to a relatively simple sea state. These tests were run with no wind, a stationary

rotor, and waves propagating along the positive X-axis (i.e., toward the rotor in the direction of platform surge).

Figure 110 shows the resulting power-spectral densities (PSDs) of the response to a periodic wave test with low-height (1.92 m) and low-period (7.9 s, 0.13 Hz) waves. Both heave and tower-top acceleration response at the wave frequency was consistent between the MARIN experiment and FAST simulation. The response of the tower top at the pitch frequency as well as the heave response at the heave natural frequency was stronger for the simulation than the experiment. The difference in heave response at the natural heave frequency suggested insufficient heave damping in the FAST model. However, the damping ratios in Figure 109 indicated agreement for the heave DOF. Similarly, Figure 109 indicates that pitch had greater damping in FAST than the experiment for both of the large displacements. This fails to explain the greater response of the tower top in the FAST model at the natural pitch frequency.

The PSD of the tower top X-acceleration for the experimental data showed a strong response at 0.26 Hz, which was twice the wave frequency. This could have been caused by second-order hydrodynamic excitation. The simulation did not show that this response was likely because it was not capable of modeling second-order hydrodynamic loading.

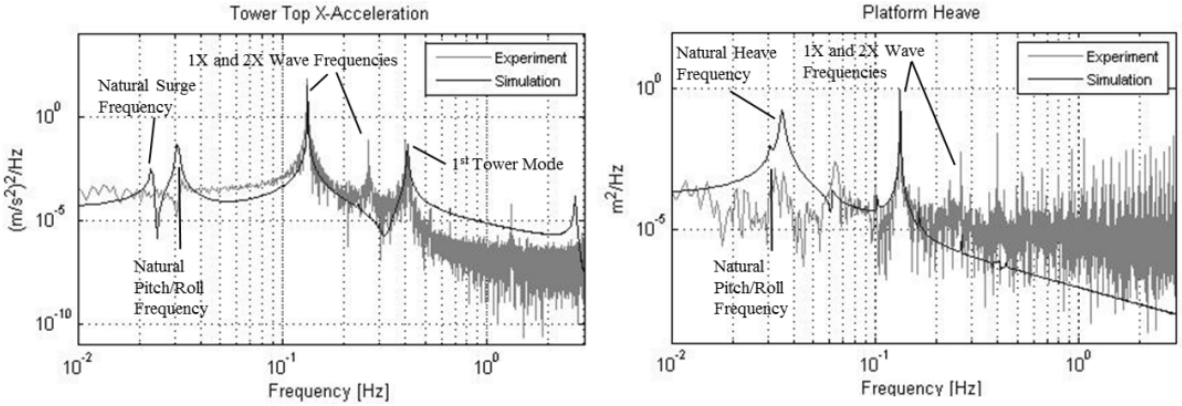

Figure 110: **Tower-top X-direction acceleration response and platform-heave response of the UMaine test model and FAST model in periodic waves with a height of 1.92 m and a wave period of 7.5 s.**

PSDs from a periodic wave test with a wave height of 7.15 m and a period of 14.3 s (0.070 Hz frequency) are shown in Figure 111. Response of both platform-heave and tower-top acceleration at the wave frequency was fairly consistent between the simulation and the experiment. However, the simulation resulted in a significantly greater tower-top response at the platform-pitch frequency than the experiment, as well as greater heave response at the heave frequency than the experiment. Again, this outcome may point toward differences in damping between the two systems that are still occurring with larger waves and platform motions and may be partially explained by damping in the UMaine test model that was caused by nonlinear drag of the mooring lines (not modeled in FAST). The MARIN test data showed large responses at two and three times the wave frequency, 0.14 Hz and 0.21 Hz, respectively; whereas the simulation showed only the 0.14 Hz response. This response was likely because of the quadratic viscous damping term in FAST, which caused a pronounced response at twice the regular wave frequency when subjected to higher waves and greater motions.

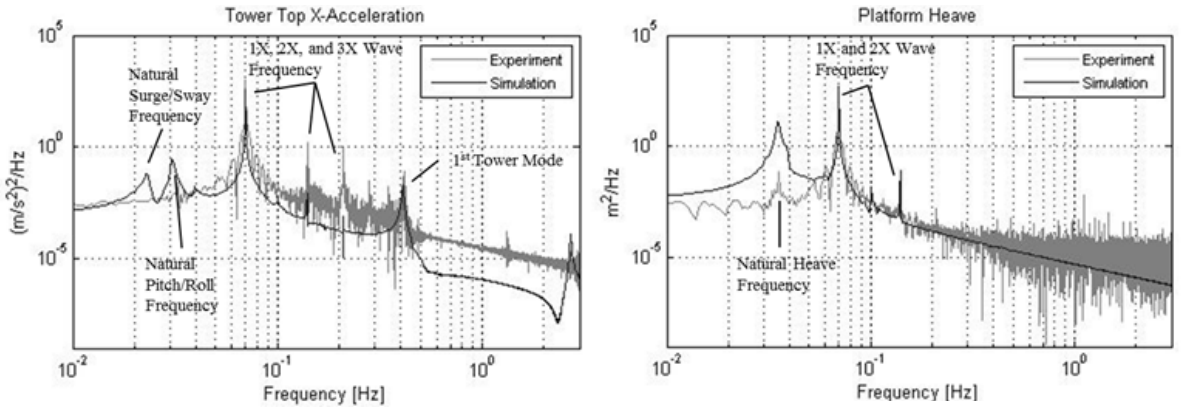

Figure 111: **Tower-top X-direction acceleration response and platform heave response of the UMaine test model and FAST models in periodic waves with a height of 7.14 m and a wave period of 14.3 s.**

5.3.3.3 Irregular Wave Tests

The MARIN spar model was tested under a variety of metocean conditions with irregular waves and steady wind. Waves in both the experiment and simulation were based on JONSWAP spectra (Jonkman, 2007). The recorded wave parameters in the experiment and wave spectra parameters in FAST were the same, and included significant wave height, peak-spectral period, peak shape factor, and propagation direction. The FAST simulation used these four parameters to produce a wave height time series that was based on the JONSWAP spectrum, which was then used in the simulation. This method resulted in sea surface elevations that were not identical in time, but had more consistent spectra than the MARIN tests.

The first irregular wave test used for validating the FAST model consisted of a significant wave height of 2 m, a peak-spectral period of 7.5 s (0.133 Hz), and a shape factor of 2.0. The steady horizontal wind speed was 11.23 meters per second (m/s) and the rotor was kept at a constant speed of 7.8 rpm (0.13 Hz). The wave direction was zero degrees (i.e., propagation was toward the downwind side of the turbine). Figure 112 shows PSDs of the moment about the Y-axis at the base of the tower, and the tower-top acceleration in the X direction. Both plots show a similar response shape within the region of the JONSWAP wave frequencies (roughly 0.009 to 0.035 Hz) between both measurements and between the experiment and simulation, as expected because of the influence of the tower-top motions on the tower-base moments. The response of the tower-top acceleration at the platform-pitch frequency was also similar between the experiment and simulation. It would be expected that similar tower-top motion spectra in the vicinity of the platform-pitch frequency would translate into similar tower-base moment spectra in that frequency range. However, it can be seen in Figure 112 that the magnitude of the tower-base moment response was somewhat larger for the FAST simulation than the experiment at the platform-pitch frequency (0.030 Hz). This outcome may have been caused by an incorrect tower/nacelle/rotor system rotational inertia, and thus a larger moment at the base for a given tower-top acceleration. This would also account for the lower pitch natural frequency for the FAST model than in the MARIN experimental model previously noted.

In both spectra, the experimental data showed prominent peaks at the blade-passing frequency (3P) of 0.39 Hz, as well as the first two blade-passing frequency harmonics (6P and 9P). Although an effort was made to produce a low turbulence and constant wind field over the rotor area for the experiments, wind calibration results showed both vertical and horizontal variation in wind velocity, with a minimum wind speed measured across the rotor of roughly 70% of the maximum.

The prominent 3P, 6P, and 9P peaks may be because of these inconsistencies in wind velocity over the rotor. In comparison, the FAST simulations (for these tests) modeled wind velocity as a constant wind field over the rotor area; thus, for this experiment, the spectra did not exhibit pronounced peaks at the blade-passing frequency or its harmonics. FAST does include the capability for modeling wind fields with horizontal and vertical shear. These effects may be examined in the future.

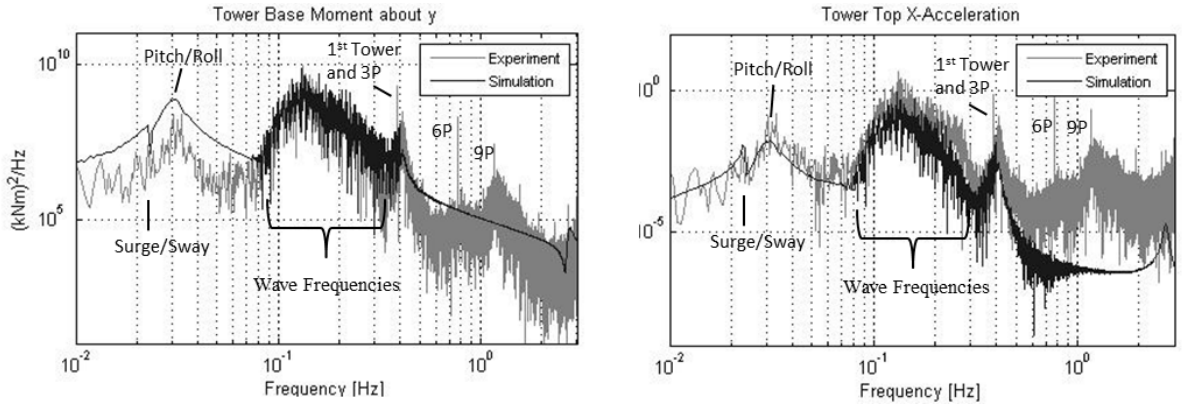

Figure 112: **Response in irregular waves of significant wave height, peak-spectral period, and shape factor of 2 m, 7.5 s, and 2.0, respectively. The horizontal wind speed was 11.23 m/s and the rotor speed was 7.8 rpm.**

The next irregular wave test used for validation consisted of an increased wave height and peak-spectral period of 7.1 m and 12.1 s (0.083 Hz), respectively. The shape factor increased to 2.2 and the wind velocity and rotor speed were kept the same as the previous test, at 11.23 m/s and 7.8 rpm (0.13 Hz). As pitching motions increased, it was expected that yaw-pitch coupling would be present because of rotor gyroscopic forces. Figure 113 shows that the tower-top X-accelerations increased with the higher height and longer period waves relative to the previous test shown in Figure 112. As shown in the PSD of the yaw response, the simulation data showed the expected pronounced peak corresponding to the model's natural platform-pitch frequency. However, rather than having a peak at the pitch frequency, the experimental data has a peak that corresponds with the natural heave frequency of 0.036 Hz. Another clear discrepancy was in the experimental peak yaw response at 0.08 Hz, or roughly the peak spectral wave frequency, which shifted to the right for the simulation response. The reason for these discrepancies is currently unknown. FAST currently utilizes the Massel wave cut-off frequency criterion, for which the JONSWAP wave spectra is truncated at three times the peak-spectral frequency (Jonkman, 2007).

An irregular wave test designed to emulate a survival condition was performed. The wave height and period were increased to 10.5 m and 14.3 s (0.070 Hz), respectively. Constant horizontal wind velocity was increased to 21.8 m/s and the rotor speed was increased to 12.7 rpm (0.21 Hz). The waves propagated at a 45-degree angle to the X-axis; the wind direction stayed at zero degrees.

The X and Y tower-top accelerations, shown on the left-hand side of Figure 114, showed agreement between them as well as between the experimental and simulation data. Unlike previous tests, a distinct peak was present at the 3P frequency for both the experiment and the simulation in both the X- and Y-acceleration plots. The presence of this 3P response in the simulation may have originated from the oblique 45-degree wave propagation direction. A noticeable discrepancy between the experiment and the simulation was the large 6P peaks in the X- and Y-acceleration PSDs that occurred only for the experimental data. Again, this discrepancy was likely caused by variations in wind speed over the rotor for the UMaine test model. Pure vertical shear produces 3P

excitations because each blade passes through a high and low wind speed region of the rotor plane once per revolution. Other nonuniformities in the wind field will result in 6P excitations. More complex variations, as were observed during the wind calibration process at MARIN, could result in a noticeable response at higher order multiples of 3P. Although 3P response may occur in the simulation data because of platform pitching and the resulting misalignment between the rotor plane and the wind vectors, higher order responses will not be present because of the constant wind field modeled in the simulation.

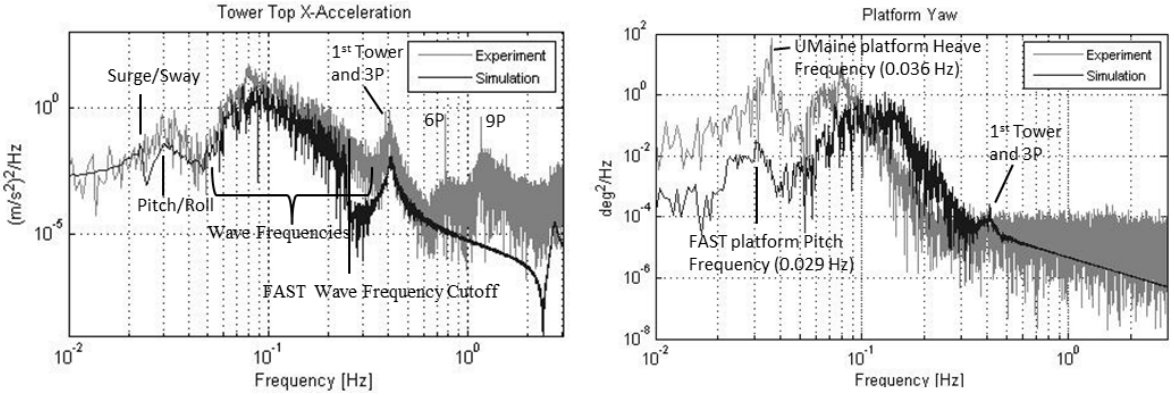

Figure 113: **Response in irregular waves of significant wave height, peak-spectral period, and shape factor of 7.1 m, 12.1 s, and 2.2, respectively. The horizontal wind speed was 11.23 m/s and the rotor speed was 7.8 rpm.**

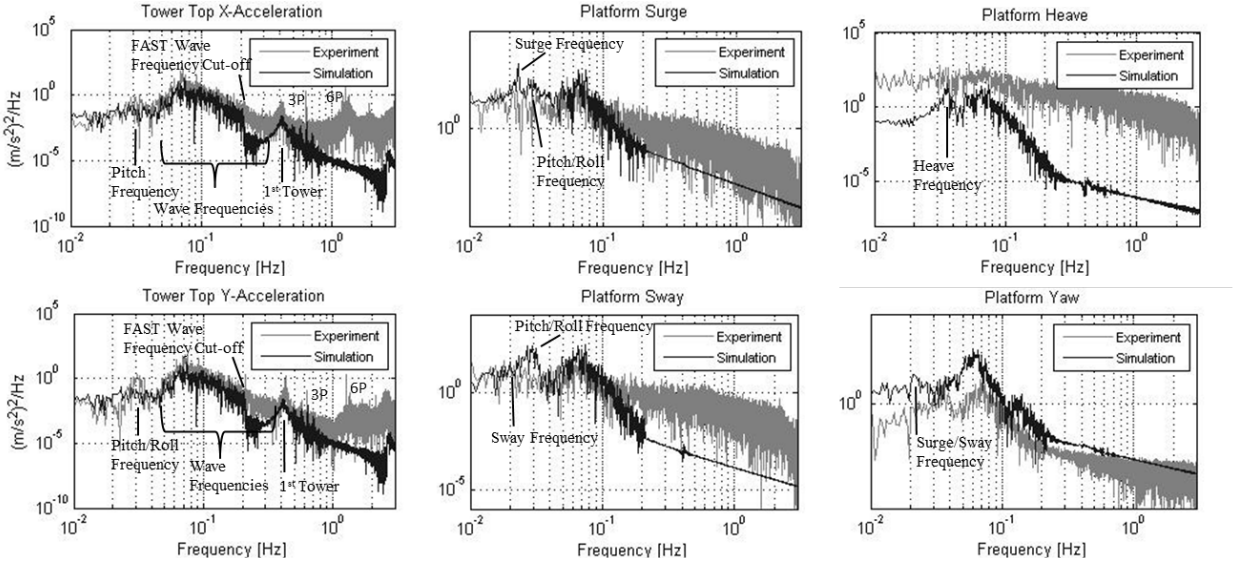

Figure 114: **Response in irregular waves of significant wave height, peak-spectral period, and shape factor of 10.5 m, 14.3 s, and 3.0, respectively. The horizontal wind speed was 21.8 m/s and the rotor speed was 12.7 rpm.**

As with the X and Y tower-top accelerations, surge and sway responses in Figure 114 show agreement between them as well as between the two experimental and simulation data in the range of wave frequencies. However, the simulation data has a distinct peak in surge response, at 0.023 Hz, and in sway, at 0.028 Hz, neither of which were apparent in the experimental data. The 0.023-Hz surge response was easily identified as the FAST model surge/sway natural frequency.

The UMaine test model demonstrated significantly greater response than the FAST model in the region of wave frequencies for heave; the opposite was true for yaw response.

5.4 Improvement of FAST Simulations

In addition to the calibration and validation work shown in the previous sections, further FAST validation of the TLP floating wind turbine system has been performed and is documented in (Prowell *et al.*, 2013). Aside from this continued FAST validation effort, improved and alternate versions of FAST have also been studied. These studies invariably investigate either improved hydrodynamic or mooring capabilities for FAST as these areas possess the most room for improvement. In (Koo *et al.*, 2013), FAST is coupled with Technip's MLTSIM hydrodynamics and dynamic mooring code to perform analysis of the TLP floating wind turbine yielding improved correlation with experimental data. In (Masciola et al., 2013), FAST is linked with the commercial floating structure code OrcaFlex and the semi-submersible system is analyzed. The results show improved correlation, particularly for mooring line tensions, when comparing the simulation and test data. In the next sections, another study investigating improvements to FAST is investigated. This study revisits the semi-submersible validation work given in previous sections and includes the second-order wave-diffraction forces neglected in the standard version of FAST to investigate the importance of including these effects for the purposes of obtaining quality simulation results.

5.4.1 Model Description

In this section, a brief description of the DeepCwind semi-submersible floating wind turbine is presented. In addition, a short discussion on tuning the FAST model with key pieces of test data is also given. This tuning is required to account for unknown test parameters and some imperfections in the numerical model. Figure 115 depicts the degrees of freedom (DOF) and the general wind and wave orientations used in this study.

Froude scaling (e.g. see (Chakrabarti, 1994)) was employed to create a 1/50th-scale model of the DeepCwind semi-submersible, shown in Figure 116, in addition to an assortment of scaled environmental conditions, for testing in the Maritime Research Institute Netherlands (MARIN) offshore basin. The properties of the DeepCwind semi-submersible, and the corresponding test results discussed in this study, are all presented at full scale. More information on the specific scaling methods employed for the DeepCwind tests can be found in (Martin *et al.*, 2012; Jain *et al.*, 2012).

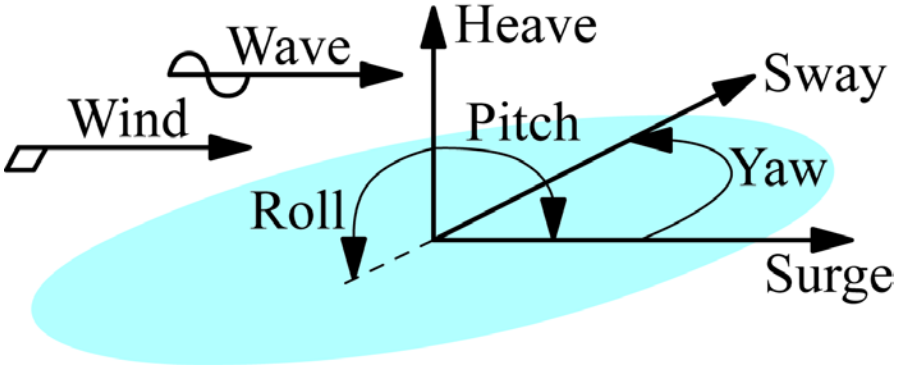

Figure 115: Depiction of degrees of freedom, wind orientations and wave orientations.

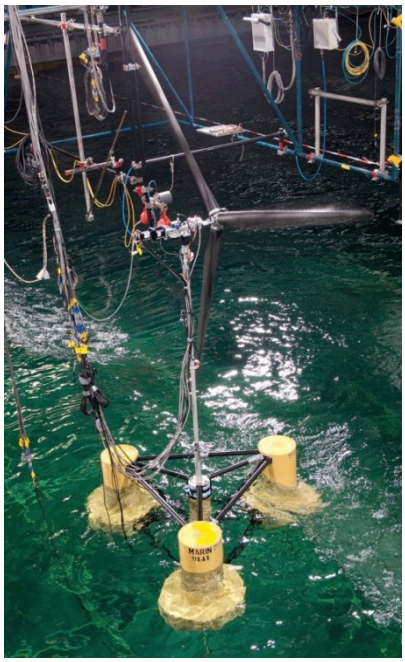

Figure 116: Image of 1/50th-scale model of the DeepCwind semi-submersible floating wind turbine.

As illustrated in Figure 116, the DeepCwind semi-submersible floating platform consists of three outer columns connected through a series of slender pontoons and braces to a central column. The platform, which was designed to be rigid, supports a modified version of the NREL 5-MW reference wind turbine (Jonkman *et al.*, 2007). The wind turbine modifications include zero blade precone, zero shaft-tilt, a slightly larger mass, and finally, rigid blades to eliminate the aero-elastic complexities of flexible blades during testing. The wind turbine is connected to the platform via a flexible tower. The entire system is moored via three slack, catenary lines attached to the outer columns. An overview of key system properties is given in Table 49, Table 50 and Table 51. Wind turbine and tower properties are given in Table 49, floating platform properties in Table 50, and mooring properties in Table 51. Additional information on system properties, such as platform geometry, hydrodynamic parameters, and mooring restoring forces, can be found in (Coulling *et al.*, 2013; Koo *et al.*, 2012). Information on the model wind turbine performance is detailed in (Coulling *et al.*, 2013; Martin *et al.*, 2012).

Table 49: Wind turbine and tower gross properties.

Rotor Orientation, Configuration	Upwind, 3 Blades
Rotor, Hub Diameter	126.0 m, 3.0 m
Hub Height Above Still-water Line (SWL)	90.0 m
Height of Tower-Top Flange Above SWL	87.6 m
Overhang, Shaft Tilt, Precone	10.58 m, 0°, 0°
Vertical Distance Along Tower Centerline Between Tower Top and Shaft	2.4 m
Total Tower-Top Mass	397,160 kg
Tower Height	77.6 m
Tower-Base Elevation Above SWL	10.0 m
Total Tower Mass	302,240 kg

Table 50: Floating platform gross properties.

Total Draft	20.0 m
Elevation to Platform Top (Tower Base) Above SWL	10.0 m
Platform Mass, Including Ballast	13,444,000 kg
Displacement	13,986.8 m^3
Center of Mass (CM) Location Below SWL Along Platform Centerline	14.4 m
Platform Roll Inertia About CM	8.011×10^9 kgm^2
Platform Pitch Inertia About CM	8.011×10^9 kgm^2
Platform Yaw Inertia About Platform Centerline	1.391×10^{10} kgm^2

Table 51: Mooring system properties.

Number of Mooring Lines	3
Angle Between Adjacent Lines	120°
Depth to Anchors Below SWL (Water Depth)	200.0 m
Depth to Fairleads Below SWL	14.0 m
Radius to Anchors from Platform Centerline	837.6 m
Radius to Fairleads from Platform Centerline	40.868 m
Unstretched Mooring Line Length	835.5 m
Equivalent Mooring Line Mass in Water	108.63 kg/m
Equivalent Mooring Line Cross Section Extensional Stiffness	753.6×10^6 N

As a final step in the completion of the FAST floating wind turbine model, certain aspects of the model must be tuned. These include wind turbine aerodynamics, tower-bending dynamics, and platform hydrodynamic damping. Tuning of the wind turbine aerodynamics is required to emulate the correct wind turbine torque, and more importantly, the thrust because this is the major aerodynamic global response driver, under multiple tip-speed ratios. The tuning is performed through a numerical optimization procedure that tailors the wind blade airfoil section lift and drag coefficients, initially created with XFOIL (Drela, 1989), to match the experimentally measured wind turbine performance. A comparison of the measured and tuned wind turbine thrust curves for a steady hub-height wind speed of 21.80 m/s is given in Figure 117. A complete summary of the wind turbine performance tuning is covered in (Stewart *et al.*, 2012; Coulling *et al.*, 2013).

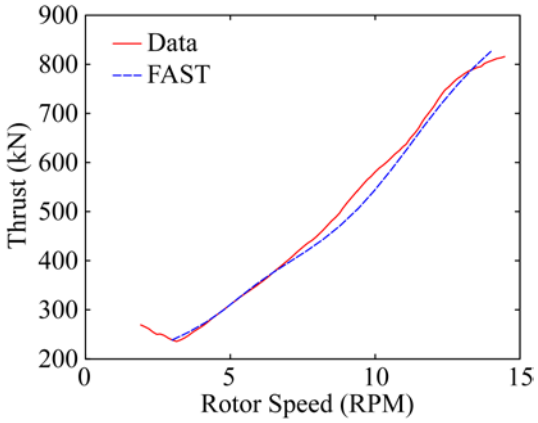

Figure 117: Comparison of wind turbine thrust data and calibrated FAST results under a steady wind of 21.80 m/s.

Next, the tuning of the FAST tower inputs is discussed. After generating and inputting the distributed tower properties and finite-element-method-generated tower mode shapes required for FAST simulations, FAST's modal stiffness tuners (Jonkman and Buhl, 2005) were altered to match the experimentally measured, fundamental tower-bending frequencies. This process, detailed in (Coulling *et al.*, 2013), yields fundamental tower-bending frequencies in the fore-aft and side-side directions of 0.35 Hz and 0.38 Hz respectively.

To complete the tuning of the FAST model, a quadratic hydrodynamic drag damping model is added to the FAST model to account for the omitted viscous drag, and the coefficients are tuned to emulate rigid-body motion, free-decay experimental results. The tuning of the drag model, which augments the radiation damping found in the standard version of FAST, is documented in (Coulling *et al.*, 2013). Because the surge response is of primary concern in this work, a comparison of the surge DOF damping ratio as a function of amplitude from experiments and the tuned FAST model is given in Figure 118. The surge quadratic-drag damping coefficient employed in (Coulling *et al.*, 2013) (1.25×10^6 Ns^2/m^2) corresponds to the simulation in Figure 118, which correlates well with the test data for modest surge amplitude motions (1.5 to 3.5 m). In this work, as will be discussed in a later section, a mild, operational sea state is considered wherein the quadratic-drag damping coefficient used in (Coulling *et al.*, 2013) tends to over-predict the surge damping for the small surge motions the sea produces. Therefore, a second surge quadratic-drag damping coefficient will be investigated that is 10% of that used in (Coulling *et al.*, 2013) (1.25×10^5 Ns^2/m^2). The free decay simulation corresponding to this reduced surge drag damping coefficient is also shown in Figure 118. As can be seen in the figure, the reduced quadratic-drag coefficient produces a better fit to the experimental data for surge amplitudes of 1 m or less.

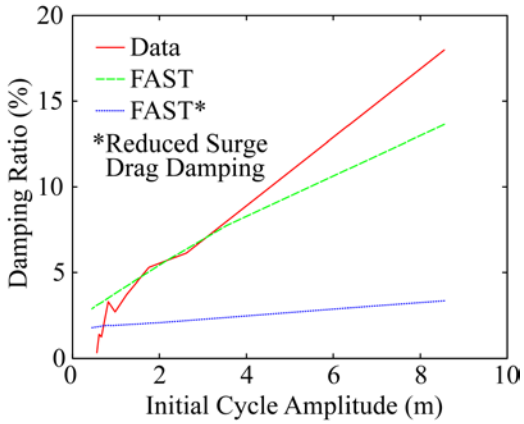

Figure 118: Comparison of surge free-decay damping response from test data and FAST simulations.

To complete this section, a comparison of the rigid-body natural periods as obtained from test data and FAST simulations is given in Table 52. As the table shows, there is good agreement between the test data and FAST predictions.

Table 52: Rigid-body natural periods obtained from test data and FAST simulations.

DOF	Data (s)	FAST (s)
Surge	107	107
Sway	112	113
Heave	17.5	17.3
Roll	26.9	26.7
Pitch	26.8	26.8
Yaw	82.3	82.7

5.4.1 Second-order Difference-Frequency Wave-diffraction Force Formulation

In the current standard version of FAST, the true linear time-domain hydrodynamics are implemented (Jonkman and Buhl, 2005). This formulation, however, omits the nonlinear, second-order wave diffraction effects that occur at the sum and difference of the frequency components in the incident waves (e.g., see (Kim and Yue, 1991)). As observed in (Goupee *et al.*, 2012 OTC; Koo *et al.*, 2012; Goupee *et al.*, 2012), the second-order difference-frequency wave-diffraction forces are important for properly simulating the global response of the DeepCwind semi-submersible. In this study, these second-order wave-diffraction forces are included in the custom FAST tool in order to assess the importance of including these effects in validating the DeepCwind semi-submersible numerical model. The remainder of this section outlines the formulation of the second-order wave-diffraction force implementation that is employed in the custom FAST tool.

To begin, we note that the time-varying wave-surface elevation $h(t)$ can be written as the sum of its wave frequency components in the form

$$h(t) = Re \sum_{n=1}^{N} a_n e^{i\omega_n t},$$

where N is the number of frequency components, a_n is the n^{th} complex-valued wave component amplitude (including phase), ω_n is the n^{th} wave component frequency, t is time and i is imaginary unity. With the coefficients a_n in the above equation obtained from a simple discrete Fourier transform analysis of the experimentally measured calibrated wave-elevation time series, the second-order difference-frequency wave diffraction force $F_j^D(t)$ can be computed with the equation (e.g., see (Langley, 1986))

$$F_j^D(t) = Re \sum_{n=1}^{N} \sum_{m=1}^{N} a_n a_m^* D_{nm}^{(j)} e^{i(\omega_n - \omega_m)t},$$

where $D_{nm}^{(j)}$ is the complex difference-frequency second-order transfer function for the j^{th} DOF and the superscript * denotes the complex conjugate. As shown in (Langley, 2012), the above equation is often separated into terms that are constant (mean-drift force) and those that are not (slowly-varying force). This is accomplished by first separating the preceding equation into three

regions: $n = m$, $n > m$, and $n < m$. Upon setting $k = n - m$, noting that $D_{nm}^{*(j)} = D_{mn}^{(j)}$, and performing a series of straightforward manipulations, the desired result is produced:

$$F_j^D(t) = \sum_{n=1}^{N} |a_n|^2 D_{nn}^{(j)} + Re \sum_{k=1}^{N-1} X_k^{(j)} e^{i\omega_k t},$$

where the first term is the mean-drift force, the second is the slowly varying force and $X_k^{(j)}$ is computed as

$$X_k^{(j)} = 2 \sum_{m=1}^{N-k} a_{m+k} a_m^* D_{m+k,m}^{(j)} e^{i\omega_k t}.$$

For implementation in the custom FAST tool, only those second-order wave diffraction forces associated with the surge DOF ($j = 1$) are included because they are the most prominent second-order wave-diffraction forces for the DeepCwind semi-submersible.

To carry out the calculation of $F_j^D(t)$, the quantities $D_{nm}^{(j)}$ must be obtained. To determine the coefficients $D_{nm}^{(j)}$, use is made of the mean-drift coefficients $D_{nn}^{(j)}$ derived from a first-order WAMIT analysis (Lee and Newman, 2006) in conjunction with Newman's approximation (Newman, 1974). The particular formulation used is that developed in (Standing *et al*., 1987), which approximates $D_{nm}^{(j)}$ from $D_{nn}^{(j)}$ using the relation

$$D_{nm}^{(j)} =$$

$$\begin{cases} sgn\left(D_{nn}^{(j)}\right)\sqrt{\left|D_{nn}^{(j)} D_{mm}^{(j)}\right|} \; if \; sgn\left(D_{nn}^{(j)}\right) = sgn\left(D_{mm}^{(j)}\right) \\ 0 \; if \; sgn\left(D_{nn}^{(j)}\right) \neq sgn\left(D_{mm}^{(j)}\right) \end{cases},$$

where $sgn(\cdot)$ indicates the sign (either positive or negative) of the argument. It is worth stating that it would be best if $D_{nm}^{(j)}$ were computed from a second-order WAMIT analysis. However, Newman's approximation is justified for this work for the following two reasons:

1. Performing the second-order WAMIT analysis requires significant computational expense, whereas computing the coefficients $D_{nn}^{(j)}$ requires solution of only the first-order wave-diffraction problem.
2. Assuming that the second-order transfer function $D_{nm}^{(j)}$ is continuous, and also assuming that only slowly-varying loads associated with resonance of the surge DOF (natural frequency of 0.0093 Hz) are important (i.e., only $D_{nm}^{(j)}$ near the diagonal $D_{nn}^{(j)}$ terms need be approximated accurately).

Therefore, Newman's approximation should yield suitable results for the DeepCwind semi-submersible study conducted here.

To complete this section, the magnitude of the approximated second-order transfer function $D_{nm}^{(1)} = D^{(1)}(\omega_1, \omega_2)$ is shown via a surface plot in Figure 119.

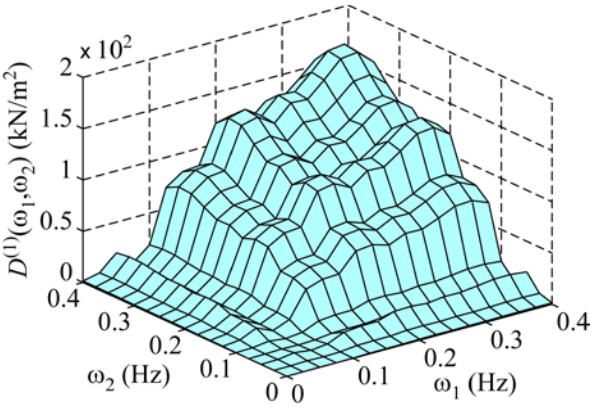

Figure 119: Surface plot of the $D^{(1)}(\omega_1, \omega_2)$ second-order difference-frequency transfer function.

5.4.2 Environmental Conditions

To investigate the impact of including second-order difference-frequency wave-diffraction forcing in FAST for analyzing the DeepCwind semi-submersible, a particular wind and wave condition is chosen. The details of these environmental conditions comprise the remainder of this section.

In this analysis, the chosen wind condition is temporally dynamic and follows a Norwegian Petroleum Directorate (NPD) (API, 2000) spectrum. In the basin, the mean wind speed at the hub height was U_m = 20.6 m/s, the standard deviation was 2.04 m/s, the maximum wind speed was 28.7 m/s, and the minimum wind speed was 12.9 m/s. This wind is chosen because it produces thrust loads similar to those experienced in the rated wind speed condition of the NREL 5-MW reference wind turbine when paired with the low thrust coefficient turbine employed in the wind/wave basin tests (Martin *et al*., 2012).

For the purposes of simulation, FAST hub-height wind files are employed which possess a constant spatial variation in wind profile, albeit, wind speed magnitudes that are time-varying. Based on surveys of the wind-generation machine output, which were recorded in the wind/wave basin (Goupee *et al*., 2012 OTC; Koo *et al*., 2012), the FAST hub-height wind file is created by multiplying the measured hub-height velocity by 0.952 and employing a wind shear exponent of 0.0912. The tested wind field possessed some spatial variation in wind speed. Hence, these hub-height wind file choices yielded the best possible representation of the wind field utilized during testing, using only the simple hub-height wind file option in the FAST simulations. The spectrum of the NPD wind used in this study is given in Figure 120.

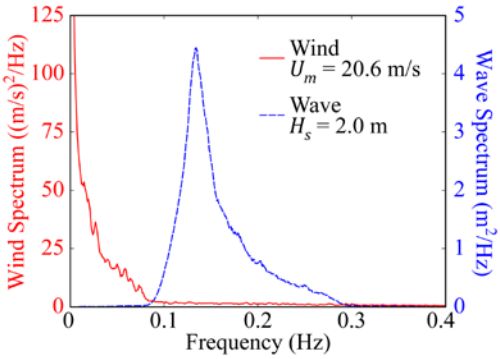

Figure 120: Spectra for the U_m = 20.6 m/s NPD dynamic wind and H_s = 2.0 m JONSWAP wave conditions.

Regarding the wave condition, an operational sea with a significant wave height of H_s = 2.0 m and a peak-spectral period of T_p = 7.5 s following a Joint North Sea Wave Project (JONSWAP) (IEC, 2009) spectrum is chosen for this work. This condition is selected because it produced large responses associated with the second-order difference-frequency wave-diffraction forces relative to those caused by the linear wave forces. In addition, this sea state will produce wave loadings that are in decent proportion to the wind loads expected with the chosen wind, based on typical joint probabilities (e.g., see (Jonkman, 2007)). For the waves tested in the basin, the wave-elevation standard deviation was 0.49 m, the maximum crest 2.14 m, the minimum trough 1.87 m and the maximum wave height 3.64 m. The spectrum of the JONSWAP wave considered here is given in Figure 120.

5.4.3 Wave-only Comparisons

In this section, the calibrated FAST model is used to simulate the response of the DeepCwind semi-submersible subjected to the H_s = 2.0 m sea state in the absence of wind. Because there is no wind, the wind turbine rotor is parked (0 rpm) and the blades are feathered. Simulations are conducted with and without the inclusion of the second-order difference-frequency wave-diffraction forces and compared to test data. All simulations are 3 hr in length with 1000 s of additional settling-in time prior to recording data. This timing is similar to the actual model tests, which were 3 hr in length with 1800 s of settling-in time.

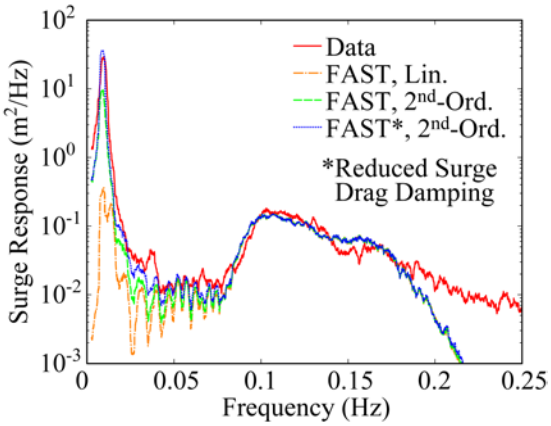

Figure 121: Comparison of surge frequency-domain response from test data and three different FAST simulations.

A comparison of the surge frequency-domain response, computed as a power spectral density, is given in Figure 121 for the test data and three different FAST simulations. The FAST simulations consist of a standard analysis with linear wave-diffraction wave forces, an analysis including the second-order difference-frequency wave-diffraction forces, and lastly, another analysis including the second-order wave forces, albeit with a reduction in the surge quadratic-drag model coefficient to 10% of the initial calibrated value from (Coulling *et al.*, 2013). Noting that the ordinate axis is displayed on a logarithmic scale, it is clearly seen by the test data shown in Figure 121 that the low-frequency response at the rigid-body surge natural frequency (0.0093 Hz) dominates the entire surge response of the system. When comparing the test data to the FAST analyses, it is evident that the FAST model that uses only linear wave-diffraction forcing severely under-predicts the low-frequency response of the system. Including the second-order difference-frequency wave-diffraction forces improves the correlation between the simulation and test data significantly, as seen in Figure 121. However, because the large response is created via resonance with relatively small second-order wave loads, the magnitude of the response at the surge natural frequency is

highly dependent on the damping employed in the FAST model. As seen in Figure 121, the model using the calibrated surge drag model coefficient of (Coulling *et al.*, 2013)under-predicts the response near surge resonance. Utilization of the reduced quadratic-drag model damping coefficient, which was discussed in the Model Description section, yields simulation results that compare much better with experimental values, as shown in Figure 121. The final observation to be made from Figure 121 is that the test data and all simulations correspond well with one another in the wave-energy frequency range (approximately 0.1 Hz to 0.3 Hz shown in Figure 120). Although there is some discrepancy at frequencies higher than 0.2 Hz, the magnitude of the response is much lower and the error appears larger due to the log scaling.

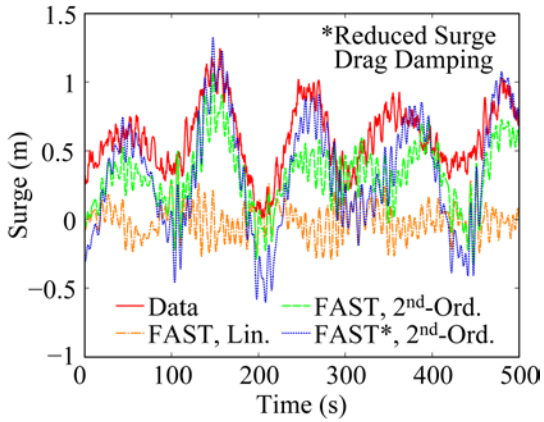

Figure 122: Comparison of surge time-series response for 0 to 500 s from test data and three different FAST simulations.

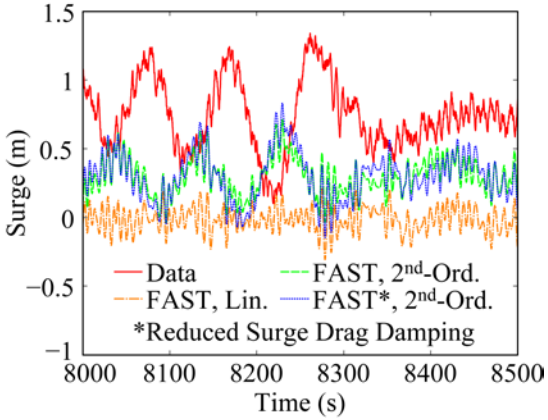

Figure 123: Comparison of surge time-series response for 8000 to 8500 s from test data and three different FAST simulations.

To continue the wave-only comparison, Figure 122 and Figure 123 show two examples of surge response time-series comparisons between the test data and various FAST simulations for the same H_s = 2.0 m sea state. As can be seen in the figures, the inclusion of the second-order difference-frequency forces greatly improves the correlation between the test data and simulations. This stated, the simulations that include the second-order wave-diffraction effects using Newman's approximation do not always capture the appropriate local time-domain response that is measured in the basin. As can be seen in Figure 122, the FAST simulation over-predicts the amplitude of the second-order response in the noted time range 0 to 500 s, and in Figure 123, the FAST simulation

under-predicts the second-order wave-diffraction-associated response and predicts the incorrect phase of this response in another time range (8000 to 8500 s) of the same simulation.

As a next step in this wave-only simulation discussion, the statistics for the surge response from the test data and three simulations is given in Table 53. As shown in the table, without inclusion of the second-order difference-frequency wave-diffraction forces, very poor predictions of the surge behavior are obtained.

Table 53: Surge motion statistics for the wave-only case.

Statistic	Data	Linear	2nd-Ord.	2nd-Ord.*
Mean (m)	0.735	0.000	0.307	0.307
Std. Dev. (m)	0.354	0.103	0.218	0.343
Max. (m)	2.200	0.486	1.137	1.385
Min. (m)	-0.507	-0.382	-0.378	-0.711
Range (m)	2.707	0.868	1.515	2.096

*Reduced Surge Drag Damping

For the simulation using only linear wave-diffraction forces, the mean surge is zero, and the standard deviation and range of the surge DOF over the simulation are only 29.1% and 32.1% of those measured from the test. For the best simulation, which includes the reduced surge quadratic-drag damping coefficient, the surge mean, standard deviation, and range are 42.3%, 96.9%, and 77.4% of the experimental values, respectively.

To complete the wave-only comparison, the response of the upwind mooring line (which lies along the negative surge axis) fairlead tension is investigated. Figure 124 compares the test data and the three FAST simulations for the fairlead tension in the frequency domain. Table 54 compares the fairlead tension statistics of the test data and three simulations. As can be seen in Figure 124, the frequency-domain fairlead tension comparison is similar to the surge comparison at low frequencies.

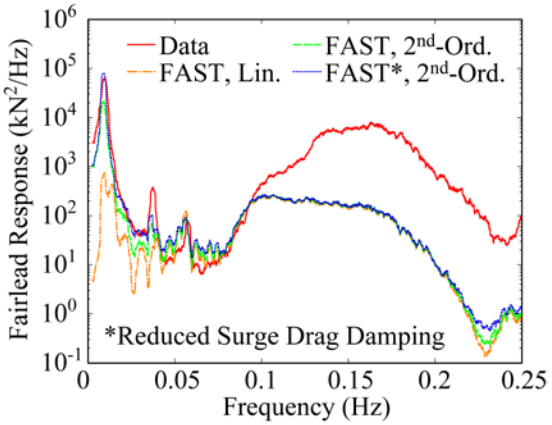

Figure 124: Comparison of upwind mooring line fairlead tension response from test data and three different FAST simulations.

Table 54: Upwind fairlead tension force statistics for the wave only case.

Statistic	Data	Linear	2nd-Ord.	2nd-Ord.*
Mean (kN)	1161	1105	1120	1120
Std. Dev. (kN)	18.6	4.7	10.1	16.0
Max. (kN)	1247	1128	1160	1173
Min. (kN)	1097	1089	1090	1075
Range (kN)	150.0	39.0	70.0	98.0

*Reduced Surge Drag Damping

This indicates that the mooring tension response is accurately predicted for the DeepCwind semi-submersible at low frequencies if the second-order difference-frequency wave-diffraction forces are included. However, the fairlead tension response in the linear wave-energy frequency range is significantly under-predicted. This is theorized to be a product of using a quasi-static catenary line solver in FAST (Jonkman, 2007), which ignores mooring line dynamics and direct wave particle excitation. The interplay of improved low-frequency prediction and poor linear wave-energy frequency range simulation is captured in the statistics of Table 54. For the best simulation, which includes second-order wave-diffraction loads and a reduced quadratic-drag damping coefficient, the standard deviation and range are 86.0% and 65.3%, respectively, of the experimental values. While these are improvements compared to the simulation that includes only linear wave loads, these improvements are less than what was found for the surge response earlier in this section.

5.4.4 Combined Wind/Wave Comparisons

With the wave-only comparisons complete, this section describes the investigation of the interaction of the dynamic wind and second-order difference-frequency wave-diffraction loads, both of which influence the global response of the floating structure at low frequencies. The investigation will be conducted by comparing the response of the DeepCwind semi-submersible subjected to the following conditions: NPD wind-only, the irregular wave-only, and the simultaneous application of the wind and wave. Note that the U_m = 20.6 m/s dynamic wind and H_s = 2.0 m irregular wave are detailed in the Environmental Conditions section. For tests and simulations with wind, the rotor blade pitch is fixed in the operational position and the rotor speed is held constant at 12.7 rpm. For the test and simulations without wind, the blades are feathered and the rotor is parked. Finally, all simulations use the reduced surge quadratic-drag damping coefficient of 1.25×10^5 Ns^2/m^2.

Figure 125 depicts the frequency-domain surge response of the wind-only, wave-only and combined wind and wave case as computed from the model test data. As can be seen by comparing the combined condition case to the other two scenarios in the figure, the dynamic wind loads control the response of the DeepCwind semi-submersible for frequencies less than 0.05 Hz, not the second-order wave-diffraction loads for the environments considered here. For frequencies between 0.05 to 0.25 Hz, the linear wave loads understandably control the response of the system.

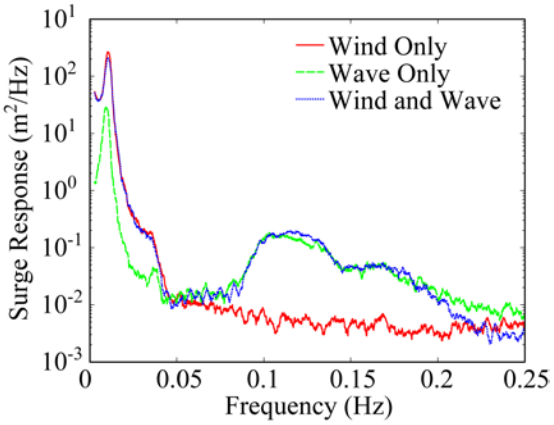

Figure 125: Comparison of model test data surge response from wind-only, wave-only, and combined wind and wave conditions.

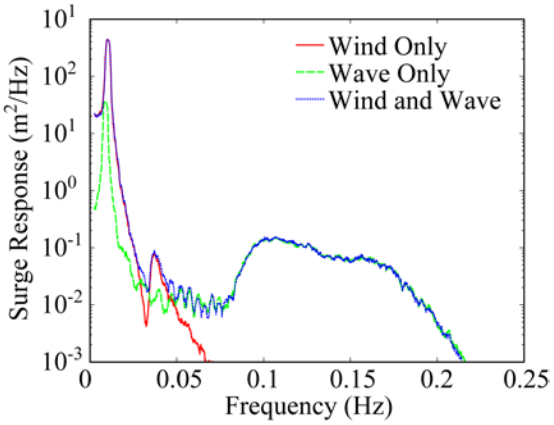

Figure 126: Comparison of FAST simulation surge response from wind-only, wave-only and combined wind and wave conditions.

With the comparative responses and trends established from model test data, the same three identical cases are simulated using the custom FAST tool. The frequency-domain surge response for the three cases, as computed from FAST simulations, is given in Figure 126. As can be seen by comparing Figure 125 and Figure 126, it is clear that FAST captures the same trends observed in the model test data. For low frequencies, the dynamic wind loads control the response of the system, and for frequencies above 0.05 Hz, the linear wave loads dictate the DeepCwind semi-submersible surge response. To further emphasize the correlation between the combined wind and wave case and the model test data and simulation, the surge motion statistics for the combined environment cases are given in Table 55. Table 55 clearly shows a fair agreement between the test data and the simulation including second-order wave-diffraction forces for this condition. However, comparing the values in Table 53 and Table 55 indicates that most of the response in the combined wind and wave case is driven by the wind loads because the mean, standard deviation, and maximum values are all much larger when the wind loads are present.

Table 55: Surge motion statistics for the combined wind and wave case.

Statistic	Data	Linear	2nd-Ord.*
Mean (m)	8.153	7.208	7.436
Std. Dev. (m)	1.131	1.221	1.232
Max. (m)	11.54	11.06	10.99
Min. (m)	4.281	3.073	2.882
Range (m)	7.259	7.987	8.108

*Reduced Surge Drag Damping

To complete this section, an additional simulation is performed for the combined wind and wave case, including only the linear wave-diffraction forces. The surge response statistics for this case are also given in Table 55, alongside the test data and simulation with second-order difference-frequency wave-diffraction forcing. As the table clearly shows, neglecting the second-order wave-diffraction forcing for the combined wind and wave case studied here is not of significant concern for the DeepCwind semi-submersible. Excluding the second-order difference-frequency wave-diffraction forces in the simulation results in reductions of only 3.1% for the mean surge, 0.9% for the surge standard deviation, and 1.5% for the surge range.

6 Development of Improved Wind Turbine Designs for Model Testing of Floating Wind Turbines

As shown earlier in this report, there are difficulties associated with performing Froude-scale wind wave basin tests since the low Reynolds numbers make for very poor performing wind turbines if the blade geometry is preserved as is customary for such experiments. In this section, the option of redesigning the wind turbine geometry to preserve wind turbine thrust is investigated. This is ideal as the correct environments and rotor speeds can be used. In addition, an improved wind turbine design can yield significantly more power production during the model tests permitting possibilities such as utilizing realistic blade pitch control to control power output in post-rated wind speed regions as would be done in a real floating wind turbine. In the next sections, the design methodology and testing of a redesigned rotor for Froude-scale model testing of floating wind turbines is presented.

6.1 Design Methodology

In this section, a brief discussion of the design methodologies employed for designing improved performance wind turbine blades for Froude model-scale testing is given. Along with outlining the objectives and techniques used for designing a suitable model-scale wind turbine for wind/wave basin testing, an overview of the numerical tools employed in the design of the blades is also presented. A review of Froude scaling relationships from prototype to model scale for floating wind turbines is given in (Martin *et al*., 2012; Jain *et al*., 2012).

As noted in (Martin *et al*., 2012), proper emulation of the prototype thrust in the Froude-scale experiment is most important as it drives most of the wind-induced global response of a floating wind turbine. This is due the fact that the floating wind turbine overturning moment due to thrust is more than an order of magnitude larger than that caused by the rotor torque. Therefore, the first objective of redesigning a wind turbine blade considered here is matching the thrust coefficient C_T for the low-Reynolds number, Froude-scale conditions encountered in the wind/wave basin. The thrust coefficient is defined as

$$C_T = \frac{T}{\frac{1}{2}\rho A U^2},$$

where T is the rotor thrust, ρ is the density of air, A is the swept area of the rotor and U is the mean wind speed. More specifically, it is desirable to reproduce the thrust coefficient of the prototype turbine over a larger number of tip-speed ratios TSR. The tip-speed ratio is a non-dimensional measure of rotor angular speed and is defined as

$$TSR = \frac{\omega R}{U},$$

where ω is the rotor angular speed and R is the wind turbine rotor radius.

The second objective is to improve the rotor performance coefficient $C_{\square}$ as much as possible in hopes of approaching the prototype non-dimensional power (and hence torque) specification. Matching the performance coefficient of the prototype over a range of operational TSR values is likely not achievable due to the elevated airfoil drag coefficients at the low Froude-scale Reynolds numbers (Martin *et al*., 2012; Jain *et al*., 2012). However, model wind turbines which exhibit C_P values closer to the prototype value will permit a much broader and more useful class of wind/wave basin model tests for floating wind turbines by permitting studies investigating the interplay of wind turbine controls, global system motion behavior and rotor power production. The performance coefficient is computed as

$$C_P = \frac{P}{\frac{1}{2}\rho A U^3},$$

where P is rotor power.

With the basic objectives defined, a discussion of the wind blade variables targeted for tuning the performance of the rotor at low Reynolds numbers is now given. Variables which are held constant include blade length, gross blade mass properties and rotor operational speeds. Maintaining these quantities will yield a rotor that produces the correct gyroscopic moments during motion of the floating platform as well as maintain the correct Froude-scale TSR values when the model is subjected to proper Froude-scale winds. As discussed in (Martin *et al*., 2012), variables which are considered for alteration for the purposes of meeting the aforementioned C_T and C_P objectives include airfoil type, airfoil section chord length and airfoil section blade twist. For the purposes of this work, the blades were designed to be rigid in order to reduce aeroelastic effects. Flexible blade effects could be incorporated into the procedures discussed, but would require more sophisticated modeling and instrumentation to deal with the aeroelastic effects.

Regarding the first variable, airfoil type, airfoil sections are selected which are generally thinner than those found in commercial wind turbines with preference given to sections designed to perform at low Reynolds numbers (e.g., the Drela AG04 airfoil selected in (Martin *et al*., 2012)). In addition, the thick shapes located near the root of commercial wind turbine blades, whose shapes are dictated by structural factors more than aerodynamic performance, are eliminated and replaced with the previously mentioned thin airfoil sections. The remaining two variables, chord length and blade twist, permit sufficient flexibility to closely emulate the $C_T(TSR)$ behavior of the prototype over a range of desired TSR values. Ideally, this will be performed in a manner that matches the $C_T(TSR)$ behavior of the prototype while producing $C_P(TSR)$ trends that are a fair representation of the prototype.

To ensure a robust design that will not be prone to laminar separation at model scale, the target airfoil section lift coefficients at the design condition should be much less than are used for full-scale wind turbine designs. For example, the blade lift coefficients for the design condition of the model-scale rotor may be only 0.5 or less, whereas the prototype values for the commercial wind

turbine may be closer to 1.0. By choosing lower lift coefficients for the model-scale wind turbine, the probability that the physical model-scale wind turbine will avoid laminar stall issues and perform as intended is much higher. This, however, necessitates larger chords for the model-scale wind turbine than would be expected based on Froude scaling.

To execute such a design, one must couple a wind turbine aerodynamic simulation tool with a numerical optimization technique that tailors parameterized features of the wind turbine blade, e.g. blade twist and chord distribution details. For example, the design detailed in a subsequent section was created by coupling NREL's WT_Perf analysis tool (Buhl, 2004) with a custom multi-objective genetic algorithm optimization code (e.g. see (Deb 2001)). With the numerical tools in place, a possible optimization problem with objectives f_i and constraints g_i to be considered for creating the desired model-scale wind blade is as follows:

$$
\begin{aligned}
\text{Find} \quad & \theta(r), \;\; 0 \le r \le R, \\
& c(r), \;\; 0 \le r \le R, \\
\text{Minimize} \quad & f_1(\theta, c) = \int_{TSR_L}^{TSR_U} \left| C_T(TSR) - C_T^{pr}(TSR) \right| dTSR, \\
& f_2(\theta, c) = \int_{TSR_L}^{TSR_U} \left| C_P(TSR) - C_P^{pr}(TSR) \right| dTSR, \\
\text{Subject to} \quad & g_1(\theta, c) = C_L(r, TSR^*) \le C_L^{max}, \;\; 0 \le r \le R, \\
& \theta_L(r) \le \theta(r) \le \theta_U(r), \\
& c_L(r) \le c(r) \le c_U(r),
\end{aligned}
$$

where r is the blade radial coordinate, R is the blade radius, $\theta(r)$ is the blade twist distribution, $c(r)$ is the chord distribution, TSR_L and TSR_U define the TSR range over which the thrust and performance coefficients are to be matched, $C_T^{pr}(TSR)$ and $C_P^{pr}(TSR)$ are the full-scale prototype target behaviors, $C_L(r, TSR^*)$ is the blade lift coefficient distribution at the design tip-speed ratio TSR^*, C_L^{max} is the prescribed maximum lift coefficient at TSR^*, $\theta_L(r)$ and $\theta_U(r)$ define the lower and upper bounds, respectively, of the twist distribution and $c_L(r)$ and $c_U(r)$ are the lower and upper bounds, respectively, of the chord distribution. There are several options for parameterizing the design variables $\theta(r)$ and $c(r)$ in addition to some leeway in the choice of TSR_L, TSR_U, TSR^*, C_L^{max}, $\theta_L(r)$, $\theta_U(r)$, $c_L(r)$ and $c_U(r)$. An obvious choice for parameterizing the design variables is to tailor the blade twist and chord lengths at the discrete locations used in typical blade element momentum theory numerical analysis. The choice of the integration limits TSR_L and TSR_U will be dictated by the range of TSR values expected in the test matrix of the model test program. C_L^{max} should be less than the full scale design (e.g., 0.5 or less) and TSR^* should be selected near the operating TSR of the wind turbine. Regarding the choice of the remaining bounds on blade twist and chord design variables, sufficient latitude should be given to search the design space. This stated, searches should occur in the neighborhood of optimal twist and chord distributions (e.g. see (Manwell *et al*., 2009) with the chords in the power-producing outer portions of the blade being at a minimum slightly larger than the Froude-scale values. Lastly, the previous problem statement structured as a multi-objective optimization problem which will produce multiple Pareto-optimal solutions to choose from. The final choice should favor designs that minimize the discrepancy between the model and prototype thrust behaviors as these will be the best choice for Froude-scale, floating wind turbine global performance wind/wave model tests.

6.2 Wind Blade Design Specifications

In this section, the blade designs considered in this work are presented. The first is the 1/50th-scale, geometrically-similar NREL 5 MW reference wind turbine blade originally presented in (Martin *et al.*, 2012). The second design is based on the Drela AG24 airfoil, which is of the same family of low-Reynolds number airfoils as the Drela AG04 proposed in (Martin *et al*., 2012). It should be noted that the aerodynamic performance of the rotors is the primary concern in this work and that no attempt has been made to maintain the aforementioned distributed blade mass properties as suggested in the design methodology section of this work. Once a design has been proven, appropriate blade mass properties can be obtained utilizing the light-weight materials and manufacturing methods that have been demonstrated in (Martin *et al*., 2012).

First, select details concerning the geometrically-scaled NREL 5 MW reference wind turbine blade are presented. For brevity, only an overview of the specifications is presented. An exhaustive description of the design can be found in (Martin *et al*., 2012). To begin, an image of the geometrically-scaled NREL 5 MW reference wind turbine blade is shown in Figure 127. The blade

Figure 127: Images of a) redesigned, thrust-matched blade and b) original geometrically-scaled, NREL 5 MW reference wind turbine blade.

possesses a chord at 70% radius that is 4.8% of the blade radius. The thickness of the airfoil sections, which are comprised of the NACA 64-618 airfoil for the outer 30% of the blade and various Delft University and Cylindrical sections for the remainder of the blade, range in thickness from 18% to 100%.

With an overview of the model-scale NREL 5 MW reference wind turbine blade given, the details of the redesigned blade considered in this work are now presented. To design the blade, the low-Reynolds number Drela AG24 airfoil was chosen. Optimization of the airfoil selection procedure is possible, but beyond the scope of this work. This aside, the Drela AG24 design was chosen in lieu of the Drela AG04 utilized in (Martin *et al*., 2012) as it offers a larger thickness which yields greater structural stiffness for the small model-scale components fabricated for testing. An image of the airfoil section, which is 8.4% thick, is given in Figure 128.

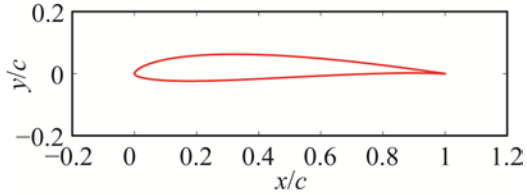

Figure 128: Image of normalized Drela AG24 airfoil section

This section was employed throughout the entire thrust-matched wind turbine design with the exception being near the root of the blade, where cylindrical sections were utilized as strength was

required for the physical blade-to-hub connection. The airfoil lift and drag coefficients required for analysis with WT_Perf for the Drela AG24 section were created using XFOIL (Drela, 1989) and NREL's AirfoilPrep tool (Hansen, 2012). The XFOIL analysis, performed at comparable model-scale Reynolds numbers, provided the lift and drag curves for small angles of attack α. The AirfoilPrep tool was then used to extend results for all possible angles of attack in addition to including rotational augmentation corrections. The obtained lift coefficients C_L and drag coefficients C_D are given in Figure 129. All cylindrical sections in the WT_Perf analyses used C_L = 0.0 and C_D = 1.0.

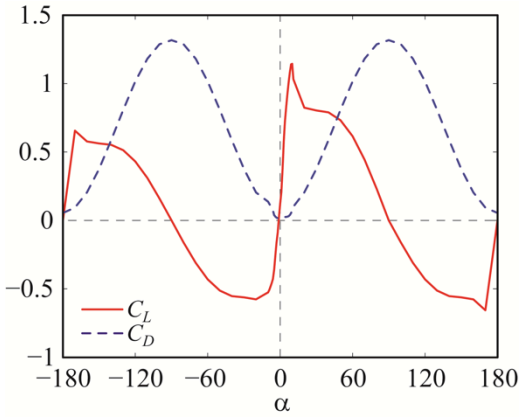

Figure 129: Lift and drag coefficients for the Drela AG24 airfoil.

To create the design, the aforementioned optimization methodology was undertaken using the performance of the full-scale, NREL 5 MW reference wind turbine as the design target. As the TSR of the NREL 5 MW reference wind turbine at the rated wind speed condition is 7, and since the NREL turbine operates near this TSR for most below-rated wind speeds due to its variable-speed design, the optimization focused on matching the performance of this design in the neighborhood of this particular TSR. In addition, a value of C_L^{max} = 0.3 was chosen at TSR^* = 7 to produce a conservative design. The optimization was directed to search for solutions which consisted of blade twist and chord distributions near the classic optimal distributions (e.g. see (Manwell *et al.*, 2009)). An image of the blade chosen from the set of Pareto-optimal designs for testing is shown in Figure 127. A non-dimensional description of the blade geometry is given in Table 56. As seen in Table 56, the chord at 70% radius is much thicker than the original geometrically-scaled design. Specifically, the chord is 14.4% of the radius at this point, a value which is three times larger than the geometrically-scaled NREL 5 reference wind turbine.

Table 56: Non-dimensional geometry of the thrust-matched wind turbine blade.

r/R	θ (deg)	c/R	Foil Type
0.046	37.18	0.058	Cylinder
0.140	37.18	0.058	Cylinder
0.148	35.84	0.244	Drela AG24
0.187	30.81	0.237	Drela AG24
0.252	23.74	0.226	Drela AG24
0.317	18.66	0.214	Drela AG24
0.382	15.02	0.202	Drela AG24
0.447	12.30	0.191	Drela AG24
0.512	10.34	0.178	Drela AG24
0.577	8.86	0.167	Drela AG24
0.642	7.69	0.155	Drela AG24
0.707	6.63	0.143	Drela AG24
0.772	5.82	0.132	Drela AG24
0.837	5.03	0.120	Drela AG24
0.892	4.36	0.110	Drela AG24
0.935	3.87	0.099	Drela AG24
0.978	3.61	0.068	Drela AG24

6.3 Laboratory Test Set-up

In this section, an overview of the laboratory test set-up used to collect the wind turbine performance data is given. The tests were performed at the University of Maine Advanced Structures and Composites Center using $1/130^{th}$-scale wind turbine components. That stated, all tests were performed at Reynolds numbers expected in a $1/50^{th}$ Froude-scale experiment.

For the experiments, data acquisition and control was handled using a National Instruments CompactDAQ (cDAQ) system with analog input and output cards. The turbine motor was controlled using a Copley Xenus XTL motor controller which received rotor speed set points via a control voltage from the cDAQ. Labview software was used to interface with the cDAQ and collect data as well as control the fan speed and turbine rotor speed. The test turbine was instrumented to collect the necessary data. Thrust force, rotor torque, and rotor rotational speed were collected for this work. Thrust force was measured using an Advanced Mechanical Testing Inc. FS6 6-axis force and moment sensor located at the tower/nacelle interface. Torque was measured using an Interface Inc. T2 precision rotary torque transducer located in-line with the turbine drive shaft. Rotor position and speed were measured using a US Digital analog encoder geared to the turbine drive shaft. All data was sent to the cDAQ as analog voltage signals and recorded with a sample rate of 500 Hz. An image of the test wind turbine is shown in Figure 130. The wind generation machine, used for creating the wind environment required for wind turbine performance testing, consisted of an aluminum frame structure which housed 6 Multifan industrial fans with analog speed. A honeycomb flow straightener was located at the exit of the fan chamber to eliminate swirl in the flow field. Upon exiting the honeycomb, the wind flow passed through a fine screen to further improve spatial wind speed uniformity and reduce the wind field turbulence intensity.

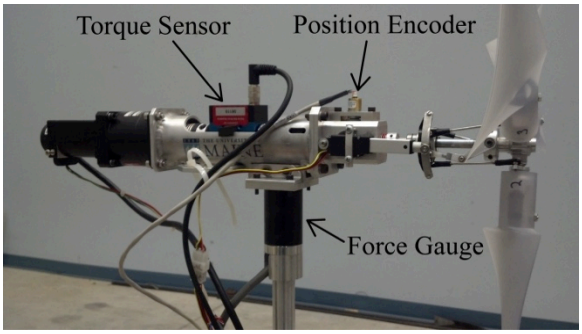

Figure 130: Image of wind test wind turbine showing the torque sensor, position encoder and force gauge.

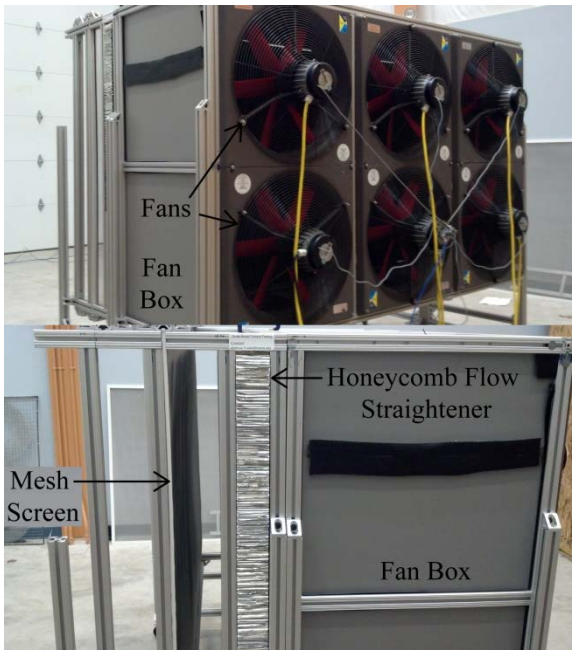

Figure 131: Images of the wind generation system showing fans, flow straighteners and mesh screen.

The wind generation system is shown in Figure 131. An image of the wind turbine being tested behind the wind machine is shown in Figure 132. The wind generation machine, which is typical of the configuration to be expected in a coupled wind/wave basin model test, utilizes an open jet configuration. This configuration mitigates wall effects present in a closed tunnel and permits the use of a more compact wind machine. A closed section tunnel would require a test section of three times the size of this open jet tunnel. The open jet allows the outer streamlines to bend more freely, which simulates the effects of an infinite freestream. Since the wake effects on turbine performance diminish rapidly downstream, it is most important to simulate the near wake effects properly. An open jet tunnel achieves this with a fairly compact and cost effective size.

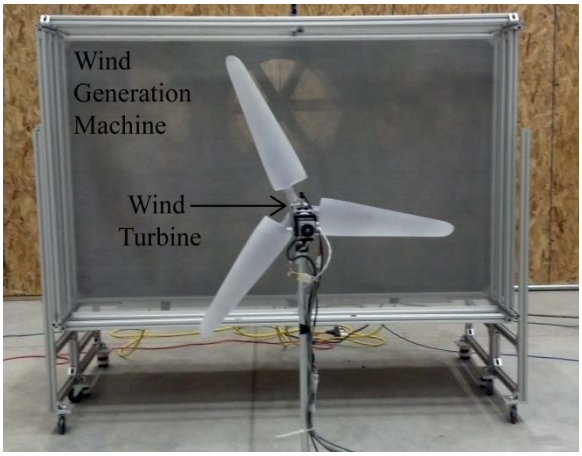

Figure 132: Image of the test wind turbine being tested behind the wind generation machine.

Prior to testing, the wind machine output was surveyed and characterized. The characterization was performed using a vertical traverse carrying a hot film wind probe. The probe had a 10 mm spatial resolution and a frequency response of about 1 ms in the range of the measurements. This is sufficient to capture the turbulence scales of the wind machine. The traverse was located such that the wind probe was in the plane of the turbine rotor and wind speed data was collected using a series of vertical profile cuts. Upon completion of the wind turbine output survey, the spatial variation of mean wind speed and turbulence intensity was obtained. A survey of the system mean wind speed, normalized relative to the maximum speed recorded, is given in Figure 133. Note that x is the horizontal distance and z is the vertical distance. This stated, the coefficient of variation of the mean wind speed over the rotor swept area is 8.5%. This is visually illustrated in Figure 134. Figure 134 displays the vertical wind profile cuts at the centerline, first cut to starboard, and the first cut to port as well as vertical lines illustrating the rotor swept area average and corresponding standard deviation. As can be seen in the figure, the spatial uniformity of the wind environment is fair. To complete the wind turbine characterization, the spatial survey of local relative wind turbine intensity is shown in Figure 135. The wind turbine intensity is defined as the temporal standard deviation in the wind speed divided by the mean. As shown in the figure, the turbulence intensity of the wind generation machine output is very good, with an average of only a few percent over most of the rotor swept area.

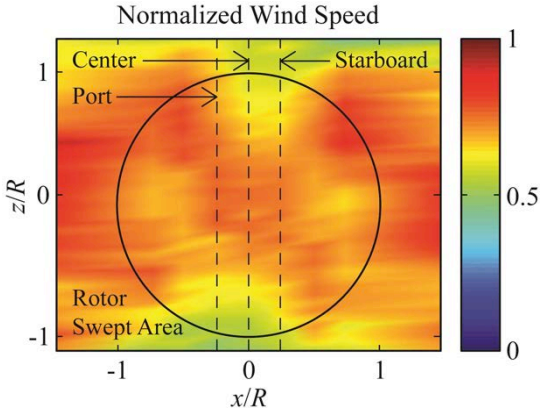

Figure 133: Spatial survey of wind generation machine mean wind speed and select vertical cut locations.

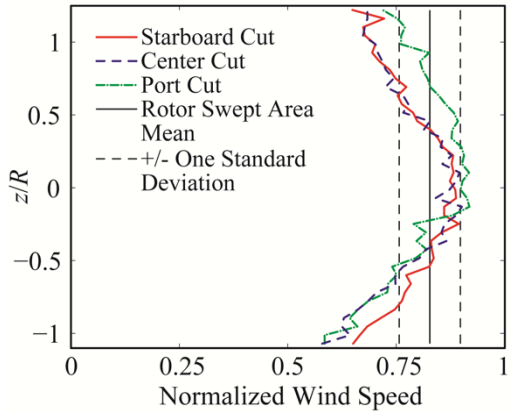

Figure 134: Vertical wind speed profiles across the first cut to starboard, center cut and first cut to port normalized to the maximum mean wind speed observed in the rotor swept area.

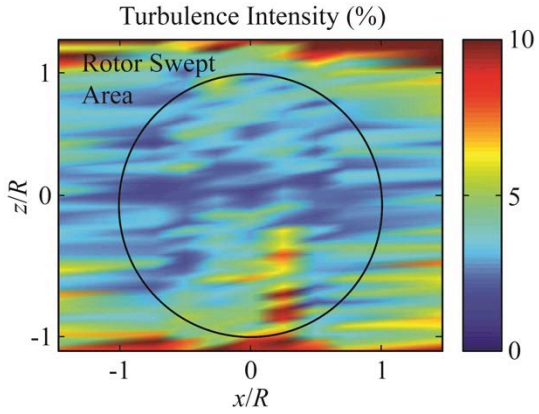

Figure 135: Spatial survey of wind generation machine turbulence intensity.

6.4 Wind Turbine Performance Results

In this section, results are presented for the wind blades considered in this work. In addition to comparisons between simulations and test data, parametric studies investigating blade pitch angle and Reynolds number are also offered.

To begin this results section, a comparison of the full-scale prototype NREL 5 MW reference wind turbine target, geometrically similar model-scale test data, redesigned thrust-matched wind turbine simulation and thrust-matched wind turbine test data is given. The curves for the thrust coefficient and performance coefficient as a function of tip-speed ratio for the aforementioned cases are given in Figure 136 and Figure 137, respectively. The prototype targets in Figure 136 and Figure 137 were obtained from a WT_Perf analysis of the full-scale, NREL 5 MW reference wind turbine. For the geometrically-similar model test data, the Reynolds number at 70% radius based on chord length at a TSR of 7 was 32.1×10^3.

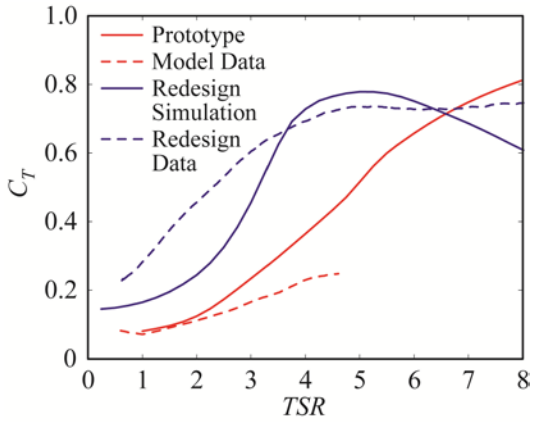

Figure 136: Comparison of thrust coefficient behavior for the prototype target, tested geometrically-similar model and redesigned thrust-matched wind turbine as obtained from simulations and test data.

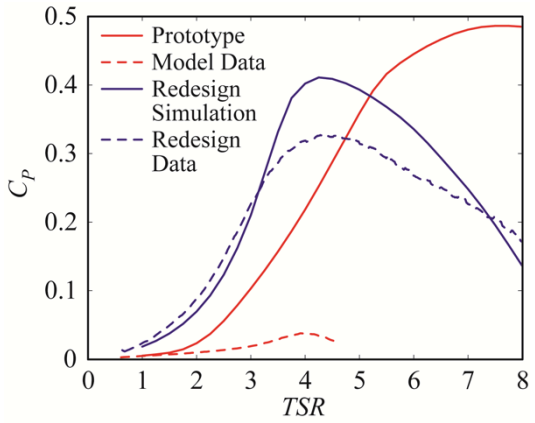

Figure 137: Comparison of performance coefficient behavior for the prototype target, tested geometrically-similar model and redesigned thrust-matched wind turbine as obtained from simulations and test data.

For the thrust-matched wind turbine, Figure 136 and Figure 137 show results of the optimal solution as computed from WT_Perf in addition to test data corresponding to a 70% radius Reynolds number at $TSR = 7$ of 88.8×10^3. As the chord length for the thrust-matched design is about three times that of the geometrically-similar design, it is expected that the Reynolds numbers be approximately three times higher for the thrust-matched design for the same test condition. That aside, Figure 136 and Figure 137 clearly show that the geometrically-similar design performs extremely poorly in replicating the full-scale prototype target performance. The thrust-matched design, on the other hand, is a fair match to the target with regard to thrust coefficient near the rated wind speed operational TSR of approximately 7. More specifically, the thrust-matched design possesses a C_T at this TSR that is 98.1% of the desired prototype value. However, it should be noted that the slope of curve differs greatly between the model and prototype. This is discussed further in the next section. Also, the peak performance coefficient, 0.33, is much greater than the tested geometrically-scaled model value of only 0.04. As evidenced by the results of these two figures, the proposed redesigned, thrust-matched wind turbine would be adequate for a Froude-scale model test as it would produce the correct thrust forces when subjected to Froude-scale winds and would also yield significantly more power than a geometrically-similar design. A final point concerning Figure 136 and Figure 137 is that the comparison between the projected

performance from the simulation of the optimized design and test data for the redesigned thrust-matched wind turbine is fairly good. The tested performance coefficient curve follows the simulation except in the neighborhood of the peak performance. A likely reason for the discrepancy is that the drag coefficients maybe somewhat higher at low angles of attack than was used in the simulation. It is worth noting that the multi-objective optimization produced designs with a peak C_P closer to the design TSR, however, the primary objective was matching C_T at the design TSR. Concerning the comparison of the thrust curve simulation and test data, the shapes are not identical but the basic trend is similar between the two.

In this next phase of this results section, the tested performance at various blade pitch angle settings is presented for the thrust-matched design. The results will be useful for demonstrating the sensitivity of the redesigned wind turbine performance to blade pitch angle, and in turn, the usefulness of the design for emulating the behavior of typical commercial-scale pitch-to-feather post-rated wind speed blade pitch control schemes. Four blade pitch offsets are considered here with the blade pitch identified as the angle of the blade tip chord relative to the rotor plane, and the offsets normalized such that the offset at the design blade pitch is 0.0°. Note that positive pitch angle offsets indicate a more feathered rotor blade with the trailing edge of the blade moving towards the downwind direction. For all results in this blade-pitch sensitivity study, the Reynolds number at 70% chord at a TSR of 7 is 88.8×10^3. The first blade pitch sensitivity result is given in Figure 138. The figure illustrates thrust coefficient performance and considers blade pitch offsets of -3.5, 0.0 (the design setting of 3.5 degrees), +3.5 and +6.5 degrees. As observed in the figure, there is a broad variation in thrust coefficient for moderate to large TSR values with -3.5 degrees producing the most thrust and +6.5 degrees the least for the configurations tested. Next, the performance coefficient curves for the same four blade pitch settings of the redesigned wind turbine are shown in Figure 139. As observed in Figure 139, the design setting produces the best performance. The performance of the turbine is slightly less at the settings of -3.5 and +3.5 degrees with the performance significantly less at the most feathered blade pitch tested, +6.5 degrees.

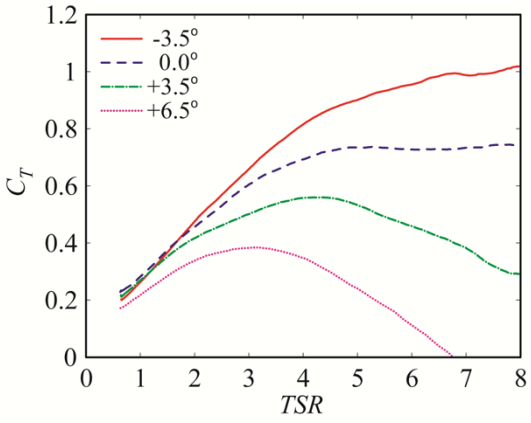

Figure 138: 12 Tested thrust-matched wind turbine thrust coefficient at four blade pitch settings.

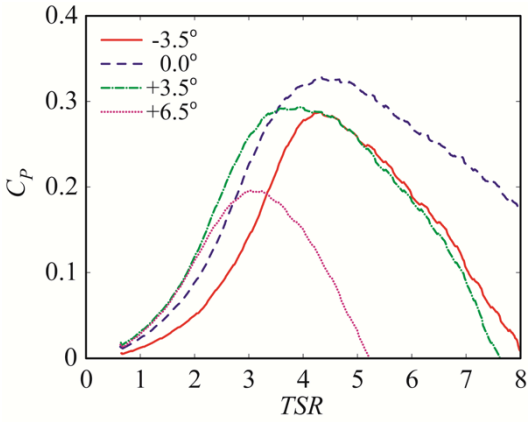

Figure 139: Tested thrust-matched wind turbine performance coefficient at four blade pitch settings.

For the purposes of comparison, the C_T and C_P trends for the full-scale NREL 5 MW reference wind turbine at the same four blade pitch settings as computed from WT_Perf are shown in Figure 140 and Figure 141, respectively. As seen from comparing Figure 138 and Figure 140, it is clear that very similar trends exist in the sensitivity of the thrust coefficient behavior between the full-scale prototype and the model-scale thrust- matched wind turbine. And while the change in C_T with blade pitch angle may not emulate the full-scale prototype directly, it is quite likely that a reasonable mapping between the two configurations can be constructed for the purposes of implementing the desired full-scale target blade pitch-to-feather control global forcing effects in a Froude-scale model test of a floating wind turbine. Comparing Figure 139 and Figure 141, it is observed that the thrust-matched design does not produce the same performance coefficient variation as the full-scale prototype. Both scenarios do, however, share a reduction in peak performance once the blade pitch setting is altered from the design setting. Nonetheless, it is likely that some care will be required for implementing blade pitch control schemes in post-rated wind speed conditions as the primary focus is the regulation of power production.

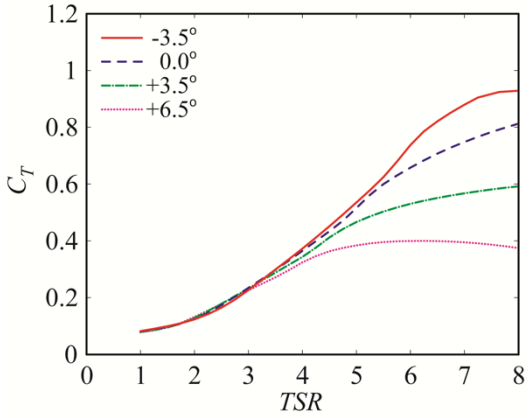

Figure 140: Full-scale NREL 5 MW reference wind turbine thrust coefficient at four different blade pitch settings.

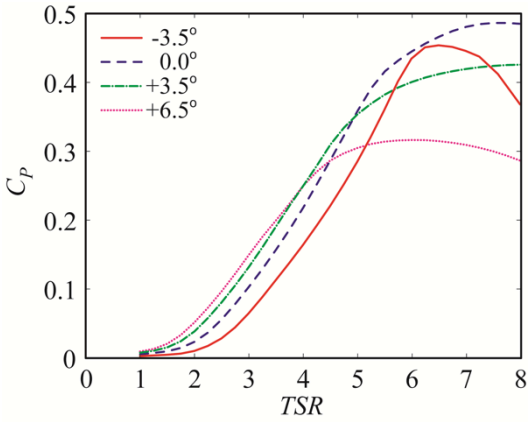

Figure 141: Full-scale NREL 5 MW reference wind turbine performance coefficient at four different blade pitch settings.

For floating wind turbines, however, this is not always the case as often control of the global motion of the floating structure is sought by devising blade pitch commands which use motion inputs, such as tower-top acceleration (e.g. see Jonkman, 2008).

To complete the results section, the sensitivity of the thrust-matched wind turbine performance to Reynolds number is investigated. Three tests are conducted with varying wind speeds to produce a range of Reynolds number conditions. The test conditions utilized produce Reynolds numbers at 70% blade radius and $TSR = 7$ of $Re = 44.4 \times 10^3$, 66.6×10^3 and 88.8×10^3. The first curves presented, shown in Figure 142, are the thrust coefficient results. As shown in the figure, the thrust performance sensitivity to Reynolds number is not very strong. In fact, the results of Figure 142 indicate that for the range of Reynolds numbers considered here, there is little change in the thrust coefficient as the Reynolds number is reduced. In other words, the thrust-matched design created in this work should perform well with regard to producing the primary wind turbine load, thrust, for Froude-scale model tests quite a bit smaller than 1/50th scale. The same cannot be said of the performance coefficient results, shown in Figure 143. As shown in the figure, the performance degrades slightly at the middle Reynolds number investigated and degrades significantly more at the lowest Reynolds number tested. Noting that the behavior for the largest Reynolds number studied is representative of 1/50th Froude-scale conditions, it is clear that the power produced by this design will begin to falter if the Froude scale chose for testing is much smaller than 1/50th scale.

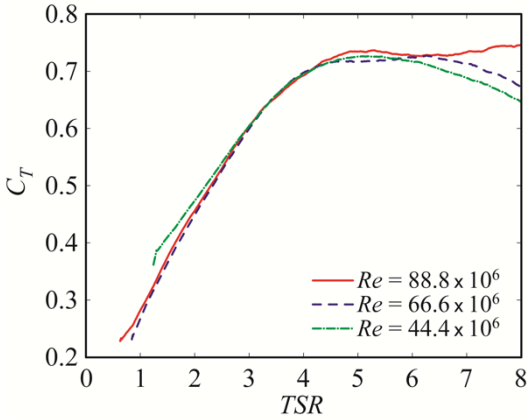

Figure 142: Tested thrust-matched wind turbine thrust coefficient for three different Reynolds number conditions.

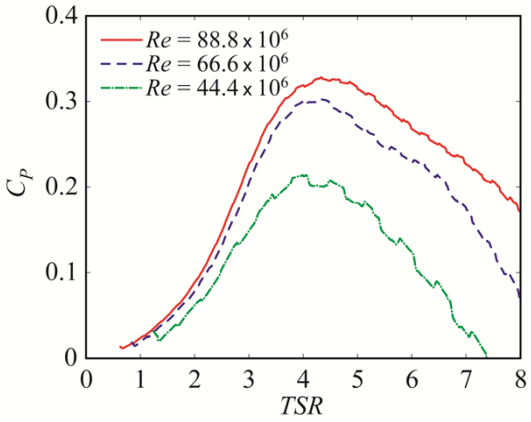

Figure 143: Tested thrust-matched wind turbine performance coefficient for three different Reynolds number conditions.

7 DeepCwind Data Verification with Retest Employing Performance-matched Turbine

In 2011 the DeepCwind Consortium, led by the University of Maine, performed an extensive series of floating wind turbine model tests at the Maritime Research Institute Netherlands offshore basin. These tests, which were conducted at 1/50th scale, investigated the response of three floating wind turbine concepts subjected to simultaneous wind and wave environments. The wind turbine blades utilized for the tests were geometrically similar models of those found on the National Renewable Energy Laboratory 5 MW reference wind turbine and performed poorly in the Froude-scaled, low-Reynolds number wind environment. As such, the primary aerodynamic load produced by the wind turbine, thrust, was drastically lower than expected for a given Froude-scaled wind speed. In order to obtain appropriate mean thrust forces for conducting the global performance testing of the floating wind turbines, the winds speeds were substantially raised beyond the target Froude-scale values. While this correction yielded the desired mean thrust load, the sensitivities of the thrust force due to changes in the turbine inflow wind speed, whether due to wind gusts or platform motion, were not necessarily representative of the full-scale system.

In hopes of rectifying the wind turbine performance issue for Froude-scale wind/wave basin testing, efforts have been made by UMaine, Maine Maritime Academy and MARIN to design performance-matched wind turbines that produce the correct thrust forces when subjected to Froude-scale wind environments. In this work, an improved, performance-matched wind turbine is mounted to the DeepCwind semi-submersible platform investigated in 2011 (also studied in the International Energy Association's OC4 Phase II Project) and retested in MARIN's offshore basin (full test report and data provided in Appendix A) with two major objectives: 1) To demonstrate that the corrective wind speed adjustments made in the earlier DeepCwind tests produced realistic global performance behaviors and 2) To illustrate the increased capability for simulating full-scale floating wind turbine responses that a performance-matched turbine has over the earlier, geometrically-similar design tested. As an example of this last point, this work presents select results for coupled wind/wave tests with active blade pitch control made possible with the use of a performance-matched wind turbine. The results of this section show that the earlier DeepCwind tests produced meaningful data; however, this section also illustrates the immense potential of using a performance-matched wind turbine in wind/wave basin model tests for floating wind turbines.

7.1 Model Descriptions

In this section, a brief description of the DeepCwind semi-submersible as tested in the 2011 and 2013 campaigns is given. Images of both systems are shown in Figure 144. While the intent was to duplicate the 2011 main particulars for the floating wind turbine system with the exception of wind turbine performance in the 2013 test, differences in the mass properties of the improved wind turbine employed for the most recent campaign yielded slightly different system properties. While the differences do not prevent a meaningful comparison, the minor dissimilarities are detailed here to help interpret the results presented in subsequent sections of this report.

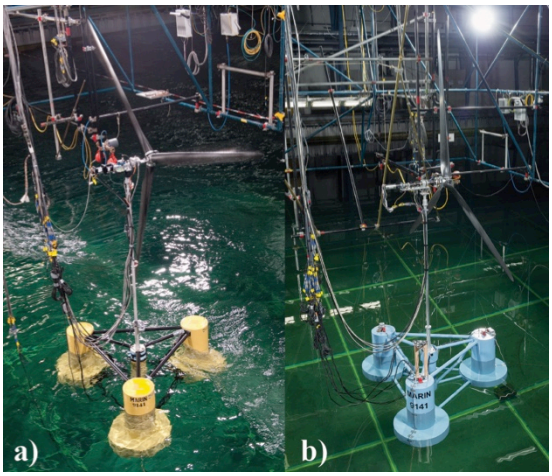

Figure 144: Images of DeepCwind semi-submersible tested at MARIN in (a) 2011 and in (b) 2013 with an improved wind turbine.

To begin, the coordinate system, degrees-of-freedom (DOF) and environment orientations used in this work are displayed in Figure 145. The platform dimensions for the system, which are identical for the 2011 and 2013 campaigns, are given in Figure 146. Other gross quantities of interest for the two systems are shown in Table 57. It should be noted that all quantities given in this portion of the report are full-scale unless otherwise noted. As seen in Table 57, many of the main particulars are essentially the same for the two systems including the primary dimensions and overall mass. One important difference is that the MARIN stock wind turbine employed for the 2013 tests was larger in mass than the 2011 DeepCwind wind turbine. This required reductions to the mass of the platform to maintain the correct draft of 20.0 m. The end result of the system mass changes was that the 2013 DeepCwind semi-submersible possessed a center of gravity over 1.8 m higher than the 2011 iteration along with larger radii of gyration in roll and pitch. As will be shown in the next section, these changes yielded less hydrostatic restoring in roll and pitch along with larger inertia in these DOF producing longer natural roll and pitch periods.

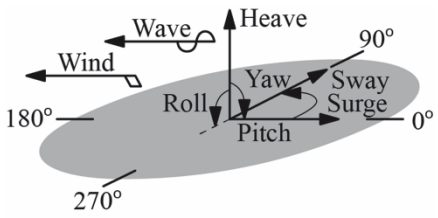

Figure 145: Degrees of freedom and environment orientations.

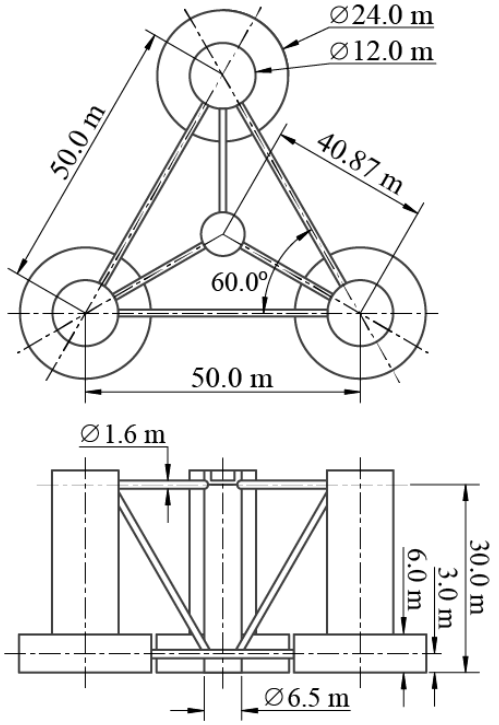

Figure 146: Dimensions of the DeepCwind semi-submersible.

Table 57: Gross properties of the 2011 and 2013 DeepCwind semi-submersible floating wind turbine systems.

Quantity	2011	2013
Rotor Diameter (m)	126.0	126.0
Hub Height (m)	90.0	90.0
Draft (m)	20.0	20.0
Mooring Spread Diameter (m)	1675	1675
Mass w/ Turbine (MT)	14,040	13,958
Displacement (MT)	14,265	14,265
CG Above Keel (m)	10.11	11.93
Roll Radius of Gyration (m)	31.61	32.63
Pitch Radius of Gyration (m)	32.34	33.38

7.2 System Identification Comparison

With the main particulars of the 2011 and 2013 DeepCwind semi-submersible floating wind turbines covered, a comparison of the system identification test results for the two systems is now presented. Results pertaining to the basic behavior of the wind turbine performance, rigid-body natural periods, platform hydrodynamic damping and mooring restoring force are discussed.

The first comparison is for the basic wind turbine performance metrics. These include the non-dimensional power coefficient C_p given in Figure 147, and the non-dimensional thrust coefficient C_t shown in Figure 148. Both are plotted as a function of the rotor's tip-speed ratio TSR and both figures include the full-scale target performance for the National Renewable Energy Laboratory (NREL) 5 MW reference wind turbine (Jonkman *et al.*, 2009). It is observed in both figures that the DeepCwind turbine used in the 2011 model tests, which was a geometrically similar model of the

NREL 5 MW reference wind turbine, performed poorly with regard to matching the power and thrust of the desired full-scale machine. It should be noted that the DeepCwind turbine results provided are for a blade pitch angle of $\theta = 6.4°$ and obtained with a steady wind speed of 21.8 m/s. The cause of the low power and thrust output, which is largely attributable to the poor performance of the full-scale blade geometry at low Reynolds numbers resulting in laminar stall, is detailed in (Martin *et al.*, 2012). The low performance of the 2011 turbine, which necessitated the use of wind speeds higher than the desired Froude-scale values to create the appropriate mean aerodynamic wind turbine loads, was the primary impetus for retesting the DeepCwind semi-submersible with an improved wind turbine. The improved wind turbine used for the 2013 test campaign was the MARIN stock wind turbine. The C_p and C_t curves for this turbine shown in the figures is for a blade pitch angle of $\theta = 1.0°$ and a steady wind speed of 13.0 m/s. The MARIN stock wind turbine uses the design methods outlined in (Marin *et al.*, 2012; Fowler *et al.*, 2013) along with detailed analyses using MARIN's in-house computational fluid dynamics software ReFRESCO to yield a turbine which more closely emulates the target performance than the 2011 DeepCwind wind turbine. Most importantly, the MARIN stock turbine C_t behavior shown in Figure 148 is similar to the NREL 5 MW reference wind turbine target allowing the use of wind speeds near the desired Froude-scale values to create the correct mean thrust force for the wind turbine, this being the dominant aerodynamic force impacting global performance. This improved C_t response also preserves the sensitivity of thrust to changes in wind speed or blade pitch angle, unlike the 2011 turbine. In addition, the improved C_p of the MARIN stock turbine permits the generation of a modest amount of power which is suitable for feedback in active blade pitch control algorithms.

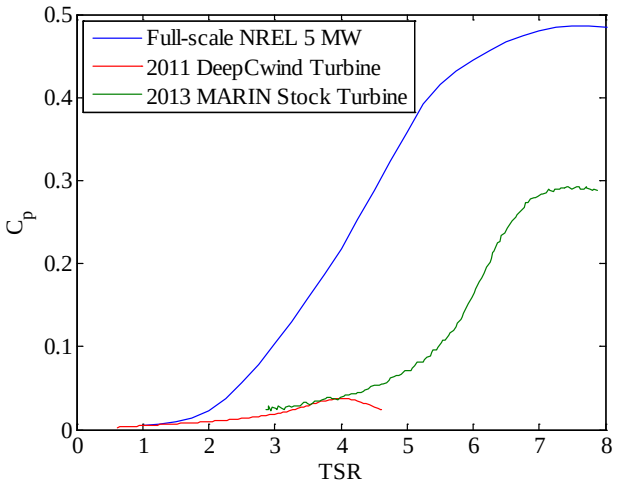

Figure 147: Comparison of full-scale NREL 5 MW turbine C_p with 2011 DeepCwind and 2013 MARIN stock turbines.

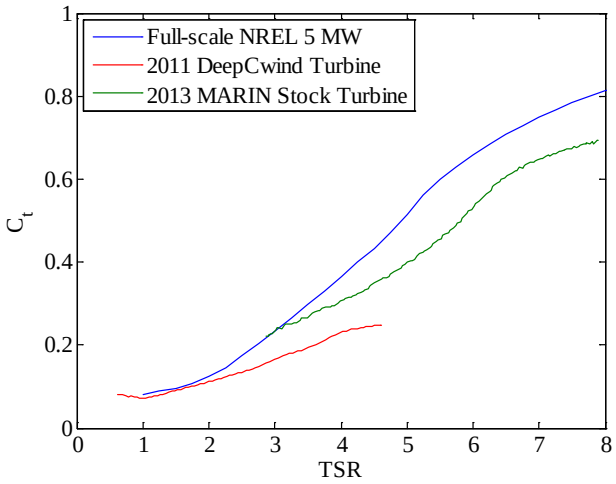

Figure 148: Comparison of full-scale NREL 5 MW turbine C_t with 2011 DeepCwind and 2013 MARIN stock turbines.

The next quantities investigated are the rigid-body natural periods and fundamental tower bending frequencies, shown in Table 58. The surge, sway and yaw natural periods are very similar for both the 2011 and 2013 campaigns indicating that the mooring system restoring behavior is essentially the same. Also, the heave natural period remains unchanged for 2013. However, the aforementioned higher center of gravity and larger inertias of the 2013 DeepCwind semi-submersible lead to roll and pitch periods that are almost 6 seconds longer than found in 2011. In addition, the heavier MARIN stock wind turbine also gave rise to reduced fundamental tower bending frequencies when placed atop the same tower. These differences must be kept in mind when comparing the performance of the two systems in future sections.

Table 58: Natural periods and frequencies for the DeepCwind semi-submersible system in 2011 and 2013.

DOF	2011	2013
Surge (s)	107	107
Sway (s)	112	112
Heave (s)	17.5	17.5
Roll (s)	26.9	32.8
Pitch (s)	26.8	32.5
Yaw (s)	82.3	80.8
Tower Fore-aft Bending (Hz)	0.35	0.32
Tower Side-side Bending (Hz)	0.38	0.34

To continue the system identification data comparison, the rigid-body motion damping ratios as a function of initial cycle amplitude as measured from free-decay tests are displayed in Figure 149. The results given are for surge (at the system center of gravity), heave and pitch DOF. Unsurprisingly, the hydrodynamic damping behavior of the system is essentially unchanged between the 2011 and 2013 iterations of the DeepCwind semi-submersible floating wind turbine.

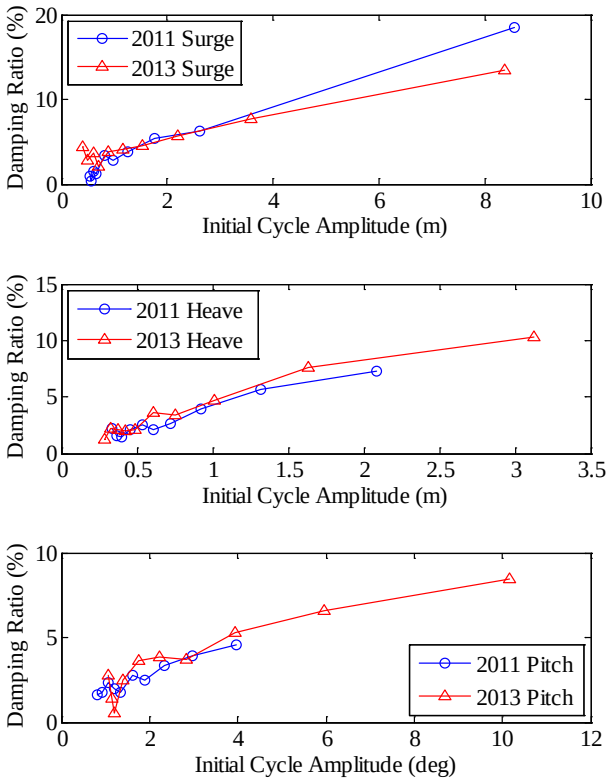

Figure 149: Comparison of surge, heave and pitch hydrodynamic damping behavior for the 2011 and 2013 DeepCwind semi-submersibles.

To complete the review of the system identification data for the 2011 and 2013 tests, a plot of the mooring restoring force in the surge direction is given in Figure 150. As is clear from the figure, the restoring force provided by the mooring system is very similar between the two campaigns.

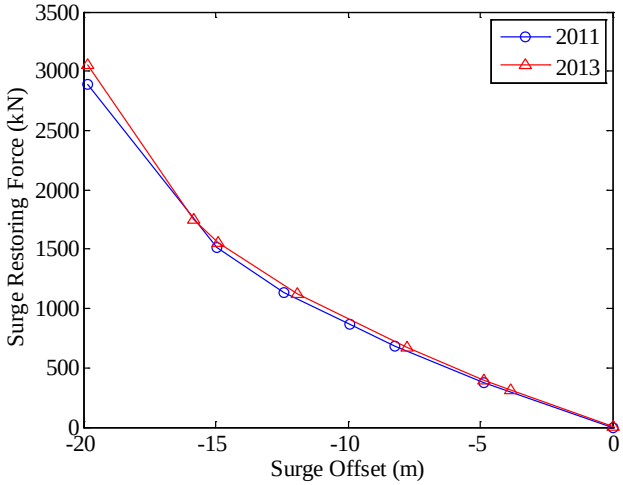

Figure 150: Comparison of surge mooring restoring force for the 2011 and 2013 DeepCwind semi-submersibles.

7.3 Global Performance Comparison

With the basic properties of the 2011 and 2013 systems established, this section attempts to address the fundamental question of this work: did the poor wind turbine performance and corrective measures used in the 2011 DeepCwind model testing campaign compromise the value of the recorded test data? To do this, sample results for several field variables of interest are compared between the 2011 and 2013 test campaigns when the DeepCwind semi-submersible is subjected to the same wave environment and steady winds that produce the same mean thrust. While the mean aerodynamic thrust is the same between the two tests, the markedly different wind speeds and turbine performance could potentially yield very different sensitivities of the thrust with respect to changes in the relative wind speed resulting from platform motion, hence changing the global performance of the floating wind turbine system. The comparisons provided in this section will help evaluate the extent to which the 2011 campaign was able to replicate the correct global performance behavior of a floating wind turbine system as the 2013 data should closely emulate the true full-scale response.

Prior to investigating the relative performance of the two systems, specifics of the environments and operating conditions for the two tests are given first. Table 59 provides the steady wind speed at the hub height U_m, the significant wave height H_s, peak spectral period T_p as well as other environmental statistics and wind turbine operational parameters. It is worth noting that despite the large reduction in wind speed used for the 2013 campaign, the mean thrust is essentially the same. In addition, the MARIN stock wind turbine produces more power than the 2011 version of the system even though the wind speed is reduced by 8.8 m/s. For both tests, the rotor speed is fixed at a constant 12.1 rpm. Regarding the H_s = 7.1 m target JONSWAP wave environment, the statistics and spectrum (displayed in Figure 151) are very similar albeit not identical. All in all, the conditions used provided the fairest comparison between the two systems as was reasonably achievable in the wind/wave basin.

Table 59: Environmental conditions and turbine settings for comparison example.

Quantity	2011	2013
U_m (m/s)	21.8	13.0
Mean Thrust (kN)	749	719
Rotor Speed (rpm)	12.1	12.1
Blade Pitch Angle	6.4	1.0
Mean Power (MW)	2.28	3.31
H_s (m)	7.04	7.05
T_p (s)	12.2	12.1
Maximum Wave (m)	13.6	13.2
Maximum Crest (m)	7.20	7.47
Minimum Trough (m)	6.37	6.69
Duration (hours)	3.0	3.0

The first results for the comparison provided are power spectral density plots for the system surge (reported at the systems' center of gravity) and pitch rigid-body motions in Figure 152 and Figure 153, respectively. For these and all subsequent plots in this section, the results are given for the 2011 and 2013 systems with and without an aerodynamically loaded, operating wind turbine. In the case where the wind turbine is not operating, the wind speed is set to 0.0 m/s, the rotor is parked (i.e. rotor speed is zero) and the blades are feathered to $\theta = 90°$ to reduce drag due to relative motion of the rotor.

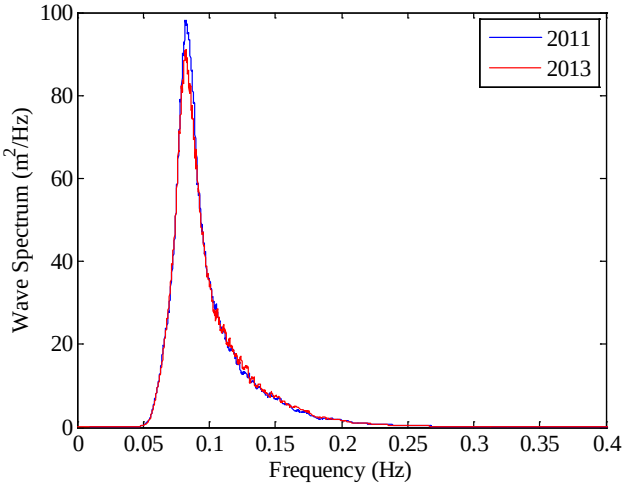

Figure 151: Comparison of the H_s = 7.1 m JONSWAP wave spectrum for the 2011 and 2013 DeepCwind semi-submersible tests.

For surge, the 2011 and 2013 responses are essentially the same for the no wind case and are also very similar for the operating wind turbine condition. For both systems, a similar reduction in the surge response near the 0.0093 Hz surge natural frequency due to the aerodynamic damping of the operating wind turbine is observed. For platform pitch, the response in the wave energy frequency range (0.05 to 0.2 Hz) is very similar for all four cases; however the resonant platform pitch response does occur at different frequencies for the 2011 (0.037 Hz) and 2013 (0.031 Hz) DeepCwind semi-submersible floating wind turbine systems as a result of the change in the 2013 system platform natural pitch period. More importantly, though, is that for both the 2011 and 2013 tests, the presence of the operating wind turbine produces a comparable reduction in the pitch response at the platform natural pitch frequency.

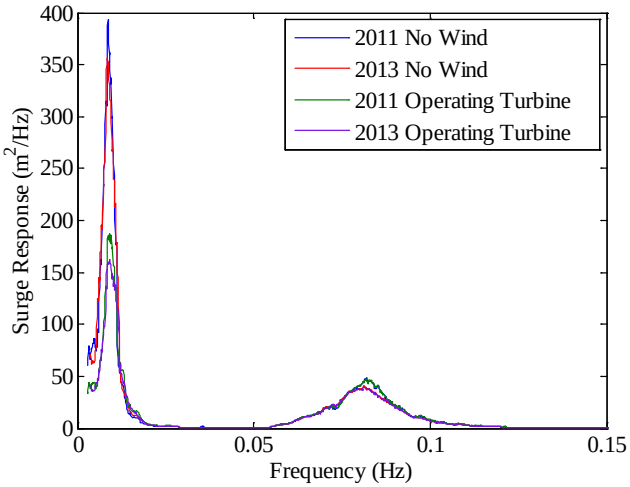

Figure 152: Comparison of surge response with and without wind for the 2011 and 2013 DeepCwind semi-submersibles.

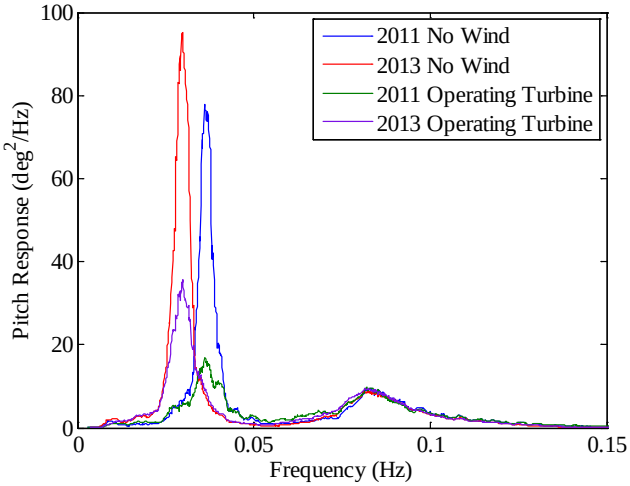

Figure 153: Comparison of pitch response with and without wind for the 2011 and 2013 DeepCwind semi-submersibles.

The next result, provided in Figure 154, is for the nacelle fore-aft (i.e. surge) acceleration for the 2011 and 2013 systems with and without an operating wind turbine. Present in the response in the absence of wind loading are peaks near the platform pitch frequency (2011 – 0.037 Hz; 2013 – 0.031 Hz), wave energy frequency range and fundamental tower bending frequency (2011 – 0.35 Hz; 2013 – 0.32 Hz). Encouragingly, both systems show similar, strong reductions in the response near the platform pitch and tower bending frequencies when the turbine is operating. In addition, the nacelle fore-aft acceleration response increases slightly in the wave energy frequency range (0.05 to 0.2 Hz) when the turbine is operating for both the 2011 and 2013 campaigns.

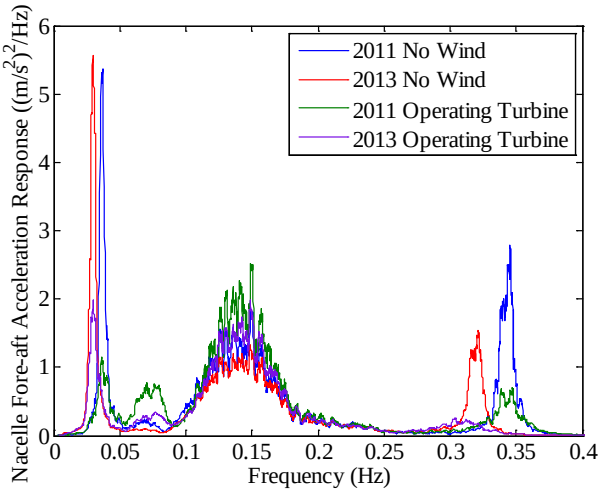

Figure 154: Comparison of nacelle fore-aft acceleration response with and without wind for the 2011 and 2013 DeepCwind semi-submersibles.

The last power spectral density plot provided is for the bow, or upwind, fairlead tension response shown in Figure 155. For both the 2011 and 2013 tests, the response in the absence of aerodynamic loads is very similar. Also, the bow fairlead tension responses increases significantly for both systems in the wave energy frequency range when the wind turbine is under load. This stated, the increase is slightly more pronounced for the 2011 version of the system as compared to

the 2013 system. This may result from the slightly reduced mean thrust of the 2013 test, this reduced thrust being consistent with the slightly diminished surge response of the 2013 system found in Figure 152. As the mooring line restoring stiffness is highly nonlinear, a slight reduction in the mean surge displacement due to a reduced mean thrust would diminish the load excursions for a given change in surge displacement about the mean. Nonetheless, the trends are very similar for both systems indicating that the influence of the operating wind turbine is not that different between the two campaigns.

To complete the comparison, statistics for the no wind and operating wind turbine cases are provided in Table 60 and Table 61, respectively. Unsurprisingly, the mean, standard deviation, maximum, minimum and range for the surge, platform pitch, nacelle fore-aft acceleration and bow fairlead tension are essentially the same for the 2011 and 2013 systems. The one exception is a slight change in the mean surge value between the two systems. With an operating wind turbine, there are a few subtle differences worth mentioning. The first is that the minimum surge value and surge range are both slightly larger in magnitude for the 2011 system as compared to the 2013 system. Another is that the mean pitch angle for the 2013 system is about 0.8 degrees larger in magnitude than for the 2011 system; however, this is attributable to the reduction in pitch stability due to the higher center of gravity of the 2013 system and is not due to changes in wind turbine loading. The last is the reductions in the standard deviation, maximum and range for the 2013 DeepCwind semi-submersible bow fairlead tension. The most significant of these is the 12.8% reduction in the tension range. This stated, the aforementioned changes are not drastic and the remainder of the statistics presented are very similar for the 2011 and 2013 operating wind turbine cases. This provides some evidence that the data produced by the 2011 campaign for the semi-submersible floating wind turbine system, and likely the simultaneously tested tension-leg platform and spar-buoy systems, properly captures the coupled aero-hydro-elastic global response behaviors of the investigated floating wind turbine configurations.

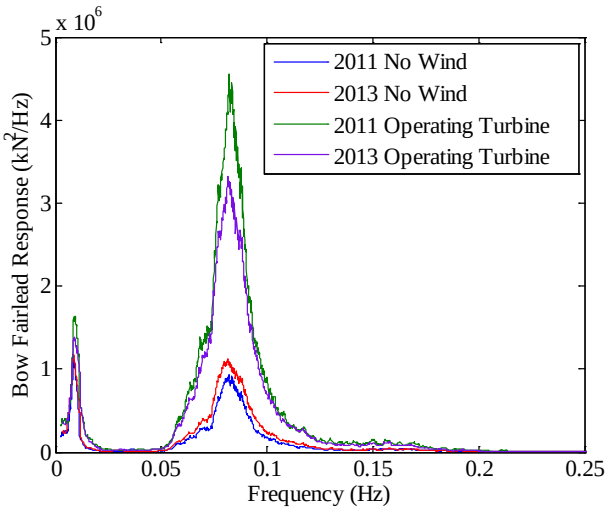

Figure 155: Comparison of bow fairlead tension response with and without wind for the 2011 and 2013 DeepCwind semi-submersibles.

Table 60: Statistical comparison for the no wind condition.

Test Year	Mean	Std. Dev.	Max.	Min.	Range
Surge (m)					
2011	-1.83	1.71	3.34	-9.57	12.91
2013	-2.66	1.70	2.27	-10.21	12.48
Pitch (deg)					
2011	0.06	0.86	3.29	-3.79	7.08
2013	-0.02	0.91	3.49	-3.75	7.24
Nacelle Fore-aft Acceleration (m^2/s)					
2011	0.01	0.41	1.93	-1.98	3.91
2013	0.01	0.37	1.85	-2.01	3.86
Bow Fairlead Tension (kN)					
2011	1221	167	2672	236	2436
2013	1234	189	2685	187	2498

Table 61. Statistical comparison for the operating turbine condition.

Test Year	Mean	Std. Dev.	Max.	Min.	Range
Surge (m)					
2011	-9.96	1.48	-5.88	-17.93	12.05
2013	-9.56	1.42	-5.39	-16.24	10.85
Pitch (deg)					
2011	-3.96	0.71	-1.12	-7.24	6.12
2013	-4.74	0.78	-1.79	-7.78	5.99
Nacelle Fore-aft Acceleration (m^2/s)					
2011	0.79	0.49	2.68	-1.24	3.92
2013	0.90	0.42	2.86	-1.16	4.02
Bow Fairlead Tension (kN)					
2011	1881	333	4592	281	4311
2013	1779	303	4086	308	3778

7.4 Performance-matched Turbine Advantages

While the data presented in the previous section indicated that the increased wind speeds and poorly performing turbine used in the 2011 campaign still yielded valuable floating wind turbine global performance data, the use of a performance-matched turbine as was done in the 2013 program permits the execution of many important tests that are not possible with the 2011 geometrically-similar wind turbine arrangement. The first example of this includes properly testing in region three of a wind turbine's power production where the mean thrust value is low but the dynamic portion of the aerodynamic loads can be quite large. A second example is properly conducting floating wind turbine experiments while using active blade pitch control, this being enabled by the reasonable power production of the performance-matched wind turbine and the very close emulation of the rotor thrust sensitivity to changes in blade pitch angle. In this section, the advantage of using a performance-matched turbine for conducting coupled wind/wave basin experiments of floating wind turbines is demonstrated through select pieces of data gathered from the 2013 DeepCwind semi-submersible test campaign.

The first result provided investigates the impact of active blade pitch control on the natural platform pitch period of a floating wind turbine. The natural periods were extracted from free-decay tests of the floating wind turbine system while simultaneously subjected to various steady wind conditions. In addition to several fixed blade pitch tests with a constant rotor speed, two

active blade pitch control algorithms were investigated in the 2013 campaign. The first was a simple, robust algorithm developed by MARIN that used integral control to reduce the error on generator power with a target of 3.5 MW. The rotor speed was maintained at a constant 12.1 rpm using a separate control loop. Several integral gains were investigated by changing the integrator gain constant C_i. The actual gain K_i was computed as C_i divided by the sensitivity of rotor power to collective blade pitch angle $\partial P/\partial\theta$. $\partial P/\partial\theta$, which is a function of collective blade pitch angle, was derived from MARIN stock wind turbine performance data taken prior to the 2013 wind/wave basin tests. The second controller, specified by UMaine, attempted to emulate a simple but realistic proportional-integral collective blade pitch control algorithm that sought to minimize rotor speed error based on a target of 12.1 rpm. This control algorithm also used a very crude variable speed generator control with torque being proportional to the square of rotor speed below 12.1 rpm, and equal to a constant value of 2690 kN-m at or above 12.1 rpm. The proportional and integral gains were computed in accordance with the equations of (Jonkman, 2007) using a damping ratio of 0.7 and the aforementioned $\partial P/\partial\theta$ function. The controller frequency ω_n was varied for the free-decay experiments. All this stated, the natural period results for each of the 2013 pitch free-decay tests are given in Table 62. As seen in the table, an operating wind turbine with a fixed blade pitch has little impact on the platform pitch frequency regardless of the wind speed. Surprisingly, the same cannot be said when active blade pitch control is present. For the MARIN controller, the larger the value of C_i, the longer the natural period. For the UMaine controller, the platform pitch period is lengthened when the value of ω_n is reduced.

Table 62: 2013 DeepCwind semi-submersible natural platform pitch periods for several different blade pitch control settings.

Wind Speed U_m	Blade Pitch θ	Rotor Speed	Controller Settings	Pitch Period
No Wind	90.0°	0.0 rpm	Fixed	32.5 s
13.0 m/s	1.0°	12.1 rpm	Fixed	32.1 s
21.0 m/s	17.2°	12.1 rpm	Fixed	32.2 s
21.0 m/s	Active	12.1 rpm	MARIN C_i = 20*	33.2 s
21.0 m/s	Active	12.1 rpm	MARIN C_i = 40*	34.4 s
21.0 m/s	Active	12.1 rpm	MARIN C_i = 80*	35.9 s
21.0 m/s	Active	Variable	UMaine ω_n = 0.6 rad/s	33.6 s
21.0 m/s	Active	Variable	UMaine ω_n = 0.2 rad/s	35.9 s

*Model-scale values

Another quantity measured from the platform pitch free-decay tests, this being the damping ratio as a function of initial cycle amplitude for each of the control configurations, is given in Figure 156. As seen in the figure, the platform pitch damping is smallest when there is no operating wind turbine. In addition, even though the mean thrust is significantly smaller for the U_m = 21.0 m/s, θ = 17.2° fixed pitch case as compared to the U_m = 13.0 m/s, θ = 1.0° fixed pitch case, the platform pitch damping is significantly larger. For each of the active blade pitch cases tested in 2013, all conducted with a mean wind speed of U_m = 21.0 m/s, the damping ratio is usually not very different from the U_m = 21.0 m/s, θ = 17.2° fixed pitch configuration. This is significant as active blade pitch-induced platform pitch instability is of great interest to the floating wind turbine community (e.g.

see (Jonkman, 2008)); this said, the 2013 DeepCwind semi-submersible tests did not find any such instability despite the fairly large range of control settings used in the program.

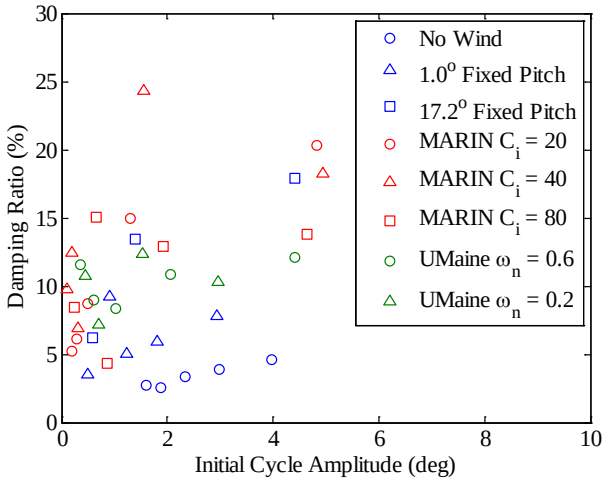

Figure 156: 2013 DeepCwind semi-submersible platform pitch damping ratio as a function of initial cycle amplitude for several blade pitch control settings.

To continue this section, the platform pitch response of the DeepCwind semi-submersible is investigated for the H_s = 7.1 m irregular wave of Table 59 and Figure 151 along with several different wind conditions and active blade pitch control settings. Platform pitch is the focus since it is a field variable that is strongly influenced by changes in the wind turbine aerodynamic thrust force. The first result shown in Figure 157 compares the response under no wind (θ = 90°) as well as fixed blade pitch, constant rotor speed (12.1 rpm) cases for steady winds with mean U_m = 13.0 m/s (θ = 1.0°) and U_m = 21.0 m/s (θ = 17.2°). As discussed earlier, the operating turbine in the 13.0 m/s wind speed environment significantly reduces the platform pitch response near the platform pitch natural frequency of 0.031 Hz. As opposed to the 2011 tests, the 2013 campaign also permitted realistic tests of global performance behavior in the post-rated wind speed regime (region three) with U_m = 21.0 m/s. The fixed blade pitch, constant rotor speed results for these wind speeds given in Figure 157 show that the region three wind speeds further reduce the platform pitch response at 0.031 Hz without altering the behavior in the wave energy frequency range (0.05 to 0.2 Hz).

The next result compares the frequency-domain platform pitch response for the fixed blade pitch with θ = 17.2° configuration as well as the MARIN and UMaine control algorithms each subjected to the H_s = 7.1 m irregular wave and 21.0 m/s steady winds. For the comparison, given in Figure 158, the MARIN controller utilizes C_i = 80 and the UMaine controller uses ω_n = 0.6 rad/s. As seen in the figure, the controllers' efforts at regulating power/rotor speed result in less damping of the platform pitch response near the platform pitch natural frequency. Also, one can visibly see that the peak response near the platform pitch natural frequency moves to a lower frequency for the active blade pitch cases. This observation is in agreement with the free-decay results of Table 62. Also, the controllers investigated here had no impact on the platform pitch response in the wave energy frequency range.

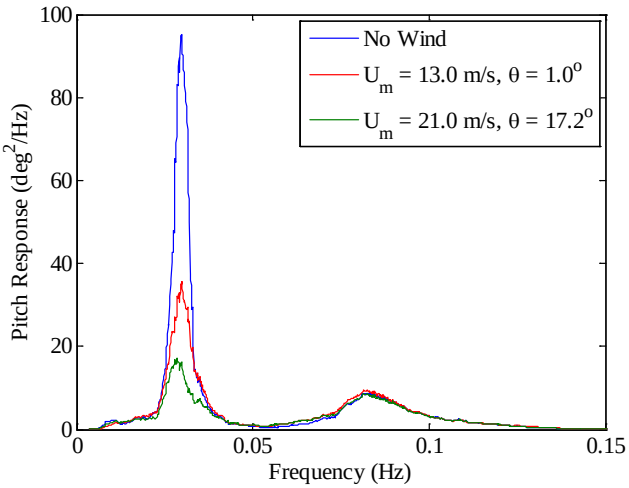

Figure 157: 2013 DeepCwind semi-submersible platform pitch response for three different steady wind speeds each using a fixed blade pitch.

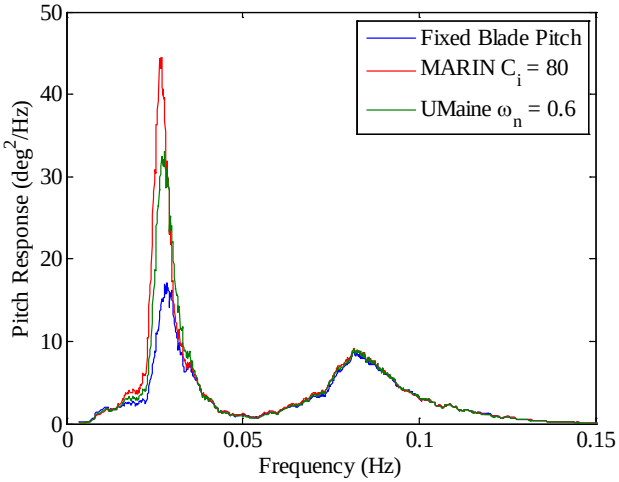

Figure 158: 2013 DeepCwind semi-submersible platform pitch response for three different control strategies when subjected to steady 21.0 m/s winds.

The last set of configurations investigated look at fixed blade pitch with $\theta = 17.2°$, MARIN $C_i = 20$, MARIN $C_i = 80$ and UMaine $\omega_n = 0.6$ rad/s control algorithm cases subjected to a dynamic wind following an NPD spectrum with a hub-height mean wind speed of 21.0 m/s. The wave environment is the same $H_s = 7.1$ m irregular sea. A comparison of the measured and theoretical target wind spectra for this case is given in Figure 159. As seen in the figure, the realized spectrum in the basin is very near the desired target quantity. This aside, the response of the aforementioned four control configurations is shown in Figure 160. Upon inspection of the figure, it is seen that the MARIN $C_i = 80$ and UMaine controllers significantly reduce the wind-induced low-frequency response occurring below 0.02 Hz that exists in the fixed blade pitch scenario while the MARIN $C_i = 20$ case does not. The MARIN $C_i = 80$ controller increases the response at the platform pitch frequency (~0.03 Hz) over the fixed pitch configuration while the UMaine and MARIN $C_i = 20$ controllers yields essentially the same response as the fixed pitch configuration in this frequency location. All four configurations possess essentially the same behavior in the wave energy frequency range. It is worth noting that the overall improved platform pitch performance of the UMaine controller as compared to the fixed pitch setting does come at the expense of significant

variation in rotor speed. During the tests, the maximum rotor speed was 15.63 rpm and the minimum was 8.96 rpm.

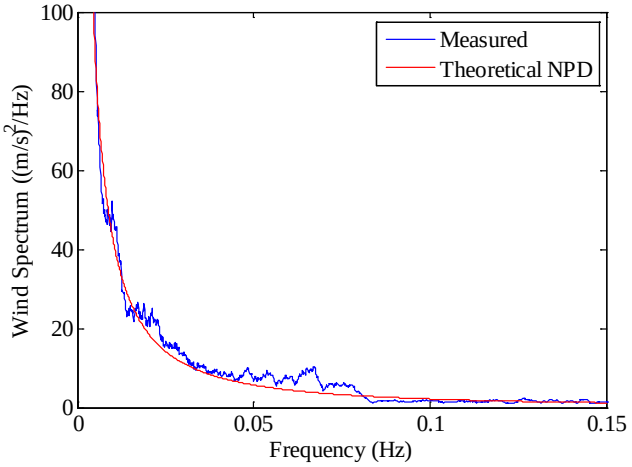

Figure 159: Measured and theoretical NPD wind spectra for the 2013 DeepCwind semi-submersible test program with a hub height mean wind speed of 21.0 m/s.

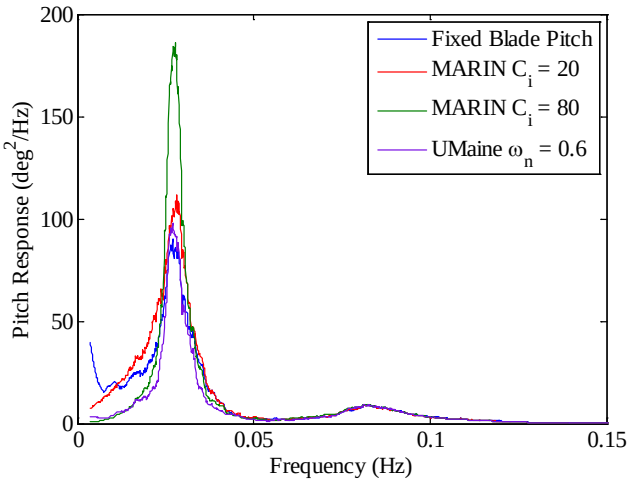

Figure 160: 2013 DeepCwind semi-submersible platform pitch response for four different control strategies when subjected to NPD dynamic 21.0 m/s winds.

To complete this section, the platform pitch statistics for all of the cases considered in Figure 157, Figure 158 and Figure 160 are provided in Table 63. For the fixed blade pitch cases, the presence of an operating wind turbine in the steady U_m = 13.0 m/s and 21.0 m/s wind cases significantly reduces the platform pitch standard deviation and range as compared to the no wind, parked turbine scenario (i.e. U_m = 0.0 m/s). Of the three, the 21.0 m/s case exhibits the smallest standard deviation and range. For the three steady U_m = 21.0 m/s configurations studied, all of the platform pitch means are essentially the same. Both the MARIN C_i = 80 and UMaine controllers increase the platform pitch standard deviation and range over the fixed blade pitch configuration with the MARIN controller possessing the largest of these quantities. It should be noted, however, that both of the MARIN C_i = 80 and UMaine controllers in steady 21.0 m/s winds exhibit smaller platform pitch standard deviation and ranges than the no wind, parked turbine case. Unlike the steady wind

cases, the MARIN C_i = 20, MARIN C_i = 80 and UMaine controllers significantly reduced the platform pitch standard deviation and range when subjected to dynamic winds with a mean of 21.0 m/s as compared to the fixed blade pitch case. The UMaine controller, which showed the largest improvements in platform pitch performance, reduced the standard deviation by 28% and the range by 27% as compared to its fixed blade pitch counterpart.

Table 63: Platform pitch statistics of the 2013 DeepCwind semi-submersible for several different blade pitch control settings.

Platform Pitch (deg)					
Remark	Mean	Std. Dev.	Max.	Min.	Range
Fixed Blade Pitch					
0.0 m/s	-0.02	0.91	3.49	-3.75	7.24
13.0 m/s	-4.74	0.78	-1.79	-7.78	5.99
21.0 m/s	-2.30	0.68	0.43	-5.40	5.83
21.0 m/s Steady Winds					
Fixed	-2.30	0.68	0.43	-5.40	5.83
MARIN C_i = 80	-2.42	0.78	0.57	-5.83	6.40
UMaine $\square_n$ = 0.6	-2.23	0.75	0.55	-5.40	5.95
21.0 m/s NPD Dynamic Winds					
Fixed	-2.31	1.52	2.56	-8.57	11.13
MARIN C_i = 20	-2.31	1.34	2.62	-7.58	10.20
MARIN C_i = 80	-2.44	1.31	2.42	-7.97	10.39
UMaine $\square_n$ = 0.6	-2.19	1.09	1.83	-6.28	8.11

8 Conclusions and Future Work

In this final section, the conclusions for the various portions of this report will be covered. The topics will include scaling methods, model test experimental results, FAST calibration and validation and redesigned model test wind turbine. Subsequently, a brief discussion of future work will also be given.

8.1 Scaling Methods Conclusions

A methodology has been presented for model testing of floating wind turbines under Froude scale conditions. The scaling relationships for all of the field variables are established with particular emphasis on the unique aspects of such testing, namely the wind turbine design, operation and accompanying wind environment. Model test data is used to demonstrate the difficulty of capturing the correct prototype aerodynamic forces as a result of Reynolds number dissimilitude, namely the thrust force which is the most critical to emulate properly for a wind/wave basin test of a floating wind turbine. Analysis reveals that the thick airfoil sections employed on commercial scale wind blades exhibit low lift and high drag forces at the low Reynolds numbers of a Froude scale experiment, in turn producing poor rotor aerodynamic performance. Corrective measures are suggested, these being to increase the wind inflow speed to compensate for low wind turbine thrust coefficients, roughen the leading edge of the blade to trip the boundary layer transition to turbulence, or lastly, to design a low-Reynolds number specific wind turbine. Test data and simulations indicate that increasing the wind speed to compensate for poor turbine performance does not greatly affect the wind turbine damping resulting from a fixed blade rotor. This method, however, may not capture all wind turbine damping effects correctly. Leading edge roughness applied to the wind turbine blades can greatly improve the performance of thick airfoil sections at low Reynolds numbers, but may result in erratic wind turbine rotor behavior. It is suggested that

this technique be used more as a fine tuning adjustment than be solely relied upon to solve all model wind turbine aerodynamic performance issues. The last recommendation, a low-Reynolds number specific blade design, allows one to match thrust forces with unaltered Froude scale winds, will better capture wind turbine damping effects, and is best suited to experiments where the impact of active blade pitch control on global motions are of interest. Therefore, if possible, a redesigned rotor is the best option with the other two thrust matching techniques being used sparingly to fine tune the model thrust forces.

8.2 Floating Wind Turbine Experimental Comparison Conclusions

This report presented experimental performance results from wind/wave basin model testing of three floating wind turbine concepts. The three platform concepts, each supporting the same horizontal axis NREL 5 MW Reference Wind Turbine, consisted of a TLP, a spar-buoy and a semi-submersible. Results were presented for a number of wind and wave environments with an emphasis on global motions, wind excitation and damping effects, nacelle acceleration and system tower and mooring loads. It should be noted that the following conclusions are specific to the load cases evaluated in this report, as well as to the specific designs tested. As such, the conclusions herein are not intended to be generalized to other TLP, spar-buoy and semi-submersible designs, nor to their response under load cases not considered herein.

8.2.1 Wave Only Performance

The results of the wave only cases indicate that the spar-buoy tested possesses the smallest surge response in irregular seas, while the TLP system tested exhibits the smallest pitch response of any of the systems. The semi-submersible response for both DOF studied is typically in between that of the TLP and spar-buoy in the wave energy frequency range, however, the semi-submersible exhibits by far the greatest second-order difference-frequency associated motion response.

8.2.2 Effect of Wind on Global Motions

Regarding the effect of wind, the difference in response for all three systems without wind or with a parked rotor with feathered blades in a severe dynamic wind is very similar. This indicates that feathering the rotor blades is an effective means of minimizing the impact of wind loads on the system. Unlike the feathered case, an operating wind turbine in moderate winds modifies the global motion response of the floating wind turbine. For a TLP floating wind turbine, the wind loading significantly increases the pitch response of the system, however, the pitch response energy as a whole is still quite small. For the spar-buoy and semi-submersible designs, the operating wind turbine significantly damps the second-order difference-frequency pitch response of the structures, and in the case of the semi-submersible, also damps the second-order surge response.

8.2.3 Nacelle Acceleration

The nacelle surge acceleration for the TLP at low energy sea states possesses significant response near the coupled platform pitch/tower bending frequency, whereas the other two systems do not. For intermediate sea states, the unique motion characteristics of the semi-submersible platform yield a near net zero motion of the 90 m hub height wind turbine, minimizing nacelle motion and the accompanying inertial loads.

8.2.4 Tower and Mooring Loads

The tower base bending moment for all three systems at low sea states is characterized by significant response at the platform pitch frequencies, this being above the wave energy frequency for the TLP and below it for the spar-buoy and semi-submersible. For severe sea state conditions, the tower bending moment response for all three systems is dominated by the wave and not the platform pitch frequencies. On the topic of moorings, the TLP mooring load response in the

frequency domain is approximately an order of magnitude greater than for the spar-buoy and semi-submersible floating wind turbine designs. In addition, the spar-buoy and semi-submersible response is primarily located at the system surge natural frequencies whereas the TLP mooring load response is substantial in the wind energy, wave energy and coupled platform pitch/tower bending natural frequencies.

8.3 FAST Calibration and Validation Conclusions

8.3.1 Semi-submersible

This work presented the validation of a FAST numerical model of the DeepCwind semi-submersible floating wind turbine system, which supported a slightly altered version of the NREL 5-MW horizontal-axis reference wind turbine using 1/50th-scale model wind/wave basin test data collected at MARIN. Details required for construction of the model are discussed, including system mass, elastic, aerodynamic, and hydrodynamic properties. The calibration procedure is also presented, and includes tuning of the aerodynamics, tower-bending frequencies, and hydrodynamic damping using system identification test data. With the calibrated FAST model complete, a validation study was undertaken comparing FAST predictions to measured test data. Conditions studied included steady and dynamic wind-only cases, platform free-decay motion under steady winds, regular and irregular wave-only conditions, and finally, a combined dynamic wind and irregular wave case. The load cases examined are representative of specific operational and extreme conditions for the Gulf of Maine.

Upon completion of the validation study, a number of important observations were made. For wind-only loading, whether steady or dynamic, FAST predictions agree very well with experimental data, producing similar statistics, PSDs, and time-series. For wave-only cases, FAST simulations captured the linear wave energy frequency response of the DeepCwind semi-submersible well. The mean drift and second-order difference-frequency responses present in the test data, which were occasionally quite strong, were not captured by FAST. Another deficiency discovered included the significant under-prediction of the mooring line fairlead tensions by FAST's quasi-static mooring module. A portion of this deficiency was likely caused in part by the neglect of platform mean and slowly-varying drift forces; however, much of the deficiency was probably caused by dynamic mooring effects, which FAST is unable to account for. In combined dynamic wind and wave cases, the test data indicated that wind forcing dominated second-order wave and tower-bending frequency effects. Because FAST performed admirably in predicting wind-induced response, the combined wind and wave case studied showed a fairly good agreement between the simulation and test data. This finding signifies that FAST's neglect of second-order wave diffraction effects may only be important in extreme events when the wind turbine blades are feathered and the rotor is parked or idling. A further observation is that a more sophisticated damping model could reduce some discrepancies in the validation studies presented here. One way to achieve this in such a model would be to represent the individual components of the submerged portion of the platform with Morison elements rather than just assigning global damping coefficients to the model.

Aside from possible improvements for the numerical model, the validation studies also revealed potential areas of improvement for experimental set-up and procedures. The cable bundle used to transmit data from the model to the computers added stiffness to both the tower and the surge motion DOF that would never exist in a full-scale, commercial system. Wireless data transmission would eliminate the need for this cable bundle altogether. The tower could also be improved because the one used here was composed of multiple cross sections. It would be more desirable to have a uniform or linearly tapered cross section along the length of the tower to make distributed properties continuous (both mass and elastic) and hence easier to quantify and model. Another experimental improvement would be to modify the wind turbine so the rotor thrust is correct at

properly scaled wind speeds. One way this could be addressed is through the use of different wind blade designs that perform better in lower Reynolds number regimes. Not having to increase wind speeds to achieve proper thrust values would also reduce the aerodynamic drag on the tower and support structure that is currently ignored by FAST; this would yield better comparisons.

In conclusion, this validation study has found FAST to perform well in predicting the coupled aero-hydro-elastic response of the DeepCwind semi-submersible floating wind turbine. The results indicate that the inclusion of second-order wave diffraction and mooring dynamic physics into FAST, the formulations and implementations for which are readily available, would create an accurate and powerful tool for the design and analysis of floating wind turbines.

8.3.2 TLP

This report presents a calibrated FAST model built to represent a scaled model of a floating wind turbine mounted on a TLP. A preliminary validation study of this model was also conducted. After calibrating the FAST model, the comparison between the simulations and experiment was very good in the wave-excitation frequency range in the DOFs that were directly forced by the wind and waves. Discrepancies between the simulations and experiment were seen in other areas, however. As a result, more research is needed in order to determine if the differences between the model and experiment are due to errors in model calibration, sensor error, test errors, or true underperformance of the simulation tool.

8.3.3 Spar-buoy

conditions were compared to results of tank tests of a 1/50th Froude-scaled model of the same system for the purposes of calibration and validation of the FAST model. The FAST model was calibrated to account for differences in mooring systems between the FAST model and UMaine test model and simplifications in the modeling of nonlinear viscous damping. Once calibrated, the natural frequencies of the platform DOFs, as well as the first tower mode, were mostly consistent between the experiment and the simulation, with a roughly 3% inconsistency in pitch and roll. Damping of the platform, as measured by the damping ratio from free-decay tests, was reasonably consistent between the simulation and experiment for heave and yaw decay (particularly for lower height motions), but was inconsistent for surge, sway, pitch, and roll. FAST surge and sway appeared to be less damped than the UMaine model; whereas pitch and roll appeared to have increased damping relative to the UMaine model.

The response of the two systems to periodic waves and zero wind compared well at the wave frequency and fundamental tower frequency, but the FAST model tended toward a greater response at the natural frequencies of platform DOFs. In addition, the experimental data showed greater responses at the first and second harmonics of the wave frequency than the simulation. A quadratic effect was noticeable at twice the wave frequency in the simulation data for higher waves, but was not present for lower waves.

Several irregular wave tests with wind were compared. The response of the two models was generally consistent at frequencies corresponding to the wave spectra. At lower wind velocities, the experimental data showed a 3P response that was not apparent in the FAST simulations until wind speeds were increased to 21.8 m/s, at which point the 3P FAST response exceeded that of the experiment, indicating an increased 3P simulation response with higher platform pitching and increased rotor loads. Responses of 6P and 9P were present in the test data but not in the simulation data. A yaw response at the heave natural frequency was present in the test data but not in the simulation. The response of the two systems in the pitch/roll and surge/sway frequency range was more consistent for simulations including wind, indicating that wind effects dominated in these lower-frequency ranges.

In general, the responses compared well between the experiment and the simulation, particularly in the region of the wave-spectra frequencies. However, differences existed in the responses to periodic and irregular waves, which may be important for full-scale turbine design. More research is needed to understand the discrepancies between the simulation and experiment before an assessment of FAST's ability to accurately model floating wind turbines can be made. In particular, there appears to be significant discrepancies in damping behavior between the experiment and the FAST simulation.

8.3.4 Redesigned Model Wind Turbine Conclusions

In this work, a numerical model of the DeepCwind semi-submersible floating wind turbine was created in the open-source coupled aero-hydro-servo-elastic CAE tool FAST. The model was calibrated using select DeepCwind model test data, and subsequently, was used to simulate wave-only and combined wind and wave cases from the model test program. Second-order difference-frequency wave-diffraction forcing played a significant role in the global response of the DeepCwind semi-submersible based on the analysis of model test data. This study included these forces in the FAST CAE simulator via Newman's approximation in an effort to understand the importance of including these effects.

For wave-only simulations, the inclusion of second-order difference-frequency wave-diffraction forces greatly improved the frequency-domain and statistical correlation between the simulation output and test data for surge and mooring fairlead tension response. To best capture the low-frequency response near the surge resonance frequency, the coefficients employed for the quadratic surge damping model had to be tailored to suit the small amplitude motions created by the operational H_s = 2.0 m sea state. This situation stemmed from two factors. First, the low-frequency resonant surge response is sensitive to the quadratic-drag damping coefficient used in the simulation. Second, the quadratic-drag damping model employed here is unable to capture the damping characteristics of the DeepCwind semi-submersible over a large range of surge amplitudes, and can at best capture the damping response of the system over a limited range of motion amplitudes. It was also found that the Newman's approximation implementation utilized here yielded improvements in the time-series comparisons of the surge response; however, the amplitudes and phases of the low-frequency response were often not in great agreement. In addition, while the inclusion of the second-order wave-diffraction forces improved the low-frequency correlation of the fairlead tension response, a significant discrepancy between the simulation and test data still persisted in the wave-energy frequency range, likely due to the hydrodynamic loading of the mooring line and mooring line dynamics that are currently excluded in the FAST CAE tool.

Upon completion of the wave-only portion of the study, simulations of a combined wind and wave environment were performed and compared to the test data. For the case studied, where the relationship of wind and wave environmental loads was considered to be representative of a realistic operating condition, the dynamic wind loads dominated the low-frequency surge response of the system, as opposed to the second-order difference-frequency wave-diffraction forces. This was confirmed by comparing FAST simulations with and without the second-order wave-diffraction forces. Excluding the second-order wave-diffraction forces for the combined wind and wave case resulted in a small 3.1% reduction in the mean surge value, and even smaller reductions in the surge standard deviation and range. These small reductions indicate that excluding the second-order wave forces, as is done in the current version of FAST, is likely a reasonable approach when simulating floating wind turbines subjected to simultaneous wind and wave loading. However, for instances where the rotor is parked/idling, and the rotor blades are feathered to reduce the rotor thrust coefficient, the response is driven by the wave loads with negligible influence of the wind loads, even in large winds. This conclusion is based on previous analysis of the DeepCwind semi-

submersible test data. In other words, this turbine configuration leads to responses very similar to a wave-only condition. Therefore, neglecting the second-order wave-diffraction forces may no longer be advisable for parked/idling turbine scenarios, as supported by the results obtained from the wave-only analyses conducted in this work.

8.4 Redesigned Model Wind Turbine Conclusions

In this effort, the groundwork laid by Martin et al. for producing a wind turbine model which properly emulates the full scale thrust behavior in a manner suitable for coupled wind/wave Froude-scale model testing of floating wind turbines was extended and validated through physical testing. A more thorough description of the numerical design procedure was presented and the method was employed to produce a design for physical testing and validation in the University of Maine Advanced Structures and Composites Center.

After performing the physical testing at equivalent Froude-scale Reynolds numbers, it was shown that the thrust-matched design performed almost as predicted by the numerical simulation procedure. And unlike the geometrically-similar model, the improved, thrust-matched design replicated the thrust coefficient of the target, NREL 5 MW reference wind turbine target at the design tip-speed ratio in addition to producing significantly more power. Additional findings gathered through testing included adequate thrust coefficient variation with blade pitch angle, a property that will enable realistic pitch-to-feather control schemes for post-rated wind speed conditions during Froude-scale model tests of floating wind turbines. A final observation from laboratory testing was that the thrust-matched design will produce appropriate thrust behavior at Reynolds numbers corresponding to Froude-scale tests significantly less than $1/50^{th}$ scale. However, the performance coefficient of the proposed design degrades sharply for Froude scales much less than 1 to 50.

Future improvements to the design of the thrust-matched wind turbine include a blade redesign to move the peak C_P closer to the design TSR of 7. This would improve the torque simulation of the model and, if done properly, should not degrade the ability to match prototype thrust which is most important for Froude-scale model testing. In addition, the authors are also focused on improving the wind quality of the wind machine for future tests using a conditioning nozzle, individual fan speed tuning and refined screens to improve the flow uniformity.

8.5 DeepCwind Data Verification with Retest Employing Performance-matched Turbine

This report presented a comparison of the DeepCwind semi-submersible floating wind turbine performance as measured in a 2011 campaign using a poor performing, geometrically-similar wind turbine and a 2013 campaign using an improved, performance-matched wind turbine. The intent of the comparison was twofold: 1) To demonstrate that the DeepCwind floating wind turbine data recorded in 2011 with the geometrically-similar wind turbine properly captured the global response behaviors of a floating wind turbine and 2) To show the advantages of model testing a floating wind turbine using a performance-matched turbine designed to work properly in a Froude-scale wind environment.

With regard to the first objective, the comparisons shown in this report indicate that the corrective measures utilized in the 2011 campaign (i.e. increased wind speeds to yield the correct mean thrust) produced global performance data that properly emulates the desired full-scale response. For a scenario using the same sea state and winds that produce the same mean thrust, both the 2011 and 2013 tests show similar trends regarding the changes in frequency-domain response for surge, platform pitch, nacelle fore-aft acceleration and bow fairlead tension when moving from the no wind condition to an operating wind turbine condition. The field variable statistics for these environments in the 2011 and 2013 DeepCwind semi-submersible floating wind turbine campaigns

are also very similar, adding further evidence that the 2011 test data properly captures the global response characteristics of a floating wind turbine subjected to simultaneous wind and wave loading.

As for the second objective, the employment of a performance-matched turbine in the 2013 DeepCwind semi-submersible test campaign permitted the execution of tests not possible in 2011 that demonstrated the unique advantages of using a performance-matched wind turbine. These advantages included testing the coupled aero-hydro-elastic response of the floating wind turbine in region three as well as investigating the influence of active blade pitch control on floating wind turbine global performance. Select data from the 2013 model tests was shown to illustrate these advantages. A first, and unique, example included free-decay test results illustrating the dependence of platform pitch natural period on active blade pitch control settings. For all settings investigated, the active blade pitch controller lengthened the platform pitch natural period. Additional examples illustrated the influence of active blade pitch control on platform pitch response when subjected to irregular seas and steady or dynamic winds. For steady wind cases, the blade pitch controllers tended to increase the pitch response of the platform relative to a similar fixed blade pitch scenario; for dynamic wind cases, the controllers had the opposite effect. The turbine employed for the 2011 test campaign would have been unable to produce these interesting findings.

9 References

API Recommended Practice 2A-WSD, 21st Edition, Recommended Practice for Planning, Designing and Constructing Fixed Offshore Platforms – Working Stress Design, 2000.

Aubault, A., Cermelli, C. and Roddier, D., 2009. WindFloat: A Floating Foundation for Offshore Wind Turbines Part III: Structural Analysis, OMAE 2009 1: 213-220.

J.S. Bendat and A.G. Piersol, Engineering Applications of Correlation and Spectral Analysis (John Wiley & Sons, New York, New York, USA 1980).

NWTC Design Codes (BModes by Gunjit Bir). http://wind.nrel.gov/designcodes/preprocessors/bmodes/. Last modified 20-March-2008; accessed 20-March-2008.

Buhl Jr., M.L., 2004, "WT_Perf User's Guide", National Renewable Energy Laboratory.

Cermelli, C., Roddier, D. and Aubault, A., 2009. WindFloat: A Floating Foundation for Offshore Wind Turbines Part II: Hydronamics Analysis, OMAE 2009 4: 135-143.

Chakrabarti, S.K., 1994. Offshore Structure Modeling. Singapore: World Scientific Publishing Co. Pte. Ltd.

R.D. Cook, D.S. Malkus, M.E. Plesha and R.J. Witt, Concepts and Applications of Finite Element Analysis, 4th Edition (John Wiley & Sons, Hoboken, New Jersey, USA, 2002).

A.J. Coulling, A.J. Goupee, A.N. Robertson, J.M. Jonkman and H.J. Dagher, 2013, Validation of a FAST semi-submersible floating wind turbine model with DeepCwind test data, Journal of Renewable and Sustainable Energy 5, 023116.

Deb, K., 2001, Multi-objective Optimization Using Evolutionary Algorithms, John Wiley & Sons, Chichester.

Drela M., 1989, XFOIL: An analysis and design system for low Reynolds number airfoils, Conference on Low Reynolds Number Airfoil Aerodynamics, University of Notre Dame.

Drela M., Giles M.B., 1987, Viscous-inviscid analysis of transonic and low Reynolds number airfoils, AIAA Journal 25(10).

US Energy Information Administration, 2011, Annual Energy Review 2010, Technical Report DOE/EIA-0384(2010).

O.M. Faltinsen, Sea Loads on Ships and Offshore Structures (Cambridge University Press, Cambridge, United Kingdom, 1990).

Fowler, M.J., Kimball, R.W., Thomas III, D.A. and Goupee, A.J., 2013, "Design and testing of scale model wind turbines for use in wind/wave basin model tests of floating offshore wind turbines," Proceedings of OMAE2013, Nantes, France.

D.L. Garrett, "Dynamic analysis of slender rods," Journal of Energy Resource Technology 104, 302-306 (1982).

Glauert H., 1926, The Elements of Aerofoil and Airscrew Theory, Cambridge University Press, Cambridge.

A.J. Goupee, B.J. Koo, K. Lambrakos and R.W. Kimball, "Model tests for three floating wind turbine concepts," Proceedings of the 2012 Offshore Technology Conference, Houston, Texas, USA, 30 April-3 May 2012.

Goupee, A.J., Koo, B, Kimball, R.W., Lambrakos, K.F. and Dagher, H.J., " Experimental Comparison of Three Floating Wind Turbine Concepts," Proc. 31st ASME International Conference on Offshore Mechanics and Arctic Engineering, Rio de Janeiro, Brazil.

C. Hansen, NWTC Design Codes: AirfoilPrep, http://wind.nrel.gov/designcodes/preprocessors/airfoilprep/, accessed August 6, 2012.

Hansen A C and Moriarty P J 2005 AeroDyn Theory Manual NREL Technical Report NREL/TP-500-36881 National Renewable Laboratory Golden Colorado United States

IEC 61400-3, 2009, Wind Turbines - Part 3: Design Requirements for Offshore Wind Turbines, International Electrotechnical Commission (IEC).

A. Jain, A.N. Robertson, J.M. Jonkman, A.J. Goupee and R.W. Swift, "FAST code verification of scaling laws for DeepCwind floating wind system tests," Proceedings of the 22nd International Offshore and Polar Engineering Conference, Rhodes, Greece, 17-22 June 2012, pp. 355-365.

Jonkman, B. J. (2009). TurbSim User's Guide: Version 1.50, National Renewable Energy Laboratory, Golden, Colorado, USA, Technical Report: NREL/TP-500-46198.

Jonkman, J.M., 2007. Dynamics Modeling and Loads Analysis of Offshore Floating Wind Turbines. NREL Technical Report NREL/TP-500-38060.

Jonkman, J.M., 2008, "Influence of control on the pitch damping of a floating wind turbine," Proceedings of the 2008 ASME Wind Energy Symposium, Reno, Nevada.

Jonkman, J.M., 2010. Definition of the Floating System for Phase IV of OC3. NREL Technical Report NREL/TP-500-47535.

Jonkman, J.M. and Buhl Jr., M.L., 2005. FAST User's Guide. NREL Technical Report NREL/EL-500-38230.

Jonkman, J.M., Butterfield, S., Musial, W. and Scott, G., 2009. Definition of a 5-MW Reference Wind Turbine for Offshore System Development. NREL Technical Report NREL/TP-500-38060.

M.H. Kim and D.K.P. Yue, "Sum- and difference-frequency wave loads on a body in unidirectional Gaussian seas," Journal of Ship Research 35(2), 127-140 (1991).

B. Koo, A.J. Goupee, K. Lambrakos and R.W. Kimball, "Model tests for a floating wind turbine on three different floaters," Proceedings of the 31st ASME International Conference on Offshore Mechanics and Arctic Engineering, Rio de Janeiro, Brazil, 1-6 July, 2012.

B. Koo, A.J. Goupee, K. Lambrakos and H.-J. Lim, 2013, Model test correlation study for a floating wind turbine on a tension leg platform, Proceedings of OMAE 2013, ASME 32nd International Conference on Offshore Mechanics and Arctic Engineering, Nantes, France, June 9-14, 2013, accepted for publication.

Langley, R.S., 1986, "On the Time Domain Simulation of Second Order Wave Forces and Induced Responses," AppliedOcean Research 8(3), pp. 134-144.

C.H. Lee and J.N. Newman, WAMIT® User Manual, Versions 6.4, 6.4PC, 6.3S, 6.3S-PC (WAMIT, Inc., Chestnut Hill, Massachusetts, USA 2006).

Leishman J.G., 2000, Principles of Helicopter Aerodynamics, Cambridge University Press, Cambridge.

Manwell J.F., McGowan J.G., Rogers A.L., 2009, Wind Energy Explained: Theory, Design and Applications 2nd Ed., John Wiley & Sons Ltd., West Sussex.

Martin H., 2011, Development of a Scale model Wind Turbine for Testing of Offshore Floating Wind Turbine Systems, M.S. Thesis, University of Maine.

H.R. Martin, R.W. Kimball, A.M. Viselli and A.J. Goupee, "Methodology for wind/wave basin testing of floating offshore wind turbines," Proceedings of the 31st ASME International Conference on Offshore Mechanics and Arctic Engineering, Rio de Janeiro, Brazil, 1-6 July, 2012.

M. Masciola, A. Robertson, J. Jonkman, A. Coulling and A. Goupee, 2013, Assessment of the importance of mooring dynamics on the global response of the DeepCwind floating semi-submersible offshore wind turbine,Proceedings of ISOPE 2013, The 23rd International Ocean and Polar Engineering Conference, June 30-July 5, 2013, accepted for publication.

Matha, D. (2010). Model Development and Loads Analysis of anOffshore Wind Turbine on a Tension Leg platform, with aComparison to Other Floating Turbine Concepts, National Renewable Energy Laboratory, Golden, Colorado, USA, Subcontract Report: NREL/SR-500-45891.

Moon III, WL, Nordstrom, CJ, (2010) "Tension leg platform turbine: A unique integration of mature technologies," Proceedings of the 16th Offshore Symposium, Houston, Texas Section of the Society of Naval Architects and Marine Engineers.

Multisurf 8.0, Version 8.0 (AeroHydro, Inc., Southwest Harbor, Maine, USA 2011).

Musial W., 2008, Status of Wave and Tidal Power Technologies for the United States, Technical Report NREL/TP-500-43240.

Musial W., Ram B., 2010, Large-Scale Offshore Wind Power in the United States, Technical Report NREL/TP-500-40745.

Neville, A., 2009. Hywind Floating Wind Turbine, North Sea, Norway. POWER 153(12): 40.

Newman, J.N., 1974, "Second-order, Slowly-varying Forces on Vessels in Irregular Waves," Proc. Dynamics of Marine Vehicles and Structures in Waves, pp. 193-197.

J.N. Newman, Marine Hydrodynamics (The MIT Press, Cambridge, Massachusetts, USA, 1977).

The Norwegian Petroleum Directorate (NPD), 1992, Guidelines Concerning Load Effects to Regulations Concerning Load Bearing Structures in the Petroleum Activities.

J.R. Paulling and W.C. Webster, "A consistent, large-amplitude analysis of the coupled response of a TLP and tendon system," Proceedings of the 5th ASME International Conference on Offshore Mechanics and Arctic Engineering, Tokyo, Japan, 13-18 April, 1986, pp. 126-133.

Peters D.A., He C.J., 1991, Correlation of measured induced velocities with a finite-state wake model, Journal of the American Helicopter Society 36(3).

I. Prowell, A. Robertson, J. Jonkman, G.M. Stewart and A.J. Goupee, 2013, Numerical prediction of experimentally observed behavior of a scale model of an offshore wind turbine supported by a tension-leg platform, Proceedings of the Offshore Technology Conference (OTC 2013), Houston, Texas, USA, May 6-9, 2013, accepted for publication.

Roddier, D., Cermelli, C. and Weinstein, A., 2009. WindFloat: A Floating Foundation for Offshore Wind Turbines Part I: Design Basis and Qualification Process, OMAE 2009 4: 845-853.

Roddier, D., Cermelli, C., Aubault. A. and Weinstin. A., 2010. WindFloat: A floating foundation for offshore wind turbines. Journal of Renewable and Sustainable Energy 2: 033104.

Skaare. B., Hanson, T.D., Nielsen, F.G., Yttervik, R., Hansen, A.M., Thomesn, K. and Larsen, T.J., 2007. Integrated Dynamic Analysis of Floating Offshore Wind Turbines. Paper presented at the European Wind Energy Conference and Exhibition, Milan, 7-10 May.

Standing, R.G., Brendling, W.J. and Wilson, D., 1987, "Recent Developments in the Analysis of Wave Drift Forces, Low-Frequency Damping and Response," Proc. 1987 Offshore Technology Conference, Houston, Texas.

Stewart, G., Lackner, M., Robertson, A., Jonkman, J. and Goupee, A., 2012, "Calibration and Validation of a FAST Floating Wind Turbine Model of the DeepCwind Scaled Tension-leg Platform," Proc. 22nd International Offshore and Polar Engineering Conference, Rhodes, Greece, pp. 380-387.

University of Maine and James W. Sewall Company, "Maine deepwater offshore wind report," February 2011.

van Walree, F., Yamaguchi, K., 1993, Hydrofoil research: model tests and computations, FAST '93, 2nd International Conference on Fast Sea Transportation, Yokohama, Japan.

WAMIT USER MANUAL (1998-2006): Versions 6.4, 6.4PC, 6.3S,6.3S-PC, WAMIT Inc., USA.

http://www.windsea.no/, accessed January 2012.